Structure and Bonding 143

Series Editor: D.M.P. Mingos

D. Michael P. Mingos
Peter Day
Jens Peder Dahl *Editors*

Molecular Electronic Structures of Transition Metal Complexes II

Springer

143

Structure and Bonding

Series Editor: D. M. P. Mingos

For further volumes:
http://www.springer.com/series/430

Structure and Bonding

Series Editor: D. M. P. Mingos

Recently Published and Forthcoming Volumes

Molecular Electronic Structures of Transition Metal Complexes II
Volume Editors: D. M. P. Mingos, Peter Day, Jens Peder Dahl
Vol. 143, 2012

Molecular Electronic Structures of Transition Metal Complexes I
Volume Editors: D. M. P. Mingos, Peter Day, Jens Peder Dahl
Vol. 142, 2012

Fuel Cells and Hydrogen Storage
Volume Editors: Andrew Bocarsly, D. M. P. Mingos
Vol. 141, 2011

Zintl Ions
Principles and Recent Developments
Volume Editor: Thomas F. Fässler
Vol. 140, 2011

Zintl Phases
Principles and Recent Developments
Volume Editor: Thomas F. Fässler
Vol. 139, 2011

Inorganic 3D Structures
Volume Editor: Angel Vegas
Vol. 138, 2011

Molecular Catalysis of Rare-Earth Elements
Volume Editor: Peter W. Roesky
Vol. 137, 2010

Metal-Metal Bonding
Volume Editor: Gerard Parkin
Vol. 136, 2010

Functional Phthalocyanine Molecular Materials
Volume Editor: Jianzhuang Jiang
Vol. 135, 2010

Data Mining in Crystallography
Volume Editors: Hofmann, D. W. M., Kuleshova, L. N.
Vol. 134, 2010

Controlled Assembly and Modification of Inorganic Systems
Volume Editor: Wu, X.- T.
Vol. 133, 2009

Molecular Networks
Volume Editor: Hosseini, M. W.
Vol. 132, 2009

Molecular Thermodynamics of Complex Systems
Volume Editors: Lu, X., Hu, Y.
Vol. 131, 2009

Contemporary Metal Boron Chemistry I
Volume Editors: Marder, T. B., Lin, Z.
Vol. 130, 2008

Recognition of Anions
Volume Editor: Vilar, R.
Vol. 129, 2008

Liquid Crystalline Functional Assemblies and Their Supramolecular Structures
Volume Editor: Kato, T.
Vol. 128, 2008

Organometallic and Coordination Chemistry of the Actinides
Volume Editor: Albrecht-Schmitt, T. E.
Vol. 127, 2008

Halogen Bonding
Fundamentals and Applications
Volume Editors: Metrangolo, P., Resnati, G.
Vol. 126, 2008

High Energy Density Materials
Volume Editor: Klapötke, T. H.
Vol. 125, 2007

Ferro- and Antiferroelectricity
Volume Editors: Dalal, N. S., Bussmann-Holder, A.
Vol. 124, 2007

Molecular Electronic Structures of Transition Metal Complexes II

Volume Editors:
D. Michael P. Mingos · Peter Day · Jens Peder Dahl

With contributions by

M. Atanasov · J.E. Avery · J.S. Avery · R.S. Berry ·
D. Ganyushin · J. Linderberg · A.J. McCaffery · F. Neese ·
K. Sivalingam · B.M. Smirnov · B.T. Sutcliffe · T. Ziegler

Springer

Editors
D. Michael P. Mingos
Inorganic Chemistry Laboratory
Oxford University
South Parks Road
Oxford OX1 3QR, UK
michael.mingos@st-edmund-hall.oxford.ac.uk

Peter Day
The Royal Institution of Great Britain
Albermarle Street 21
W1X 4BS London
United Kingdom
profpday@msn.com

Jens Peder Dahl
Department of Chemistry
Technical University of Denmark
DTU 207, 2800 Lyngby
Denmark
dahlhome@webspeed.dk

ISSN 0081-5993 e-ISSN 1616-8550
ISBN 978-3-642-27377-3 e-ISBN 978-3-642-27378-0
DOI 10.1007/978-3-642-27378-0
Springer Heidelberg Dordrecht London New York

Library of Congress Control Number: 2011944826

Printed on acid-free paper

Springer is part of Springer Science+Business Media (www.springer.com)

Series Editor

Volume Editors

D. Michael P. Mingos

Inorganic Chemistry Laboratory
Oxford University
South Parks Road
Oxford OX1 3QR, UK
michael.mingos@st-edmund-hall.oxford.ac.uk

Jens Peder Dahl

Department of Chemistry
Technical University of Denmark
DTU 207, 2800 Lyngby
Denmark
dahlhome@webspeed.dk

Peter Day

The Royal Institution of Great Britain
Albermarle Street 21
W1X 4BS London
United Kingdom
profpday@msn.com

Editorial Board

Structure and Bonding
Also Available Electronically

Structure and Bonding is included in Springer's eBook package *Chemistry and Materials Science*. If a library does not opt for the whole package the book series may be bought on a subscription basis. Also, all back volumes are available electronically.

For all customers who have a standing order to the print version of *Structure and Bonding*, we offer the electronic version via SpringerLink free of charge.

If you do not have access, you can still view the table of contents of each volume and the abstract of each article by going to the SpringerLink homepage, clicking on "Chemistry and Materials Science," under Subject Collection, then "Book Series," under Content Type and finally by selecting *Structure and Bonding*.

You will find information about the

- Editorial Board
- Aims and Scope
- Instructions for Authors
- Sample Contribution

at springer.com using the search function by typing in *Structure and Bonding*.

Color figures are published in full color in the electronic version on SpringerLink.

Aims and Scope

The series *Structure and Bonding* publishes critical reviews on topics of research concerned with chemical structure and bonding. The scope of the series spans the entire Periodic Table and addresses structure and bonding issues associated with all of the elements. It also focuses attention on new and developing areas of modern structural and theoretical chemistry such as nanostructures, molecular electronics, designed molecular solids, surfaces, metal clusters and supramolecular structures. Physical and spectroscopic techniques used to determine, examine and model structures fall within the purview of *Structure and Bonding* to the extent that the focus is on the scientific results obtained and not on specialist information concerning the techniques themselves. Issues associated with the development of bonding models and generalizations that illuminate the reactivity pathways and rates of chemical processes are also relevant.

The individual volumes in the series are thematic. The goal of each volume is to give the reader, whether at a university or in industry, a comprehensive overview of an area where new insights are emerging that are of interest to a larger scientific audience. Thus each review within the volume critically surveys one aspect of that topic and places it within the context of the volume as a whole. The most significant developments of the last 5 to 10 years should be presented using selected examples to illustrate the principles discussed. A description of the physical basis of the experimental techniques that have been used to provide the primary data may also be appropriate, if it has not been covered in detail elsewhere. The coverage need not be exhaustive in data, but should rather be conceptual, concentrating on the new principles being developed that will allow the reader, who is not a specialist in the area covered, to understand the data presented. Discussion of possible future research directions in the area is welcomed.

Review articles for the individual volumes are invited by the volume editors.

In references *Structure and Bonding* is abbreviated *Struct Bond* and is cited as a journal.

Impact Factor in 2010: 4.659; Section “Chemistry, Inorganic & Nuclear”:
Rank 4 of 43; Section “Chemistry, Physical”: Rank 25 of 127

This volume is dedicated to
Carl Johan Ballhausen

Preface

When I heard in August 2010 that Carl Ballhausen had died at the age of 84, I was very sad because he had played such an important part in the development of my interests in coordination and theoretical inorganic chemistry in the 1960s. Indeed lectures given by Carl, Al Cotton, Dick Fenske, and Harry Gray at a NATO Summer School held at Selsdon Park Hotel near London in 1967 did much to stimulate my interest in theoretical inorganic chemistry. Later, when I embarked on my first semiempirical molecular orbital calculations to understand why nitrosyl complexes adopted linear and bent geometries, I was greatly assisted by "Molecular Orbital Theory," which Carl coauthored with Harry Gray (W.A. Benjamin New York, 1965). My sense of loss must have been small when compared with those of the many graduate students and postdoctoral fellows who had been supervised by him. His many international collaborators would also have missed his profound theoretical insights and friendly, jovial manner. Therefore, I was pleased when Peter Day after consulting with Jens Peder Dahl proposed a volume of *Structure and Bonding* dedicated to Carl's life and his seminal contributions to quantum chemistry. The large number of Carl's co-workers who have gone on to occupy senior academic positions made it relatively easy to propose a list of authors for the volume. Their response to invitations to contribute has been so enthusiastic that it proved necessary to expand the project into two volumes. The first one deals with the application of Carl's Ligand Field Theory to spectroscopic and chemical properties of transition metal complexes. The second volume concentrates on more theoretical topics and reviews the development of modern ab initio theoretical methods and discusses the broader implications of fundamental theoretical concepts.

Jens Peder Dahl was closely associated with Carl's research group for many years, and his introductory chapter summarizes his scientific achievements and in particular his contributions to the inorganic renaissance which unfolded from 1950. Harry Gray recounts his very fruitful collaboration with Carl which resulted in a general molecular orbital description of the metal-oxo bond, and he and Jay Winkler review more recent experimental and spectroscopic data on metal-oxo complexes of the later transition metals. Colin Flint also provides a brief review of his work with Carl in 1967–1968, and then describes his subsequent research on the assignments of the vibronic sidebands in the emission spectra of chromium ammine complexes. He also comments on the Jahn–Teller effect in the emissive state.

Joshua Palmer discusses the transition metal complexes of the noninnocent, electron-rich corrole macrocycle. This includes a detailed summary of investigations to determine the physical oxidation states of formally copper(III), iron(IV), and cobalt(IV) corroles. The electronic structures and reactivities of other metallocorroles are also discussed, and comparisons made between corrole and porphyrin complexes. William Trogler reviews thin film conductivity sensors that use metal phthalocyanine semiconductors which offer properties distinct from those of organic thin film transistor sensors. Phthalocyanines (Pc) are planar ligands that are closely related to porphyrins (Por), as both can be deprotonated to form dianions that yield a wide variety of square planar metal(II) chelate complexes MPc and MPor. Porphyrins are crucial redox active metalloenzymes that play key roles in metabolism, oxygen storage, photosynthesis, and other biological processes. Phthalocyanines are also important dye and paint pigments, as well as having electronic device applications in CD-recordable media, xerography, photovoltaics, and organic light-emitting devices. Kyle Lancaster reviews the concept of outer-sphere coordination (OSC) in the context of bioinorganic chemistry. A distinction is made between electronic and structural OSC, which arises from the interaction of the protein matrix with inner sphere ligands. Electronic OSC entails the electronic interaction between the polypeptide and inner-sphere ligands. These effects principally arise from hydrogen-bonding interactions, though through-space dipolar interactions are also encountered.

Rosalie Hocking and Ed Solomon in the next chapter note that Carl Ballhausen taught them how to interpret ground and low lying excited state spectral features in terms of ligand field and covalency effects. With the availability and development of synchrotron radiation, this has been extended to the X-ray region where ligand field and covalency effects have an impact on the metal K and L-edges. The L-edge intensity and its distribution over the multiplets are particularly powerful in experimentally determining the bonding in highly covalent systems, where ligand spectral features can obscure the use of more traditional methods. Klaus Møller and Niels Henriksen in their review discuss how time-resolved X-ray diffraction may lead to important insights into the dynamics of the chemical bond. The focus of the review is the underlying theoretical concepts which are required in order to extract the dynamics of the chemical bond from the time-resolved X-ray diffraction data.

In the first chapter of the second volume, Tom Ziegler reviews the development of electronic structure theories for transition metal complexes from the 1950s to the present day. Jan Linderberg also focuses on the emergence of quantitative means for the study of the electronic properties of complexes and molecules. The development, refinement, and application of the orbital picture have elucidated the electric and magnetic features of molecules and used for the interpretation of electronic transitions, electron spin resonance parameters, rotatory dispersion, nuclear quadrupole couplings, and geometric bonding patterns. In a chapter which addresses some fundamental issues, John and James Avery discuss the theory of Sturmians and generalized Sturmians. They show that when generalized Sturmians are used as basis functions, calculations on the spectra and physical properties of few electron atoms can be performed with great ease and good accuracy. Brian Sutcliffe considers the implications of Carl Ballhausen's research on vibrational spectra, and it is suggested that his use of the Born–Oppenheimer approximation is capable of some refinement and extension in the light of later developments. A consideration of the potential energy surface in the context of a full Coulomb Schrödinger Hamiltonian in which translational and rotational motions are explicitly considered would seem to require a reformulation of the Born–Oppenheimer approach. The resulting potential surface for vibrational motion allows for the rotational motion and the nuclear permutational symmetry of the molecule. Tony McCaffery considers the role played by angular momentum in chemical physics, an interest which was first aroused by a Carl Ballhausen lecture early in the author's scientific career. Later came a deeper understanding of the fundamental nature of angular momentum and the power of its formal algebraic expression. Spectroscopy using light of precisely defined energy and (z-component of) angular momentum represents a unique experimental probe with the potential to reveal the underlying physics of chemical processes. Experiments using circularly polarized emission of gas phase molecules led to new insights in the field of molecular collision dynamics. Further work, and that of others, has suggested an alternative formulation of the mechanics of bimolecular collisions

Frank Neese and his coauthors summarize recent developments in AI methods for strongly correlated electronic systems, and they discuss their implementation in highly efficient quantum chemistry programs which allow one to calculate – from first principles – the spectroscopic and magnetic properties of transition metal complexes with open d- and f-shells. For a long time, this field was the domain of ligand field theory (LFT), subject to various assumptions and approximations which are solely justified by the success of using this theory for the interpretation of experimental data. Yet the chemical significance of the ligand field parameters, while being under intense debate, remains unclear as far as the roots of LFT in its relation to rigorous quantum chemistry are concerned. In the present review, the authors attempt to answer the question how well ligand field performs from the point of view of state-of-the-art first principle calculations and how to connect the two areas. In his chapter, Steve Berry notes that the Gibbs Phase Rule relating the number of degrees of freedom f of a system to the number of components c and the number of coexisting phases p is a central, universally used relation. However, for small systems, notably atomic clusters the Phase Rule shows the coexistence of two or more phases in thermodynamic equilibrium over *bands* of temperature and pressure (with no other forces acting on them). He demonstrates that it is consistent with the laws of thermodynamics and even allows one to estimate the upper size limit of any particular system for which such apparent violation could be observed.

These two volumes provide a fine endorsement of the way in which Carl's contributions have influenced so many scientists and led them explore important new areas of transition metal chemistry, quantum theory, and spectroscopy. The authors have successfully illuminated the fundamental and broad question which guided much of Carl's research – "What is a molecule and in particular a transition metal complex?". As an interesting postscript, Carl Ballhausen and Christian Klixbull Jørgenson were both in University of Copenhagen in the early 1950s and did their doctoral theses with Jannik Bjerrum at about the same time. At an early stage they collaborated on a series of papers titled "Studies of Absorption Spectra," but their relationship was not always an easy one. Jorgenson moved from Copenhagen at the age of 29 and did research at Cyanamid and the University of Geneva in Switzerland. He died in 2001 and a pair of commemorative volumes were published as part of the *Structure and Bonding* Series in 2004 (volumes 106 and 107). The four volumes will remind us and future generations the important role played by Danish coordination and theoretical chemists in the renaissance of inorganic chemistry.

Oxford D. Michael P. Mingos
August 2011

Contents

Struct Bond (2012) 143: 1–38
DOI: 10.1007/430_2011_47

A Chronicle About the Development of Electronic Structure Theories for Transition Metal Complexes

Tom Ziegler

Abstract We review here the development of electronic structure theories for transition metal complexes from the 1950s to present days. The different methods are compared through applications to permanganate and other tetroxo systems.

Keywords Constricted density functional theory · Density functional theory · Electronic structure theory · Hartree–Fock method · Post-Hartree–Fock methods · Time-dependent density functional theory

Contents

T. Ziegler (✉)
Department of Chemistry, University of Calgary, Calgary, AB, Canada T2N1N4
e-mail: ziegler@ucalgary.ca

1 Introduction

The formulation of an electron structure theory for coordination compounds containing transition metals began shortly after the introduction of quantum mechanics with the development by Becquerel [1], Bethe [2] and Van Vleck [3] of crystal-field theory. A giant step forward was taken in the 1950s by the development of ligand field theory [4, 5] that combines the ideas of crystal field theory with those of molecular orbital theory [6] and allows for an elegant interpretation of the spectra of coordination complexes. C. J. Ballhausen was one of the pioneers in this development and his book on ligand field theory from 1962 [5] influenced a whole generation of coordination chemists.

Ballhausen started his carrier in the lab of J. Bjerrum at the University of Copenhagen in the early 1950s. This was an environment that continued the strong Danish tradition in coordination chemistry dating back to S.M. Sørensen and N. Bjerrum. At the time (1950), the lab attracted several international visitors including F.A. Cotton and F. Basolo. It testifies to the strength of the group that it fostered two other young members that went on to contribute significantly to ligand field theory, namely C.E. Schäffer and C. K. Jørgensen. The theoretical interest by the three young members of the Bjerrum team was very much whetted by the appearance in 1951 of a paper [7] due to F.E. Ilse and H. Hartmann in which the two authors explained the electronic spectrum of the Ti(+3) ion based on crystal field theory.

After establishing his own lab, Ballhausen began in the 1960s on a research program that combined high-resolution spectroscopic measurements with interpretations based on theoretical methods. These methods included not only ligand field theory but increasingly also other schemes based on Roothaan's formulation [8, 9] of molecular orbitals theory as they emerged in the 1960s and 1970s. Ballhausen would not take directly part in the development of these new methods but he encouraged people in his lab to do so. This encouragement was also extended to young students such as myself. Thus when I started an a M.Sc. student in the Ballhausen lab (1969), I was given the task to evaluate semi-empirical methods that were applied to transition metals at the time and possibly come up with improvements. I was very fortunate to be introduced to the electronic structure theory of transition metal complexes at a time when the field was undergoing a revolution [10]. Thus although I soon lost all interest in semi-empirical methods, my time with Ballhausen and his collaborator J.P. Dahl launched a lifelong interest in transition metal complexes and methods that could describe their electronic structure. It is the objective of this account to chronicle some of the highlights from the early beginnings of theoretical transition metal chemistry in the 1950s to present days powerful electronic structure theories.

In the period (1969–1972) when I was a student with Ballhausen, his lab was an international center with visitors from many different parts of the world representing a multitude of different research interest. One particular subject that caught my interest was the electronic structure and absorption spectrum of permanganate and related tetroxo complexes. The electronic spectrum of permanganate was first studied by Teltow [11] in 1938. However, with modern techniques Holt and Balhausen [12] had in 1967 recorded a high resolution low temperature absorption spectrum of MnO_4^-. Shortly after, attempts were made to assign the observed spectrum with any available computational method. It was felt that permanganate as a small system with a pleasingly high symmetry should be an easy task for theory. The implication here was that if theory cannot treat as simple a system as MnO_4^-, it would appear not to be of much use at all. As we shall see, the notion of permanganate being an easy system is completely wrong. In fact permanganate is one of the most difficult electronic systems to describe. We shall demonstrate this through a number of applications to MnO_4^- that are used to gauge the ability of the different theories chronicled in this account.

2 Ground State Electronic Structure Theory

We shall in this section give a historic overview of how the electronic structure theory for transition metal complexes in their ground state has evolved from the 1950s to the present time. The account will include a discussion of wave function methods based on Hartree Fock and post-Hartree Fock approaches as well as Kohn–Sham density functional theory (KS-DFT).

2.1 *The Hartree–Fock Method*

In Hartree–Fock theory, we approximate the many-electron wave function with a single Slater determinant

$$\Psi = \frac{1}{\sqrt{N!}} \begin{vmatrix} \psi_1(x_1)\psi_2(x_2)\ldots\psi_1(x_N) \\ \psi_2(x_1)\psi_2(x_2)\ldots\psi_2(x_N) \\ \ldots \\ \psi_N(x_1)\psi_N(x_2)\ldots\psi_N(x_N) \end{vmatrix} = |\psi_1\psi_2..\psi_i\psi_j..\psi_n| \tag{1}$$

for which the corresponding energy is given by

$$\begin{aligned} <\Psi|\hat{H}|\Psi> = H_0 + \sum_{i=1}^{N} <\psi_i|\hat{h}|\psi_i> \\ + \frac{1}{2}\sum_{i,j}{}' \{<\psi_i\psi_j|g|\psi_i\psi_j> - <\psi_i\psi_j|g|\psi_j\psi_i>\}. \end{aligned} \tag{2}$$

In (2), H_0 represents the nuclear–nuclear repulsion, whereas $\hat{h}$ contains the one-electron kinetic energy operator as well at the operator for the attraction of one electron from all the nuclei. Finally

$$< \psi_r \psi_s | g | \psi_p \psi_q >= \int\int \psi_r^*(\vec{r}) \psi_s^*(\vec{r}_2) \frac{e^2}{r_{12}} \int \psi_p(\vec{r}_1) \psi_q(\vec{r}_2) dv_1 dv_2 \tag{3}$$

is a two-electron repulsion integral between the charge distributions $\psi_r^*(\vec{r}_1)\psi_p(\vec{r}_1)$ and $\psi_s^*(\vec{r}_1)\psi_q(\vec{r}_1)$. Thus, the third term on the right hand side of (2) constitutes the Hartree term E_{H} describing the Coulomb interaction of the electron density with itself whereas the last term is the HF-exchange energy $E_{\mathrm{X}}^{\mathrm{HF}}$. In practical calculations, the "occupied orbitals" defining Ψ are written as a linear combination of known atomic orbitals (LCAO) also referred to as basis functions

$$\psi_i = \sum_{r=1}^{M} C_{ri}\ \chi_r, \quad i = 1, 2, \ldots, n;\ M \geq n, \tag{4}$$

where $\mathbf{C_i} = \{C_{1i}, C_{2i}, .., C_{ri}, C_{si}, \ldots C_{Mi}\}$ is a vector containing all expansion coefficients defining orbital ψ_i. The expansion coefficients are now determined in such a way as to minimize $< \Psi | \hat{H} | \Psi >$ under the constraint that the set $\{\psi_i; i = 1, n\}$ be orthornormal. This requirement leads to the well-known Hartree–Fock eigenvalue equation in its Roothan [8] formulation

$$\mathbf{F}\ \mathbf{C}_i = \varepsilon_i \mathbf{S}\ \mathbf{C}_i \tag{5}$$

from which $\mathbf{C_i}$ can be determined. In (5),

$$S_{rs} = \int \chi_r^*(\vec{r}_1) \chi_s(\vec{r}_1) d\vec{r}_1, \tag{6}$$

whereas $\mathbf{F} = \mathbf{h} + \mathbf{G}$ with

$$h_{rs} = \int \chi_r^*(\vec{r}_1) \hat{h} \chi_s(\vec{r}_1) d\vec{r}_1 \tag{7}$$

and

$$G_{rs} = \sum_{t,u=1}^{M} P_{t,u} \{< rs | g | tu > - < ru | g | ts >\}, \tag{8}$$

whereas

$$P_{tu} = \sum_{j=1}^{n} C_{tj}^* C_{uj} \tag{9}$$

In the 1950s, the Roothan equation was too complex and computational demanding to be of practical use due to the occurrence of the many two electron repulsion integrals $< rs|g|tu >$. Thus, the number of such integrals increases as M^4 with the number of atomic orbitals M. As a consequence, application of the Roothan equation was in the 1950s and 1960s characterized by a number of approximations.

2.1.1 The Wolfberg Helmholz Approximation and the Extended Hückel Method

In the first LCAO calculation on MnO_4^-, Wolfberg and Helmholz [13] suggested as early as 1952 to use empirical data such as ionization potentials for the diagonal elements F_{rr} of (5) since F_{rr} represents the energy of an electron in χ_r in the field of the nuclear skeleton and the remaining valence electrons. For the off-diagonal elements, they introduced what has become known as the Wolfberg and Helmholz (WH) approximation

$$F_{rs} = kS_{rs}[F_{rr} + F_{ss}]/2, \tag{10}$$

where k is an empirical factor usually taken to be close to one.

R. Hoffmann adopted the same approximation when he introduced the extended Hückel (EH) method in 1963 [14]. The EH scheme gained considerable popularity through Hoffmann's masterful analyses of the bonding in classical transition metal complexes and organometallic compounds [15]. To this date, organometallic chemists are influenced by Hoffmann's powerful orbital interaction approach originally based on the EH scheme [16]. The EH method can provide a qualitative description of the bonding. It is also able to some degree to distinguish between the stability of different conformational isomers as illustrated by J.K. Burdett [17] in his angular overlap approach. R.F. Fenske and his (at that time) student M.B. Hall [18] developed a kindred scheme also based on the WH-approximation. Their method has also been used widely in the 1960s and 1970s to analyze chemical bonding in transition metal compounds with many important contributions from M.B. Hall [19]. It is a common feature of all schemes discussed above that they are computationally expedient thanks to the WH-approximation. At the same time, the WH-approximation is too rough to allow for an accurate determination of bond energies and optimized molecular structures in general.

2.1.2 Approaches Based on Integral Approximations

An alternative approach to the one described above has been to reduce the number of two-electron integrals considered in evaluating G of (8) by assuming that the omitted integrals are small. This procedure was adopted by Pople et al. [20] who introduced complete neglect of differential overlaps (CNDO) in which

$$\langle r_A s_B | g | t_C u_D \rangle = \delta_{AC}\delta_{BD}\delta_{rt}\delta_{su}\langle r_A s_B | g | r_A s_B \rangle, \tag{11}$$

where A, B, C and D are the centres at which the atomic orbitals $\chi_r, \chi_s, \chi_t, \chi_u$, respectively, are situated. The same authors also proposed intermediate neglect of differential overlap (INDO) where (11) applies if A and B represent different centres, whereas all one-center integrals of the form $\langle r_A s_A | g | t_A u_A \rangle$ are retained. At the highest level of complexity, Pople et al. proposed neglect of diatomic differential overlap (NDDO) with the approximation

$$\langle r_A s_B | g | t_C u_D \rangle = \delta_{AC}\delta_{BD}\langle r_A s_B | g | t_A u_B \rangle. \tag{12}$$

For compounds containing main group s, p elements all three schemes have been employed and improved considerably leading to the widely used AM1 [21] (Austin model 1), PM3 [22] (Parameterized model number 3) and MNDO [23] (modified neglect of differential overlap) methods that all are extensions or modifications of the NDDO approach. The three schemes are able to predict geometries and energetics of *s*, *p* main group compounds quite well. Part of the success stems from the fact that the required one and two centre integrals are parameterized to fit experimental data.

In the case of transition metal complexes, the CNDO theory was first applied by Dahl and Ballhausen [24] to MnO_4^-. Their scheme was later extended to INDO by Ziegler [25] and implemented into the general package ODIN [26]. Better known is the INDO program ZINDO [27] by M. Zerner and the NDDO implementation due to D.S. Marynick [28]. Both have been applied with some success in transition metal chemistry for structure determination and studies of excited states. Attempts have also been made to extend AM1, PM3 and MNDO to transition metals. All in all it must be said that the methods based on integral approximations have been more prolific in studies of main group compounds than transition metal complexes. The reason for that is likely the considerable extra complexity added by the *d*-orbitals combined with the fact that other attractive schemes are available for *d*-block compounds.

2.1.3 Ab Initio Hartree Fock with Full Integral Evaluation

The 1960s were barely drawing to an end before I.H. Hillier and V.R. Saunders in Manchester [29] as well as A. Veillard in Strasbourg [30] published the first ab initio Hartree Fock calculations on transition metal complexes without integral approximations. It seemed as if the stage had been set for series of nearly quantitative studies of coordination compounds in the 1970s, without possible errors introduced by an approximate evaluation of **F** in (5). However, already a few years into the 1970s it became apparent that the ab initio Hartree Fock results were far from quantitative especially for complexes of 3*d*-elements. Thus, optimized metal–ligand distances were often much too long and calculated metal–ligand dissociation energies too small as exemplified by early studies on ferrocene [31] and $Cr(CO)_6$. Also orbital plots based on ab initio Hartree Fock calculations often made less chemical sense than those based on the "approximate" schemes. By the end of the 1970s, the sobering consensus had been reached that ab initio Hartree Fock only is the first step and that more demanding post-HF methods where electron correlation is considered had to be introduced in order to obtain quantitative results. The developments of such schemes will be discussed in Sect. 2.3.

2.2 Density Functional Theory and the Kohn–Sham Equation

In the yearly 1970s, a new electronic structure approach found its way from the physics to the chemistry community in the form of density functional theory (DFT), where the total energy of an electronic system is expressed as a functional of the total electronic density. The basic notion in DFT that the energy of an electronic system can be expressed in terms of its electronic density is almost as old as quantum mechanics and dates back to the early work by P.A.M. Dirac [32], E. Fermi [33] and L.H. Thomas [34].

J.C. Slater [35] embrace in part this idea in 1951 when he replaced the Hartree–Fock exchange energy $E_{\mathrm{X}}^{\mathrm{HF}}$appearing as the last term on the right hand side of (2) with the simple expression

$$E_{\mathrm{X}}^{\mathrm{HFS}} = -9/4\alpha_{\mathrm{ex}}[3/4\pi]^{1/3}\sum_{\gamma}\int[\rho_1^{\gamma}(\vec{r}_1)]^{4/3}d\vec{r}_1 \tag{13}$$

depending only on the density of electrons of either α or β spin. This approximation where α_{ex} is an adjustable parameter evolved out of the need to develop techniques that were able to handle solids within a reasonable time frame. The actual dependence of $E_{\mathrm{X}}^{\mathrm{HFS}}$ on $\rho_1^{\gamma}(\vec{r}_1)$ can be justified based on a simple model for exchange [36]. Slater [37] has given a vivid account of how his Hartree–Fock-Slater or Xα method evolved during the 1950s and 1960s with reference to numerous applications up to 1974.

The Thomas–Fermi method and the Xα scheme were at the time of their inceptions considered as useful models based on the notion that the energy of an electronic system can be expressed in terms of its density. A formal proof of this notion came in 1964 when it was shown by Hohenberg and Kohn [38] that there is a unique relation between density and energy. The year after Kohn and Sham put forward a practical variational DFT approach in which they replaced $E_{\mathrm{X}}^{\mathrm{HF}}$ of (2) with a combined exchange and correlation term

$$E_{\mathrm{XC}}^{\mathrm{KS}} = E_{\mathrm{X}}^{\mathrm{KS}} + E_{\mathrm{X}}^{\mathrm{KS}} = \sum_{\gamma}^{\alpha,\beta}\int\rho^{\gamma}(\vec{r}_1)\varepsilon_{\mathrm{XC}}[\rho^{\alpha}(\vec{r}_1),\rho^{\beta}(\vec{r}_1)]d\vec{r}_1, \tag{14}$$

where the energy density $\varepsilon_{\mathrm{XC}}$ is a functional of $\rho^{\alpha}(\vec{r}_1)$,$\rho^{\beta}(\vec{r}_1)$. As in the HF case, the N (Kohn–Sham) orbitals can be expanded into atomic orbitals according to (4). Furthermore, the expansion coefficients C_i can be determined by requiring that they optimize the total (Kohn–Sham) energy. This results in the (Kohn–Sham) matrix equation similar to (5)

$$\mathrm{F}^{\mathrm{KS}}\mathrm{C}_i = \varepsilon_i \mathrm{S}\,\mathrm{C}_i \tag{15}$$

where now

$$F_{rs}^{\mathrm{KS}} = \int \chi_r(\vec{r}_1)[\hat{h} + V_{\mathrm{C}}(\vec{r}_1) + V_{\mathrm{XC}}(\vec{r}_1)]\chi_s(\vec{r}_1)d\vec{r}_1. \tag{16}$$

Furthermore

$$\begin{aligned} V_{\mathrm{C}}(1) &= \int \frac{\rho(\vec{r}_2)}{|\vec{r}_1 - \vec{r}_2|} d\vec{r}_2 = \sum_i^N \int \frac{\psi_i(\vec{r}_2)\psi_i(\vec{r}_2)}{|\vec{r}_1 - \vec{r}_2|} d\vec{r}_2 \\ &= \sum_{t,u}^M P_{tu} \int \frac{\chi_t(\vec{r}_2)\chi_u(\vec{r}_2)}{|\vec{r}_1 - \vec{r}_2|} d\vec{r}_2, \end{aligned} \tag{17}$$

where the exchange correlation potential V_{XC} is given as the functional derivative of the exchange correlation energy with respect to the density or

$$V_{\mathrm{XC}} = \partial E_{\mathrm{XC}}/\partial \rho. \tag{18}$$

2.2.1 Practical Implementations of the Kohn–Sham Method

In the earliest implementation applied to molecular problems, K. Johnson [39] used scattered-plane waves as a basis and the exchange-correlation energy was represented by (13). This SW-Xα method employed in addition an (muffin-tin) approximation to the Coulomb potential of (17) in which V_{C} is replaced by a sum of spherical potentials around each atom. This approximation is well suited for solids for which the SW-Xα method originally was developed [40]. However, it is less appropriate in molecules where the potential around each atom might be far from spherical. The SW-Xα method is computationally expedient compared to standard ab initio techniques and has been used with considerable success [41] to elucidate the electronic structure in complexes and clusters of transition metals. However, the use of the muffin-tin approximation precludes accurate calculations of total energies. The method has for this reason not been successful in studies involving molecular structures and bond energies [42].

The first implementations of a self-consistent KS-scheme, without recourse to the muffin-tin approximations, are due to Ellis and Painter [43], Baerends et al. [44], Sambe and Felton [45], Dunlap et al. [46] as well as Gunnarson et al. [47]. The accurate representation of V_{C} is in general accomplished by fitting the molecular density to a set of one-center auxiliary functions [44, 46] $f_\eta(\vec{r}_1)$ as

$$\rho(\vec{r}_1) \approx \sum_\eta a_\eta f_\eta(\vec{r}_1) \tag{19}$$

from which the Coulumb potential can be calculated analytically [44, 46] in each point $\vec{r}_1$ as

$$V_{\mathrm{C}}(\vec{r}_1) = \sum_\eta \int \frac{a_\eta f_\eta(\vec{r}_2)}{|\vec{r}_1 - \vec{r}_2|} d\vec{r}_2. \tag{20}$$

The matrix elements F_{rs}^{KS} can subsequently be obtained from numerical integration as

$$F_{rs}^{\mathrm{KS}} = \sum_k [\chi_r(\vec{r}_k)\hat{h}\chi_s(\vec{r}_k) + \chi_r(\vec{r}_k)V_{\mathrm{C}}(\vec{r}_k)\chi_s(\vec{r}_k) + \chi_r(\vec{r}_k)V_{\mathrm{XC}}(\vec{r}_k)\chi_s(\vec{r}_k)]W(\vec{r}_k), \tag{21}$$

where $W(\vec{r}_k)$ is a weight factor [43, 48–52]. F_{rs}^{KS} can now be evaluated as $\chi_r(\vec{r}_k)$, $\chi_s(\vec{r}_k)$, $\hat{h}\chi_r(\vec{r}_k)$, $V_{\mathrm{C}}(\vec{r}_k)$, $V_{\mathrm{XC}}(\vec{r}_k)$and $W(\vec{r}_k)$ readily are calculated at each sample point $\vec{r}_k$. The extensive use of numerical integration [43, 48–52] is amiable to modern vector machines. Numerical integration also makes it easy to deal with complicated expressions for V_{XC}. The often intricate form of V_{XC} and $E_{\mathrm{XC}}^{\mathrm{KS}}$ precludes on the other hand a completely analytical evaluation of F_{rs}^{KS} and E^{KS}.

Some of the earliest DFT programs such as ADF [44] and DMOL [50] make use of Slater-type orbitals (STOs), which necessitated that all parts of F_{rs}^{KS} and E^{KS} are calculated by numerical integration. In that case, special care must be exercised in order to calculate total energies [53, 54], energy gradients [55] and energy Hessians [56–58] sufficiently accurate. Other early packages including LCGTO [45, 46], DeMon [59], DGauss [60] and ParaGauss [61]. Later adaptations have also been introduced into Gaussian, QChem, Jaguar, Spartan, Turbomol, Dalton, Gamess BDF [62], Molpro, Molcas ORCA, all make use of Gaussian-type orbitals (GTOs) where only the exchange-correlation part of F_{rs}^{KS} and E^{KS} is evaluated by numerical integration. However in several of these packages fitting of the density as in (19) is employed to speed up the calculation of Coulomb integrals by making use of the resolution of the identity [63, 64] or Cholesky decomposition techniques [65, 66]. A unique approach has been taken by A. Becke in which the Kohn–Sham orbitals and energy are optimized without the use of basis functions as in (4). The approach implemented in the Numol program [67] was first applied to diatomic molecules and later also to polyatomic systems.

2.2.2 The Development of New Density Functionals

The quality of the DFT calculations obviously depends on how well the approximate expression for $E_{\mathrm{XC}}^{\mathrm{KS}}$ represents the exact (but unknown) exchange correlation functional. Throughout the 1970s, the large majority of DFT calculations were based on the local density approximation (LDA) in which the exchange $E_{\mathrm{X}}^{\mathrm{LDA}}$ [68] and correlation $E_{\mathrm{C}}^{\mathrm{LDA}}$ [69] energies both are taken from the homogeneous electron gas and expressed as a simple function of the electron density with $E_{\mathrm{X}}^{\mathrm{LDA}}$ quite similar to $E_{\mathrm{X}}^{\mathrm{HFS}}$ of (13) where $\alpha_{\mathrm{ex}} = 2/3$. The LDA calculations afforded in general metal–ligand distances in much better agreement with experiment than HF as shown in Table 1. Furthermore, orbital plots based on LDA tented to make more chemical sense than those from HF calculations.

It might seem surprising that the "approximation" of $E_{\mathrm{X}}^{\mathrm{HF}}$ by $E_{\mathrm{X}}^{\mathrm{LDA}}$ should lead to substantially better structures. An extensive analysis [74, 75] has shown that the difference $E_{\mathrm{X}}^{\mathrm{LDA}} - E_{\mathrm{X}}^{\mathrm{HF}}$ which is added to $E_{\mathrm{X}}^{\mathrm{HF}}$ in order to obtain $E_{\mathrm{X}}^{\mathrm{LDA}}$ in fact to some degree mimic "static correlation" which is absent in the HF-scheme. Unfortunately, towards the end of the 1970s when the DFT-based methods finally were sufficiently numerically stable [53, 54] to calculate metal–ligand dissociation energies, it became evident that the LDA scheme systematically overestimates bond energies. Thus after one decade of excitement, it seemed as if practical DFT calculations would be limited in scope and unable to deal with the subject of reactivity and thermochemistry.

This prospect was changed when A. D. Becke through a series of seminal papers [76–78] introduced expressions for $E_{\mathrm{XC}}^{\mathrm{KS}}$ that depended not only on the density ρ but also on its gradient $\nabla\rho$. This modification has become known as the generalized gradient approximation (GGA) and it significantly improved the accuracy of the energetics as shown in Table 2. Well-known GGAs are BP86 and BLYP in which the exchange part is due to Becke [76] and the correlation based on the work of Perdew [80] and Lee [81] et al., respectively.

The work by Becke had a profound impact on the quantum chemistry community. Thus by 1992 most theoretical chemists that up to that time had been sceptical about DFT embraced the method and in a short period DFT was incorporated into

Table 1 A comparison of bond distances (Å) from HF and LDA calculations with experiment

	A–B	HF	LDA	Expt
$Fe(CO)_5$	Fe–C_{ax}	2.047[a]	1.774[b]	1.807
	Fe–C_{eq}	1.874[a]	1.798[b]	1.827
$Fe(C_5H_5)_2$	Fe–C	1.88[c]	1.60[d]	1.65
$HCo(CO)_4$	Co–C_{eq}	2.02[e]	1.753[f]	1.764
	Co–C_{ax}	1.96[e]	1.779[f]	1.818

[a] [68]
[b] [70]
[c] [69]
[d] [71]
[e] [72]
[f] [73]

Table 2 First metal-carbonyl dissociation energy (kJ/Mol) in a number of metal carbonyls[a]

Molecule	HFS	LDA	BP86	Exp
$Cr(CO)_6$	278	276	147	162
$Mo(CO)_6$	226	226	119	126
$W(CO)_6$	247	249	142	166
$Ni(CO)_4$	194	192	106	104

[a] [79]

Table 3 Calculated metal-ligand bond length[a]

Compound	Bond	B3LYP	Exp
TiF_4	Ti–F	1.74	1.75
$TiCl_4$	Ti–Cl	2.17	2.17
$Cr(CO)_6$	Cr–C	1.91	1.92
$Cr(C_6H_6)(CO)_3$	Cr–C (C_6H_6)	2.23	2.21
$Cr(C_6H_6)(CO)_3$	Cr–C (CO)	1.85	1.86
$Mn_2(CO)_{10}$	Mn–Mn	2.96	2.98
$Mn_2(CO)_{10}$	Mn–C_{ax}	1.80	1.80
$Mn_2(CO)_{10}$	Mn–C_{eq}	1.85	1.87
$Fe(CO)_5$	Fe–C_{ax}	1.81	1.81
$Fe(CO)_5$	Fe–C_{eq}	1.80	1.83
$Fe(C_5H_5)_2$	Fe–C	2.06	2.06
$Fe(C_2H_4)(CO)_4$	Fe–C(CO)	2.11	2.12
$Fe(C_2H_4)(CO)_4$	Fe–C_{ax}	1.81	1.82
$Fe(C_2H_4)(CO)_4$	Fe–C_{eq}	1.79	1.81
$CoH(CO)_4$	Co–C_{eq}	1.79	1.82
$Co_2(CO)_4$	Co–Co	2.61	2.53
$Ni(CO)_4$	Ni–C	1.81	1.84
CuF	Cu–F	1.66	1.75
Mean absolute error		0.02	

[a] From [88]. Distances in Å

all major program packages such as Gaussian, Gamess and Turbomol. The popularity of DFT has led to the development of many new functionals as reviewed elsewhere [82–87].

Perhaps the most popular has been the hybride functional B3LYP [78] by Becke in which 20% of E_X^{LYP} is replaced by E_X^{KS}. We present in Table 3 a number of metal–ligand distances optimized by B3LYP [88]. For most systems, the error is only 0.02 Å. In Table 4, we compare metal–ligand bond energies calculated by BLYP [76, 81] and B3LYP [76, 80]. Obviously, B3LYP represents a clear improvement over BLYP.

Progress in the development of functionals have up to now involved modeling of both E_X^{KS} and E_C^{KS}. However, some theoreticians including Becke are increasingly of the opinion that further progress in DFT will require the use of exact exchange E_X^{HF} for E_X^{KS}. What is left is to augment the approximate E_C^{KS} functionals which only consider dynamic correlation with static correlation. Becke has introduced such functionals DF07 [89] in which static correlation is modeled by modified

Table 4 Average M-L dissociation energies[a]

Complex	BLYP	B3LYP	DF07[b]	Exp
$Cr(CO)_5$	29.7	22.8	25.0	23.4
$Cr(CO)_6$	30.6	24.8	26.9	25.6
$Mn_2(CO)_{10}$	28.6	20.3	22.9	22.7
$MnH(CO)_5$	34.7	27.4	29.0	27.4
$Fe(CO)_4$	33.7	23.4	25.8	24.7
$Fe(CO)_5$	34.0	25.9	28.4	28.0
$Co_2(CO)_8$	40.4	26.4	31.2	30.6
$CoH(CO)_4$	45.6	36.9	38.1	36.9
$Ni(CO)_3$	36.5	35.0	39.1	38.8
$Ni(CO)_4$	41.7	32.5	34.5	35.3

[a] From [88] with energy in kcal/mol
[b] Functional due to Becke from [89]

expressions for $E_X^{LDA} - E_X^{HF}$. It can be seen in Table 3 that the results [88] are quite encouraging. For a larger sample of systems, the mean absolute error was 6.3 kcal/mol, 4.3 kcal/mol and 2.3 kcal/mol for BLYP, B3LYP and DF07 [89], respectively. It is in a way ironic that DFT from its promising Xα start with a local exchange approximation $E_X^{X\alpha}$ is back to Hartree–Fock and E_X^{HF} as a starting point.

2.3 Post-Hartree–Fock Methods

It is an attractive feature of ab initio wave function theory that there is a clear hierarchy of methods leading from Hartree–Fock to the exact solution of the Schrödinger equation. Post-Hartree–Fock methods can be divided into three main categories [88]. The first is based on (Møller–Plesset) perturbation theory [89] and referred to as *MPn* where n is the order of the perturbation. *MPn* is excellent when Hartree–Fock already is giving a reasonable description, as is often the case for complexes involving 4*d* and 5*d* elements. Otherwise, it fails or might only converge slowly with the order *n*. *MP2* can be used for medium size systems of 100–200 atoms.

The second category is based on configuration interaction (CI) in which the HF determinant Ψ_0 is augmented by a number of determinants Ψ_k constructed from Ψ_0 by replacing one or more of the occupied HF orbitals with virtual HF orbitals

$$\Psi_{CI} = \sum_{k=0}^{n} D_k \Psi_k. \tag{22}$$

In simple CI, the expansion coefficients D_k are optimized in such a way that Ψ_{CI} has the minimum energy. The expansion in (22) can be slowly converging requiring millions of terms. The number of needed terms can be reduced in the multi-configuration SCF procedure (MCSCF), where both D_k and the orbital expansion coefficients of (4) are optimized simultaneously with respect to the energy of Ψ_{CI} [88]. One of the better known MCSCF schemes is the complete active space self-consistent field method (CASSCF) [90]. In this scheme, one considers an active space of M_{occ} occupied HF orbitals and M_{vir} virtual HF orbitals. From this space, Ψ_{CI} is constructed by taking into account all possible displacement of orbitals from M_{occ} to M_{vir}. As the number of terms in (22) rapidly goes up with the size of the active space, a more limited number of terms can be selected in the restricted active space self-consistent field method (RASSCF). Both CASSCF and RASSCF can be augmented with second-order perturbation theory in CASPT2 and RASPT2 [91]. CASSCF, RASSCF as well as CASPT2, RASPT2 have been used extensively in transition metal chemistry. They are the methods of choice in those cases where a system is poorly described by a single Slater determinant. Other methods that can be used in a similar situation are the generalized valence bond method (GVB) [92], valence bond theory (VB) [93] and the symmetry adapted cluster/configuration interaction (SAC-CI) method [94]. All of these methods scale as $(n_e)^5$ or worse with the number of electrons n_e and can as a consequence only be used for smaller systems.

The third and last category is the couple cluster (CC) method [88]. In this scheme, one writes the wave function Ψ_{CC} as

$$\Psi_{\mathrm{CC}} = e^{T}\Psi_0, \tag{23}$$

with

$$e^{T} = 1 + T + \frac{1}{2}T^2 + \frac{1}{6}T^3 = \sum_{k=0}^{\infty}\frac{1}{k!}T^k \tag{24}$$

and the cluster operator T given by

$$T = T_1 + T_2 + T_3 + \ldots.T_N + \ldots. \tag{25}$$

Here, the T_i operator when working on Ψ_0 affords the ith excited Slater determinants. In practical, CC calculations T of (25) is truncated. Thus keeping $T_1 + T_2$ gives rise to CCSD whereas the addition of T_3 and subsequently T_4 leads to CCSDT and CCSDTQ, respectively. The CCSD scheme which scales as $(n_e)^6$ is used routinely for up to 100 electrons. It is considered as the most accurate method for metal complexes in those cases where the reference HF determinant Ψ_0 affords a reasonable description. CCSDT and CCSDTQ scales as $(n_e)^8$ and $(n_e)^{10}$, respectively, they can only be used for very small systems.

2.4 Applications to the Ground State of Permanganate and Related Tetroxo Systems

The methods described above have been applied to ground state properties of a large number of complexes. These properties include parameters from infrared

(IR), Raman nuclear magnetic resonance (NMR), electron spin resonance (ESR), Mösbauer and vibronic circular (VCD) spectroscopy as well as electric and magnetic dipole moments, polarizability and magnetic susceptibility [83]. We shall in the following as an example discuss some applications to permanganate and related tetroxo complexes.

2.4.1 Electronic Structure of Permanganate

The permanganate anion MnO_4^- has a tetrahedral geometry with a T_d point group symmetry, Fig. 1. At each oxygen atom, we have a core like $2s$ orbital as well as two $2p_\pi$ and one $2p_\sigma$valance orbitals. The total number of valence electrons is 32 of which 8 are in core type 2s levels and the remaining 24 in molecular orbitals spanned by $2p_\pi$, $2p_\sigma$ and $3d$. We show in Fig. 2 the levels represented by orbitals made up of $2p_\pi$, $2p_\sigma$ and $3d$.

The lowest level is represented by $1t_2$ which is a bonding combination between a d orbital transforming as t_2 and a t_2 ligand combination. The corresponding antibonding combination is given by the empty $3t_2$ orbital, Fig. 3. Slightly above is the $1e$ level corresponding to the bonding combination between a d orbital transforming as e and a ligand combination of e-symmetry. The related antibonding combination is $2e$, Fig. 3. Further above is $1a$ made up of $2p_\sigma$ ligand combinations interacting in-phase with $4s$ on the metal. At highest energy among the occupied orbitals are the $2t_2$ and $1t_1$ combinations that both are ligand based with no contributions from the metal, Table 3. The empty $3t_2$ and $2e$ levels correspond to the d many- fold split by the ligand orbitals with $2e$ below $3t_2$ as predicted by ligand field theory [5]. The compositions and relative energies of the frontier orbitals for MnO_4^- is what one would obtain from an LDA or GGA calculation [36] on MnO_4^-. It is interesting to note that Wolfberg and Helmholz [13] in the very first LCAO calculation on MnO_4^- found $2e$ above $3t_2$ in

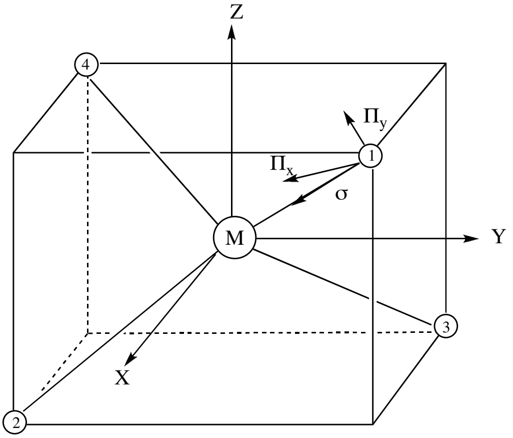

Fig. 1 Geometry of MnO_4^-

Fig. 2 Orbital level diagram for MnO_4^-

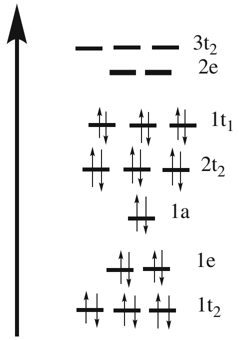

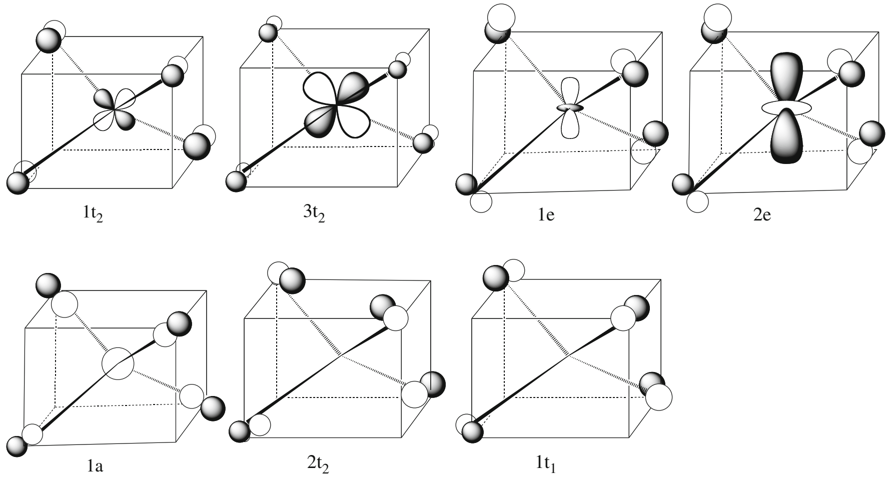

Fig. 3 Frontier molecular orbitals of MnO_4^-

disagreement with ligand field theory. Later calculations both based on wave function theory and DFT have always recovered the ligand field ordering.

There has been a number of HF ab initio calculations on MnO_4^- [95–102]. All of these calculations exhibit a very different picture from that of Fig. 3 with $1t_2$ being a pure *d*-orbital and $1e$ exclusively a ligand orbital. Thus, HF reveals an ionic bonding mode as opposed to the covalent DFT picture displayed in Fig. 3. Buijse and Baerends have analyzed the bonding in MnO_4^- based on HF, post-HF and DFT calculations [103]. They point out the special circumstances encountered in complexes of 3*d* elements where one has 3*s* and 3*p* core-type orbitals of the same radial extent as 3*d*. The 3*s*,3*p* orbitals will interact repulsively with the ligands making it impossible to reach metal–ligand distances where the 3*d* to ligand overlaps are optimal. The HF method responds to the relatively weak metal–ligand interactions by localizing the electrons on either the metal or the ligands in each orbital and thus optimize the exchange interaction. The covalent bond picture provided by DFT is recovered nicely in extensive CI and MCSCF calculations.

At the HF-level, MnO_4^- is unstable with respect to dissociation into one electron and the neutral species. Introducing post-HF calculations makes MnO_4^- stable with respect to such a dissociation. The problems encountered for HF in 3*d* metal complexes are not present in systems involving nd ($n = 4{,}5$) elements since the corresponding *ns*, *np* orbitals are much more contracted than nd for $n = 4{,}5$. Also, the HF error seems to be more severe for late 3*d* elements than early 3*d* elements.

2.4.2 ^{17}O Chemical Shifts in Permanganate and Related Tetroxo Systems

There are a number of spectroscopic parameters that can be formulated as the second derivative of the total energy with respect to two perturbations [88]. One such parameter is the nuclear shielding tensor [104]

$$\sigma_{st}^{\mathrm{N}} = \left(\frac{\delta^2 E}{\delta B_s \delta \mu_t^{\mathrm{N}}} \right)_{(\vec{B}=0,\vec{\mu}^{\mathrm{N}}=0)}, \tag{26}$$

where B_r, μ_t^{N} are Cartesian components of, respectively, an external homogeneous magnetic field $\vec{B}$ and a nuclear magnetic moment $\vec{\mu}^{\mathrm{N}}$of nucleus N. Related to the shielding tensor of nuclei N is the shielding constant

$$\sigma^{\mathrm{N}} = \frac{1}{3}[\sigma_{xx}^{\mathrm{N}} + \sigma_{YY}^{\mathrm{N}} + \sigma_{ZZ}^{\mathrm{N}}] \tag{27}$$

as well as the chemical shift given by

$$\delta^{\mathrm{N}} = \sigma^{\mathrm{N}} - \sigma^{\mathrm{ref}}. \tag{28}$$

Here, σ^{ref} is the shielding constant of the reference with respect to which the chemical shift δ^{N} of nuclei N is measured. Finally, the shielding tensor component σ_{st}^{N} has a diamagnetic contribution $\sigma_{st}^{d,\mathrm{N}}$ and a paramagnetic contribution $\sigma_{st}^{p,\mathrm{N}}$. Here $\sigma_{st}^{d,\mathrm{N}}$ only depends on the occupied ground state orbitals whereas $\sigma_{st}^{p,\mathrm{N}}$ depends on the coupling between ground state occupied and virtual orbitals induced by the external homogeneous magnetic field $\vec{B}$ [104]. We present in Table 5 the ^{17}O chemical shift of several tetroxo complexes including permanganate.

It is clear from Table 5 that the chemical shifts calculated with HF are too negative with the possible exception of the two 5*d* complexes WO_4^{2-} and ReO_4^-. The agreement with experiment is especially poor for MnO_4^-. An analysis reveals that the deviation for permanganate comes from the paramagnetic contribution $\sigma_{st}^{p,\mathrm{N}}$, where the coupling between occupied and virtual orbitals are exaggerated due to their localized nature. Thus, occupied and virtual orbitals both localized on either the metal or the ligands will lead to a strong coupling. Introducing next the MP2 method is seen to lead to an overcompensation, where most shifts goes from negative in HF to positive in MP2. On the other hand, the GGA scheme BP86

Table 5 ^{17}O Chemical shifts [ppm] for tetroxo complexes calculated by different methods and compared to experiment

Compound	HF[a]	MP2[a]	BP86[b]	B3LYP[a]	Exp[a]
WO_4^{2-}	−194	−21	−140	−183	−129
MoO_4^{2-}	−335	−60	−251	−289	−239
CrO_4^{2-}	−1,308	2,173	−508	−640	−544
ReO_4^-	−464	3	−282	−339	−278
TcO_4^-	−819	184	−421	−518	−458
MnO_4^-	−7,248	54,485	−832	−1,149	−939
OsO_4	−1,295	1,069	−517	−657	−505
RuO_4	−3,330	8,262	−740	−1,037	−820

[a] [105]

[b] [106]

with delocalized orbitals, Fig. 3, and a covalent bonding description leads to shifts in reasonable agreement with experiment for all systems, even permanganate. Adding 20% HF exchange in the hybrid B3LYP leads as expected to more negative shifts but not to an overall improved agreement with experiment.

2.4.3 M-O Spin–Spin Coupling Constants in Permanganate and Related Tetroxo Systems

Another spectroscopic parameter that we can write as a second-order energy derivative is the spin–spin coupling tensor of NMR defined as [107–109]

$$K_{st}^{\mathrm{AB}} = \left(\frac{\delta^2 E}{\delta \mu_s^{\mathrm{A}} \delta \mu_t^{\mathrm{B}}} \right)_{(\vec{\mu}^{\mathrm{A}}=0, \vec{\mu}^{\mathrm{B}}=0)}, \tag{29}$$

where $\mu_s^{\mathrm{A}}, \mu_t^{\mathrm{B}}$ are Cartesian components of the nuclear magnetic moments $\vec{\mu}^{\mathrm{A}}$ and μ_t^{B} on nuclei A and B, respectively. Related to the coupling tensor K_{st} is the reduced coupling constant

$$K_{\mathrm{AB}} = \frac{1}{3}[K_{xx}^{\mathrm{AB}} + K_{yy}^{\mathrm{AB}} + K_{zz}^{\mathrm{AB}}]. \tag{30}$$

There are four contributions to K_{AB}

$$K_{\mathrm{AB}} = K_{\mathrm{AB}}^{\mathrm{FC}} + K_{\mathrm{AB}}^{\mathrm{PSO}} + K_{\mathrm{AB}}^{\mathrm{DSO}} + K_{\mathrm{AB}}^{\mathrm{SD}}, \tag{31}$$

represented by the Fermi-contact term $(K_{\mathrm{AB}}^{\mathrm{FC}})$, the paramagnetic spin-orbit term $(K_{\mathrm{AB}}^{\mathrm{PSO}})$, the diamagnetic spin-orbit term $(K_{\mathrm{AB}}^{\mathrm{DSO}})$ and the spin-dipolar term $(K_{\mathrm{AB}}^{\mathrm{SD}})$. Of these the first two are in most cases dominating.

We compare in Table 6 calculated [107] reduced coupling constants K_{MO} based on BP86 with experiment. The agreement is in general good with the possible exception of MnO_4^-. The largest contribution comes from the Fermi-contact term

Table 6 Reduced coupling constants ${}^{a,b}K_{MO}$ in some tetroxo complexes

Molecule	$R_{M–O}$	${}^{c}K^{FC}_{MO}$	${}^{d}K^{PSO}_{MO}$	${}^{e}K_{MO}$ calculated	K_{MO} Exp
VO_4^{3-}	1.711	243	−94	150	144
CrO_4^{2-}	1.653	244	−140	104	108
MnO_4^{-}	1.629	218	−189	29	75
MoO_4^{2-}	1.765	464	−118	346	380
TcO_4^{-}	1.676	531	−128	403	359

[a] In SI units of 10^{19} kg m^{-2} s^{-2} A^{-2}
[b] From [107]
[c] Fermi-contact contribution
[d] Paramagnetic spin-orbit contribution
[e] Total reduced coupling constant

K^{FC}_{MO}, Table 6. This term arises from a generation of net spin-density at the position of the metal nuclei due to the nuclear magnetic moments on the oxygen $\vec{\mu}^{O}$. The generation of net spin density requires the coupling of occupied and virtual ground state orbitals of a_1 symmetry with contributions from both 2*s* orbitals on oxygen and 3*s*,4*s* orbitals on the metal. K^{FC}_{MO} is as explained elsewhere [107] positive for all the systems and larger for complexes of 4*d*-elements than 3*d*-elements. The second important contribution is K^{PSO}_{MO}. It arises when the magnetic field due to the magnetic dipole of the metal couples occupied and virtual orbitals to generate a current density that interacts with the nuclear magnetic moment of the oxygens. The negative K^{PSO}_{MO} is established by the coupling between $1t_2$ and $3t_2$. It is proportional to the coupling integral between the two orbitals as well as $1/(\varepsilon_{3t_2} - \varepsilon_{1t_2})$. As MnO_4^{-} has the smallest $\varepsilon_{3t_2} - \varepsilon_{1t_2}$energy gap, it has the most negative contribution from K^{PSO}_{MnO} and the smallest K_{MnO}. In fact, it is likely that K^{PSO}_{MnO} is too negative for MnO_4^{-}, leading to a too small estimate of K_{MnO}.

3 Excited State Electronic Structure Theory

The development of electronic structure theories for metal complexes has always been closely linked with electron spectroscopy of transition metal compounds. We shall in the following describe both DFT and wave function methods that have been used in the study of excited states. We shall also discuss their application to the tetroxo systems.

3.1 Different DFT-Based Methods Used in the Study of Excited States

As we have seen in Sect. 2, KS-DFT has been very successful in dealing with ground state properties, especially for closed shell molecules. KS-DFT owes this success to its simplicity as well as the development of increasingly accurate energy density functionals $\varepsilon[\rho]$ or exchange correlation potentials $V_{\mathrm{XC}}[\rho]$ [82–87]. There has been considerable interest in also applying KS-DFT to excited states.

3.1.1 Variational DFT Approaches in the Study of Excited States

The first category of DFT-based methods applied to excited states is the variational approaches. They include ensemble DFT [110, 111], variation of bifunctionals [112] and ΔDFT/ΔSCF-DFT [36, 113–116]. Of the variational methods, ΔDFT/ΔSCF-DFT can be readily implemented and applied whereas only few applications have appeared based on the two first approaches due to their computational complexity. In ΔDFT/ΔSCF-DFT [36, 113–116], one generates new "excited state" KS-Slater determinants from the ground state determinant by substituting one (or more) of the occupied ground state KS-orbitals with one or more ground state virtual KS-orbitals. An evaluation of the energy of the new determinants followed by subtraction of the ground state energy makes it possible to determine excitation energies corresponding to one-, two- and multi-electron excitations. In addition, the ΔSCF-DFT scheme (but not ΔDFT) allows for the occupied orbitals in the excited state to be optimized variationally.

The ΔDFT/ΔSCF-DFT scheme has been met with considerable reservation. Thus, ΔDFT/ΔSCF-DFT assumes implicitly that a transition can be represented by an excitation involving only two orbitals, an assumption that seems not generally to be satisfied. Also, the variational optimization in ΔSCF-DFT of the orbitals makes it difficult to ensure orthogonality between different excited state determinants when many transitions are considered, resulting ultimately in a variational collapse. Finally, it has been questioned [110] whether there exists a variational principle for excited states in DFT. In spite of this, some of the first pioneering chemical applications of DFT involved ΔSCF-DFT calculations on excitation energies [36, 113–116] for transition metal complexes and ΔSCF-DFT is still widely used [117–121].

3.1.2 DFT Approaches in the Study of Excited States Based on Response Theory

A popular alternative to variational approaches in the study of excited state properties is time-dependent DFT (TD-DFT) in its adiabatic formulation [122–128]. In this scheme, one considers the first-order change in the ground state density $\rho^{(\gamma)}(\omega, \vec{r})$ due to a perturbation from the γ-component $E_{\gamma}(\omega)$ of a frequency-dependent electric field and the associated frequency-dependent polarizability $\alpha^{\gamma\beta}(\omega)$. The excitation energies ω_0 are subsequently found as poles or resonances for $\alpha^{\gamma\beta}(\omega)$.

The adiabatic TD-DFT approach [122–124] seems to be free of much of the problems associated with ΔSCF-DFT. In the first place, TD-DFT transition energies

ω_0 are calculated from a ground state property $\alpha^{\gamma\beta}(\omega)$ by a frequency-dependent response method rather than excited state variation theory. Furthermore, orthogonality is ensured as all excitation energies are found as eigenvalues to a common matrix constructed from the ground state Hessian [88, 122–124, 129–131].

Extensive benchmarking of adiabatic TD-DFT [132–137] has revealed that the calculated excitation energies are in fair agreement with experiment. It is thus to be expected that adiabatic TD-DFT be used increasingly as a reasonable compromise between accuracy and computational cost in many applications [132–137]. However, the extensive benchmarking has revealed some systematic errors [132–137] in the calculated excitation energies when use is made of the GGA as well as the popular approximate hybrid functionals containing fractions of exact Hartree–Fock exchange. The largest deviations [132–137] are found for transitions where electrons are moved between two separated regions of space (charge transfer transitions) or between orbitals of different spatial extend (Rydberg transitions) [138–140].

Ziegler et al. have in two recent studies [141, 142] analyzed the reason for the deviations between experimental charge transfer (CT) excitation energies and estimates obtained from TD-DFT applications. It was found that the deviations for a large part can be traced back to the simple approach taken in standard TD-DFT where terms depending on the linear orbital response parameter set U only is kept to second order in U for the energy expression [141, 142]. While this simple linear response approach is adequate for the corresponding Hartree–Fock time-dependent formulation where self-interaction is absent [143], it is inadequate for TD-DFT applied to most approximate functionals where self-interaction terms are present [141–143]. In those cases, higher order terms in U must be included into the energy expression [141–143].

With the intention of including higher order terms, we have developed a constricted variational density functional approach (CV(n)-DFT) for the calculation of excitation energies and excited state properties [144, 145]. We shall introduce this method in the next section and show that adiabatic TD-DFT and ΔSCF-DFT both are special cases of the more general constricted variational DFT scheme.

3.1.3 Constricted Variational Density Functional Theory

In the constricted variational density functional theory, CV(n)-DFT, we carry out a unitary transformation [145] among occupied $\{\phi_i; i = 1, \mathrm{occ}\}$ and virtual $\{\phi_a; a = 1, \mathrm{vir}\}$ ground state orbitals

$$Y\begin{pmatrix}\phi_{\mathrm{occ}}\\ \phi_{\mathrm{vir}}\end{pmatrix} = e^{U}\begin{pmatrix}\phi_{\mathrm{occ}}\\ \phi_{\mathrm{vir}}\end{pmatrix} = \left(\sum_{n=0}^{\infty}\frac{\left(U^2\right)^n}{2n!}\right)\begin{pmatrix}\phi_{\mathrm{occ}}\\ \phi_{\mathrm{vir}}\end{pmatrix} = \begin{pmatrix}\phi'_{\mathrm{occ}}\\ \phi'_{\mathrm{vir}}\end{pmatrix}. \tag{32}$$

Here, ϕ_{occ} and ϕ_{vir} are concatenated column vectors containing the sets $\{\phi_i; i = 1, \mathrm{occ}\}$and $\{\phi_a; a = 1, \mathrm{vir}\}$ whereas ϕ'_{occ} and $\phi'_{\mathrm{vir}}$are concatenated column vectors containing the resulting sets $\{\phi'_i; i = 1, \mathrm{occ}\}$ and $\{\phi'_a; a = 1, \mathrm{vir}\}$ of occupied and virtual excited state orbitals, respectively. The unitary transformation matrix Y is in (33) expressed in terms of a skew symmetric matrix U as

$$Y = e^{U} = I + U + \frac{U^2}{2} + \cdots = \sum_{n=0}^{\infty} \frac{U^n}{n!} = \sum_{n=0}^{\infty} \frac{\left(U^2\right)^n}{2n!} + U \sum_{n=0}^{\infty} \frac{\left(U^2\right)^n}{(2n+1)!}. \tag{33}$$

Here, $U_{ij} = U_{ab} = 0$ where "*i,j*" refer to the occupied set $\{\phi_i; i = 1, \mathrm{occ}\}$ whereas "*a,b*" refer to $\{\phi_a; a = 1, \mathrm{vir}\}$. Furthermore, U_{ai} are the variational mixing matrix elements that combines virtual and occupied ground state orbitals in the excited state with $U_{ai} = -U_{ia}$. Thus, the entire matrix U is made up of occ × vir independent elements U_{ai} that also can be organized in the column vector $\vec{U}$. For a given $\vec{U}$, we can by the help of (33) generate a set of "occupied" excited state orbitals

$$\phi_i{}' = \sum_{p}^{\mathrm{occ+vir}} Y_{pi}\phi_p = \sum_{j}^{\mathrm{occ}} Y_{ji}\phi_j + \sum_{a}^{\mathrm{vir}} Y_{ai}\phi_a \tag{34}$$

that are orthonormal to any order in U_{ai}.

In the simple CV(2)-DFT theory [144], the unitary transformation of (33) is carried out to second order in U. We thus obtain the occupied excited state orbitals to second order as

$$\phi_i{}' = \phi_i + \sum_{a}^{\mathrm{vir}} U_{ai}\phi_a - \frac{1}{2}\sum_{j}^{\mathrm{occ}}\sum_{a}^{\mathrm{vir}} U_{ai}U_{aj}\phi_j, \tag{35}$$

from which we can generate the excited state Kohn–Sham density matrix to second order as

$$\begin{aligned}
\rho^{'}(1,1') &= \rho^{(0)}(1,1') + \Delta\rho^{'}(1,1') \\
&= \rho^{(0)}(1,1') + \sum_{i}^{\mathrm{occ}}\sum_{a}^{\mathrm{vir}} U_{ai}\phi_a(1')\phi_i^*(1) + \sum_{i}^{\mathrm{occ}}\sum_{a}^{\mathrm{vir}} U_{ai}^*\phi_a^*(1)\phi_i(1') \\
&+ \sum_{i}^{\mathrm{occ}}\sum_{a}^{\mathrm{vir}}\sum_{b}^{\mathrm{vir}} U_{ai}^*U_{bi}\phi_a(1')\phi_b^*(1) - \sum_{i}^{\mathrm{occ}}\sum_{j}^{\mathrm{occ}}\sum_{a}^{\mathrm{vir}} U_{ai}U_{aj}^*\phi_i(1')\phi_j^*(1).
\end{aligned} \tag{36}$$

The expression for $\rho'(1,1')$ makes it next possible to write down the corresponding excited state Kohn–Sham energy to second order as

$$\begin{aligned}
E_{KS}\left[\rho'(1,1')\right] = E_{\mathrm{KS}}\left[\rho^0\right] &+ \sum_{ai} U_{ai}U_{ai}^*(\varepsilon_a^0 - \varepsilon_i^0) + \sum_{ai}\sum_{bj} U_{ai}U_{bj}^*K_{ai,bj} + \frac{1}{2} \\
&\times \sum_{ai}\sum_{bj} U_{ai}U_{bj}K_{ai,jb} + \frac{1}{2}\sum_{ai}\sum_{bj} U_{ai}^*U_{bj}^*K_{ai,jb} + O[U^{(3)}].
\end{aligned} \tag{37}$$

Here, $E_{\mathrm{KS}}[\rho^0]$ is the ground state energy and "*a,b*" run over virtual ground state canonical orbitals, whereas "*i,j*" run over occupied ground state canonical orbitals. Furthermore

$$K_{ru,tq} = K^{\mathrm{C}}_{ru,tq} + K^{\mathrm{XC}}_{ru,tq} \tag{38}$$

where

$$K^{\mathrm{C}}_{ru,tq} = \int\int \phi^*_r(1)\phi_u(1)\frac{1}{r_{12}}\phi^*_t(2)\phi_q(2)dv_1dv_2 \tag{39}$$

whereas

$$K^{\mathrm{XC(HF)}}_{ru,tq} = -\int\int \phi^*_r(1)\phi_q(1)\frac{1}{r_{12}}\phi^*_t(2)\phi_u(2)dv_1dv_2 \tag{40}$$

for Hartree–Fock exchange correlation and

$$K^{\mathrm{XC(DFT)}}_{ru,tq} = \delta(m_{sr}, m_{su})\delta(m_{st}, m_{sq})\int \phi^*_r(\vec{r}_1)\phi_u(\vec{r}_1)[f^{(m_{sr},m_{st})}(\rho^0)]\phi^*_t(\vec{r}_1)\phi_q(\vec{r}_1)d\vec{r}_1 \tag{41}$$

for DFT exchange correlation. In (41), $m_{sr} = 1/2$ for a spin orbital $\phi_r(1)$ of α-spin whereas $m_{sr} = -1/2$ for a spin orbital $\phi_r(1)$ of β-spin. In addition, the kernel $f^{(\tau,\upsilon)}(\rho^0)$ is the second functional derivative ofE_{XC} with respect to ρ_α and ρ_β

$$f^{\tau,\upsilon}(\rho^0_\alpha, \rho^0_\beta) = \left(\frac{\delta^2 E_{\mathrm{XC}}}{\delta\rho_\tau\delta\rho_\upsilon}\right)_0 \tau{=}\alpha,\beta\ ;\ \upsilon = \alpha, \beta. \tag{42}$$

Finally $\varepsilon^0_i, \varepsilon^0_a$ in (37) are the ground state orbital energies of, respectively, $\phi_i(1)$ and $\phi_a(1)$.

In CV(2)-DFT [144], we seek points on the energy surface $E_{\mathrm{KS}}[\rho']$ such that $\Delta E_{\mathrm{KS}}[\Delta\rho']{=}E_{\mathrm{KS}}[\rho'] - E_{\mathrm{KS}}[\rho^0]$ represents a transition energy. Obviously, a direct optimization of $\Delta E_{\mathrm{KS}}[\Delta\rho']$ without constraints will result in $\Delta E_{\mathrm{KS}}[\Delta\rho'] = 0$ and $U = 0$. We [144] now introduce the constraint that the electron excitation must represent a change in density $\Delta\rho'$ where one electron in (36) is transferred from the occupied space represented by $\Delta\rho_{\mathrm{occ}} = -\sum_{ija} U_{ai}U^*_{aj}\varphi_i(1')\varphi^*_j(1)$ to the virtual space represented by $\Delta\rho_{\mathrm{vir}} = \sum_{iab} U_{ai}U^*_{bi}\varphi_a(1')\varphi^*_b(1)$. An integration of $\Delta\rho_{\mathrm{occ}}$ and $\Delta\rho_{\mathrm{vir}}$ over all space affords $-\Delta q_{\mathrm{occ}} = \Delta q_{\mathrm{vir}} = \sum_{ai} U_{ai}U^*_{ai}$. We shall thus introduce the constraint $\sum_{ai} U_{ai}U^*_{ai} = 1$. Constructing next the Lagrangian $L = E_{\mathrm{KS}}[\rho'] + \lambda(1 - \sum_{ai} U_{ai}U^*_{ai})$ with λ being a Lagrange multiplier and demanding that L be stationary to any real variation in U results in the eigenvalue equation

$$\left(A^{\mathrm{KS}}+B^{\mathrm{KS}}\right)\vec{U}^{(I)}=\lambda_{(I)}\vec{U}^{(I)}, \tag{43}$$

where

$$A^{\mathrm{KS}}_{ai,bj}=\delta_{ab}\delta_{ij}(\varepsilon_a^0-\varepsilon_i^0)+K^{\mathrm{KS}}_{ai,bj};\ B^{\mathrm{KS}}_{ai,bj}=K^{\mathrm{KS}}_{ai,jb}. \tag{44}$$

We can now from (43) determine the sets of mixing coefficients $\{\vec{U}^{(I)};I=1,\mathrm{occ}\times\mathrm{vir}\}$ that make L stationary and represent excited states. The corresponding excitation energies are given by $\lambda_{(I)}$ as it can be seen by multiplying by $\vec{U}^{(I)+}$ from the left in (43) and making use of the constraint and normalization condition $\vec{U}^{(I)+}\vec{U}^{(I)}=1$.

Within the Tamm–Dancoff approximation [146] $(B^{\mathrm{KS}}=0)$ (43) reduces to

$$A^{\mathrm{KS}}\vec{U}^{(I)}=\lambda_{(I)}\vec{U}^{(I)} \tag{45}$$

which is identical in form to the equation one obtains from TDDFT in its adiabatic formulation [132–137] after applying the same Tamm–Dancoff [146] approximation.

Having determined $\vec{U}^{(I)}$ from either (43) or (45) allows us [145] now to carry out the unitary transformation of (32) to all orders. The resulting occupied excited state orbitals are given by [145]

$$\varphi'_j=\cos[\eta\gamma_j]\varphi_j^o+\sin[\eta\gamma_j]\varphi_j^v;j=1,\mathrm{occ}, \tag{46}$$

here φ_j^o and φ_j^v are according to the corresponding orbital theory of Hall and Amos[27] eigenvectors to, respectively, D_{occ} and D_{vir} with the same eigenvalues γ_i where $(D^2_{\mathrm{occ}})_{ij}=\sum_a^{\mathrm{vir}}U_{ai}U_{aj}$ and $(D^2_{\mathrm{vir}})_{ab}=\sum_i^{\mathrm{occ}}U_{ai}U_{bi}$. Here, φ_j^o is a linear combination of occupied ground state orbitals whereas φ_j^v is a linear combinations of virtual ground state orbitals. Thus in the corresponding orbital representation [145] only one occupied orbital φ_j^o mixes with one corresponding virtual orbital φ_j^v for each occupied excited state orbital φ'_j when the unitary transformation is carried out to all orders according to (32). Martin [145] has used the representation of corresponding orbitals to analyze excitations described by TDDFT and TDHF. In his interesting analysis, $\{\varphi_j^o(1),\varphi_j^v(1)\}$ are referred to as natural transition orbitals (NTO).

The change in the density matrix $\Delta\rho^{(\infty)}$ due to a one-electron excitation takes on the compact form of

$$\begin{aligned}\Delta\rho^{(\infty)}(1,1')=&\sum_j^{occ}\sin^2[\eta\gamma_j][\varphi_j^v(1')\varphi_j^v(1)-\varphi_j^o(1')\varphi_j^o(1)]\\&+\sum_j^{\mathrm{occ}}\sin[\eta\gamma_j]\cos[\eta\gamma_j][\varphi_j^v(1)\varphi_j^o(1\prime)+\varphi_j^v(1')\varphi_j^o(1')]\end{aligned} \tag{47}$$

when the unitary transformation in (32) is carried out to all orders. In (46) and (47), the scaling factor η is introduced to ensure that $\Delta\rho^{(\infty)}(1,1')$ represent the transfer of a single electron from the occupied orbital space density $-\sin^2[\eta\gamma_j]\varphi_j^o(1\prime)\varphi_j^o(1)$ to the virtual orbital space density $\sum_j^{\text{occ}}\sin^2[\eta\gamma_j]\varphi_j^v(1\prime)\varphi_j^v(1)$ or

$$\sum_j^{\text{occ}}\sin^2[\eta\gamma_j]=1. \tag{48}$$

Here, the constraint of (48) is a generalization of the corresponding second order constraint $\sum_{ai}U_{ai}U_{ai}^*=1$ used to derive (43) and (45).

We finally get for the excitation energy including terms to all orders in U

$$\begin{aligned}\Delta E^{(\infty)} &= E_{\text{KS}}^{\infty}[\rho^0+\Delta\rho^{(\infty)}]-E_{\text{KS}}[\rho^0]\\ &= -\sum_j^{occ}\sin^2[\eta\gamma_j]F_{j^oj^o}^{KS}[\rho^0+\frac{1}{2}\Delta\rho^{(\infty)}]+\sum_j^{\text{occ}}\sin^2[\eta\gamma_j]F_{j^vj^v}^{KS}[\rho^0+\frac{1}{2}\Delta\rho^{(\infty)}]\\ &\quad+\sum_j^{occ}\cos[\eta\gamma_j]\sin[\eta\gamma_j]F_{j^oj^v}[\rho^0+\frac{1}{2}\Delta\rho^{(\infty)}]\\ &\quad+\sum_j^{\text{occ}}\cos[\eta\gamma_j]\sin[\eta\gamma_j]F_{j^vj^0}[\rho^0+\frac{1}{2}\Delta\rho^{(\infty)}]+O^{[3]}(\Delta\rho^{(\infty)}).\end{aligned} \tag{49}$$

Here, (49) is derived by Taylor expanding [54] $E_{\text{KS}}^{\infty}[\rho^0+\Delta\rho^{(\infty)}]$ and $E_{\text{KS}}[\rho^0]$ from the common intermediate density$\rho^0+1/2\Delta\rho^{(\infty)}$. Further, $F^{\text{KS}}[\rho^0+1/2\Delta\rho^{(\infty)}]$ is the Kohn–Sham Fock operator defined with respect to the intermediate Kohn–Sham density matrix $\rho^0+1/2\Delta\rho^{(\infty)}$, whereas $F_{pq}^{\text{KS}}[\rho^0+1/2\Delta\rho^{(\infty)}]$ is a matrix element of this operator involving the two orbitals ϕ_p,ϕ_q. The expression in (49) is exact to third order in $\Delta\rho^{(\infty)}$, which is usually enough [54]. However, its accuracy can be extended to any desired order in $\Delta\rho^{(\infty)}$ [54].

The energy expression in (49) is perturbative in the sense that we make use of a U matrix optimized with respect to the second-order energy expression of (37). We refer to this method as $\text{CV}(\infty)-\text{DFT}$ [145]. We shall now seek ways in which to find vectors $\vec{U}_{(\infty)}^{(I)}$ that optimize $E_{\text{KS}}^{\infty}[\rho^0+\Delta\rho^{(\infty)}(U)]$. To this end, we can start with $\vec{U}_{(2)}^{(I)}=\vec{U}^{(I)}$ found from (45). Let us call this solution set U^0. We can now carry out a Taylor expansion

$$\begin{aligned}E^{(\infty)}(\rho^0+U) &= E^{(\infty)}(\rho^0+U^0)+\sum_{ai}\left(\frac{dE^{(\infty)}}{dU_{ai}}\right)_0\Delta U_{ai}\\ &\quad+\frac{1}{2}\sum_{ai}\sum_{bj}\left(\frac{d^2E^{(\infty)}}{d^2U_{ai}U_{bj}}\right)_0\Delta U_{ai}\Delta U_{bj}\\ &= E^{(\infty)}(\rho^0+U^0)+\sum_{ai}g(U^0)_{ai}\Delta U_{ai}+\frac{1}{2}\sum_{ai}\sum_{bj}H(U^0)_{ai,bj}\Delta U_{ai}\Delta U_{bj}\quad+O^{(3)}[\Delta U].\end{aligned} \tag{50}$$

Here, the gradient, $\vec{g}$, evaluated at U^0 has matrix elements given by

$$\begin{aligned} g(U^o)_{ai} &= \left(\frac{dE^{(\infty)}}{dU_{ai}}\right)_0 = \sum_{\sigma}^{\alpha,\beta}\left(\frac{\partial E}{\partial \rho_\sigma}\right)_0\left(\frac{\partial \rho_\sigma}{dU_{ai}}\right)_0 \\ &= \sum_{\sigma}^{\alpha,\beta}\int \hat{F}_{\sigma}^{KS}[(U^0)]\left(\frac{\partial \rho_\sigma}{dU_{ai}}\right)_0 dv_1. \end{aligned} \tag{51}$$

Furthermore the Hessian $\overset{\leftrightarrow}{H}(U^o)$ evaluated at U^0 has matrix elements given by

$$\begin{aligned} H(U^o)_{ai,bj} &= \left(\frac{d^2E^{(\infty)}}{dU_{ai}dU_{bj}}\right)_0 = \frac{d}{dU_{bj}}\left(\frac{dE^{(\infty)}}{dU_{ai}}\right) = \frac{d}{dU_{bj}}\sum_{\sigma}^{\alpha,\beta}\left(\frac{\partial E^{(\infty)}}{\partial \rho_\sigma}\right)_0\left(\frac{\partial \rho_\sigma}{\partial U_{ai}}\right)_o \\ &= \sum_{\sigma}^{\alpha,\beta}\sum_{\tau}^{\alpha,\beta}\left[\iint\left(\frac{\partial \rho_\sigma(1)}{\partial U_{bj}}\right)_0 \frac{1}{r_{12}}\left(\frac{\partial \rho_\tau(2)}{\partial U_{ai}}\right)_0 dv_1 dv_2\right. \\ &\quad \left. + \int f^{\sigma\tau}\left[\rho(U^0)\right]\left(\frac{\partial \rho_\sigma}{\partial U_{bj}}\right)_0\left(\frac{\partial \rho_\tau}{\partial U_{ai}}\right)_0 dv_1\right] + \sum_{\sigma}^{\alpha,\beta}\int F_{\sigma}^{\mathrm{KS}}\left[\rho(U^0)\right]\left(\frac{\partial^2 \rho_\sigma}{\partial U_{ai}\partial U_{bj}}\right)_0 dv_1 \\ &\cong \sum_{\sigma}^{\alpha,\beta}\sum_{\tau}^{\alpha,\beta}\int\left\{F_{\tau}^{\mathrm{KS}}\left[\rho(U^0)] + \left(\frac{\partial \rho_\sigma}{\partial U_{bj}}\right)_0\right] - F_{\tau}^{\mathrm{KS}}\left[\rho(U^0)\right]\right\}\left(\frac{\partial \rho_\tau}{\partial U_{ai}}\right)_0 dv_1 \\ &\quad + \sum_{\sigma}^{\alpha,\beta}\int F_{\sigma}^{\mathrm{KS}}\left[U^0\right]\left(\frac{\partial^2 \rho_\sigma}{\partial U_{ai}\partial U_{bj}}\right)_0 dv_1. \end{aligned} \tag{52}$$

The calculation of $\vec{g}$ and $\overset{\leftrightarrow}{H}(U^o)$ requires closed form expressions for $d\rho_{\sigma}^{(\infty)} \times (1,1')/dU_{ai}$ and $d^2\rho_{\sigma}^{(\infty)}(1,1')/dU_{ai}dU_{bj}$ [145]. Also required are F_{pq}^{KS} and $K_{rv,st}$ integrals already available in standard DFT programs. We can now from (50) obtain the optimal step within the quadratic region

$$\Delta U_{ai} = -\sum_{bj}(H^{-1})_{ai,bj}g_{bj} \tag{53}$$

Next, in order to satisfy (48), we must scale ΔU from (53) to obtain $U^{'} = \eta(U^0 + \Delta U)$. Here η is determined by substituting $\eta(U^0 + \Delta U)$ into (48). In addition, U' must be orthogonal to all previously found solutions $\{\vec{U}_{(\infty)}^{(K)}; K = 1, I-1\}$. Thus, we obtain a new solution U''

$$U'' = U' - \sum_{K}^{I-1}\langle U'|U^{(K)}\rangle/|U^{(K)}| \tag{54}$$

After having calculated U'' from (54), we now set $U^0 = U''$ and go back to (50) for another iteration. The procedure is continued until $\left|U^0 - U''\right|$ is smaller than a certain threshold. After that, the search might be extended to excited state $I + 1$.

We have already seen that adiabatic TD-DFT within the Tamm–Dancoff approximation is equivalent to CV(2) with $B^{\mathrm{KS}} = 0$. Another scheme that has been used in the past is ΔDFT [36, 113–116] where one generates new "excited state" KS-Slater determinants from the ground state determinant by substituting one of the occupied ground state KS-orbitals $\{\phi_i(1); i = 1, \mathrm{occ})$ with a virtual KS-orbitals $\{\phi_a(1); a = 1, \mathrm{vir})$. An evaluation of the energy of the new determinant followed by subtraction of the ground state energy makes it possible to determine the excitation energy $\Delta E^{\Delta\mathrm{DFT}}_{i\to a}$. In relation to CV(n)-DFT, the ΔDFT scheme is equivalent to applying the following approximations in (50):

$$(U^0)_{bj} = (U^0)_{ai}\delta_{ab}\delta_{ij}; \quad \Delta U = 0, \tag{55}$$

where $\Delta U = 0$ indicates that ΔDFT is a non-SCF method. The resulting excitation energy is given as

$$\begin{aligned} \Delta E^{\Delta\mathrm{DFT}}_{i\to a} &= E^{(\infty)}(\rho^0 + U^0) - E^{(\infty)}(\rho^0) \\ &\cong \int F^{\mathrm{KS}}\left[\rho^0 + \frac{1}{2}U_{ai}U_{ai}[\phi_a\phi_a - \phi_i\phi_i]\right]U_{ai}U_{ai}[\phi_a\phi_a - \phi_i\phi_i]dv_1 \\ &= \varepsilon^0_a - \varepsilon^0_i + \frac{1}{2}K^{\mathrm{KS}}_{aa,aa} + \frac{1}{2}K^{\mathrm{KS}}_{ii,ii} - K^{\mathrm{KS}}_{ii,aa}, \end{aligned} \tag{56}$$

where we in the last line has used that $U_{ai} = 1$.

Another method mentioned above is the ΔSCF scheme. In this method [36, 113–116], one promotes as in ΔDFT an electron from an occupied ground state KS-orbital $\{\phi_i(1); i = 1, \mathrm{occ}\}$ to a virtual KS-orbital $\{\phi_a(1); a = 1, \mathrm{vir}\}$ by introducing $(U^0)_{bj} = (U^0)_{ai}\delta_{ab}\delta_{ij}$. However, in contrast to ΔDFT where $\Delta U = 0$, the ΔSCF scheme updates ΔU and $\Delta\rho^{(\infty)}(1, 1')$ of (47) with the help of the diagonal part of the Hessian, or an approximation, as $\Delta U_{bj}{=}{-}g_{bj}[\rho^0{+}\Delta\rho^{(\infty)}]\, H^{-1}_{bj,bj}$ (b=1,vir; j=1,occ) until self-consistency when $g_{bj}[\rho^0{+}\Delta\rho^{(\infty)}]{=}0$. The resulting excitation energy is given by

$$\Delta E^{\Delta\mathrm{SCF}}_{a\to i} = \int F^{\mathrm{KS}}\left[\rho^0 + \frac{1}{2}\Delta\rho^{(\infty)}\right]\Delta\rho^{(\infty)}dv_1 \tag{57}$$

As in ΔDFT, "a" and "i" in U_{ai} belongs to the same symmetry representation. This can be seen by realizing that the initial guess for $\Delta\rho^{(\infty)}$ is $\psi_a\psi_a - \psi_i\psi_i$ which is totally symmetric. Thus, in subsequent updates $\Delta U_{bj} = -g_{bj}[\rho^0 + \Delta\rho^{(\infty)}]H^{-1}_{bj,bj}$ we have that $\Delta U_{bj} = 0$ if "b" and "j" in U_{bj} belongs to different representations. That is clearly a limitation compared to TDDFT where $\Delta U_{bj} \neq 0$ provided that

$\Delta\rho^{(\infty)}$ has contributions from U_{ck} where the direct product between "bj" and "ck" has a contribution from the totally symmetric representation.

On the other hand, ΔDFT and ΔSCF includes the higher order "self-interaction terms" missing in TDDFT for a qualitatively correct description of charge transfer transitions. Furthermore, the orbitals in ΔSCF are specifically optimized for the $i \rightarrow a$ transition. Unfortunately, the unconstrained optimization applied in traditional ΔSCF often leads to the variational collapse of the energy for higher lying excited states unto the energy of lower lying excited states. Finally, in ΔSCF we start with $U_{ai} = 1$. As orbitals of different symmetry are not allowed to mix, this ensures that the occupation of orbitals belonging to a certain symmetry representation in ΔSCF remains the same throughout the SCF procedure from the initial ΔDFT step ($U_{ai} = 1$) to the converged result.

3.2 Different Hartree–Fock and Post-Hartree–Fock Methods Used in the Study of Excited States

The approximate LCAO methods have all been applied to the excited states of transition metal complexes. This is the case for the schemes based on the Wolfberg–Helmholtz approximation [13] (WH) as well as the more quantitative CNDO, INDO and NDDO methods [21]. Results from the Extended Hückel [14] and Fenske–Hall [18] approaches where the WH approximation is applied can only be considered qualitative [24]. However, in contrast to ligand field theory [5], these schemes describe also CT between metals and ligands as well as ligand to ligand transitions [147]. Of the differential overlap methods [21], the most widely used for excited states of transition metals has been the ZINDO [27] scheme by Zerner. However, the predicted excitation energies depend heavily on the exponents chosen for the minimal Slater- type basis set. Applications of the ab initio HF method to the absorption spectra of transition metal complexes such as MnO_4^- [95–100] became possible in the early 1970s [29, 30]. However, the results were often disappointing. This is not surprising since the correlation energy neglected by HF can be quite different for the ground and excited states.

Post-Hartree–Fock methods were in the 1970s and 1980s mostly applied to diatomic molecules with one or two transition metals where comparison could be made to high-resolution gas phase experiments [148]. As computers became faster, the applications were extended to larger systems. However, coupled cluster and MCSCF schemes that are best suited for the study of transition metal complexes in their excited states scales as $(n_e)^6$ or worse. This puts severe limits one the size of the studied systems even today. Among the CC methods, the iterative coupled cluster approach including connected triples (CC3) [149] as well as the equation of motion (EOM) [150] affords the most accurate results for systems, where Hartree–Fock gives a reasonable description of the ground state [151]. Alternatives that also works for cases where Hartree–Fock is a poor zero-order description are the symmetry adapted cluster/configuration interaction (SAC-CI) method [94] and schemes based on MCSCF such as the CASSCF [90] and its CASPT2 extension [91]. Especially CASPT2 has been employed extensively in studies of transition metal systems by Björn Ross and collaborators [152, 153].

3.3 Theoretical Studies on the Absorption Spectrum of Permanganate and Related Tetroxo Complexes

Permanganate has served as a testing ground and litmus test for many computational methods as they emerged over the past 60 years. Of particular interest has been the absorption spectrum and we shall in this section discuss the performance of a number of the methods described above.

The low temperature and high-resolution absorption spectrum of permanganate as recorded by Holt and Ballhausen [12] is shown in Fig. 4. The first allowed band (I) starting at 2.27 eV (18,300 cm^{-1}) has a well-resolved vibronic structure. It is followed by a featureless shoulder (II) at 3.47 eV (28,000 cm^{-1}) and another strong band (III) at 3.99 eV (32,000 cm^{-1}) with a clear vibronic fine structure. We finally have a strong featureless band (IV) at 5.45 eV (43,960 cm^{-1}).

Wolfberg and Helmholz [13] put their newly developed LCAO method (1952) to the test by calculating the first two excitation energies of $\mathrm{MnO_4}^-$. They had in their calculation an inversion of the order of the first two virtual orbitals of Fig. 2 with $\varepsilon_{3t_2} < \varepsilon_{2e}$. This ordering is at odds with ligand field theory and lead to the controversial assignment of the first two bands as (I): (b) $t_1 \rightarrow 3t_2$ and (II): (d) $2t_2 \rightarrow 3t_2$, Table 7. The ligand field ordering was subsequently recovered in other semi-empirical calculations [161–167]. However, these schemes are too parameter dependent to afford a reliable detailed assignment [167]. The introduction by Hillier and Saunders [29] as well as Veillard [30] of first principle Hartree Fock programs lead shortly after to a series of ab initio HF calculations on the electronic

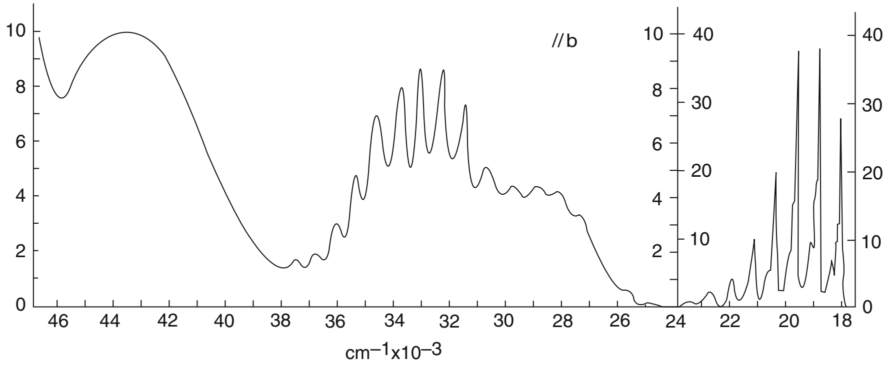

Fig. 4 Experimental absorption spectrum of $\mathrm{MnO_4}^-$ from Holt and Ballhausen [12]

Table 7 Calculated[a] and experimental excitation energies[b] for MnO_4^-

WH[c]	HF[d]	EOM[e]	STEOM[f]	HF + CI[g]	SAC–CI[h]	SW-Xα[i]	Xα[j]	LDA[k]	TDDFT[l]	[c]Exp
1.68[m]	1.04[n]	2.24[n]	1.92[n]	2.6[n]	2.48[n]	2.3[n]	2.48[n]	2.71[n]	2.87[n]	2.27
2.78[a]	2.54[o]	3.60[o]	3.08[m]	4.1[o]	3.96[m]	3.3[o]	3.96[o]	4.02[o]	3.89[o]	3.47
	2.94[m]	3.67[m]	3.51[o]	4.5[m]	4.15[o]	4.7[m]	4.15[m]	4.22[m]	4.77[m]	3.99
	4.77[p]	5.80[a]		6.1	5.82 [a,b]	5.3[a]	5.65[a]	5.70[a]	5.77[a]	5.45

[a] $2t_2 \rightarrow 3t_2$
[b] eV
[c] [12]
[d] [97]
[e] [154]
[f] [155]
[g] [98, 99]
[h] [156]
[i] [157]
[j] [158]
[k] [159]
[l] [160]
[m] $t_1 \rightarrow 3t_2$
[n] $t_1 \rightarrow 2e$
[o] $2t_2 \rightarrow 2e$
[p] $1t_2 \rightarrow 2e$[13]

spectrum of MnO_4^- [97–102]. While the first calculations were limited to small basis sets, Hsu [97] et al. published in 1976 a basis set limit calculation, Table 7. Their results are only in fair agreement with experiment, Table 7. There have finally been four post-HF studies. The first two by Nooijen employ EOM-CCSD [154] and STEOM [155], whereas the third by Johansen and Retrup [98] is based on HF augmented by single and double excitations (HF + CI). The fourth by Nakatsuji [156] et al. employs SAC + CI. All assign (I) to $t_1 \rightarrow 2e$. However, the closely spaced next two bands are assigned as (II): $t_1 \rightarrow 3t_2$, (III): $2t_2 \rightarrow 2e$ for SAC + CI and STEOM with (II): $2t_2 \rightarrow 2e$, (III): $t_1 \rightarrow 3t_2$ for HF + CI and EOM. We shall refer to these assignments as the bc and cb orderings, respectively. It is obvious that all four methods are able to reach semi-quantitative accuracy. However they are likely not accurate enough to conclusively settle which of the two orderings (bc or cb) is the correct one. It would be very interesting to have a study of permanganate based on CASPT2

Also shown in Table 7 are results based on DFT. The three first entries are due to ΔSCF calculations using the SW-Xα [157], the Xα [158] and the LDA [159] approaches of which the last provides full resolution of all space and spin multiplets. The results are quite similar and in reasonable agreement with experiment. All three methods point to the cb ordering. We finally have a number of TDDFT [160, 168, 169] calculations with the one by Neugebauer et al. [159] shown in Table 7. TDDFT allows in principle one-electron excitations such as $t_1 \rightarrow 3t_2$ and $2t_2 \rightarrow 2e$ to mix. Nevertheless, all TDDFT calculations are consistent with a cd ordering similar to ΔSCF although some mixing of $t_1 \rightarrow 3t_2$ and $2t_2 \rightarrow 2e$ takes place in II and III.

Neugebauer et al. [160] have recently simulated the absorption spectrum for permanganate by including the vibronic fine structure as shown in Fig. 5.

Their simulation catches the main features of the experimental spectrum in Fig. 4. It is also argued by the authors that the assignment of bands in terms of one electron transitions such as $t_1 \rightarrow 3t_2$ and $2t_2 \rightarrow 2e$ is too simplistic as these transitions are mixed by vibronic coupling. More quantitative calculations are needed to see whether this in fact is the case for permanganate.

We finally have in Table 8 calculated excitation energies for a number of tetroxo systems by SAC-CI [170] and three DFT-based methods of which the first two are ΔSCF schemes [158, 159] and the last an adiabatic TDDFT approach [171]. All schemes find the first band to be due to $t_1 \rightarrow 2e$ with the exception of $MoO_4{}^{2-}$ where SAC-CI finds the assignment $t_1 \rightarrow 3t_2$. For the $4d$ samples RuO_4, $MoO_4{}^{2-}$ and the $5d$ complex OsO_4, the general assignment for II and III is $2t_2 \rightarrow 2e$ and $t_1 \rightarrow 3t_2$, respectively, corresponding to the cb ordering with the exception of $MoO_4{}^{2-}$ for the case of SAC-CI. The cb ordering is to be expected for $4d$ and $5d$ complexes where the ligand field splitting $\varepsilon_{3t_2} - \varepsilon_{2e}$ is large. For the $3d$ systems such as $CrO_4{}^{2-}$ and $MnO_4{}^{-}$, the ligand splitting $\varepsilon_{3t_2} - \varepsilon_{2e}$ is smaller resulting in quite similar calculated energies for $2t_2 \rightarrow 2e$ and $t_1 \rightarrow 3t_2$ as well as a close experimental positions of bands II and III. It can be seen that SAC-CI for 3d systems give rise to the bc ordering whereas all DFT methods point to the cb ordering.

We will conclude by stating that there is general consensus on the assignment of the first three bands for $4d$ and $5d$ tetroxo complexes. However, for the $3d$ tetroxo complexes more work has to be done before a definitive assignment can be given of bands II and III. This is a somewhat sobering conclusion given the fact that the work on permanganate has been ongoing for more than 60 years.

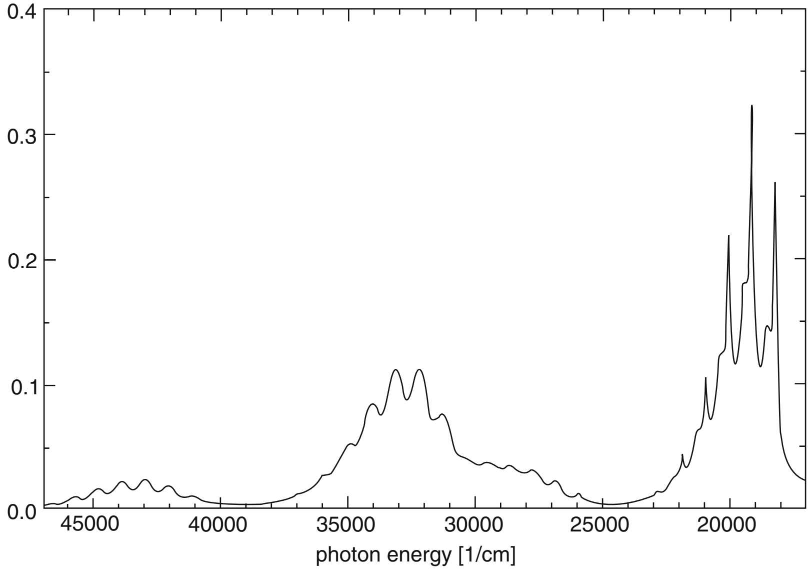

Fig. 5 Simulated absorption spectrum for permanganate due to Neugebauer et al. [160]

Table 8 Calculated[a] and experimental excitation energies for some tetroxo complexes

Complex	SAC–CI[b]	ΔSCF(Xα)[c]	ΔSCF(LDA)[d]	[e]TDDFT	[c]Exp
CrO_4^{2-}	3.41[f]	3.30[f]	3.64[f]	3.79[f]	3.32
	4.16[g]	4.58[h]	4.83[h]	4.67[h]	4.53
	4.51[h]	4.90[g]	5.18[g]	5.39[g]	4.86
MoO_4^{2-}	4.37[g]	5.17[f]	5.40[f]	5.66[f]	5.34
	5.14[h]	5.84[h]	5.89[h]	6.15[h]	5.95
	5.52[f]	7.16[g]	7.22[g]		
MnO_4^-	2.57[f]	2.48[f]	2.71[f]	2.87[f]	2.27
	3.58[g]	3.96[h]	4.02[h]	3.89[h]	3.47
	3.72[h]	4.15[g]	4.22[g]	4.77[g]	3.99
RuO_4	3.22[f]	3.02[f]	3.28[f]	3.69[f]	3.22
	4.55[h]	3.81[h]	4.00[h]	4.51[h]	4.09
	5.23[g]	4.56[g]	5.06[g]	5.87[g]	5.03
OsO_4	3.90[f]	-	4.29[f]	5.06[f]	4.34
	5.46[h]	-	4.75[h]	5.81[h]	5.21
	6.41[g]	-	6.76[g]	7.11[g]	5.95

[a] eV
[b] [170]
[c] [158]
[d] [159]
[e] [171]
[f] $t_1 \rightarrow 2e$
[g] $t_1 \rightarrow 3t_2$
[h] $2t_2 \rightarrow 2e$

3.4 Theoretical Studies on the Magnetic Circular Dichroism Spectrum of Permanganate and Related Tetroxo Complexes

Magnetic circular dichroism (MCD) spectroscopy [171, 172] involves the measurement of the difference in absorption of left and right circularly polarized light in the presence of a magnetic field. An MCD signal can be negative or positive and MCD spectra can provide useful information about the nature of the excited states of a molecule that may not be available from the positive absorption spectrum. MCD spectroscopy is particularly useful when degenerate states are present since the applied magnetic field then will perturb the energies of these states to first order.

The observed MCD spectrum can be expressed in terms of three parameters or terms (A_J, B_J and C_J) as

$$MCD(\hbar\omega) = \chi\hbar\omega B\sum_J A_J\left(-\frac{\partial f_J(\hbar\omega - \hbar\omega_J)}{\partial\hbar\omega}\right) + \left(B_J + \frac{C_J}{kT}\right)f_J(\hbar\omega - \hbar\omega_J),$$

where $\hbar\omega$ is the energy of the incident light, $\hbar\omega_J$ is the excitation energy to state J, B is the amplitude of the applied magnetic field, k is Boltzmann's constant, T is the temperature and f_J is a band shape function, whereas χ is a collection of constants and experimental parameters. The parameters A_J, B_J and C_J can on the one hand be calculated from first principle and on the other hand be extracted from the experimentally measured MCD intensity $MCD(\hbar\omega)$. We shall here exclusively be interested in the contribution from A_J as the excited states in tetroxo systems to which transitions are allowed are degenerate and of T_2 symmetry.

The presence of an intense A term is a strong indication that the excited state of a transition is spatially degenerate thereby helping to assign that transition and perhaps providing evidence as to the overall symmetry of the molecule under investigation. In addition to A_J, the ratio A_J/D_J is often obtained from an experimental spectrum. Here, D_J is the dipole strength of the transition to state J in the absorption spectrum and is closely related to the oscillator strength. The ratio A_J/D_J is of interest because it can be directly related to the magnetic moment of the excited state and is less subject to environmental effects than A_J (Table 9).

We present in Fig. 6 the simulated [171] and experimental MCD spectra for $VO_4{}^{3-}$, $CrO_4{}^{2-}$ and MnO_4. Except for a blue shift, the agreement between the calculated and observed spectra is rather good. For all three systems, the first band gives rise to a negative A term and a negative A_J/D_J ratio in agreement with experiment. For $CrO_4{}^{2-}$ and $MnO_4{}^{-}$ theory predicts that the second band should be weak whereas the third band exhibits a strong positive A term with a large positive A_J/D_J ratio, in good agreement with experiment. The predicted MCD spectrum involving bands II and III is also in good agreement with experiment for $VO_4{}^{3-}$.

The good fit between theory and experiment for $CrO_4{}^{2-}$ and $MnO_4{}^{-}$ in the simulation of their MCD spectra provides perhaps the strongest support for the assignment II: $2t_2 \to 2e$ and III: $t_1 \to 3t_2$ provided to date for these two systems.

Table 9 Calculated[a] and experimental excitation energies, A_J terms[b] and A_J/D_J[b] parameters

	Theory			[a]Exp		
	[c]$\hbar\omega_J$	A_J	A_J/D_J	[c]$\hbar\omega_J$	A_J	A_J/D_J
$VO_4{}^{3-}$	4.66[d]	−0.04	−0.37	4.58	−0.29	−0.46
	5.38[e]	0.0003	0.06	5.58	+	+
	5.87[f]	0.042	0.61	6.15		
$CrO_4{}^{2-}$	3.79	−0.057	−0.53	3.32	−0.191	−0.58
	4.67	0.0016	0.08	4.53		
	5.39	0.063	0.85	4.86	0.195	0.63
$MnO_4{}^{-}$	2.87[d]	−0.061	−0.66	2.27	−0.085	−0.48
	3.89[e]	0.0025	0.10	3.47	-	-
	4.77[f]	0.071	0.97	3.99	0.155	0.86

[a] [171]

[b] All values in au

[c] eV

[d] $t_1 \to 2e$[f] $t_1 \to 3t_2$

[e] $2t_2 \to 2e$

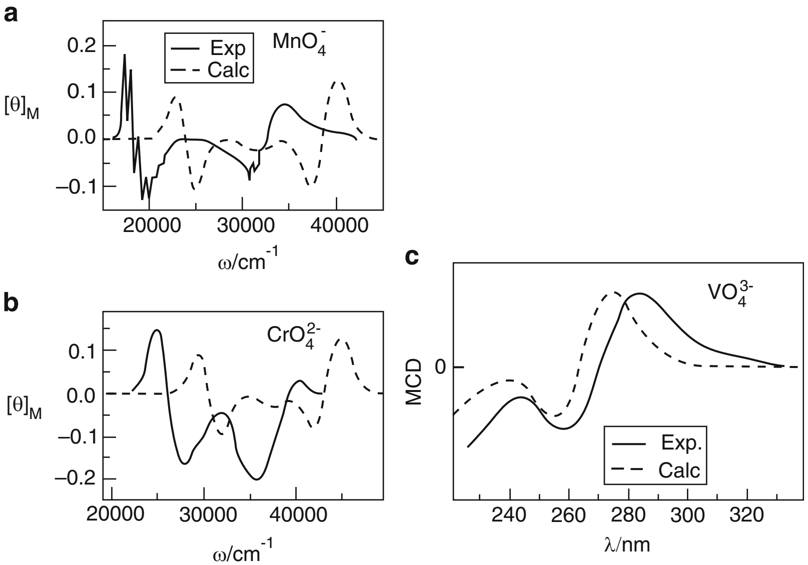

Fig. 6 Simulated and observed MCD spectra for VO_4^{3-}, $CrO_4^{2-}$and MoO_4^{-} from [171]

4 Concluding Remarks

Some 60 years have passed since the first LCAO calculations on transition metal complexes appeared [13]. Electronic structure theory is now at the point where it is possible to describe the potential energy surface (PES) of a gas phase molecule containing up to 20 atoms with great accuracy using high level wave function methods such as CCSD(T) (ground state) or EOM/CASSPT2/SAC-CI (excited states). For larger systems, acceptable accuracy can be obtained by DFT (ground state) or TD-DFT/ΔSCF-DFT (excited states). Great strides have also been taken in describing the PES for reactions on surfaces in the interface between gas phase and solid state. Here, DFT will continue to be the electronic structure theory of choice. Of special importance for transition metals is the development of methods that include relativistic effects since they are required to describe periodic trends correctly within a triad of transition metals. As hardware becomes faster larger molecules can be treated with higher accuracy using existing methodology. Known methods are also likely to become faster by neglecting interactions between fragments in large molecules that are “far apart”. In this way, most methods will eventually become linear in the number of atoms if this number is large enough. It is finally possible that further progress in approximate DFT will result in new methods with the same accuracy as highly correlated wave functions and speeds still comparable to GGA-DFT.

Many chemical systems of interest have large bulky groups that exert steric pressure on the reactive centre as an essential part of how they function. For such systems increasing use will be made of dual- or multi-level approaches in which the steric bulk is treated at a lower level of theory than the reactive system. The reason that one would like to treat bulky groups by simple theories such as molecular mechanics (MM) is not only that they have a large number of electrons but also (rather) that they potentially possess a formidable number of conformations. The many conformations make it difficult (expensive) to determine the global energy minimum even with MM.

Solvent effect can have a profound effect on chemical reactions, yet we do not at the moment have a proven methodology (as in the case of electronic structure theory) that by well-known routes can converge to chemical accuracy. Continuum methods are going to carry the bulk of the workload in the foreseeable future. However, it will be one of the major challenges within the next decade to develop solvation theories that by standard procedures will converge to chemical accuracy. Such methods are likely to combine explicit solvation for the first few solvation shelves with bulk descriptions (continuum or mean-field) for the remaining part of the solvent.

Turning next to dynamics on the PES and calculations of reaction rates, one might expect that these rates for the majority of cases will be determined with the help of Eyring's transition state method. To this end, locating saddle points on the PES is still time consuming in terms of manpower, and more systematic and automated procedures would be welcome.

The number of studies of inorganic reaction mechanisms by theoretical methods has increased drastically in the last decade. The studies cover ligand substitution reactions, insertion reactions oxidative addition, nucleophilic and electrophilic attack as well as metallacycle formation and surface chemistry, in addition to homogeneous and heterogeneous catalysis as well as metalloenzymes. We can expect the modeling to increase further both in volume and in sophistication [173].

Acknowledgement T.Z. would like to thank the Canadian government for a Canada research chair in theoretical inorganic chemistry and NSERC for financial support. Thanks also go to Drs. M. Seth and M. Krykunov for many interesting discussions.

References

1. Becquerel J (1929) Z Phys 58:205
2. Bethe H (1929) Ann Phys 3:133–208
3. Van Vleck JH (1935) J Chem Phys 3:803–806
4. Orgel LE (1960) An introduction to the transition-metal chemistry: ligand-field theory. Methuen, London
5. Ballhausen CJ (1962) Introduction to ligand field theory. McGraw-Hill, New York
6. Mulliken RS (1932) Phys Rev 40:55
7. Ilse FE, Hartmann H (1951) Z Naturforsch 6a:751
8. Roothan CCJ (1951) Rev Mod Phys 23:69–89
9. Hall GG (1951) Proc R Soc Lond A 205:541–552
10. Bursten BE, Drummon FF, Li J (2003) Faraday Discuss 124:1

11. Teltow J (1938) Z Phys Chem B 40:397
12. Holt SL, Ballhausen CJ (1967) Theor Chim Acta 7:313
13. Wolfsberg M, Helmholz LJ (1952) J Chem Phys 20:837
14. Hoffmann R (1963) J Chem Phys 39:1397–1412
15. Hoffmann R (1982) Angew Chem Int Ed Engl 21:711–724
16. Albright TA, Burdett JK, Whangbo MH (1985) Orbital interactions in chemistry. Wiley, New York
17. Burdett JK (1980) Molecular shapes: theoretical models of inorganic stereochemistry. Wiley, New York
18. Hall MB, Fenske RF (1972) Inorg Chem 11:768–775
19. Hall MB (1978) J Am Chem Soc 100:6333–6338
20. Pople JA, Santry DP, Segal GA (1965) J Chem Phys 43:S129
21. Dewar MJS, Zoebisch EG, Healy EF, Stewart JJP (1985) J Am Chem Soc 107:3902
22. Stewart JJP (1989) J Comput Chem 10:221
23. Dewar MJS, Thiel W (1977) J Am Chem Soc 99:4899–4907
24. Dahl JP, Ballhausen CJ (1968) Adv Quantum Chem 4:170
25. Ziegler T (1974) Acta Chem Scand A28:29
26. Truax DR, Geer JA, Ziegler T (1973) J Chem Phys 59:6662
27. Zerner M (1991) In: Lipkowitz KB, Boyd DB (eds) Reviews in computational chemistry, vol 2. VCH, New York, p 313
28. Marynick DA, Lipscomb WN (1982) Proc Natl Acad Sci USA 79:1341–1345
29. Hillier IH, Saunders VR (1969) J Chem Soc Chem Commun 1275–1276
30. Veillard A (1969) J Chem Soc Chem Commun 1022–1023
31. Coutière M-M, Demuynck J, Veillard A (1972) Theor Chim Acta 27:281–287
32. Dirac PAM (1930) Proc Cambridge Philos Soc 26:376
33. Fermi E (1928) Z Phys 48:73
34. Thomas H (1927) Proc Cambridge Philos Soc 23:542
35. Slater JC (1951) Phys Rev 81:385
36. Ziegler T, Rauk A, Baerends EJ (1977) Theor Chim Acta 43:261
37. Slater JC (1974) The self-consistent field for molecules and solids: quantum theory of molecules and solids, vol 4. McGraw Hill, New York
38. Hohenberg P, Kohn W (1964) Phys Rev 136:864
39. Johnson KH (1966) J Chem Phys 45:3085
40. Korringa J (1947) J Physica 13:392
41. Case DA (1982) Annu Rev Phys Chem 33:151
42. Salahub DR, Messmer RP, Johnson KH (1976) Mol Phys 31:521
43. Ellis DE, Painter GS (1970) Phys Rev B2:2887
44. Baerends EJ, Ellis DE, Ros P (1973) Chem Phys 2:41
45. Sambe H, Felton RH (1975) J Chem Phys 62:1122
46. Dunlap BI, Connolly JWD, Sabin JF (1979) J Chem Phys 71:4993
47. Gunnarson O, Harris J, Jones RO (1977) Phys Rev 15:3027
48. Becke AD (1988) J Chem Phys 88:2547
49. Boerrigter PM, te Velde G, Baerends EJ (1988) Int J Quantum Chem 33:87
50. Delley BJ (1990) Chem Phys 92:508
51. te Velde G, Baerends EJ (1992) J Comput Phys 99:84
52. Pederson MR, Ackson MRKA (1990) Phys Rev 41:7453
53. Delley BJ, Ellis E (1982) J Chem Phys 76:1949
54. Ziegler T, Rauk A (1977) Theor Chim Acta 46:1
55. Versluis L, Ziegler T (1988) J Chem Phys 88:322
56. Jacobsen H, Berces A, Swerhone DP, Ziegler T (1997) Comput Phys Commun 100:263–276
57. Berces A, Dickson RM, Fan L, Jacobsen H, Swerhone DP, Ziegler T (1997) Comput Phys Commun 100:247–262
58. Wolff SK (2005) Int J Quantum Chem 104:645

59. Andzelm J, Salahub DR (1986) Int J Quantum Chem 14:1091
60. Andzelm J (1991) In: Density functional methods in chemistry. Springer, New York
61. Dunlap DI, Rösch N (1990) Adv Quantum Chem 21:317
62. Liu WJ, Wang F, Li LM (2003) J Theor Comput Chem 2:257–272
63. Almlöf J, Korsel K, Faegri K Jr (1982) J Comput Chem 3:385
64. Horn H, Weiss H, Häser M, Ehring M, Ahlrichs R (1991) J Comput Chem 12:1058
65. Ahlrichs R, Tsereteli K (2001) J Comput Chem 23:306–309
66. Boström J, Delcey MG, Aquilante F, Serrano-Andrés L, Pedersen TB, Lindh R (2010) J Chem Theor Comput 6:747–754
67. Becke AD, Dickson RM (1990) J Chem Phys 92:3610
68. Luthi HP, Siegbahn PEM, Almlof J (1985) J Phys Chem 89:2156
69. Lüthi HP, Ammeter JA, Almlof J, Faegri K (1982) J Chem Phys 77:2002
70. Rosch N, Jorg NH, Dunlap BI (1985) NATO ASZ 1:176
71. Dunlap BI (1986) J Phys Chem 90:5524
72. Antolovic A, Davidson ER (1988) J Chem Phys 88:4967
73. Versluis L, Ziegler T (1989) J Am Chem Soc 111:2018
74. Tschinke V, Ziegler T (1990) J Chem Phys 93:8051–8060
75. Buijse MA, Baerends EJ, Snijders JG (1989) Phys Rev A 40:4190–4202
76. Becke AD (1986) J Chem Phys 85:7184
77. Becke AD (1988) J Chem Phys 88:1053
78. Becke AD (1993) J Chem Phys 98:5648
79. Ziegler T, Tschinke V, Ursenbach CJ (1987) J Am Chem Soc 109:4827
80. Perdew JP (1986) Phys Rev B33:8822
81. Lee C, Yang W, Parr RG (1988) Phys Rev B 37:785
82. Sholl DS, Steckel JA (2009) Density functional theory: a practical introduction. Wiley, Hoboken
83. Koch W, Holthausen MC (2000) A chemist's guide to density functional theory. Wiley-VCH, New York
84. Burke K (2009) The ABC of DFT. http://dft.uci.edu/materials/bookABCDFT/gamma/g1.pdf
85. Perdew JP (2009) Density functional theory. http://007-chbooks.blogspot.com/2009/07/density-functional-theory-john-p-perdew.html
86. Becke AD, Johnson ER (2007) J Chem Phys 127:124108
87. Johnson ER, Becke AD (2009) Can J Chem 87:1369
88. Jensen F (2006) Introduction to computational chemistry, 2nd edn. Wiley, New York
89. Head-Gordon M, Pople JA, Frisch MJ (1988) Chem Phys Lett 153:503–506
90. Olsen J, Ross BO, Jørgensen P, Aa. Jensen HJ (1988) J Chem Phys 89:2185
91. Finley J, Malmqvist P-A, Roos BO, Serrano-Andrés L (1998) Chem Phys Lett 288:299
92. Goddard WA, Dunning TH, Hunt WJ, Hay PJ (1973) Acc Chem Res 6:368
93. Shaik S, Hiberty PC (2008) A chemist's guide to valence bond theory. Wiley-Interscience, New Jersey
94. Nakatsuji H, Hiraro K (1978) J Chem Phys 68:2053
95. Johansen H (1972) Chem Phys Lett 17:569
96. Wood MH (1973) Theoret Chim Acta 36:309
97. Hsu H, Peterson C, Pitzer RM (1976) J Chern Phys 64:791
98. Rettrup S (1978) Spin-coupled wave functions in ab initio SCF and CI calculations with application to the manganate ion. Dissertation, The Technical University of Denmark, DK-2800 Lyngby
99. Johansen H, Rettrup S (1983) Chern Phys 74:77
100. Johansen H (1983) Mol Phys 49:1209
101. Hillier H, Saunders VR (1970) Proc R Soc Lond A 320:161
102. Hillier H, Saunders VR (1971) Chern Phys Lett 9:219
103. Buijse M, Baerends EJ (1990) J Chem Phys 93:4129

104. Kaupp M, Bühl M, Malkin VG (eds) (2002) Calculation of NMR and ESR parameters. Willey-VCH, Weinheim
105. Kaupp M, Malkin OL, Malkin VG (1997) J Chem Phys 106:9201
106. Schreckenbach G, Ziegler T (1997) Int J Quantum Chem 61:899
107. Khandogin J, Ziegler T (1999) Spectrochim Acta 55:607
108. Malkina OL, Salahub DR, Malkin VG (1996) J Chem Phys 105:8793
109. Autschbach J, Ziegler T (2000) J Chem Phys 113:9410
110. Gaudoin R, Burke K (2004) Phys Rev Lett 93:173001–1
111. Oliveira LN, Gross EKU, Kohn W (1988) Phys Rev A 37:2821
112. Gidopoulos NI, Papaconstantinou PG, Gross EKU (2002) Phys Rev Lett 88:03300
113. Levy M, Nagy A (1999) Phys Rev Lett 83:4361
114. Slater JC, Wood JH (1971) Int J Quantum Chem 4S:3
115. Slater JC (1972) Adv Quantum Chem 6:1
116. Levy M, Perdew JP (1985) Phys Rev A 32:2010
117. Nagy A (1996) Phys Rev A 53:3660
118. Besley N, Gilbert A, Gill P (2009) J Chem Phys 130:124308
119. Liu TQ, Han WG, Himo F, Ullmann GM, Bashford D, Toutchkine A, Hahn KM, Noodleman L (2004) J Phys Chem A 108:3545–3555
120. Gavnholt J, Olsen T, Engelund M, Schiötz J (2008) Phys Rev B 78:075441
121. Zope R, Baruah T, Richardson S, Pederson M, Dunlap BI (2010) J Chem Phys 133:034301
122. Runge RE, Gross EKU (1984) Phys Rev Lett 52:997
123. Casida ME (1995) In: Chong DP (ed) Recent advances in density functional methods. World Scientific, Singapore, pp 155–193
124. Casida ME (1999) Workshop proceedings of the joint ITP/INT workshop on time-dependent density functional theory, 15–17 April 1999 at http://www.itp.ucsb.edu/online/tddft_c99
125. van Gisbergen SJA, Snijders JG (1995) J Chem Phys 103:9347
126. Petersilka M, Grossmann UJ, Gross EKU (1996) Phys Rev Lett 76:12
127. Bauernschmitt R, Ahlrichs R (1996) Chem Phys Lett 256:454
128. Stratmann RE, Scuseria GE, Frisch MJ (1998) J Chem Phys 109:8218
129. Helgaker T, Jørgensen P, Olsen J (2000) Molecular electronic-structure theory. Wiley, New York
130. Autschbach J, Ziegler T (2003) Coord Chem Rev 238:83
131. McWeeny R (1982) Methods of molecular quantum mechanics, 2nd edn. Academic, London
132. Jacquemin D, Perpete EA, Ciofini I, Adamo C, Valero R, Zhao Y, Truhlar DG (2010) J Chem Theory Comput 6:2071
133. Goerigk L, Grimme S (2010) J Chem Phys 132:184103
134. Tawada Y, Tsuneda T, Yanagisawa S, Yanai T, Hirao K (2004) J Chem Phys 120:8425
135. Song J-W, Watson MA, Hirao K (2009) J Chem Phys 131:144108
136. Schreiber M, Silva-Junior M, Sauer S, Thiel W (2008) J Chem Phys 128:134110
137. Stein T, Kronik L, Baer R (2010) J Am Chem Soc 131:2818
138. Neugebauer J, Gritsenko O, Baerends EJ (2006) J Chem Phys 124:214102
139. Schipper PRT, Gritsenko OV, van Gisberger SJA, Baerends EJ (2000) J Chem Phys 112:1344–1352
140. Gritsenko O, Baerends EJ (2004) J Chem Phys 121:655–660
141. Ziegler T, Krykunov M (2010) J Chem Phys 133:074104
142. Ziegler T, Seth M, Krykunov M, Autschbach J, Wang F (2009) J Mol Struct Theochem 914:106
143. Ziegler T, Seth M, Krykunov M, Autschbach J (2008) J Chem Phys 129:184114
144. Ziegler T, Seth M, Krykunov M, Autschbach J, Wang F (2009) J Chem Phys 130:154102
145. Cullen J, Krykunov M, Ziegler T (2011) Chem Phys doi: 10.1016/j.chemphys.2011.05.021
146. Hirata S, Head-Gordon SM (1999) Chem Phys Lett 314:291
147. Ballhausen CJ (1977) In: Segal GA (ed) Semi-empirical methods of electronic calculation, Part B. Plenum Press, New York

148. Lawley KP (1987) In: Advances in chemical Physics, vol 67. Wiley, New York
149. Koch H, Christiansen O, Jørgensen P, Sanchez de Merás AM, Helgaker T (1997) J Chem Phys 106:1808
150. Nooijen M, Bartlett RJ (1997) J Chem Phys 106:6441
151. Bartlett RJ, Stanton JF (2007) Applications of post-Hartree–Fock methods: a tutorial. In: Lipkowitz KB, Boyd DB (eds) Reviews in computational chemistry, vol 5. VCH, New York
152. Pierloot K (2011) Int J Quant Chem (Published online)
153. Special issue on electronic structure of metal complexes (2003) Faraday Discuss 124:1–455
154. Nooijen M (1999) J Chem Phys 11:10815
155. Nooijen M, Lotrich V (2000) J Chem Phys 111:494
156. Nakai H, Ohmori Y, Nakatsuji H (1991) J Chem Phys 95:8287
157. Johnson KH, Smith FC Jr (1971) Chem Phys Lett 10:219
158. Ziegler T, Rauk A, Baerends EJ (1976) Chem Phys 16:209
159. Stückel AC, Daul CA, Güdel HU (1997) J Chem Phys 107:4606
160. Neugebauer J, Baerends EJ, Nooijen M (2005) J Phys Chem A 109:1168
161. Fenske KF, Sweeney C (1964) Inorg Chem 3:1105
162. Viste A, Gray HB (1964) Inorg Chem 3:1113
163. Dahl JP, Johansen H (1968) Theor Chim Acta 11:8
164. Oleari L, De Michelis G, Di Sipio L (1966) Mol Phys 10:111
165. Brown RD, James BH, O'Dwyer MF, Roby KR (1967) Chem Phys Lett 1:459
166. Canadine RM, Hillier IH (1969) J Chem Phys 50:2984
167. Ballhausen CJ, Gray HB (1971) Electronic structures of metal complexes. In: Martell AE (ed) Coordination chemistry, vol 1. Van Norstrand Reinhold, New York
168. van Gisbergen SJA, Groeneveld JA, Rosa A, Snijders JG, Baerends EJ (1999) J Phys Chem A 103:6835
169. Boulet P, Chermette H, Daul CA, Gilardoni F, Weber J, Zuber G (2001) J Phys Chem A 105:885
170. Jitsuhiro S, Nakai H, Hada M, Nakatsuji H (1994) J Chem Phys 101:1029
171. Seth M, Krykunov M, Ziegler T, Autschbach J (2008) J Chem Phys 128:234102
172. Seth M, Ziegler T (2010) Adv Inorg Chem 62:41–109
173. Ziegler T, Autschbach J (2005) J Chem Rev 105:2695

Struct Bond (2012) 143: 39–52
DOI: 10.1007/430_2011_50

Orbital Models and Electronic Structure Theory

Jan Linderberg

Abstract This tribute to the work by Carl Johan Ballhausen focuses on the emergence of quantitative means for the study of the electronic properties of complexes and molecules. Development, refinement, and application of the orbital picture elucidated electric and magnetic features of ranges of molecules when used for the interpretation of electronic transitions, electron spin resonance parameters, rotatory dispersion, nuclear quadrupole couplings as well as geometric bonding patterns. Ballhausen's profound impact on the field cannot be overestimated.

Keywords Crystal field · Hubbard · Hückel · Propagators

Contents

J. Linderberg (✉)
Department of Chemistry, Aarhus University, Langelandsgade 140, 8000 Aarhus C, Denmark

Department of Chemistry, University of Florida, Gainesville, FL, USA

Department of Chemistry, University of Utah, Salt Lake City, UT, USA
e-mail: jan@chem.au.dk

1 Opening

It is appropriate to quote from Ballhausen's thesis, which he defended for the degree of Doctor of Philosophy in 1958, his view of the status of theory within chemistry:

> *Intet synes i vor Tid at være lettere – specielt inden for Kemien – end at slynge ubeviste Paastande ud og "forklare" eksperimentelle Data ved hjælp af taagede teoretiske Talemaader, medens kvantitative Beregninger bygget paa teoretiske Grundprincipper ikke synes at være i høj Kurs.*
>
> C.J. Ballhausen, Elektrontilstande i Komplexer af 1. Overgangsgruppe. En Studie i Krystalfelt Teori (J. Jørgensen & Co. Bogtrykkeri A/S, København 1958)
>
> "Nothing seems to be simpler these days – particularly within chemistry – than to put forth unproven postulates and "explain" experimental data through foggy theoretical modes of speech, while quantitative calculations based on basic theoretical principles are not rated at a high value." (Translation by JL)

This critical view of the situation was well put and the coming years saw an extraordinary improvement in the quality and quantity of theoretical effort. These were made possible through training of young quantum chemists and the access to electronic computers. Ballhausen, who assumed the chair of Physical Chemistry in 1959, made his institute to a major center of research where theory and experiment could grow in each others company.

There is a short and formal presentation of the elements of the quantum mechanics of orbitals and states of electronic systems in the next paragraph. A simple variant of the maximum overlap model is used as an example. The Hückel model is used, in the third section, to present electric and magnetic perturbations in simplified contexts. There follows, in the fourth part, an account of crystal field theory with attention to the self-consistent grand canonical ensemble Hartree–Fock approach in the two-component spin orbital form. Further detail is also given of the options for a separable representation of the electron interaction. The fifth section indicates the nature of the theory for narrow energy bands in transition metals as suggested by Hubbard. A summary and a short literature guide ends this homage to Carl Johan Ballhausen.

2 Stationary States and Orbitals

Niels Bohr suggested that the spectrum of atoms derived from transitions between stationary states and even though the orbits he proposed have not survived his notion was vindicated through the advent of quantum mechanics. Schrödinger showed how to find the states and to represent them through wave functions. Pauli and Dirac supplemented with the electron spin and Mulliken coined the word: *orbital*.

It was evident from numerous studies that atoms of the same column in the periodic system had similarities in their electronic build up and the concept of valence electrons or more appropriate valence orbitals as the elements for a structural classification was established. The present discussion is limited to considerations based on a description departing from a simple basis of spin orbitals formed by the union of atomic valence spin orbitals.

Each atom provides a set $\mathbf{u}_{\mathrm{A}}$:$\{u_{Aj}(\mathbf{r}\sigma) \mid j = 1,2,\ldots n_A\}$ and the entire basis is the union $\mathbf{u} = \mathbf{u}_{\mathrm{A}}$ U $\mathbf{u}_{\mathrm{B}}$ U…U $\mathbf{u}_{\mathrm{M}}$. Its dimension is $n = n_A + n_A + \ldots + n_M$ and the associated power set $P(\mathbf{u})$ of dimension 2^n provides a basis for many-electron states. The power set $P(\mathbf{u})$ is the set of all subsets of $\mathbf{u}$, including the empty set and the set itself.

The basis set $\mathbf{u}$ defines annihilation, $\{a_s \,/\, s = 1,2,\ldots n\}$, and creation operators, $\{a_s{}^{\dagger} \,/\, s = 1,2,\ldots n\}$, that generate an algebra with the rules

$$a_s a_{s'} + a_{s'} a_s = 0; a_s^{\dagger} a_{s'}^{\dagger} + a_{s'}^{\dagger} a_s^{\dagger} = 0; a_s a_{s'}^{\dagger} + a_{s'}^{\dagger} a_s = \delta_{ss'} + S_{ss'}.$$

Overlap integrals $S_{ss'} = \int d\mathbf{r} d\sigma\; u_s{}^{*}(\mathbf{r}\sigma) u_{s'}(\mathbf{r}\sigma) - \delta_{ss'}$ appear here with the convention that they vanish for an orthonormal set. Their values can be readily calculated once a suitable form is chosen for the atomic orbitals.

A representation of the Hamiltonian is more elusive and has been the subject of many a theoretical exposé. The simplest, one-electron, model requires estimates of the value of effective Hamiltonian in the form

$$F_{ss'} = <[a_s, [H, a_{s'}^{\dagger}]]_+>$$

and the average value refers to some state or ensemble, depending on the system whose properties are to be resolved. A notation is chosen so as to relate to the formal Hartree–Fock theory, where the elements $F_{ss'}$ represent the Fock matrix. It will generally be assumed that the Fock matrix is diagonal in the limit of separated atoms,

$$F_{ss'} - > W_s \delta_{ss'}, S_{ss'} - > 0.$$

The Hamiltonian is then expressed as the sum of a diagonal form and a residual, which represents the electronic interactions beyond the mean field included in the Fock operator,

$$H = \Sigma_s W_s a_s^{\dagger} a_s + H_{res}.$$

Use of this form for an overlapping basis gives the expression

$$F_{ss'} = W_s \delta_{ss'} + S_{ss'}(W_s + W_{s'}) + \Sigma_{s''} S_{ss''} W_{s''} S_{s''s'} + <[a_s, [H_{res}, a_{s'}^{\dagger}]\,]_+>$$

and one recognizes that the first two terms are the ones used by Hoffmann in his Extended Hückel Theory but for a factor $^7/_8$ in the second one. The third term is negative definite and is kept in the Energy Weighted Molecular Orbital model. The last term is neglected in the simplest cases.

An initial approximation to the electron propagator matrix $\mathbf{G}(E) = \{G_{ss'}(E)\}$ neglects the residual H_{res} and it holds then that

$$E\ G_{ss'}(E) = \delta_{ss'} + S_{ss'} + W_s G_{ss'}(E) + \Sigma_{s''} S_{ss''} W_{s''} G_{s''s'}(E)$$

or, in matrix form,

$$[E\mathbf{I} - (\mathbf{I} + \mathbf{S})\mathbf{W}]\ \mathbf{G}(E) = \mathbf{I} + \mathbf{S}.$$

Thus, it follows that

$$\mathbf{G}(\mathrm{E}) = [E(\mathbf{I} + \mathbf{S})^{-1} - \mathbf{W}]^{-1}$$

and one determines the molecular orbitals and their energies from the residues and poles of the matrix on the right.

Further properties of the model arise from interpretations based on mutually orthogonal and normalized atomic orbitals. The common Löwdin symmetrically orthogonalized basis gives

$$\mathbf{G}^{\mathbf{L}}(E) = (\mathbf{I} + \mathbf{S})^{-1/2}\mathbf{G}(E)(\mathbf{I} + \mathbf{S})^{-1/2} = [E\mathbf{I} - (\mathbf{I} + \mathbf{S})^{1/2}\mathbf{W}(\mathbf{I} + \mathbf{S})^{1/2}]^{-1}.$$

An energy weighted orthonormalization results in the simple expression

$$\mathbf{G}^{\mathbf{W}}(E) = \mathbf{A}\,\mathbf{G}(E)\mathbf{A}^{\dagger} = [E\mathbf{I} + \mathbf{k}(\mathbf{I} + \mathbf{S})\mathbf{k}]^{-1}$$
$$\mathbf{W} = -\,\mathbf{k}^2,\ \mathbf{A} = [\mathbf{k}(\mathbf{I} + \mathbf{S})\mathbf{k}]^{-1/2}\mathbf{k}.$$

It is assumed that the diagonal matrix $\mathbf{W}$ is negative definite and that $\mathbf{k}$ and the square root in the transformation matrix are chosen positive definite. The elements of $\mathbf{G}^{\mathbf{W}}(E)$ are closely related to the original basis since they are obtained by a process which is similar to Löwdin's with the property of being optimally close to initial ones. Accordingly, it is useful to derive populations and bond orders from its elements.

The transformation to an orthonormal basis offers the simple form for the Fock operator

$$F^{w}_{ss'} = -\,[\mathbf{k}(\mathbf{I} + \mathbf{S})\mathbf{k}]_{ss'} = W_s \delta_{ss'} - S_{ss'}\sqrt{W_s W_{s'}},$$

where the Ballhausen–Gray geometric mean appears as the appropriate off-diagonal form. A feature of the model examined here is that all molecular orbitals are bound with negative orbital energies and do not correspond to regular Hartree–Fock calculations where only occupied orbitals are bound normally for neutral systems. The model should not be thought of as an approximation to accurate calculations.

3 Hückel Model and Theory

Hückel theory concerns itself with planar organic systems. The basis is then limited to atomic p-orbitals that change sign upon reflection in the molecular plane, conventionally denoted as π-orbitals. There is then one orbital per atom and the orbitals are labeled accordingly. The effective dynamic matrix representative admits only couplings between neighboring atoms, so that

$$\mathbf{H}^{w} = -\,[\mathbf{k}(\mathbf{I}+\mathbf{S})\mathbf{k}]_{ss'} = \alpha_s\delta_{ss'} + \beta_{ss'}, \beta_{ss'} = 0,\ s \text{ and } s' \text{ not neighbors.}$$

Traditional notation is introduced here. A pattern of the bonds in the system is obtained when all β's are set equal to unity and the α's are omitted. The remaining matrix is called the topological matrix and has been the subject of studies in graph theory.

Poles and residues of the electron propagator $\mathbf{G}^{W}(E)$ provide the spin orbital energies and the molecular orbital amplitudes. The sum of the energies of the occupied spin orbitals is used as a measure of the total energy of the π-orbital system and Coulson observed that this could be expressed as a contour integral in the complex energy plane

$$E_\pi = \int_\Gamma Tr\ z\mathbf{G}^{W}(z)dz/2\pi i = \int_\Gamma Tr(\mathbf{I} - \mathbf{H}^{w}/z)^{-1}dz/2\pi i.$$

The contour surrounds the poles at the occupied levels. A rough estimate of the integrand may be obtained from the moment expansion of the inverse:

$$Tr(\mathbf{I} - \mathbf{H}^{w}/z)^{-1} = n(1 + \mu/z + Tr\ \mathbf{H}^{W2}/nz^2 - \cdots) \approx n(z-\mu)[(z-\mu)^2 - C\beta^2]^{-1},$$

where C is an average coordination number and β an average coupling parameter that generally is chosen with a negative energy value. Then it holds that

$$E_\pi \approx (n/2)(\mu + \beta\sqrt{C}).$$

The number of electrons in the system is $\partial E_\pi/\partial\mu \approx n/2$, while a measure of the mobile bond order is $(1/n)\partial E_\pi/\partial\beta \approx \sqrt{C}/2$. This value is close to the accurate one, 0.79, for the graphene sheet with a coordination number 3.

Several properties are accessible through Hückel theory. Electric and magnetic fields induce perturbations of the dynamic matrix. London introduced the effect of a magnetic field **B** through a phase factor in the β's,

$$\beta_{ss'} - > \beta_{ss'}\exp[-(i/2c)(\mathbf{r}_s \times \mathbf{r}_{s'}) \bullet \mathbf{B}],$$

so that a translation of the reference system occurs as a unitary transformation of the dynamic matrix. The position vectors of the orbital locations define the electric dipole operator representation and the diamagnetic term in the diagonal elements. Thus,

$$\alpha_s -> \alpha_s - \mathbf{E} \cdot \mathbf{r}_s + (\chi_s/2c^2)(\mathrm{B}_\pi^2 + 2\mathrm{B}_\sigma^2)$$

for the electric field **E** and a magnetic field with components B_π and B_σ perpendicular to and in the molecular plane, respectively. The atomic parameter χ_s is a measure of the size of the orbital.

The representative of the electric dipole moment operator is then the diagonal matrix

$$\mathbf{m} = -\ \mathrm{grad}_\mathbf{E}\ \mathbf{H}^W$$

while the magnetic dipole moment operator has the representation

$$\boldsymbol{\mu} = -\mathrm{grad}_\mathbf{B}\ \mathbf{H}^W.$$

This form is consistent with the expression for the electric dipole velocity operator

$$d\mathbf{m}/dt = -\ i[\mathbf{m}, \mathbf{H}^W]$$

and this is preferable to use when one considers properties of extended systems. Further perturbations arise from the part of the electronic system that is left dormant within Hückel's model and are considered later.

4 Crystal Field Model

Ballhausen's comment in his thesis about the lack of accurate theories for inorganic complexes came at a pivotal time and he established himself as an authority in the quest for advances. He could create a modern research environment at the new H. C. Ørsted institute under The University of Copenhagen in the early 1960s.

Presently, it will be a concern to review the basics of crystal field theory as a vehicle to understand the electronic features of transition metal atoms and ions in an octahedral environment. Thus is considered the limited basis of ten spinorbitals of the partially occupied atomic d-shell for the relevant transition metal. A particular choice of basis is made in order to obtain a convenient form for the spin–orbital interaction and to simplify the application of the point group symmetry. The e-type orbitals $d\sigma[2z^2 - x^2 - y^2]$ and $d\omega[x^2 - y^2]$ provide, together with spin factors, a basis for the four-dimensional irreducible representation U'. The Kramers pairs will be used:

$$\{u_1, u_2, u_3, u_4\} = \{d\sigma\alpha, id\sigma\beta, d\omega\alpha, id\omega\beta\}.$$

The t_2-type orbitals $d\xi$ [yz], $d\eta$ [zx] and $d\zeta$ [xy] with spin factors give rise to a six-dimensional reducible representation which resolves into the irreducible U' and E''. It is expedient to choose the set

$$\begin{aligned}&\{u_5, u_6, u_7, u_8\} = \{(d\eta + id\xi)\beta/2, (-id\eta - d\xi)\alpha/2,\\&(-2id\zeta\alpha - d\eta\beta + id\xi\beta)/\sqrt{6}, (-2d\zeta\beta + id\eta\alpha - d\xi\alpha)/\sqrt{6}\}\end{aligned}$$

for the four-dimensional representation and

$$\{u_9, u_{10}\} = \{(\delta\xi\alpha - id\eta\alpha\ d\zeta\beta)/\sqrt{3}, (id\xi\beta - d\eta\beta + id\zeta\alpha)/\sqrt{3}\}$$

for the E'' for the remaining irreducible one.

The basis offers a simple representation of the spin–orbit operator H_{so}, where the non-zero elements are:

$$\begin{aligned}&<u_s|H_{\text{so}}|u_s> = 0;\ s = 1, 2, 3, 4;\\&<u_s|H_{\text{so}}|u_{s+4}> = <u_{s+4}|H_{so}|u_s> = -\zeta_{so}\sqrt{6};\ s = 1, 2, 3, 4;\\&<u_s|H_{\text{so}}|u_s> = -\zeta_{so};\ s = 5, 6, 7, 8;\ <u_s|H_{so}|u_s> = 2\zeta_{so};\ s = 9, 10.\end{aligned}$$

Electron–electron interaction is significant in studies where spin–orbital degeneracy, or near degeneracy, is present. The atomic d-orbitals have a common radial factor and their 15 distinct products give rise to 120 density–density integrals. These are expressed in terms of three basic ones, F_0, F_2, and F_4 in the Slater–Condon formulation. The 100 spin–orbital densities are linear combination of the orbital ones and the 100 by 100 interaction integral matrix has a rank of 15 and is expressed by the Slater–Condon parameters.

The octahedral field V lifts the degeneracy of the atomic d-levels and it holds, in terms of the traditional Dq-parameter, that

$$\begin{aligned}&<u_s|V|u_s> = -6Dq;\ s = 1, 2, 3, 4;\\&<u_s|V|u_s> = 4Dq;\ s = 5, 6, 7, 8, 9, 10.\end{aligned}$$

Neglect of the spin–orbit coupling results in the splitting of the degenerate d-level into a fourfold degenerate e-level and a sixfold degenerate t_2-level. Inclusion of the spin–orbit term couples the e-levels with t_2-levels and gives two sets of fourfold degenerate levels of U' symmetry. An illustration is offered in the figure:

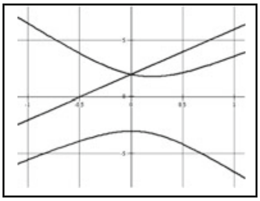

Eigenvalues of the one-electron perturbation matrix in units of the spin–orbit parameter ζ_{so} as functions of the crystal field parameter Dq. The straight line is the twofold E''-level while the curved ones are fourfold and of U' symmetry. Positive and negative values of Dq are expected for sixfold and eightfold coordination, respectively.

Explicit account of the electron interaction within a self-consistent approach modifies the interpretation of the parameters. Slater's notion of the average of configurations and fractional occupation will be consistently applied in the grand canonical ensemble form. The one-particle reduced density matrix retains the symmetry of the crystal field and spin–orbit matrices, thus

$$<a_s^\dagger a_s> = \gamma_{11},\ s = 1,2,3,4;\ <a_s^\dagger a_s> = \gamma_{55}, s = 5,6,7,8;\ <a_s^\dagger a_s> = \gamma_{99},\ s = 9,10;$$
$$<a_{s+4}^\dagger a_s> = <a_s^\dagger a_{s+4}>^* = \gamma_{15},\ s = 1,2,3,4.$$

while all other elements vanish.

The expectation value of the electron–electron interaction,

$$<H_{int}> = \Sigma<a_s^\dagger a_t><a_{s'}^\dagger a_{t'}>[(st|s't') - (st'|s't)]/2 = \Sigma<a_s^\dagger a_t> M_{\mathrm{st}}/2,$$

defines the Coulomb and exchange terms in the Fock matrix, $\{M_{st}\}$. They are linear in the Slater–Condon parameters as follows:

$$\begin{aligned}
M_{11} &= (3\gamma_{11}+4\gamma_{55}+2\gamma_{99})F_0 - (8\gamma_{11}+4\gamma_{55}+2\gamma_{99})F_2+(33\gamma_{11} - 106\gamma_{55} - 53\gamma_{99})F_4\\
M_{15} &= (\gamma_{99}\sqrt{}6\gamma_{55}\sqrt{}6)F_2+(35\gamma_{15}+35\gamma_{51}+5\gamma_{55}\sqrt{}6 - 5\gamma_{99}\sqrt{}6)F_4\\
M_{55} &= (4\gamma_{11}+3\gamma_{55}+2\gamma_{99})F_0 - (4\gamma_{11}+\gamma_{15}\sqrt{}6+\gamma_{51}\sqrt{}6 + 5\gamma_{55}+5\gamma_{99})F_2 -\\
&\quad (106\gamma_{11} - 5\gamma_{15}\sqrt{}6 - 5\gamma_{51}\sqrt{}6 + 16\gamma_{55}/3 + 44\gamma_{99}/3)F_4\\
M_{99} &= (4\gamma_{11}+4\gamma_{55}+\gamma_{99})F_0 - (4\gamma_{11} - 2\gamma_{15}\sqrt{}6 - 2\gamma_{51}\sqrt{}6 + 10\gamma_{55})F_2 -\\
&\quad (106\gamma_{11}+10\gamma_{15}\sqrt{}6 + 10\gamma_{51}\sqrt{}6 + 88\gamma_{55}/3 - 28\gamma_{99}/3)F_4.
\end{aligned}$$

It holds that $F_0 \gg F_2 > F_4$ and that the dominance of the spherical term shifts the levels with regard to their populations. The spin–orbit parameter ζ_{so} is comparable in size to F_4 and enters with the off-diagonal elements M_{15} and M_{51} as well as in the diagonal ones with M_{55} and M_{99}.

A vanishing crystal field, $Dq = 0$, gives back the free atom or ion levels appearing for $j = 2 \pm ½$. This implies that the self-consistent density matrix is diagonal and proportional to the unit matrix:

$$<a_j^\dagger a_k> = \delta_{jk}\, q/10.$$

The number of electrons in the system is denoted by q. This conclusion depends on the assumption that the radial factor of the atomic orbitals is the same and will be void when a more general model is invoked.

The energy expectation value for the crystal field model in the ensemble form is supplemented by the subsidiary conditions that diagonal elements of the density matrix are between 0 and 1, that their sum equals q, and that the matrix is nonnegative. A variational form is then

$$\begin{aligned} L = {} & 2\gamma_{11}M_{11}+2\gamma_{15}M_{51}+2\gamma_{51}M_{15}+2\gamma_{55}M_{55}+\gamma_{99}M_{99} - Dq(24\gamma_{11} - 16\gamma_{55} - 8\gamma_{99}) \\ & -4\zeta_{\mathrm{so}}(\gamma_{55} - \gamma_{99}+2\gamma_{15}\surd 6+2\gamma_{51}\surd 6) - \mu(4\gamma_{11}+4\gamma_{55}+2\gamma_{99}) \end{aligned}$$

and it is stationary when

$$\begin{aligned} \delta L = {} & 4\delta\gamma_{11}(M_{11} - 6Dq - \mu) + 4\delta\gamma_{15}(M_{51} - \zeta_{so}\surd 6) + 4\delta\gamma_{51}(M_{15} - \zeta_{\mathrm{so}}\surd 6) \\ & + 4\delta\gamma_{55}(M_{55} + 4Dq - \mu - \zeta_{\mathrm{so}}) + 2\delta\gamma_{99}(M_{99} + 4Dq - \mu + 2\zeta_{so}) \end{aligned}$$

vanishes. A satisfactory solution for the density matrix elements is resolved from the linear equation system from $\delta L = 0$ with the acceptable variations of the density matrix. These are chosen here from the forms

$$\begin{aligned} &\gamma_{11} = q/10 + q_u + q_\zeta \cos \omega;\ \gamma_{15} = \gamma_{51} = q_\zeta \sin \omega; \\ &\gamma_{55} = q/10 + q_u - q_\zeta \cos \omega;\ \gamma_{99} = q/10 - 4q_u; \end{aligned}$$

where the variable q_u allows for a larger occupation in the u-type spin orbitals and the parameter q_ζ differentiates the occupation of the two canonical levels of u-type. The angular variable ω provides the self-consistent form of the Fock matrix. It is determined from the equation

$$\sin \omega(M_{55} - M_{11}+10Dq - \zeta_{\mathrm{so}}) + \cos \omega\,(M_{15} + M_{51} - 2\zeta_{\mathrm{so}}\surd 6) = 0.$$

The parameter q_u enters as an adjustment to the spin–orbit and crystal field values,

$$\zeta_{eff} = \zeta_{so}+5q_u(F_2 - 5F_4),\ Dq_{eff} = Dq + q_u(F_2 - 50F_4/3),$$

so that the equation can be rewritten as

$$\begin{aligned} &(\zeta_{eff} - 10Dq_{eff})\sin \omega + 2\zeta_{eff}\surd 6\cos \omega = q_\zeta[(F_0+5F_2/2 - 299F_4/6)\sin 2\omega \\ &+ 2\surd 6(F_2 - 5F_4)\cos 2\omega]. \end{aligned}$$

This transcendental equation is equivalent to a quartic in the variable tan(ω/2). The large value F_0 dominates the right hand side and a nonzero value q_ζ leads to a small value ω.

It is neither feasible nor illustrative to detail a general solution of the self-consistency equations. The five input parameters in the crystal field model, Dq, ζ_{so}, F_0, F_2, and F_4, determine the five independent density matrix elements when the choice of “chemical potential” μ and the relative population of the molecular spin orbital energy levels are chosen. It is characteristic for the transition metal complexes that the electronic ground state is an open shell, e.g. a high spin state, and the role of the calculations above is to provide a suitable basis for the description of the manifold of states. The grand canonical density matrix preserves the octahedral symmetry and the influence on the spin orbital spectrum from the electronic interactions as appearing through the exchange terms.

Ballhausen suggested that the parameter values, in the iron series, can be set so that $F_2 = 10F_4 = 20\zeta_{\mathrm{so}} \approx 1{,}000\ \mathrm{cm}^{-1}$ or some 6 milliHartrees (mH). The large parameter F_0 is put to 600 mH here. Its presence in the self-consistency equation above is such that a differentiation of the occupation of the u-type spin orbitals increases their splitting in proportion to the magnitude of the occupation number difference. The more occupied set will get a lower spin orbital energy while the lesser occupied ones will rise. This is the effect of the occurrence, in the exchange terms, of the self-interaction of the spin orbital density. An approximate solution which departs from a diagonal form of terms proportional to q_ζ in the Fock matrix has the diagonal elements, less a common constant,

Symmetry	*Spinorbital energy in mH*
U'	$0.031\zeta_{so} - 6Dq - 540.1q_u - 540.6q_\zeta$
E''	$2\zeta_{so} + 4Dq + 2212q_u - 10.37q_\zeta$
U'	$-1.031\zeta_{so} + 4Dq - 566.1q_u + 545.8q_\zeta$

and it is evident that the occupancy is an important element in the determination of the canonical spin orbitals for the continued analysis of the many-particle states. It may be feasible to determine separate radial factors of the basis functions from atomic calculations. The ensemble approach offers a means for designing a basis for a range of states close to the ground state as envisaged by Slater and equal occupation will retain the near degeneracy of the conventional model.

The examination of the role of the two-electron term in the Hamiltonian shows that elements of the many-electron basis with occupied Kramers pairs of spin orbitals generally will have a larger energy than others and that the ground state configuration conforms with Hund's rule. Kramers pairs are related to the Racah seniority approximate quantum number. The rotationally invariant geminal creator

$$g_o^\dagger = (a_1^\dagger a_2^\dagger + a_3^\dagger a_4^\dagger + a_5^\dagger a_6^\dagger + a_7^\dagger a_8^\dagger + a_9^\dagger a_{10}^\dagger)/\sqrt{5}$$

generates, from the formal vacuum, the two-electron ${}^1S$ state of the d^2 configuration. A state which is annihilated by g_0 is assigned a seniority number equal to the particle number of the state and will have a lower energy than other states of the same number of electrons.

Electron pair creators provide a representation for the electron interactions of the form

$$H_{\mathrm{int}} = \Sigma(H_{\mathrm{int}})_j g_j^\dagger g_j,$$

where the elements of the term energies appear. The pair creators generate the corresponding states in the relevant coupling. A d-shell, as treated here, has five distinct $(H_{int})_j$ while there are 45 pair operators. The separable form of the interaction is more readily exhibited in terms of density operators. Three parameters determine three sets of terms, F_0 enters only in conjunction with the number operator and is relevant only for positioning states of different number of particles, F_2 associates with d-type densities, while F_4 comes in with g-type and will have a small influence on the separation of the terms. This leaves a reduced form of the electron interaction

$$H_{int} = F_2(L_\sigma^\dagger L_\sigma + L_\omega^\dagger L_\omega + L_\xi^\dagger L_\xi + L_\eta^\dagger L_\eta + L_\zeta^\dagger L_\zeta),$$

where each symmetry species has a Hermitian operator and a linear term in the number operator is neglected. No closed algebra is offered by the density operators.

Substantial advantages are derived from the separable form of the electron interaction. Seven one-particle Hermitian matrices are required for the generation of the Hamiltonian in the present, reduced form. The matrices will be sparse and demand modest storage. Savings in storage become essential with increasing basis sets but even for the present case it is notable that seven 10-by-10 matrices has the data for the full 2^{10}-by-2^{10} Fock space Hamiltonian. Symmetry and number conservation does reduce the number of non-vanishing matrix elements.

5 Towards Band Theory

Transition metals are important materials with intriguing properties and they have been studied with ever improved methods. A major difficulty is posed by the standard one-electron models where the tight-binding model seems appropriate for the narrow, so-called d-bands while “near-plane-wave” crystal orbitals are adequate for the conduction bands. Canonical Hartree–Fock solutions are awkward starting points for the description of magnetic structures and the use of spin-polarized versions destroys basic symmetry properties.

Hubbard initiated a treatment where some electron interaction is included in a localized description with the aim to deal with magnetic features. His model has become a popular and widely used vehicle for the study of electron correlation. It is based on the reduction of the electron repulsion terms to intraatomic ones and to use only the form with the largest pair parameter, $(H_{int})_{A0}\ g_{A0}{}^\dagger g_{A0}$, for each atom A. Interatomic coupling is represented by a one-particle operator which moves particles from one atom to another, so-called hopping terms. The Hamiltonian is then

$$H_{tot} = \Sigma\, h_{Aj,Bk}\, a_{Aj}^\dagger\, a_{Bk} + \Sigma U_{A0}\ g_{A0}^\dagger\ g_{A0}$$

and the equation of motion becomes

$$[a_{Aj},\, H_{\text{tot}}] = \Sigma h_{Aj,Bk} a_{Bk} \pm U_{A0}\ \mathrm{K}(a_{Aj}^{\dagger}) g_{A0}/\sqrt{5}$$

with K as the operator for the Kramers conjugation. The choice of sign depends on the definition of the geminal creator. Each elementary annihilator or creator is then associated with a composite operator derived from the same atom and the basic operator manifold is doubled in size.

The additional operators, that will be denoted $b_{Aj} = [a_{Aj},\, g_{A0}{}^{\dagger}]\ g_{A0}$, have the same local symmetry features as their partners, a_{Aj}, and they introduce a coupling between the removal or addition of a particle with an excitation of the system. It is a very limited set of such processes, only intraatomic excitations occur. None the less one gains insight on electron correlation. Lattice symmetry applies also to the additional operators and there will be, for a d-band, a 20-by-20 secular problem for each point in the Brillouin zone. Neglect of the spin–orbit coupling reduces these to 10-by-10.

An important consequence of the inclusion of an intraatomic repulsion term is the possibility of modeling magnetic features in partially filled, narrow bands. Some elements of the two-particle density matrix, for instance $<a_{Aj}^{\dagger}\, b_{Aj'}>$, derive from the propagator matrix and give an indication of the local spin features. The use of the additional operators requires some further algebra. The metric measures

$$<[b_{Aj'}, a_{Aj}^{\dagger}]_{+}> = <[a_{Aj'}, g_{A0}^{\dagger}][g_{A0}, a_{Aj}^{\dagger}]>$$

$$<[b_{Aj'}, b_{Aj}^{\dagger}]_{+}> = \delta_{jj'} <g_{A0}^{\dagger}\, g_{A0}>/5 + <[a_{Aj'}, g_{A0}^{\dagger}][g_{A0}, g_{A0}^{\dagger}][g_{A0}, a_{Aj}]>$$

are reasonably straightforward while the dynamical ones like

$$<[[b_{Aj'}, g_{A0}^{\dagger} g_{A0}], b_{Aj}^{\dagger}]_{+}> = <[b_{Aj'},\, [g_{A0}^{\dagger} g_{A0}, b_{Aj}^{\dagger}]]_{+}> + <[[b_{Aj'}, b_{Aj}^{\dagger}]_{+}, g_{A0}^{\dagger}\, g_{A0}],>$$

need attention. The last term above should vanish for a proper ground state ensemble in order for the dynamical matrix to be Hermitian.

Hubbard's original study involved only one orbital per center and the isolated atom propagator is then fully determined in the operator manifold $\{a_{Aj},\, b_{Aj}\}$ and their adjoints. It does then differentiate between the poles for removing and adding electrons. This feature carries over to the band theory approximation where the ground state for the situation of one electron per atom leads to, for small couplings between atoms, an antiferromagnetic Heisenberg model. Metallic chromium exhibits an antiferromagnetic ordering and appears to have the half-filled band population in the d-orbitals.

Spin polarized, single-particle models can simulate antiferromagnetic systems at the expense of the sacrifice of spatial symmetry. This device is employed in generalizations of density functional theory but is often unsatisfactory for the description of complex magnetic structures in compounds of the rare earth metals. The Heisenberg model is then more adequate.

6 Recapitulation

Ballhausen pioneered the modern study of the electronic structures of inorganic complexes and based his work on accurate numerical calculations on clearly defined orbital models. The present review focuses on the formal aspects of molecular orbital theory in terms of the Green function or propagator formulation. Some illustrations of the consistency requirements for operator representations in limited basis set relate alternative interatomic interactions in the Hückel model and its generalizations. The Ballhausen–Gray and the Wolfsberg–Helmholz couplings appear as complementary forms through an energy weighted orthogonalization procedure.

Electron–electron interactions determine the detailed state formation for a partially filled shell from nearly degenerate atomic d-orbitals. The emphasis here is to demonstrate the nature of the grand canonical ensemble Hartree–Fock which allows partial occupancy of spin orbitals while maintaining point group or spherical symmetry. The analysis is set in the proper spin orbital basis with spin–orbit coupling as well as octahedral symmetry accounted for in the canonical Hartree–Fock solutions. Explicit expressions for the separable representation of the electron interaction are offered to exemplify the available reductions.

An alternative view of the electron interactions is to keep only the term that penalizes the double occupancy of atomic orbitals such as was considered by Hubbard in his original paper on narrow energy bands. This notion has generated a considerable body of literature and insight into electronic correlation. The d-orbitals of the valence shell of the transition metals give rise to narrow energy bands and the consideration of the largest pair interaction indicates that a simple reduction would attribute an energy penalty on the presence of atomic singlet paired orbitals in the state. The ensuing operator analysis of the equations-of-motion is somewhat more involved than in the original Hubbard model but offers the option to go beyond the single-particle models.

7 Literature

Second quantization was frowned upon by many 50 years ago, see e.g. Slater's review [1] of Judd's book. "This stylish technique," Slater *ibid.,* has gained acceptance and the formulations from *Propagators in Quantum Chemistry* [2] have evolved to the forms presented here. Ballhausen and Gray [3] offered their interatomic coupling form as an alternative to the choice by Wolfsberg and Helmholz [4]. It was London who introduced the field dependent couplings in the

Hückel model [5]. Hubbard presented the model that now carries his name in a paper [6] on narrow energy bands.

Acknowledgments Courtesy appointments at the University of Florida and the University of Utah are gratefully and proudly acknowledged and the continued acceptance by the University of Aarhus is much valued by this author.

References

1. Slater JC (1968) Am J Phys 36:69
2. Linderberg J, Ohrn Y (1973) Propagators in quantum chemistry, Academic Press, London, 2nd edn. Wiley, Hoboken, New Jersey, 2004
3. Ballhausen CJ, Gray HB (1962) Inorg Chem 1:111
4. Wolfsberg M, Helmholz L (1952) J Chem Phys 20:837
5. London F (1937) J Phys Radium 8:397
6. Hubbard J (1963) Proc Roy Soc (London) A276:238

Struct Bond (2012) 143: 53–100
DOI: 10.1007/430_2011_53

Sturmians and Generalized Sturmians in Quantum Theory

John Scales Avery and James Emil Avery

Abstract The theory of Sturmians and generalized Sturmians is reviewed. It is shown that when generalized Sturmians are used as basis functions, calculations on the spectra and physical properties of few-electron atoms can be performed with great ease and good accuracy. The use of many-center Coulomb Sturmians as basis functions in calculations on N-electron molecules is also discussed. Basis sets of this type are shown to have many advantages over other types of ETO's, especially the property of automatic scaling.

Keywords Exponential-type orbitals · Generalized Sturmians · Hyperspherical harmonics · Interelectron repulsion integrals · Isoenergetic configurations · Momentum space · Quantum theory · Sturmians

Contents

J.S. Avery (✉)
Department of Chemistry, University of Copenhagen, Snebærhaven 42, Albertslund, 2620 Copenhagen, Denmark
e-mail: avery.john.s@gmail.com

J.E. Avery
Department of Computer Science, University of Copenhagen (DIKU), Copenhagen, Denmark

Centre for Theoretical Chemistry and Physics, NZIAS, Massey University, Auckland, New Zealand
e-mail: avery@diku.dk

1 Dedication and Historical Remarks

This chapter is dedicated to the memory of Professor Carl Johan Ballhausen, one of the great pioneers of quantum chemistry. His laboratory was a splendid place to work.

The history of quantum chemistry is very closely tied to the history of computation, and in order to place Carl Ballhausen's work in context, it is relevant to review the enormously rapid development of computing during the twentieth century. The fundamental equations governing the physical properties of matter, while deceptively simple to write down, are notoriously difficult to solve. Only the simplest problems, for example the harmonic oscillator and the problem of a single electron moving in the field of a fixed nucleus, can be solved exactly. However, no solutions to the wave equations for interacting many-particle systems such as atoms or molecules are known, and it is quite possible that no simple solutions exist. In 1929, P.A.M. Dirac summarized the position since the discovery of quantum theory with his famous remark:

> "The underlying physical laws necessary for the mathematical theory of a large part of physics and the whole of chemistry are thus completely known, and the difficulty is only that the exact application of these laws leads to equations much too complicated to be soluble. It therefore becomes desirable that approximate practical methods of applying quantum mechanics should be developed, which can lead to an explanation of the main features of complex atomic systems without too much computation."

The Schrödinger equation for even a single N-electron atom is a partial differential equation with $3N$ variables, and to make matters worse, the interelectron interaction causes the solutions to be true $3N$-dimensional functions that cannot simply be broken down into smaller constituent parts. Nevertheless, despite the staggering complexity of even small-sized systems, quantum theory has yielded great success in calculating useful properties of complex systems and in producing insight into the fundamental workings of chemistry. However, this necessitated – and still necessitates – heavy handed approximations.

In the 1930s Douglas Hartree and his father William Hartree used a mechanical analog computer to explore the idea that an electron in an atom moves partly in the attractive potential of the nucleus and partly in an averaged repulsive potential due to all the other electrons. Later, V. Fock added to the Hartrees' model an exchange term due to the effects of the antisymmetry of the many-electron wave function. The Hartree–Fock approximation is still a basic tool of quantum chemistry.

In 1927, Heitler and London used valence bond theory to treat the H_2 molecule; but to treat larger molecules, further simplifications were needed. In 1931, Erich Hückel introduced an extremely simple approximation which could be used to treat the π-electrons in flat organic molecules such as benzene, napthaline, and so on. This approximation yielded matrices to be diagonalized, and it is a measure of the state of computers at that time to remember that during World War II, Alberte Pullman sat in a basement room in Paris diagonalizing Hückel matrices with a mechanical desk calculator, while her husband-to-be Bernard drove a tank with the Free French Forces in North Africa. Alberte's hand-work led to the publication of the Pullmans' early book "Quantum Biochemistry."

In the 1950s and 1960s, digital computers became available for calculations in quantum chemistry, but by today's standards, both the computers and the programming languages were extremely primitive. C.C.J. Roothaan devised a computer-adapted matrix form for the Hartree–Fock equations, but his early work with Enrico Clementi on the wave functions of atoms had to be done in a primitive form of machine language.

In England, quantum chemists used a machine called "Mercury." The name was derived from a mercury delay line down which sound waves passed. This delay line was used as a short-term memory device. Mercury was a machine that antedated transistors, and its many-thousand vacuum tubes had to be cooled. Often the cooling system failed, and often one of the vacuum tubes burned out, so there were only short periods of uninterrupted running time between stops for repairs. Machine errors were also common.

By the middle of the 1960s, computers had improved, but they were still incredibly slow by today's standards. Therefore, the quantum chemistry of the time was dominated by semiempirical methods, such as the Pople–Pariser–Parr Method, the Wolfsberg–Helmholtz Method, and the Extended Hückel Method.

In the meantime, Carl Ballhausen had been studying quantum theory with W. Moffitt at Harvard. He returned to Copenhagen determined to introduce the new quantum ideas into Danish chemistry. In 1962, he published his influential book, "Introduction to Ligand Field Theory," [1] which dealt with the quantum theory of transition metal ions surrounded by ligands. The ligands were groups involving less heavy atoms such as carbon, hydrogen, and oxygen. Ballhausen's book built on the previous work of Henri Bequerel, who had proposed the idea that heavy metal ions in compounds are largely unaltered by their environment, and by Hans Bethe, Robert Schlapp, and William Penney, who had treated the electrostatic effects of ligands surrounding a heavy metal ion by means of group theory.

Ballhausen's book extended this model by including the effects of hybridization and charge transfer between the metal and the surrounding ligands. But because of the limitations of the computers of the time, the theories put forward in the book were semiempirical ones.

Carl Ballhausen spent many years as Professor of Physical Chemistry at the University of Copenhagen. Besides the theoretical work in his department [2–4], which attracted distinguished visitors from many parts of the world, there was an experimental laboratory with splendid equipment for vacuum ultraviolet spectroscopy, and an X-ray crystallographic laboratory, both of which attracted many visitors [5].

During Carl Ballhausen's long tenure as Professor, computers continued to develop at an astonishing rate, and before his retirement it became possible to dispense with the empirical parameters that had for so long been a feature of quantum chemistry. The words ab initio came to be used to characterize the new quantum chemistry in which no empirical parameters appeared, and where everything was calculated from first principles: "from the beginning." Carl Ballhausen's first Ph.D. student, Jens Peder Dahl, became a pioneer in the application of ab initio methods to compounds containing transition metal ions [6, 7].

The new methods of mainstream quantum chemistry were built on the use of Cartesian Gaussian basis functions of the form $Nx^n\, y^{n'}\, z^{n''}\, \mathrm{e}^{-\alpha r^2}$. Gaussian basis functions had been introduced by S.F. Boys and Roy McWeeny, who used the fact that the product of two Cartesian Gaussians centered at two different points is a small linear combination of Cartesian Gaussians centered at an intermediate point. This property allows many-center interelectron repulsion integrals to be evaluated with great ease and speed, making possible molecular calculations that were until then far out of reach. Because of this, an entire technology has been formed around Gaussian orbitals, and mainstream quantum chemistry now relies almost exclusively on Gaussians. However, Gaussian basis functions have serious drawbacks, since very many of them are needed to approximate the molecular orbitals, and since the cusp at the nucleus is never adequately represented. Furthermore, Gaussian basis functions cannot accurately represent the exponential decay of the orbitals at large distances from the nuclei. Thus, while the mainstream effort of quantum chemistry today follows the path of Gaussian technology, there exists a small group of researchers who struggle with the difficult mathematical problems involved in using exponential-type orbitals (ETO's) as basis functions [8–15]. We hope that the present paper will contribute to the theory needed for the replacement of Gaussian basis functions by ETOs.

2 Coulomb Sturmians

One of the very early triumphs of quantum theory was the exact solution of the wave equation for hydrogenlike atoms. It was therefore natural to try to use hydrogenlike orbitals to build up solutions to the Hartree–Fock equations for many-electron atoms. It was soon realized, however, that without the inclusion of the continuum, hydrogen-like orbitals do not form a complete set; and inclusion of the continuum proved to be prohibitively difficult. This difficulty led Høloien, Shull and Löwdin [16] to introduce basis sets where the radial function was a polynomial in r multiplied by the factor e^{-kr}, where k is a constant whose value is kept the same for all members of the basis set. These basis sets proved to have the desired completeness property without the inclusion of the continuum. Later Rotenberg [17, 18] gave the name *Sturmians* to basis sets of this type, to emphasize their connection with Sturm–Liouville theory. *Coulomb Sturmians* [19] are Sturmian basis sets of a particular form: They are solutions to the one-electron wave equation

$$\left[-\frac{1}{2}\nabla^2 - \frac{nk}{r} + \frac{1}{2}k^2\right]\chi_{nlm}(\mathbf{x}) = 0. \tag{1}$$

The reader will recognize that this is just the wave equation obeyed by the familiar hydrogenlike orbitals, except that Z/n has been replaced by the constant k. Thus, if we start with a hydrogenlike orbital and replace Z/n everywhere by the constant k, we will have generated a set of Coulomb Sturmians. They have the form

$$\chi_{nlm}(\mathbf{x}) = R_{nl}(r)Y_{lm}(\theta,\phi), \tag{2}$$

where the radial functions are given by

$$R_{nl}(r) = \mathcal{N}_{nl}(2kr)^l\, e^{-kr}F(l+1-n|2l+2|2kr) \tag{3}$$

with

$$\mathcal{N}_{nl} = \frac{2k^{3/2}}{(2l+1)!}\sqrt{\frac{(l+n)!}{n(n-l-1)!}} \tag{4}$$

and

$$F(a|b|x) \equiv \sum_{j=0}^{\infty}\frac{a^{\bar{j}}}{j!\,b^{\bar{j}}}x^j = 1 + \frac{a}{b}x + \frac{a(a+1)}{2b(b+1)}x^2 + \cdots \tag{5}$$

The first few Coulomb Sturmian radial functions are

$$\begin{aligned} R_{1,0}(r) &= 2k^{3/2}e^{-kr}, \\ R_{2,0}(r) &= 2k^{3/2}(1-kr)e^{-kr}, \\ R_{2,1}(r) &= \frac{2k^{3/2}}{\sqrt{3}}kr\, e^{-kr}. \end{aligned} \tag{6}$$

The reader may verify that these become the familiar hydrogenlike orbitals if k is replaced by Z/n, where Z is the nuclear charge and n is the principal quantum number. It can be shown [19] that the Coulomb Sturmians obey a set of potential-weighted orthonormality relations of the form:

$$\int d^3x\, \chi^*_{n'l'm'}(\mathbf{x})\frac{1}{r}\chi_{nlm}(\mathbf{x}) = \frac{k}{n}\delta_{n'n}\delta_{l'l}\delta_{m'm}. \tag{7}$$

A Coulomb Sturmian basis set is isoenergetic. All the members of the set correspond to the energy

$$\varepsilon = -\frac{1}{2}k^2. \tag{8}$$

The potential in the wave equation obeyed by the members of the basis set is especially weighted so that all the basis functions will correspond to this energy. We can rewrite (1) in the form

$$\left[-\frac{1}{2}\nabla^2 - \beta_n\frac{Z}{r} + \frac{1}{2}k^2\right]\chi_{nlm}(\mathbf{x}) = 0, \tag{9}$$

where the weighting factor $\beta_n = nk/Z$ is especially chosen in such a way as to make all the members of the basis set correspond to the energy $-k^2/2$. Thus we have here an example of what has been called the *Conjugate eigenvalue problem.* The eigenvalue is no longer the energy, as it is in the Hamiltonian formulation. The eigenvalue is instead the value of the weighting factor needed to make the basis set isoenergetic.

3 Generalized Sturmians and Many-Particle Problems

In a pioneering 1968 study, [20, 21], Osvaldo Goscinski generalized the concept of Sturmians to many-electron wave equations of the form

$$\left[-\frac{1}{2}\nabla + \beta_\nu V_0(\mathbf{x}) - E_k\right]\Phi_\nu(\mathbf{x}) = 0. \tag{10}$$

Here,

$$\nabla \equiv \sum_{j=1}^{N}\frac{1}{m_j}\nabla_j^2. \tag{11}$$

In the case of equal masses, this becomes

$$\nabla \equiv \sum_{j=1}^{d} \frac{\partial^2}{\partial x_j^2} \tag{12}$$

with

$$\mathbf{x} = (x_1, x_2, ..., x_d). \tag{13}$$

E_κ is the same for all the members of a generalized Sturmian basis set, while the weighting factor β_ν is chosen in such a way as to make all the members of the basis set isoenergetic. Generalized Sturmian basis sets can be shown to obey the following orthonormality relation [22, 23]:

$$\int \mathrm{d}x \; \Phi^*_{\nu'}(\mathbf{x}) V_0(\mathbf{x}) \, \Phi_\nu(\mathbf{x}) = \delta_{\nu',\nu} \frac{2E_\kappa}{\beta_\nu}. \tag{14}$$

Unfortunately, Goscinski's pioneering 1968 paper was only published as an internal report of the Uppsala University Quantum Chemistry Group, and it did not reach a wider audience until much later.

3.1 Sturmian Basis Sets and Sobolev Spaces

The orthonormality relations for generalized Sturmian basis functions in direct space and reciprocal space can be written in the form [22–24]

$$\int \mathrm{d}x \, \Phi^*_{\nu'}(\mathbf{x}) \left(\frac{-\nabla + p_\kappa^2}{2p_\kappa^2} \right) \Phi_\nu(\mathbf{x}) = \delta_{\nu',\nu} \tag{15}$$

and

$$\int \mathrm{d}p \, \Phi^{t*}_{\nu'}(\mathbf{p}) \left(\frac{p^2 + p_\kappa^2}{2p_\kappa^2} \right) \; \Phi^t_\nu(\mathbf{p}) = \delta_{\nu',\nu}. \tag{16}$$

where $p_\kappa^2 \equiv -2E_\kappa$. Generalized Sturmians thus have orthonormality relations appropriate for the Sobolev space H^1 $(\mathbb{R}^d)$.

3.2 Use of Generalized Sturmian Basis Sets to Solve the Many-Particle Schrödinger Equation

Now suppose that we wish to solve the many-particle Schrödinger equation

$$\left[-\frac{1}{2}\nabla + V(\mathbf{x}) - E_\kappa \right] \Psi_\kappa(\mathbf{x}) = 0. \tag{17}$$

If we are in possession of solutions to the approximate Schrödinger equation (10), we can represent the wave function of a state by an expansion of the form

$$\Psi_\kappa(\mathbf{x}) = \sum_\nu \Phi_\nu(\mathbf{x})\, B_{\nu,\kappa}. \tag{18}$$

Substituting this expansion into (17), we obtain [22, 23]

$$\begin{aligned}\sum_\nu \left[-\frac{1}{2}\nabla + V(\mathbf{x}) - E_\kappa\right] \Phi_\nu\, (\mathbf{x}) B_{\nu,\kappa} \\ = \sum_\nu \left[V(\mathbf{x}) - \beta_\nu V_0(\mathbf{x})\right] \Phi_\nu(\mathbf{x})\, B_{\nu,\kappa} = 0\end{aligned} \tag{19}$$

where we have used the fact that all of the basis functions $\Phi_\nu\,(\mathbf{x})$ obey (10). Multiplying from the left by a conjugate basis function and integrating over all the coordinates, we obtain the generalized Sturmian secular equation

$$\sum_\nu \int \mathrm{d}x\, \Phi^*_{\nu'}(\mathbf{x})\ \left[V(\mathbf{x}) - \beta_\nu V_0(\mathbf{x})\right]\ \Phi_\nu(\mathbf{x})\, B_{\nu,\kappa} = 0. \tag{20}$$

If we introduce the notation [22, 23]

$$T_{\nu',\nu} \equiv -\frac{1}{p_\kappa} \int \mathrm{d}x\, \Phi^*_{\nu'}(\mathbf{x})\, V(\mathbf{x})\ \Phi_\nu(\mathbf{x}) \tag{21}$$

and

$$p_\kappa \equiv \sqrt{-2E_\kappa} \tag{22}$$

and if we make use of the potential-weighted orthonormality relation (14), we can rewrite (20) in the form

$$\sum_\nu \left[T_{\nu',\nu} - p_\kappa\, \delta_{\nu',\nu}\right] B_{\nu,\kappa} = 0. \tag{23}$$

The generalized Sturmian secular equation (23) has several remarkable features:

- The kinetic energy term has disappeared.
- The matrix representing the approximate potential $V_0(\mathbf{x})$ is diagonal.
- The roots of the secular equations are not energies, but values of the scaling parameter p_κ, from which the energy can be obtained through the relationship $E_\kappa = -p_\kappa^2/2$.
- For Coulomb potentials, the matrix $T_{\nu',\nu}$ is energy independent.
- Because of the scaling factor p_κ, which is different for each state, the Sturmian basis functions adjust in scale automatically: For tightly bound states they are contracted, while for highly excited states they are diffuse.

4 Goscinskian Configurations

In solving the many-particle Schrödinger equation, it is desirable to choose the approximate potential $V_0(\mathbf{x})$ to be as close as possible to the actual potential $V(\mathbf{x})$, since this leads to rapid convergence of the expansion (18). Goscinski showed [20, 21] that for atoms, the approximate Schrödinger equation (10) can be solved exactly provided that $V_0(\mathbf{x})$ is chosen to be the attractive Coulomb potential of the bare atomic nucleus:

$$V_0(\mathbf{x}) = -\sum_{i=1}^{N} \frac{Z}{r_i}. \tag{24}$$

He showed that (10) will then be satisfied exactly by a Slater determinant of the form

$$\Phi_\nu(\mathbf{x}) = |\chi_\mu \, \chi_{\mu'} \, \chi_{\mu''} \ldots| \equiv \frac{1}{\sqrt{N!}} \begin{vmatrix} \chi_\mu(1) & \chi_{\mu'}(1) & \chi_{\mu''}(1) & \cdots \\ \chi_\mu(2) & \chi_{\mu'}(2) & \chi_{\mu''}(2) & \cdots \\ \chi_\mu(3) & \chi_{\mu'}(3) & \chi_{\mu''}(3) & \cdots \\ \vdots & \vdots & \vdots & \end{vmatrix}, \tag{25}$$

where the spin-orbitals χ_μ that appear in the Slater determinant are the familiar hydrogen-like spin-orbitals with an effective nuclear charge given by

$$Q_\nu = \beta_\nu Z = \left(\frac{-2E_\kappa}{\frac{1}{n^2} + \frac{1}{n'^2} + \frac{1}{n''^2} + \cdots} \right)^{1/2}. \tag{26}$$

In other words, the radial parts of the spin orbitals that appear in the Slater determinant are

$$\begin{aligned} R_{1,0}(r) &= 2Q_\nu^{3/2} \mathrm{e}^{-Q_\nu r} \\ R_{2,0}(r) &= \frac{Q_\nu^{3/2}}{\sqrt{2}} \left(1 - \frac{Q_\nu r}{2}\right) \mathrm{e}^{-Q_\nu r/2} \\ R_{2,1}(r) &= \frac{Q_\nu^{5/2}}{2\sqrt{6}} r \; \mathrm{e}^{-Q_\nu r/2} \\ R_{3,0}(r) &= \frac{2Q_\nu^{3/2}}{3\sqrt{3}} \left(1 - \frac{2Q_\nu r}{3} + \frac{2Q_\nu^2 r^2}{27}\right) \mathrm{e}^{-Q_\nu r/3} \\ \vdots \quad & \vdots \quad \vdots \end{aligned} \tag{27}$$

To see that $\Phi_\nu(\mathbf{x})$ will then satisfy (10), we notice that the hydrogenlike spin-orbitals with weighted charge Q_ν satisfy the 1-electron wave equation:

$$\left[-\frac{1}{2}\nabla_j^2 + \frac{Q_\nu^2}{2n^2} - \frac{Q_\nu}{r_j}\right]\chi_\mu(\mathbf{x}_j) = 0. \tag{28}$$

Then

$$\begin{aligned}\left[-\tfrac{1}{2}\sum_{j=1}^{N}\nabla_j^2\right]\Phi_\nu(\mathbf{x}) &= \left[-\left(\frac{Q_\nu^2}{2n^2} + \frac{Q_\nu^2}{2n'^2} + \cdots\right) + \left(\frac{Q_\nu}{r_1} + \frac{Q_\nu}{r_2} + \cdots\right)\right]\Phi_\nu(\mathbf{x}) \\ &= [E_\kappa - \beta_\nu V_0(\mathbf{x})]\Phi_\nu(\mathbf{x}).\end{aligned} \tag{29}$$

Comparing (29) with (10), and noting that (26) implies the relationship

$$E_\kappa = -\frac{Q_\nu^2}{2}\left(\frac{1}{n^2} + \frac{1}{n'^2} + \frac{1}{n''^2} + \cdots\right). \tag{30}$$

we can see that (29) and (10) are the same. Therefore, (10) is exactly satisfied by the Slater determinant (25) provided that the effective charges Q_ν are chosen in the special way shown in (26). The hydrogenlike spin-orbitals χ_μ satisfy the relations

$$\int d^3x_j\, \chi_{\mu'}^*(\mathbf{x}_j)\chi_\mu(\mathbf{x}_j) = \delta_{\mu',\mu} \tag{31}$$

and

$$-\int d^3x_j \left|\chi_\mu(\mathbf{x}_j)\right|^2 \frac{Q_\nu}{r_j} = -\frac{Q_\nu^2}{n^2} \tag{32}$$

from which it follows that [22, 23]

$$\int \mathrm{d}x\;\; \Phi_{\nu'}^*(\mathbf{x})\, V_0(\mathbf{x})\, \Phi_\nu(\mathbf{x}) = \delta_{\nu',\nu}\frac{2E_\kappa}{\beta_\nu}. \tag{33}$$

If we introduce the notation

$$p_\kappa \equiv \sqrt{-2E_\kappa} \tag{34}$$

and

$$\mathcal{R}_\nu \equiv \sqrt{\frac{1}{n^2} + \frac{1}{n'^2} + \cdots}, \tag{35}$$

then we can write

$$Q_\nu = \beta_\nu Z = \frac{p_\kappa}{\mathcal{R}_\nu} \tag{36}$$

and

$$E_\kappa = -\frac{p_\kappa^2}{2}. \tag{37}$$

We also let

$$\begin{aligned} V(\mathbf{x}) &= V_0(\mathbf{x}) + V'(\mathbf{x}) \\ V_0(\mathbf{x}) &= -\sum_{j=1}^{N} \frac{Z}{r_j} \\ V'(\mathbf{x}) &= \sum_{j>i}^{N} \sum_{i=1}^{N} \frac{1}{r_{ij}} \end{aligned} \tag{38}$$

and

$$\begin{aligned} T^0_{\nu',\nu} &\equiv -\frac{1}{p_\kappa} \int \mathrm{d}x \; \Phi^*_{\nu'}(\mathbf{x}) V_0(\mathbf{x}) \, \Phi_\nu(\mathbf{x}) \\ T'_{\nu',\nu} &\equiv -\frac{1}{p_\kappa} \int \mathrm{d}x \; \Phi^*_{\nu'}(\mathbf{x}) V'(\mathbf{x}) \, \Phi_\nu(\mathbf{x}). \end{aligned} \tag{39}$$

From the potential-weighted orthonormality relation (14), it follows that

$$T^0_{\nu',\nu} = \delta_{\nu',\nu} Z \mathcal{R}_\nu. \tag{40}$$

Thus, when Goscinskian configurations are used, the generalized Sturmian secular equation for atoms (23) takes on the form:

$$\sum_\nu \left[\delta_{\nu',\nu} Z \mathcal{R}_\nu + T'_{\nu',\nu} - p_\kappa \, \delta_{\nu',\nu} \right] \; B_{\nu,\kappa} = 0. \tag{41}$$

Notice that the nuclear attraction matrix $T^0_{\nu',\nu}$ is both diagonal and energy-independent. In order to see that $T'_{\nu',\nu}$ is also energy independent, we notice that it is built up from terms of the form

$$\frac{1}{p_\kappa} J_{\mu_1,\mu_2,\mu_3,\mu_4} = \frac{1}{p_\kappa} \int d^3x \int d^3x' \;\; \rho_{\mu_1,\mu_2}(\mathbf{x}) \frac{1}{|\mathbf{x} - \mathbf{x}'|} \rho_{\mu_3,\mu_4}(\mathbf{x}'), \tag{42}$$

where densities are defined by

$$\begin{aligned} \rho_{\mu_1,\mu_2}(\mathbf{x}) &\equiv \chi^*_{\mu_1}(\mathbf{x}) \, \chi_{\mu_2}(\mathbf{x}) \\ \rho_{\mu_3,\mu_4}(\mathbf{x}') &\equiv \chi^*_{\mu_3}(\mathbf{x}') \, \chi_{\mu_4}(\mathbf{x}') \end{aligned} \tag{43}$$

and where the orbitals are the hydrogenlike orbitals with weighted nuclear charge shown in (26). We now let

$$\begin{aligned}\mathbf{s} &\equiv p_\kappa \mathbf{x} \\ \mathbf{s}' &\equiv p_\kappa \mathbf{x}'.\end{aligned} \tag{44}$$

Then, making the substitution $Q_\nu \to p_\kappa/R_\nu$ in (27) we have

$$\begin{aligned}\rho_{\mu_1,\mu_2}(\mathbf{x}) &\equiv p_\kappa^3 \tilde{\rho}_{\mu_1,\mu_2}(\mathbf{s}) \\ \rho_{\mu_3,\mu_4}(\mathbf{x}') &\equiv p_\kappa^3 \tilde{\rho}_{\mu_3,\mu_4}(\mathbf{s}'),\end{aligned} \tag{45}$$

where $\tilde{\rho}_{\mu_1,\mu_2}(\mathbf{s})$ and $\tilde{\rho}_{\mu_3,\mu_4}(\mathbf{s}')$ are pure functions of $\mathbf{s}$ and $\mathbf{s}'$ respectively. Finally, noticing that

$$\frac{1}{p_\kappa|\mathbf{x}-\mathbf{x}'|} = \frac{1}{|\mathbf{s}-\mathbf{s}'|}, \tag{46}$$

we can write

$$\frac{1}{p_\kappa} J_{\mu_1,\mu_2,\mu_3,\mu_4} = \int d^3s \int d^3s' \, \tilde{\rho}_{\mu_1,\mu_2}(\mathbf{s}) \frac{1}{|\mathbf{s}-\mathbf{s}'|} \tilde{\rho}_{\mu_3,\mu_4}(\mathbf{s}'). \tag{47}$$

Since the building-blocks from which it composed are independent of p_κ, the interelectron repulsion matrix $T'_{\nu',\nu}$ is also independent of p_κ and hence independent of energy. The energy-independent interelectron repulsion matrix $T'_{\nu',\nu}$ consists of pure numbers (in atomic units) which can be evaluated once and for all and stored.

4.1 The Large-Z Approximation: Restriction of the Basis Set to an $\mathcal{R}_\nu$-Block

The term $T'_{\nu',\nu}$ in (41) represents the effects of interelectron repulsion. If we neglect this term entirely, the energy E_κ of a state of the atom reduces to the energy of N noninteracting electrons moving in the attractive potential of the nucleus:

$$E_\kappa = -\frac{p_\kappa^2}{2} \to -\frac{1}{2}Z^2\mathcal{R}_\nu^2 = -\frac{Z^2}{2n_1^2} - \frac{Z^2}{2n_2^2} - \cdots - \frac{Z^2}{2n_N^2}. \tag{48}$$

In the large-Z approximation, we restrict the basis to those configurations that belong to a particular value of $\mathcal{R}_\nu$, i.e. those configurations that correspond

Table 1 Roots of the ground state $\mathcal{R}$-block of the interelectron repulsion matrix for the Li-like, Be-like, B-like and C-like isoelectronic series

Li-like $\lvert\lambda_\kappa\rvert$	term	Be-like $\lvert\lambda_\kappa\rvert$	term	B-like $\lvert\lambda_\kappa\rvert$	term	C-like $\lvert\lambda_\kappa\rvert$	term
0.681870	^{2}S	0.986172	^{1}S	1.40355	^{2}P	1.88151	^{3}P
0.729017	^{2}P	1.02720	^{3}P	1.44095	^{4}P	1.89369	^{1}D
		1.06426	^{1}P	1.47134	^{2}D	1.90681	^{1}S
		1.09169	^{3}P	1.49042	^{2}S	1.91623	^{5}S
		1.10503	^{1}D	1.49395	^{2}P	1.995141	^{3}D
		1.13246	^{1}S	1.52129	^{4}S	1.96359	^{3}P
				1.54037	^{2}D	1.98389	^{3}S
				1.55726	^{2}P	1.98524	^{1}D
						1.99742	^{1}P
						2.04342	^{3}P
						2.05560	^{1}D
						2.07900	^{1}S

to a particular value of E_κ if the effects of interelectron repulsion are entirely neglected. However, in the large-Z approximation we do not neglect interelectron repulsion. Instead, we notice that if the entire basis set consists of configurations corresponding to the same value of $\mathcal{R}_\nu$, the term $\delta_{\nu',\nu}\, Z\mathcal{R}_\nu$ will be a multiple of the

Table 2 Roots of the ground state $\mathcal{R}$-block of the interelectron repulsion matrix $T'_{\nu',\nu}$ for the N-like, O-like, F-like, and Ne-like isoelectronic series

N-like $\lvert\lambda_\kappa\rvert$	term	O-like $\lvert\lambda_\kappa\rvert$	term	F-like $\lvert\lambda_\kappa\rvert$	term	Ne-like $\lvert\lambda_\kappa\rvert$	term
2.41491	^{4}S	3.02641	^{3}P	3.68415	^{2}P	4.38541	^{1}S
2.43246	^{2}D	3.03769	^{1}D	3.78926	^{2}S		
2.44111	^{2}P	3.05065	^{1}S				
2.49314	^{4}P	3.11850	^{3}P				
2.52109	^{2}D	3.14982	^{1}P				
2.53864	^{2}S	3.24065	^{1}S				
2.54189	^{2}P						
2.61775	^{2}P						

unit matrix, and the coefficients $B_{\nu\kappa}$ will be eigenfunctions of the simplified secular equation: [22]

$$\sum_{\nu} [T'_{\nu'\nu} - \lambda_\kappa \, \delta_{\nu'\nu}] \; B_{\nu\kappa} = 0. \tag{49}$$

Since only Coulomb potentials are involved, the matrix $T'_{\nu',\nu}$ turns out to be energy independent. Its elements are pure numbers that depend only on N, the number of electrons, and are independent of the nuclear charge Z. The roots λ_κ of the energy-independent interelectron repulsion matrix $T'_{\nu',\nu}$ are also pure numbers (Table 1). In the large-Z approximation, the generalized Sturmian secular equation (41) reduces to the requirement:

$$p_\kappa = Z\mathcal{R}_\nu + \lambda_\kappa = Z\mathcal{R}_\nu - |\lambda_\kappa|, \tag{50}$$

Table 3 ^{3}S excited state energies calculated with 78 Goscinskians, using the crude relativistic correction described in the text. The calculation of similar tables for ^{1}P, ^{3}P, ^{1}D, ^{3}D, doubly excited autoionizing states, etc., is equally easy, rapid, and of comparable accuracy. Tables are given in Chaps. 3 and 4 in [22], but may easily be reproduced using our programs, as shown in Tutorial 1 on [26]

	He	Li^+	Be^{2+}	B^{3+}	C^{4+}	N^{5+}
1s2s ^{3}S	-2.1737	-5.1085	-9.2957	-14.735	-21.427	-29.373
expt.	-2.1750	-5.1109	-9.2983	-14.738	-21.429	-29.375
1s3s ^{3}S	-2.0683	-4.7509	-8.5459	-13.454	-19.476	-26.612
expt.	-2.0685	-4.7522	-8.5480	-13.457	-19.478	-26.614
1s4s ^{3}S	-2.0364	-4.6365	-8.2999	-13.027	-18.820	-25.678
expt.	-2.0363	-4.6373	-8.3015	-13.030	-18.822	-25.680
1s5s ^{3}S	-2.0226	-4.5859	-8.1896	-12.835	-18.522	-25.253
expt.	-2.0224	-4.5862	-8.1905		-18.524	-25.254
1s6s ^{3}S	-2.0154	-4.5591	-8.1309	-12.732	-18.363	-25.024
expt.	-2.0152	-4.5592			-18.364	
1s7s ^{3}S	-2.0112	-4.5432	-8.096	-12.67	-18.267	-24.888
expt.	-2.0109	-4.5431			-18.268	
1s8s ^{3}S	-2.0085	-4.5330	-8.0736	-12.631	-18.206	-24.799
expt.	-2.0082	-4.5328			-18.206	
1s9s ^{3}S	-2.0067	-4.5261	-8.0583	-12.604	-18.164	-24.739
expt.	-2.0064					
1s10s ^{3}S	-2.0051	-4.5212	-8.0475	-12.585	-18.134	-24.696
expt.	-2.0051					

so that [22]

$$E_\kappa = -\frac{1}{2}\left(Z\mathcal{R}_\nu - |\lambda_\kappa|\right)^2. \tag{51}$$

This gives us a simple closed-form expression for the energy of a state in the large-Z approximation. If the number of electrons N is kept constant while Z is allowed to increase, the energies calculated from this formula approach those found by solution of the nonrelativistic Schrödinger equation, but a relativistic correction must be added in order for the energies to approach experimental values. A crude relativistic correction can be found for a multiconfigurational state $\Psi_\kappa(\mathbf{x}) = \Sigma_\nu\, \Phi_\nu(\mathbf{x}) B_{\nu\kappa}$ by calculating the ratio of the relativistic energy of the with interelectron repulsion entirely neglected to the nonrelativistic energy, again with interelectron repulsion entirely neglected. The ratio can be written in the form

$$f_\kappa(Z) = \frac{E_{\text{rel}}}{E_{\text{nonrel}}} = \frac{\sum_\nu B_{\nu\kappa}^2 \langle \Phi_\nu | H_0 | \Phi_\nu \rangle_{\text{rel}}}{-\frac{1}{2} Z^2 \sum_\nu B_{\nu\kappa}^2 \mathcal{R}_\nu^2}. \tag{52}$$

Here,

$$\langle \Phi_\nu | H_0 | \Phi_\nu \rangle_{\text{rel}} = \sum_{\mu \in \nu} \varepsilon_{\mu,\text{rel}} \qquad \mu = (n,\ l,\ m,\ m_s), \tag{53}$$

is the relativistic energy of the configuration $\phi_\nu(\mathbf{x})$ with interelectron repulsion entirely neglected, while

$$-\sum_{\mu \in \nu} \frac{1}{2}\frac{Z^2}{n^2} = -\frac{1}{2} Z^2 R_\nu^2 \qquad \mu = (n,\ l,\ m,\ m_s) \tag{54}$$

is its nonrelativistic energy. In order to calculate the relativistic correction, we only need to know the relativistic energy of a single electron moving independently in the Coulomb potential of a nucleus. If effects such as vacuum polarization and Lamb shift are neglected, this energy can be calculated exactly and is given by

$$\varepsilon_{\mu,\text{rel}} = \frac{c^2}{\left[1 + \left(\frac{Z}{c(\gamma + n - |j+1/2|)}\right)^2\right]^{1/2}} - c^2 \tag{55}$$

$$\gamma \equiv \sqrt{\left(j + \frac{1}{2}\right)^2 - \left(\frac{Z}{c}\right)^2} \qquad c = 137.036, \tag{56}$$

where j is the total angular momentum (orbital plus spin) of a single electron, i.e., $l \pm \frac{1}{2}$. The corrected energy,

$$\widetilde{E}_\kappa = -\frac{1}{2} f_\kappa(Z)\ (Z\mathcal{R}_\nu - |\lambda_\kappa|)^2 \tag{57}$$

agrees closely with the experimental values of energies when Z is large compared with N (Fig. 1). The simple approximate relativistic correction discussed here is by no means confined to use in connection with the Generalized Sturmian Method. It can be used to correct quantum calculations of every kind.

In solving the simplified secular equation (49), it is useful to add an extremely small perturbation of the form

$$T_p = aL_z + bS_z, \tag{58}$$

where a and b are very small random numbers. The eigenfunctions can then be easily identified as Russell–Saunders states, i.e., besides being solutions to the nonrelativistic Schrödinger equation, they are simultaneously eigenfunctions of the operators L^2, S^2, L_z and S_z. Here the operators L^2 and S^2 represent the squares of total orbital angular momentum and total spin, while L_z and S_z represent their z-components. The Russell–Saunders states found by diagonalizing $\mathcal{R}_\nu$-blocks are

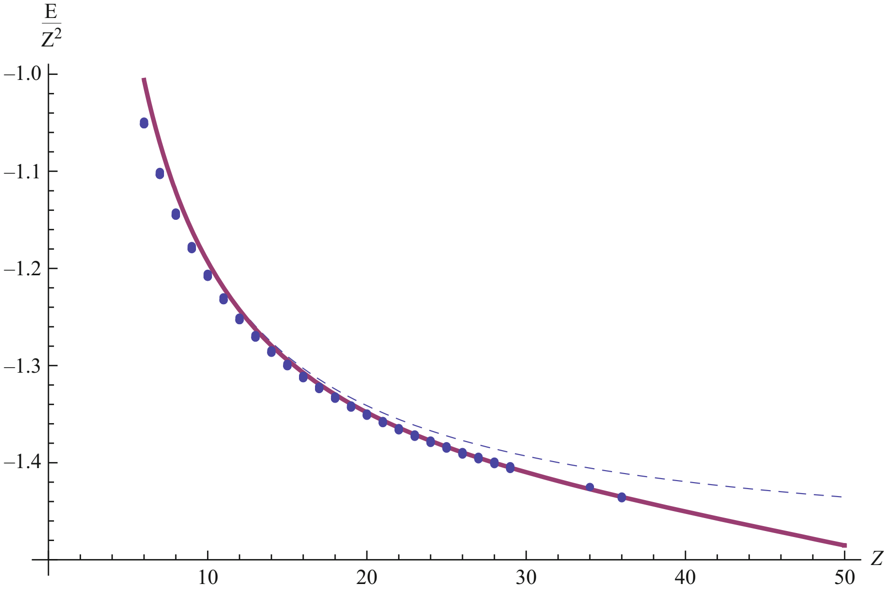

Fig. 1 The ground state of the carbon-like isoelectronic series, calculated in the large-Z approximation. The energies divided by Z^2 are shown as functions of Z. Experimental values are indicates by *dots*, while the energies calculated from (51) are shown as *curves*. The *lower (solid) curve*, which approaches the experimental values with increasing Z, has been corrected for relativistic effects. The *upper (dashed) curve* is uncorrected

symmetry-adapted basis sets that can be used in more refined calculations where the large-Z approximation has been abandoned. Thus, for example, we can use the ^{3}S states automatically generated by the diagonalization of many $\mathcal{R}_\nu$-blocks as basis functions for a more refined calculation specifically aimed at ^{3}S states, as illustrated in Table 3. Notice that since the interelectron repulsion matrix $T'_{\nu',\nu}$ is independent of the nuclear charge Z, the states of an entire isoelectronic series can be calculated using the same values of the matrix. The number of configurations in an $\mathcal{R}_\nu$-block is given by the binomial coefficient

$$\binom{N_s}{N_\upsilon} = \frac{N_s!}{N_\upsilon!(N_s - N_\upsilon)!}, \tag{59}$$

where N_s is the number of atomic spin-orbitals in the highest filled shell, and where N_υ is the number of valence electrons. For example, for the lithium ground state, we have

$$\binom{N_s}{N_\upsilon} = \binom{8}{1} = \frac{8!}{1!(8-1)!} = 8, \tag{60}$$

while for the carbon ground state we have

$$\begin{pmatrix} N_s \\ N_\upsilon \end{pmatrix} = \begin{pmatrix} 8 \\ 4 \end{pmatrix} = \frac{8!}{4!(8-4)!} = 70. \tag{61}$$

The reader can verify that these correspond to the sum of the degeneracies of the Russell–Saunders states generated by diagonalizing the 8×8 $\mathcal{R}_v$-block for the lithium ground state and the 70×70 block for the carbon ground state, as shown in Table 1.

4.2 Advantages and Disadvantages of Goscinskian Configurations

The use of Goscinskian configurations allows us to calculate the spectra and properties of few-electron atoms with great speed and reasonable accuracy. Highly-excited states are particularly well-represented by linear combinations of Goscinskian configurations. However, convergence is less good when the method is applied to atoms with large numbers of electrons. This is because the Goscinskian configurations are solutions to the approximate Schrödinger equation (10) with $V_0(\mathbf{x})$ chosen to be the attractive Coulomb potential of the bare nucleus. When the effects of interelectron repulsion are large compared with those of nuclear attraction, a more realistic choice of $V_0(\mathbf{x})$ is needed. One could, for example let $V_0(\mathbf{x})$ be the Hartree potential or the Hartree plus Slater potentials, or the Kohn–Sham potential [27]. These potentials still have the form

$$V_0(\mathbf{x}) = \sum_{i=1}^{N} \upsilon(\mathbf{x}_i) \tag{62}$$

and therefore (10) will still be separable and therefore soluble (although some of the neatness of the Goscinskian configurations will be lost). We are exploring these possibilities for extending the range of applicability of the method. Prof G. Gasaneo and his students are also working to extend the method's range, [28, 29].

5 Molecular Orbitals Based on Sturmians

5.1 The One-Electron Secular Equation

Can the Generalized Sturmian Method be applied to N-electron molecules? This is another question that we are starting to explore. Let us consider a single electron moving in the field of a number of nuclei. The Schrödinger equation obeyed by this single electron is given by

$$\left[-\frac{1}{2}\nabla^2 + \upsilon(\mathbf{x}) - \varepsilon_\zeta\right] \varphi_\zeta(\mathbf{x}) = 0, \tag{63}$$

where

$$\upsilon(\mathbf{x}) = -\sum_a \frac{Z_a}{|\mathbf{x} - \mathbf{X}_a|}. \tag{64}$$

(We have dropped the index *i* because for the moment we are dealing with a single electron). The use of Coulomb Sturmian basis functions located on the different atoms of a molecule to solve (63) was pioneered by C.E. Wulfman, B. Judd, T. Koga, V. Aquilanti, and others [30–37]. These authors solved the Schrödinger equation in momentum space, but here we will use a direct-space treatment to reach the same results. Our basis functions will be labeled by the set of indices

$$\tau \equiv (n,\ l,\ m,\ a). \tag{65}$$

Here, n, l, and m are the quantum numbers of the Coulomb Sturmians, while a is the index of the atom on which the basis function is localized. Thus we write

$$\chi_\tau(\mathbf{x}) \equiv \chi_{nlm}(\mathbf{x} - \mathbf{X}_a), \tag{66}$$

where the Coulomb Sturmians $\chi_{nlm}(\mathbf{x}) = R_{nl}(r)Y_{lm}(\theta,\ \phi)$ are those defined in (1)–(9). The molecular orbitals are then expressed as linear combinations of many-center Coulomb Sturmians:

$$\varphi_\zeta(\mathbf{x}) = \sum_{n,l,m,a} \chi_{n,l,m}(\mathbf{x} - \mathbf{X}_a)\, C_{\tau,\zeta} \equiv \sum_\tau \chi_\tau(\mathbf{x})\, C_{\tau,\zeta}. \tag{67}$$

Then, letting

$$\varepsilon_\zeta \equiv -\frac{1}{2}k^2, \tag{68}$$

we can write

$$\sum_\tau \left[-\frac{1}{2}\nabla^2 + \frac{1}{2}k^2 + \upsilon(\mathbf{x})\right] \chi_\tau(\mathbf{x})C_{\tau,\zeta} = 0. \tag{69}$$

Multiplying from the left by a conjugate basis function and integrating over the coordinates we have

$$\sum_\tau \int d^3x\ \chi^*_{\tau'}(\mathbf{x}) \left[-\frac{1}{2}\nabla^2 + \frac{1}{2}k^2 + \upsilon(\mathbf{x})\right] \chi_\tau(\mathbf{x})\, C_{\tau,\zeta} = 0. \tag{70}$$

If we introduce the notation

$$\mathfrak{W}_{\tau',\tau} \equiv -\frac{1}{k}\int d^3x \chi^*_{\tau'}(\mathbf{x})\upsilon(\mathbf{x})\chi_\tau(\mathbf{x}) \tag{71}$$

and

$$\mathfrak{S}_{\tau',\tau} \equiv \frac{1}{k^2}\int d^3x\, \chi^*_{\tau'}(\mathbf{x}) \left[-\frac{1}{2}\nabla^2 + \frac{1}{2}k^2\right] \chi_\tau(\mathbf{x}), \tag{72}$$

the secular equation (70) can be written in the form

$$\sum_\tau \left[\mathfrak{W}_{\tau',\tau} - k\mathfrak{S}_{\tau',\tau}\right] C_{\tau,\zeta} = 0. \tag{73}$$

The integrals defined by (72) are the well-studied Shibuya–Wulfman integrals; those defined by (71) we can call the *Wulfman integrals* to honor the pioneering work of C.E. Wulfman [35–37]. The roots of the secular equations (73) are not energies, but are values of the scaling parameter k, which is related to the 1-electron energies by (68). For diatomic molecules, both $\mathfrak{W}_{\tau'\ \tau}$ and $\mathfrak{S}_{\tau',\tau}$ are pure functions of the parameter $S = kR$. The procedure for solving for the molecular orbitals is to solve the secular equations (73) for many values of S. For each value of S, a spectrum of k values is generated – one for each molecular orbital. Then the orbital energies and wave functions, $\varepsilon_\zeta(R)$ and $\varphi_\zeta(R)$, can be found by interpolation as functions of the internuclear distance R.

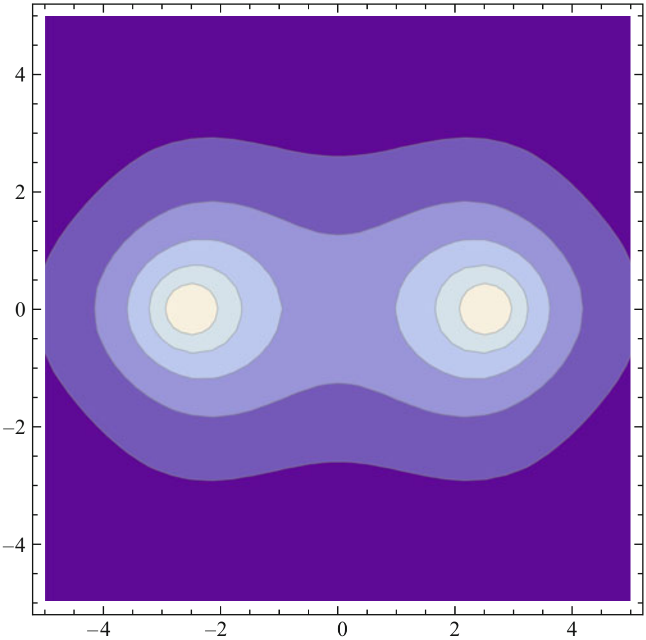

Fig. 2 This figure shows the Sturmian molecular orbital corresponding to the ground state of the H_2^+ ion, with $S = 6$, $k = 1.16885$, and $R = 5.13325$ Bohrs

5.2 Shibuya–Wulfman Integrals and Sturmian Overlap Integrals Evaluated in Terms of Hyperpherical Harmonics

In a remarkably brilliant early paper, the Russian physicist V. Fock showed that the Fourier transforms of Coulomb Sturmian basis functions can be related in a simple way to 4-dimensional hyperspherical harmonics [38, 39]. Fock discovered this relationship by projecting momentum space onto the surface of a 4-dimensional hypersphere using the relationship

$$\hat{\mathbf{u}} = (u_1, u_2, u_3, u_4) = \left(\frac{2kp_1}{k^2+p^2}, \frac{2kp_2}{k^2+p^2}, \frac{2kp_3}{k^2+p^2}, \frac{k^2-p^2}{k^2+p^2}\right). \tag{74}$$

Here, (p_1, p_2, p_3) are the coordinates of momentum space, while (u_1, u_2, u_3, u_4) are unit vectors characterizing points on the surface of the hypersphere. (In (74), and throughout this paper, we indicate a unit vector by means of a “hat”). He then transformed the Schrödinger equation for hydrogenlike atom in momentum space to a problem involving the unit vector $\hat{\mathbf{u}}$ on the surface of the 4-dimensional hypersphere.

Fock first noted that the 1-electron orbital $\chi_\mu(\mathbf{x})$ and its Fourier transform $\chi^t_\mu(\mathbf{p})$ are related by

$$\begin{aligned}\chi_\mu(\mathbf{x}) &= \frac{1}{(2\pi)^{3/2}} \int d^3p\ \mathrm{e}^{i\mathbf{p}\cdot\mathbf{x}}\, \chi^t_\mu(\mathbf{p}) \\ \chi^t_\mu(\mathbf{p}) &= \frac{1}{(2\pi)^{3/2}} \int d^3x\ \mathrm{e}^{-i\mathbf{p}\cdot\mathbf{x}} \chi_\mu(\mathbf{x}),\end{aligned} \tag{75}$$

where $\mu \equiv (n, l, m)$. If we let

$$k^2 \equiv -2\varepsilon_\mu, \tag{76}$$

then the 1-electron Schrödinger equation

$$\left[-\frac{1}{2}\nabla^2 + \upsilon(\mathbf{x}) - \varepsilon_\mu\right]\ \chi_\mu(\mathbf{x}) = 0 \tag{77}$$

can be written in the form

$$[-\nabla^2 + k^2 + 2\upsilon(\mathbf{x})]\ \chi_\mu(\mathbf{x}) = 0. \tag{78}$$

Substituting the expression for the wave function χ_μ $(\mathbf{x})$ in terms of its Fourier transform (75) into (78), we have

$$\begin{aligned}&[-\nabla^2 + k^2 + 2\upsilon(\mathbf{x})]\ \int d^3p\ \mathrm{e}^{i\mathbf{p}\cdot\mathbf{x}}\, \chi^t_\mu(\mathbf{p}) \\ &\quad = \int d^3p\ \mathrm{e}^{i\mathbf{p}\cdot\mathbf{x}}\ [p^2 + k^2 + 2\upsilon(\mathbf{x})]\ \chi^t_\mu(\mathbf{p}) = 0,\end{aligned} \tag{79}$$

since ∇^2 acting on the plane wave brings down the factor p^2. If we now multiply (79) by $\mathrm{e}^{-i\mathbf{p}'\cdot\mathbf{x}}$ and integrate over the space coordinates, we obtain

$$\begin{aligned}&\int d^3p\ (p^2+k^2)\ \chi_\mu^t(\mathbf{p})\ \int d^3x\ \ \mathrm{e}^{i(\mathbf{p}-\mathbf{p}')\cdot\mathbf{x}}\\&\quad+2\int d^3p\ \ \int d^3x\ \ \mathrm{e}^{i(\mathbf{p}-\mathbf{p}')\cdot\mathbf{x}}\,\upsilon(\mathbf{x})\,\chi_\mu^t(\mathbf{p})=0.\end{aligned}\tag{80}$$

Then remembering that

$$\int d^3x\,\mathrm{e}^{i(\mathbf{p}-\mathbf{p}')\cdot\mathbf{x}}=(2\pi)^3\delta(\mathbf{p}-\mathbf{p}'),\tag{81}$$

we have

$$\begin{aligned}&(2\pi)^3\int d^3p\ \delta(\mathbf{p}-\mathbf{p}')(p^2+k^2)\chi_\mu^t(\mathbf{p})\\&+2\int d^3p\ \int d^3x\ \mathrm{e}^{i(\mathbf{p}-\mathbf{p}')\cdot\mathbf{x}}\upsilon(\mathbf{x})\chi_\mu^t(\mathbf{p})=0.\end{aligned}\tag{82}$$

Using the Dirac delta function to perform the first p-integration in (82), we obtain the momentum-space Schrödinger equation:

$$(p'^2+k^2)\chi_\mu^t(\mathbf{p}')=\frac{2}{(2\pi)^{3/2}}\int d^3p\,\upsilon^t\,(\mathbf{p}'-\mathbf{p})\chi_\mu^t(\mathbf{p}),\tag{83}$$

where

$$\upsilon^t\,(\mathbf{p}'-\mathbf{p})\ \equiv\ \frac{1}{(2\pi)^{3/2}}\int d^3x\,\mathrm{e}^{-i(\mathbf{p}'-\mathbf{p})\cdot\mathbf{x}}\upsilon(\mathbf{x}).\tag{84}$$

In the special case of hydrogenlike atoms, where

$$\upsilon(\mathbf{x})=-\frac{Z}{r},\tag{85}$$

we have

$$\upsilon^t(\mathbf{p}-\mathbf{p}')=-\sqrt{\frac{2}{\pi}}\frac{Z}{|\mathbf{p}-\mathbf{p}'|^2}.\tag{86}$$

Thus, the momentum-space Schrödinger equation for hydrogenlike atoms becomes

$$(p'^2+k^2)\chi_\mu^t(\mathbf{p}')=\frac{Z}{\pi^2}\int d^3p\frac{1}{|\mathbf{p}-\mathbf{p}'|^2}\chi_\mu^t(\mathbf{p}).\tag{87}$$

V. Fock was able to solve this integral equation by letting

$$\chi^t_\mu(\mathbf{p}) = \frac{4k^{5/2}}{(k^2+p^2)^2} f_\mu(\hat{\mathbf{u}}), \tag{88}$$

where $\hat{\mathbf{u}} = (u_1,\ u_2,\ u_3,\ u_4)$ denotes the unit vectors defining points on Fock's 4-dimensional hypersphere, (74). With this transformation, (87) takes on the simple form

$$f_\mu(\hat{\mathbf{u}}') = \frac{Z}{2\pi^2 k}\int \mathrm{d}\Omega \frac{1}{|\hat{\mathbf{u}} - \hat{\mathbf{u}}'|^2} f_\mu(\hat{\mathbf{u}}'). \tag{89}$$

Fock then expanded the kernel of this integral equation in terms of Gegenbauer polynomials and hyperspherical harmonics:

$$\begin{aligned}\frac{1}{|\hat{\mathbf{u}} - \hat{\mathbf{u}}'|^2} &= \sum_{\lambda=0}^{\infty} C^1_\lambda(\hat{\mathbf{u}}\cdot\hat{\mathbf{u}}')\\ &= \frac{2\pi^2}{\lambda+1}\sum_{\lambda=0}^{\infty}\sum_{l=0}^{\lambda}\sum_{m=-l}^{l} Y_{\lambda,l,m}(\hat{\mathbf{u}}')Y^*_{\lambda,l,m}(\hat{\mathbf{u}}).\end{aligned} \tag{90}$$

In (90), $Y_{\lambda.l.m}$ $(\hat{\mathbf{u}})$ is a 4-dimensional hyperspherical harmonic:

$$Y_{\lambda,l,m}(\hat{\mathbf{u}}) = \mathcal{N}_{\lambda,l}\, C^{1+l}_{\lambda-l}(u_4)\, Y_{l,m}(u_1,\ u_2,\ u_3). \tag{91}$$

Here $Y_{l,m}(u_1,u_2,u_3)$ is a familiar 3-dimensional spherical harmonic, while

$$\mathcal{N}_{\lambda,l} = (-1)^\lambda\, i^l (2l)!!\sqrt{\frac{2(\lambda+1)(\lambda-l)!}{\pi(\lambda+l+1)!}} \tag{92}$$

is a normalizing factor and

$$C^a_n(u_4) = \sum_{t=0}^{[n/2]} \frac{(-1)^t \Gamma(n+a-t)}{t!(n-2t)!\Gamma(a)}(2u_4)^{n-2t} \tag{93}$$

is a Gegenbauer polynomial. The Gegenbauer polynomials are sometimes called *ultraspherical polynomials* because of their close relationship with spherical and hyperspherical harmonics. The Gegenbauer polynomial corresponding to $a = 1/2$ is a Legendre polynomial, and the sum rule shown in (90) is closely analogous to the familiar sum rule for spherical harmonics. The first few 4-dimansional hyperspherical harmonics are shown in Table 4.

Inserting the expansion (90) into the integral equation (89), and making use of the orthonormality relation for hyperspherical harmonics,

$$\int d\Omega\, Y^{*}_{\lambda',l',m'}(\hat{\mathbf{u}})Y_{\lambda,l,m}(\hat{\mathbf{u}}) = \delta_{\lambda'\lambda}\delta_{l',l}\delta_{m',m}. \tag{94}$$

Fock was able to show that the momentum-space Schrödinger equation for hydrogenlike atoms has solutions of the form

$$\begin{aligned} f_\mu(\hat{\mathbf{u}}) &= Y_{\lambda,l,m}(\hat{\mathbf{u}}) \\ \chi^t_\mu(\mathbf{p}) &= \frac{4k^{5/2}}{(k^2+p^2)^2} Y_{\lambda,l,m}(\hat{\mathbf{u}}) \qquad \lambda = 0,1,2,3,\ldots \end{aligned} \tag{95}$$

provided that

$$k = \frac{Z}{\lambda+1}. \tag{96}$$

By inserting this requirement into (76), Fock could see that it was equivalent to specifying that

Table 4 4-Dimensional hyperspherical harmonics

λ	l	m	$\sqrt{2}\pi\ Y_{\lambda,l,m}(\mathbf{u})$
0	0	0	1
1	1	1	$i\sqrt{2}(u_1+iu_2)$
1	1	0	$-i2u_3$
1	1	−1	$-i\sqrt{2}(u_1-iu_2)$
1	0	0	$-2u_4$
2	2	2	$-\sqrt{3}(u_1+iu_2)^2$
2	2	1	$2\sqrt{3}u_3(u_1+iu_2)$
2	2	0	$-\sqrt{2}(2u_3^2-u_1^2-u_2^2)$
2	2	−1	$-2\sqrt{3}u_3(u_1-iu_2)$
2	2	−2	$-\sqrt{3}(u_1-iu_2)^2$
2	1	1	$-i2\sqrt{3}\ u_4(u_1+iu_2)$
2	1	0	$2i\sqrt{6}\ u_4u_3$
2	1	−1	$2i\sqrt{3}\ u_4(u_1-iu_2)$
2	0	0	$4u_4^2-1$

$$\varepsilon_\mu = -\frac{1}{2}\left(\frac{Z}{\lambda + 1}\right)^2. \tag{97}$$

He identified λ+1 with the quantum number *n*, and thus obtained the well-known result for hydrogenlike atoms:

$$\varepsilon_\mu = -\frac{1}{2}\left(\frac{Z}{n}\right)^2. \tag{98}$$

At the same time, Fock uncovered an explanation for the puzzling n^2-fold degeneracy of hydrogenlike atomic orbitals, since the number of linearly independent 4-dimensional hyperspherical harmonics corresponding to a given value of λ is $(\lambda + 1)^2$, as is illustrated in Table 4. Fock's momentum-space treatment of hydrogen-like atoms and the connection which he established between the solutions and the set of 4-dimensional hyperspherical harmonics was later generalized to the analogous d-dimensional problem [40–42].

5.3 The Shibuya–Wulfman Generalization of Fock's Result to Molecules

In a famous 1965 paper [35], T.I. Shibuya and C.E. Wulfman were able to generalize Fock's result to molecules. They considered the case where

$$\upsilon(\mathbf{x}) = -\sum_a \frac{Z_a}{|\mathbf{x} - \mathbf{X}_a|}. \tag{99}$$

In that case, the integral equation analogous to (87) becomes

$$(p'^2 + k^2)\varphi^t_\zeta(\mathbf{p}') = \frac{1}{\pi^2}\int d^3p \frac{1}{|\mathbf{p} - \mathbf{p}'|^2}\sum_a Z_a \mathrm{e}^{i(\mathbf{p}-\mathbf{p}')\cdot\mathbf{X}_a}\varphi^t_\zeta(\mathbf{p}). \tag{100}$$

Following a path similar to that of Fock, Shibuya, and Wulfman let

$$\varphi^t_\zeta(\mathbf{p}) = \frac{4k^{5/2}}{(k^2 + p^2)^2}f_\zeta(\hat{\mathbf{u}}). \tag{101}$$

With this transformation, (100) becomes

$$kf_\zeta(\hat{\mathbf{u}}') = \sum_\tau \eta_\tau(\hat{\mathbf{u}}')\int \mathrm{d}\Omega\, \eta^*_\tau(\hat{\mathbf{u}})f_\zeta(\hat{\mathbf{u}}), \tag{102}$$

where

$$\tau \equiv (\lambda, l, m, a) \tag{103}$$

and

$$\eta_\tau(\hat{\mathbf{u}}) \equiv \left(\frac{Z_a}{\lambda+1}\right)^{1/2} \mathrm{e}^{-i\mathbf{p}\cdot\mathbf{X}_a} Y_{\lambda,l,m}(\hat{\mathbf{u}}). \tag{104}$$

The hyperangular overlap integral between two such functions is

$$\begin{aligned} K_{\tau',\tau} &\equiv \int \mathrm{d}\Omega\, \eta^*_{\tau'}(\hat{\mathbf{u}})\eta_\tau(\hat{\mathbf{u}}) \\ &= \left(\frac{Z_{a'}Z_a}{(\lambda'+1)(\lambda+1)}\right)^{1/2} \int \mathrm{d}\Omega\ \mathrm{e}^{i\mathbf{p}\cdot(\mathbf{X}_{a'}-\mathbf{X}_a)} Y^*_{\lambda',l',m'}(\hat{\mathbf{u}}) Y_{\lambda,l,m}(\hat{\mathbf{u}}) \end{aligned} \tag{105}$$

Shibuya and Wulfman then let

$$f_\zeta(\hat{\mathbf{u}}') = \sum_\tau \eta_\tau(\hat{\mathbf{u}}')C'_{\tau,\zeta}. \tag{106}$$

With this substitution, (102) becomes

$$k\sum_\tau \eta_\tau(\hat{\mathbf{u}}')\, C'_{\tau,\zeta} = \sum_{\tau'} \eta_{\tau'}(\hat{\mathbf{u}}')K_{\tau',\tau}C'_{\tau,\zeta}. \tag{107}$$

The linear independence of the functions $\eta_\tau(\hat{\mathbf{u}}')$ then implies that the solutions satisfy the secular equation

$$\sum_\tau [K_{\tau',\tau} - k\delta_{\tau',\tau}]C'_{\tau,\zeta} = 0, \tag{108}$$

where

$$\varepsilon_\mu = -\frac{1}{2}k^2. \tag{109}$$

Of course in practice, the basis set needs to be truncated. The momentum–space molecular orbitals then become

$$\begin{aligned} \varphi^t_\zeta(\mathbf{p}) &= \frac{4k^{5/2}}{(k^2+p^2)^2} f_\zeta(\hat{\mathbf{u}}) \\ &= \sum_\tau \sqrt{\frac{Z_a}{n}} \frac{4k^{5/2}}{(k^2+p^2)^2} \mathrm{e}^{-i\mathbf{p}\cdot\mathbf{X}_a} Y_{\lambda,l,m}(\hat{\mathbf{u}})C'_{\tau,\zeta} \\ &= \sum_\tau \chi^t_\tau(\mathbf{p})C_{\tau,\zeta} \end{aligned} \tag{110}$$

with

$$C'_{\tau,\zeta} = \sqrt{\frac{Z_a}{n}}\, C_{\tau,\zeta}. \tag{111}$$

In direct space, this becomes

$$\begin{aligned}\varphi_\zeta(\mathbf{x}) &= \sum_\tau \chi_\tau(\mathbf{x}) C_{\tau,\zeta} \\ &\equiv \sum_{n,l,m,a} \chi_{n,l,m}(\mathbf{x}-\mathbf{X}_a) C_{\tau,\zeta}.\end{aligned} \tag{112}$$

The matrix $K_{\tau',\tau}$ can be written in the form

$$K_{\tau',\tau} = \sqrt{\frac{Z_{a'} Z_a}{n' n}}\, \mathfrak{S}_{\tau',\tau}, \tag{113}$$

where

$$\mathfrak{S}_{\tau',\tau} \equiv \int d\Omega\, e^{i\mathbf{p}\cdot\mathbf{R}} Y^*_{\mu'}(\hat{\mathbf{u}})\, Y_\mu(\hat{\mathbf{u}}), \tag{114}$$

where $\mathbf{R} = \mathbf{X}_{a'} - \mathbf{X}_a$ and $Y_\mu(\hat{\mathbf{u}}) \equiv Y_{n-1,l,m}(\hat{\mathbf{u}})$. Shibuya and Wulfman [35] evaluated these integrals by expanding $e^{i\mathbf{p}\cdot\mathbf{R}}$ in terms of hyperspherical harmonics. Alternatively, it is possible to show [43] that

$$\int d\Omega\; e^{i\mathbf{p}\cdot\mathbf{R}} Y_\mu(\hat{\mathbf{u}}) = (2\pi)^{3/2}\, f_{n,l}(S) Y_{l,m}(\hat{\mathbf{S}}), \tag{115}$$

where

$$\mathbf{S} = \{S_x, S_y, S_z\} \equiv k\mathbf{R} \quad S = k|\mathbf{R}|, \tag{116}$$

and

$$\mathbf{R} \equiv \mathbf{X}_{a'} - \mathbf{X}_a \tag{117}$$

and where

$$\begin{aligned}k^{3/2} f_{n,l} \equiv{}& R_{n,l} - \frac{1}{2}\sqrt{\frac{(n-l)(n+l+1)}{n(n+1)}} R_{n+1,l} \\ & - \frac{1}{2}\sqrt{\frac{(n+l)(n-l-1)}{n(n-1)}} R_{n-1,l}\end{aligned} \tag{118}$$

with

$$R_{n-1,l} \equiv 0 \qquad \text{if } l > n-1. \tag{119}$$

Here, the functions $R_{n,\,l}$ are the Coulomb Sturmian radial functions (Table 5). If we let then

$$c_{\mu'';\mu',\mu} = \int d\Omega_4\, Y^*_{\mu''}(\hat{\mathbf{u}}) Y^*_{\mu'}(\hat{\mathbf{u}}) Y_{\mu}(\hat{\mathbf{u}}), \tag{120}$$

then

$$Y^*_{\mu'}(\hat{\mathbf{u}})\, Y_{\mu}(\hat{\mathbf{u}}) = \sum_{\mu''} Y_{\mu''}(\hat{\mathbf{u}}) c_{\mu'';\mu',\mu} \tag{121}$$

and

$$\mathfrak{S}_{\tau',\tau} = (2\pi)^{3/2} \sum_{\mu''} Y_{l'',m''}(\hat{\mathbf{S}}) f_{n'',l''}(S) c_{\mu'';\mu',\mu}. \tag{122}$$

Table 5 $g_{n,l}(S), f_{n,l}(S)$, and $R_{n,l}(S)$, where $S \equiv k|\mathbf{X}_a{}' - \mathbf{X}_a|$. The functions $g_{n,l}(S)$ and $f_{n,l}(S)$ appear respectively in the two-center overlap integrals and the Shibuya–Wulfman integrals, while the functions $R_{n,l}(S)$ are Coulomb Sturmian radial functions

n	l	$g_{n,l}(S)$	$f_{n,l}(S)$	$R_{n,l}(S)/(2k^{3/2})$
1	0	$\frac{e^{-S}\left(3+3S+S^2\right)}{3}$	$e^{-S}(1+S)$	e^{-S}
2	0	$-\frac{1}{6}e^{-S}\left(3+3S+2S^2+S^3\right)$	$-\frac{2}{3}e^{-S}S^2$	$e^{-S}(1-S)$
2	1	$\frac{e^{-S}S\left(3+3S+S^2\right)}{6\sqrt{3}}$	$\frac{2e^{-S}S(1+S)}{3\sqrt{3}}$	$\frac{e^{-S}S}{\sqrt{3}}$
3	0	$\frac{1}{15}e^{-S}S^4$	$\frac{1}{3}e^{-S}S^2(-2+S)$	$\frac{1}{3}e^{-S}(3-6S+2S^2)$
3	1	$-\frac{e^{-S}S^3(1+S)}{15\sqrt{2}}$	$\frac{e^{-S}S(1+S-S^2)}{3\sqrt{2}}$	$\frac{2e^{-S}S(2-S)}{3\sqrt{2}}$
3	2	$\frac{e^{-S}S^2(3+3S+S^2)}{15\sqrt{10}}$	$\frac{e^{-S}S^2(1+S)}{3\sqrt{10}}$	$\frac{2e^{-S}S^2}{3\sqrt{10}}$

Table 6 This table shows the first few Shibuya–Wulfman integrals $\mathfrak{S}_{\tau',\tau}$, as functions of $\mathbf{S} \equiv k(\mathbf{X}_{a'} - \mathbf{X}_a)$, with $S \equiv |\mathbf{S}|$ and $\mathbf{S} \equiv (S \sin\theta \cos\phi, S \sin\theta \sin\phi, S \cos\theta)$. The integrals were generated by means of (122)

τ'	$\tau = (1,0,0,a)$	$\tau = (2,0,0,a)$
$(1,0,0,a')$	$e^{-S}(1+S)$	$-\frac{2}{3}e^{-S}S^2$
$(2,0,0,a')$	$-\frac{2}{3}e^{-S}S^2$	$\frac{1}{3}e^{-S}(3+3S-2S^2+S^3)$
$(2,1,-1,a')$	$-\frac{\sqrt{2}}{3}e^{-S}S(1+S)\sin\theta\ e^{i\phi}$	$\frac{1}{3\sqrt{2}}e^{-S}S(-1-S+S^2)\sin\theta\ e^{i\phi}$
$(2,1,0,a')$	$-\frac{2}{3}e^{-S}S(1+S)\cos\theta$	$\frac{1}{3}e^{-S}S(-1-S+S^2)\cos\theta$
$(2,1,1,a')$	$\frac{\sqrt{2}}{3}e^{-S}S(1+S)\sin\theta\ e^{-i\phi}$	$-\frac{1}{3\sqrt{2}}e^{-S}S(-1-S+S^2)\sin\theta\ e^{-i\phi}$

The matrix $c_{\mu'';\mu',\mu'}$ is a large but very sparse matrix that can be precalculated and stored. Thus, (122) gives us a rapid and convenient way of evaluating the Shibuya–Wulfman integrals. Similarly, the Wulfman integrals $\mathfrak{W}_{\tau',\tau}$ can be evaluated by means of Fock's projection, as can the molecular Sturmian overlap integrals

$$m_{\tau',\tau} \equiv \int d^3x\, \chi^*_{\tau'}(\mathbf{x})\chi_\tau(\mathbf{x}). \tag{123}$$

These are given by

$$m_{\tau',\tau} = (2\pi)^{3/2} \sum_{\mu''} Y_{l'',m''}(\hat{\mathbf{S}}) g_{n'',l''}(S) c_{\mu'';\mu'\mu}, \tag{124}$$

where the radial functions $g_{n,l}$ are given by

$$g_{n,l} \equiv f_{n,l} - \frac{1}{2}\sqrt{\frac{(n-l)(n+l+1)}{n(n+1)}} f_{n+1,l} - \frac{1}{2}\sqrt{\frac{(n+l)(n-l-1)}{n(n-1)}} f_{n-1,l} \tag{125}$$

with

$$f_{n-1,l} \equiv 0 \qquad \text{if } l > n-1. \tag{126}$$

5.4 Relationships Between the Momentum–Space and Direct–Space Formulations

From Fock's projection, one can show that the generalized solid angle on Fock's hypersphere is related to the volume element in momentum space by

$$d\Omega = d^3p \left(\frac{2k}{k^2+p^2}\right)^3. \tag{127}$$

Using this result, together with Fock's solution (95), we can rewrite the Shibuya–Wulfman integrals of (114) in the form

$$\mathfrak{S}_{\tau',\tau} = \int d^3p\, \chi^{t*}_{\tau'}(\mathbf{p}) \left(\frac{p^2+k^2}{2k^2}\right) \chi^t_\tau(\mathbf{p}). \tag{128}$$

But in discussing the direct–space formulation of the problem, we gave a different formula for the Shibuya–Wulfman integrals

$$\mathfrak{S}_{\tau',\tau} = \int d^3x\, \chi^{*}_{\tau'}(\mathbf{x}) \left(\frac{-\nabla^2+k^2}{2k^2}\right) \chi_\tau(\mathbf{x}). \tag{129}$$

Table 7 The first few overlap integrals $m_{\tau',\tau} \equiv \int d^3x \chi^*_{\tau'}(\mathbf{x})\chi_\tau(\mathbf{x})$ between displaced Coulomb Sturmians. The definitions of S, θ and ϕ are the same as in Table 6. The integrals were evaluated by means of equation (124)

τ'	$\tau = (1,0,0,a)$	$\tau = (2,0,0,a)$
$(1,0,0,a')$	$\frac{1}{3}e^{-S}(3+3S+S^2)$	$-\frac{1}{6}e^{-S}(3+3S+2S^2+S^3)$
$(2,0,0,a')$	$-\frac{1}{6}e^{-S}(3+3S+2S^2+S^3)$	$\frac{1}{15}e^{-S}(15+15S+5S^2+S^4)$
$(2,1,-1,a')$	$-\frac{1}{6\sqrt{2}}e^{-S}S(3+3S+S^2)\sin\theta\ e^{i\phi}$	$\frac{1}{15\sqrt{2}}e^{-S}S^3(1+S)\sin\theta\ e^{i\phi}$
$(2,1,0,a')$	$-\frac{1}{6}e^{-S}S(3+3S+S^2)\cos\theta$	$\frac{1}{15}e^{-S}S^3(1+S)\cos\theta$
$(2,1,1,a')$	$\frac{1}{6\sqrt{2}}e^{-S}S(3+3S+S^2)\sin\theta\ e^{-i\phi}$	$-\frac{1}{15\sqrt{2}}e^{-S}S^3(1+S)\sin\theta\ e^{-i\phi}$

To see that these two definitions of the Shibuya–Wulfman integrals are really the same, we insert the expression for $\chi_\tau\,(\mathbf{x})$ in terms of its Fourier transform into the direct-space definition of $\mathfrak{S}_{\tau',\tau}$. Thus we obtain the relation

$$\begin{aligned}\mathfrak{S}_{\tau',\tau} &= \int d^3x\ \chi^*_{\tau'}\,(\mathbf{x})\left(\frac{-\nabla^2+k^2}{2k^2}\right)\ \chi_\tau(\mathbf{x})\\ &= \frac{1}{(2\pi)^{3/2}}\int d^3x\,\chi^*_{\tau'}(\mathbf{x})\int d^3p\,\mathrm{e}^{i\mathbf{p}\cdot\mathbf{x}}\left(\frac{p^2+k^2}{2k^2}\right)\chi_\tau(\mathbf{p})\\ &= \int d^3p\left(\frac{1}{(2\pi)^{3/2}}\int d^3\,x\,\mathrm{e}^{-i\mathbf{p}\cdot\mathbf{x}}\,\chi_{\tau'}(\mathbf{x})\right)^*\left(\frac{p^2+k^2}{2k^2}\right)\ \chi_\tau(\mathbf{p})\\ &= \int d^3p\,\chi^{t*}_{t'}(\mathbf{p})\left(\frac{p^2+k^2}{2k^2}\right)\chi^t_\tau(\mathbf{p})\end{aligned} \tag{130}$$

From (130), it can also be seen that the Shibyya–Wulfman integrals can be interpreted as a species of nuclear attraction integrals, as Koga has pointed out [33, 34]. To see this, we note that $\chi_\tau(\mathbf{x})$ obeys the Schrödinger equation

$$\left(\frac{-\nabla^2+k^2}{2k^2}-\frac{Z_a}{k^2|\mathbf{x}-\mathbf{X}_a|}\right)\ \chi_\tau\,(\mathbf{x})=0. \tag{131}$$

Therefore,

$$\mathfrak{S}_{\tau',\tau}=\frac{1}{k^2}\int d^3x\ \chi^*_{\tau'}(\mathbf{x})\ \left(\frac{Z_a}{|\mathbf{x}-\mathbf{X}_a|}\right)\chi_\tau\,(\mathbf{x}), \tag{132}$$

which can be seen to be a nuclear attraction integral. For the special case where $\mathbf{X}_{a'}=\mathbf{X}_a$, (130) can be related to the generalized Sturmian orthonormality relations in direct space and reciprocal space, (15) and (16). In that case, making use of (94), (95), and (127), we have

$$\begin{aligned}&\int d^3x\,\chi^*_{\mu'}\,(\mathbf{x})\left(\frac{-\nabla^2\,+\,k^2}{2k^2}\right)\chi_\mu(\mathbf{x})\\ &\qquad=\int d^3p\,\chi^{t*}_{\mu'}(\mathbf{p})\left(\frac{p^2\,+\,k^2}{2k^2}\right)\chi^t_\mu\,(\mathbf{p})\\ &\qquad=\int \mathrm{d}\Omega\,Y^*_{\mu'}\,(\hat{\mathbf{u}})Y_\mu(\hat{\mathbf{u}})=\delta_{\mu',\mu}.\end{aligned} \tag{133}$$

This is, of course, also consistent with the potential-weighted orthonormality relation of the Coulomb Sturmian basis function, (7), as can be seen by making use of (132) for the special case where $\mathbf{X}_{a'}=\mathbf{X}_a=0$ and making the substitution $k=Z_a/n$. Looking at Table 6, we can see that for the special case where $S=0$, the diagonal elements of $\mathfrak{S}_{\tau',\tau}$ are equal to 1, while the off-diagonal elements vanish, as is required by the orthonormality relations (94). The momentum–space orthonormality relations for Coulomb Sturmians can be used to make a weakly convergent expansion of a plane wave in terms of $\chi_\mu(\mathbf{x})$ and $\chi_\mu(\mathbf{p})$ [25]. The orthonormality relations (133) can be used to determine the coefficients a_μ in the series

$$e^{i\mathbf{p}\cdot\mathbf{x}} = \left(\frac{p^2+k^2}{2k^2}\right)\sum_\mu \chi_\mu^{t*}(\mathbf{p})a_\mu. \tag{134}$$

Multiplying (134) on the left by $\chi_{\mu'}^t(\mathbf{p})$ and integrating over d^3p, we obtain

$$\int d^3p\, e^{i\mathbf{p}\cdot\mathbf{x}}\chi_{\mu'}^t(\mathbf{p}) = \sum_\mu \delta_{\mu'\mu}a_\mu = a_{\mu'}, \tag{135}$$

so that

$$a_\mu = \int d^3p\, e^{i\mathbf{p}\cdot\mathbf{x}}\,\chi_\mu^t\,(\mathbf{p}) = (2\pi)^{3/2}\,\chi_\mu(\mathbf{x}). \tag{136}$$

Thus, finally we obtain an expansion of the form

$$e^{i\mathbf{p}\cdot\mathbf{x}} = (2\pi)^{3/2}\left(\frac{p^2+k^2}{2k^2}\right)\sum_\mu \chi_\mu^{t*}(\mathbf{p})\chi_\mu(\mathbf{x}). \tag{137}$$

As Vincenzo Aquilanti has shown, the Shibuya–Wulfman integrals can be related to the effect of a translation on Coulomb Sturmians. Combining (75) and (137), we obtain

$$\begin{aligned}\chi_{n,l,m}(\mathbf{x}-\mathbf{X}_a) = &\sum_{n'l'm'}\chi_{n'l'm'}(\mathbf{x}-\mathbf{X}_{a'})\\ &\times\int d^3p\left(\frac{k^2+p^2}{2k^2}\right)e^{i\mathbf{p}\cdot(\mathbf{X}_{a'}-\mathbf{X}_a)}\chi_{n'l'm'}^{t*}(\mathbf{p})\chi_{nlm}^t(\mathbf{p}),\end{aligned} \tag{138}$$

which can be rewritten in the form

$$\chi_{nlm}(\mathbf{x}-\mathbf{X}_a) = \sum_{n'l'm'}\chi_{n'l'm'}(\mathbf{x}-\mathbf{X}_{a'})\,\mathfrak{S}_{\tau',\tau} \tag{139}$$

or, more simply,

$$\chi_\tau\,(\mathbf{x}) = \sum_{n'l'm'}\chi_{\tau'}(\mathbf{x})\mathfrak{S}_{\tau',\tau}. \tag{140}$$

In other words, if a Coulomb Sturmian located on one center is expanded in terms of Coulomb Sturmians located on another center, the expansion coefficients are Shibuya–Wulfman integrals. It should be noted, however, that this expansion is very slowly convergent when $k|\mathbf{X}_{a'} - \mathbf{X}_a|$ is large. Since two translations performed in succession can be expressed as a single translation, we have

$$\sum_{n'l'm'} \mathfrak{S}_{\tau'',\tau'} \mathfrak{S}_{\tau',\tau} = \mathfrak{S}_{\tau'',\tau}. \tag{141}$$

Thus the Shibuya–Wulfman integrals form a representation of the group of translations.

Koga and his co-workers also derived a sum rule obeyed by the matrices $\mathfrak{S}_{\tau',\tau}$ and the Wulfman matrix $\mathfrak{W}$. Koga's sum rule can be derived with the help of (140) and (132):

$$\begin{aligned}
&\sum_a \int d^3x\, \chi^*_{n'l'm'}(\mathbf{x} - \mathbf{X}_{a'})\, \frac{Z_a}{|\mathbf{x}-\mathbf{X}_a|}\, \chi_{n''l''m''}(\mathbf{x} - \mathbf{X}_{a''}) \\
&\quad = \sum_{nlma} \mathfrak{S}_{\tau,\tau''} \int d^3x \chi^*_{n'l'm'}(\mathbf{x} - \mathbf{X}_{a'}) \frac{Z_a}{|\mathbf{x} - \mathbf{X}_a|}\, \chi_{nlm}(\mathbf{x} - \mathbf{X}_a) \\
&\quad = \sum_\tau \mathfrak{S}_{\tau',\tau}\, \frac{Z_a k}{n}\, \mathfrak{S}_{\tau,\tau''}.
\end{aligned} \tag{142}$$

This result can be used to evaluate matrix elements of the many center potential $\upsilon(\mathbf{x})$ of (71):

$$\mathfrak{W}_{\tau',\tau''} \equiv -\frac{1}{k} \int d^3x\, \chi^*_{\tau'}(\mathbf{x})\, \upsilon(\mathbf{x}) \chi_{\tau''}(\mathbf{x}) = \sum_\tau \mathfrak{S}_{\tau',\tau} \frac{Z_a}{n} \mathfrak{S}_{\tau,\tau''}. \tag{143}$$

Essentially what is happening in (142) is that the functions $\chi^*_{n'l'm'}(\mathbf{x} - \mathbf{X}_{a'})$ and $\chi_{nlm}(\mathbf{x} - \mathbf{X}_a)$ are translated respectively from the points $\mathbf{X}_{a'}$ and $\mathbf{X}_{a''}$ to the point $\mathbf{X}_a$. Here the matrix element of the attractive Coulomb potential of nucleus a is evaluated by means of (133). We now remember (113), which can be written in the form

$$\mathfrak{S}_{\tau',\tau} = \sqrt{\frac{n'}{Z_{a'}}} K_{\tau',\tau} \sqrt{\frac{n}{Z_a}}. \tag{144}$$

Combining this with the sum rule of (143), we have

$$\mathfrak{W}_{\tau',\tau''} = \sum_\tau \mathfrak{S}_{\tau',\tau}\, \frac{Z_a}{n} \mathfrak{S}_{\tau,\tau''} = \sum_\tau \sqrt{\frac{n'}{Z_{a'}}} K_{\tau',\tau}\, K_{\tau,\tau''} \sqrt{\frac{n''}{Z_{a''}}}. \tag{145}$$

Then the direct–space secular equation (73) can be rewritten as

$$\sum_{\tau''} \left[\sum_\tau K_{\tau',\tau} K_{\tau,\tau''} - k K_{\tau',\tau''} \right] C'_{\tau'',\zeta} = 0, \tag{146}$$

which is a second iterated form of (108): Thus the direct–space and momentum–space solutions for molecular orbitals based on Coulomb Sturmians are seen to be the same, always remembering that coefficients that appear in the two forms are related by (111). Since we have two forms of the molecular Sturmian secular equation, (73) and (108), one might ask which form is the best. The answer is that if the number of basis functions used is small, (73) gives the most accurate results. However, particularly for small values of the parameter S, (73) suffers from problems of overcompleteness when the number of basis functions is increased. By contrast, as Monkhorst and Jeziorski have pointed out [44], (108) has no such problems, and therefore it is the method of choice when the basis set used is very large or when S is small. With a large basis set, (108) is capable of yielding solutions of very high accuracy. Koga and Matsuhashi [34] used an iterated version of this equation to obtain energies with 10-figure accuracy for the ground state of the H_2^+ ion. We can call the matrix $K_{\tau',\tau}$ the *Koga matrix* to honor the contributions of Prof. T. Koga and his group.

6 Molecular Calculations Using Isoenergetic Configurations

We have just seen that the treatment of a single electron moving in the field of several nuclei has been developed by a number of authors. Let us now turn to the question of whether molecular orbitals based on Coulomb Sturmians can be used to treat N-electron molecules. To answer this question, let us consider a Slater determinant of the form

$$\Phi_\nu(\mathbf{x}) = |\varphi_{\zeta 1}\varphi_{\zeta 2}\cdots\varphi_{\zeta N}| \equiv \frac{1}{\sqrt{N!}}\begin{vmatrix} \varphi_{\zeta_1}(1) & \varphi_{\zeta_2}(1) & \varphi_{\zeta_3}(1) & \cdots \\ \varphi_{\zeta_1}(2) & \varphi_{\zeta_2}(2) & \varphi_{\zeta_3}(2) & \cdots \\ \varphi_{\zeta_1}(3) & \varphi_{\zeta_2}(3) & \varphi_{\zeta_3}(3) & \cdots \\ \vdots & \vdots & \vdots & \end{vmatrix} \tag{147}$$

built up from molecular orbitals of the form shown in (67), where the coefficients $C_{\tau,\zeta}$ are solutions to (73). The Slater determinant will then satisfy

$$\sum_{j=1}^{N}\left[-\frac{1}{2}\nabla_j^2 + \frac{k^2}{2} + \beta_\nu v(\mathbf{x}_j)\right]\Phi_\nu(\mathbf{x}) = 0, \tag{148}$$

which can be rewritten in the form

$$\begin{aligned}&\left[\sum_{j=1}^{N}\left(-\frac{1}{2}\nabla_j^2 + \frac{k^2}{2}\right) + \beta_\nu V_0(\mathbf{x})\right]\Phi_\nu(\mathbf{x}) \\ &\qquad = \left[-\frac{1}{2}\sum_{j=1}^{N}\nabla_j^2 + \beta_\nu V_0(\mathbf{x}) + \frac{Nk^2}{2}\right]\Phi_\nu(\mathbf{x}) = 0,\end{aligned} \tag{149}$$

where

$$V_0\left(\mathbf{x}\right) = \sum_{j=1}^{N} \upsilon(\mathbf{x}_j) = -\sum_{j=1}^{N}\sum_{a} \frac{Z_a}{|\mathbf{x}_j - \mathbf{X}_a|}. \tag{150}$$

It can be seen that if we let

$$E_\kappa = -\sum_{j=1}^{N} \frac{k^2}{2} = -\frac{Nk^2}{2}, \tag{151}$$

then (150) has the same form as (10). In other words, if the constants β_ν are chosen in such a way that the solutions to (149) are isoenergetic, all belonging to the energy $E_\kappa = -Nk^2/2$, the set of functions $\Phi_\nu\left(\mathbf{x}\right)$ will be a generalized Sturmian basis set. We now wish to solve the nonrelativistic Schrödinger equation for the molecule:

$$\left[\sum_{j=1}^{N}\left(-\frac{1}{2}\nabla_j^2 + \frac{k^2}{2}\right) + V(\mathbf{x})\right]\Psi_\kappa(\mathbf{x}) = 0, \tag{152}$$

where

$$V(\mathbf{x}) = \sum_{j=1}^{N} \upsilon(\mathbf{x}_j) + \sum_{i>j}^{N}\sum_{j=1}^{N}\frac{1}{r_{ij}}. \tag{153}$$

If we substitute the superposition

$$\Psi_\kappa\left(\mathbf{x}\right) = \sum_{\nu} \Phi_\nu(\mathbf{x})\, B_{\nu\kappa}, \tag{154}$$

into the Schrödinger equation, multiply from the left by a conjugate basis function, and integrate over all the coordinates, we obtain a generalized Sturmian secular equation of the form

$$\sum_{\nu}\int \mathrm{d}x\, \Phi_{\nu'}^{*}(\mathbf{x}) \left[\sum_{j=1}^{N}\left(-\frac{1}{2}\nabla_j^2 + \frac{k^2}{2}\right) + V(\mathbf{x})\right]\Phi_\nu\left(\mathbf{x}\right) B_{\nu\kappa} = 0. \tag{155}$$

Introducing the k-independent matrices

$$T_{\nu'\nu}^{(N)} \equiv -\frac{1}{k}\int \mathrm{d}x\, \Phi_{\nu'}^{*}\left(\mathbf{x}\right) V(\mathbf{x})\, \Phi_\nu(\mathbf{x}) \tag{156}$$

and

$$\mathfrak{S}^{(N)}_{\nu'\nu} \equiv \frac{1}{k^2}\int \mathrm{d}x\, \Phi^*_{\nu'}(\mathbf{x}) \sum_{j=1}^{N} \left(-\frac{1}{2}\nabla_j^2 + \frac{k^2}{2}\right) \Phi_\nu(\mathbf{x}), \tag{157}$$

we can rewrite (155) in the form

$$\sum_{\nu} \left[T^{(N)}_{\nu'\nu} - k\mathfrak{S}^{(N)}_{\nu'\nu}\right] B_{\nu\kappa} = 0. \tag{158}$$

6.1 Constructing $T^{(N)}_{\nu'\nu}$ and $\mathfrak{S}^{(N)}_{\nu'\nu}$ from 1-Electron Components

In order to construct the k-independent matrices $T^{(N)}_{\nu'\nu}$ and $\mathfrak{S}^{(N)}_{\nu'\nu}$, we first need to normalize the molecular orbitals. The normalization condition is given by

$$\tilde{m}_{\zeta,\zeta} \equiv \int d^3x_j\, \varphi^*_\zeta(\mathbf{x}_j)\, \varphi_\zeta(\mathbf{x}_j) = \sum_{\tau'}\sum_{\tau} C^*_{\tau',\zeta} m_{\tau',\tau} C_{\tau,\zeta} = 1, \tag{159}$$

where

$$m_{\tau'\tau} \equiv \int d^3x_j\, \chi^*_{\tau'}(\mathbf{x}_j)\chi_\tau(\mathbf{x}_j). \tag{160}$$

Having normalized the molecular orbital coefficients $C_{\tau,\zeta}$, we construct the 1-electron matrices

$$\tilde{\upsilon}_{\zeta'\zeta} \equiv \int d^3x_j\, \varphi^*_{\zeta'}(\mathbf{x}_j)\upsilon(\mathbf{x}_j)\varphi_\zeta(\mathbf{x}_j) = -k\sum_{\tau'}\sum_{\tau} C^*_{\tau'\zeta'}\mathfrak{W}_{\tau'\tau}C_{\tau\zeta} \tag{161}$$

and

$$\tilde{\mathfrak{S}}_{\zeta'\zeta} \equiv \sum_{\tau'}\sum_{\tau} C^*_{\tau'\zeta'}\mathfrak{S}_{\tau'\tau}C_{\tau\zeta}. \tag{162}$$

Once we are in possession of the matrices $\tilde{m}_{\zeta,\zeta}$, $\tilde{\upsilon}_{\zeta'\zeta}$ and $\tilde{\mathfrak{S}}_{\zeta'\zeta}$, the Slater–Condon rules can be used to build up the k-independent N-electron matrices $\mathfrak{S}^{(N)}_{\nu'\nu}$ and

$$T^{0,(N)}_{\nu'\nu} \equiv -\frac{1}{k}\int \mathrm{d}x\, \Phi^*_{\nu'}(\mathbf{x})V_0(\mathbf{x})\Phi_\nu(\mathbf{x}), \tag{163}$$

which are based on the Slater determinants of our generalized Sturmian basis set. The construction of the interelectron repulsion matrix

$$T'^{(N)}_{\nu'\nu} \equiv -\frac{1}{k}\int \mathrm{d}x\ \Phi^*_{\nu'}(\mathbf{x})V'(\mathbf{x})\Phi_\nu(\mathbf{x}) \tag{164}$$

is more difficult, but we have developed methods for evaluating interelectron repulsion integrals based on molecular Sturmians. The most important of these integrals can be evaluated by a rapid method that makes use of Fock's relationship and the properties of hyperspherical harmonics. This method will be discussed in the next section. The fact that $T'^{(N)}_{\nu'\nu}$ is independent of k can be established by an argument similar to that used in (42)–(47).

6.2 Interelectron Repulsion Integrals for Molecular Sturmians from Hyperspherical Harmonics

Consider an interelectron repulsion integral of the form

$$J_{\mu_1,\mu_2,\mu_3,\mu_4,} = \int d^3x \int d^3x'\, \rho_{\mu_1,\mu_2}(\mathbf{x}-\mathbf{X}_a)\frac{1}{|\mathbf{x}-\mathbf{x}'|}\rho_{\mu_3,\mu_4}(\mathbf{x}'-\mathbf{X}_{a'}). \tag{165}$$

Here, $\rho_{\mu_1,\mu_2}(\mathbf{x}-\mathbf{X}_a)$ is a charge distribution centered at the point $\mathbf{X}_a$, while $\rho_{\mu_3,\mu_4}(\mathbf{x}'-\mathbf{X}_{a'})$ is another charge distribution centered on a different point $\mathbf{X}_{a'}$, and $\mu_i \equiv (n_i,\ l_i,\ m_i)$. We now introduce the Fourier representation of the Green's function of Poisson's equation:

$$\frac{1}{|\mathbf{x}-\mathbf{x}'|} = \frac{1}{2\pi^2}\int d^3p\,\frac{1}{p^2}e^{-i\mathbf{p}\cdot(\mathbf{x}-\mathbf{x}')}. \tag{166}$$

Then $J_{\mu_1,\mu_2,\mu_3,\mu_4}$ can be rewritten in the form

$$J_{\mu_1,\mu_2,\mu_3,\mu_4} = 4\pi\int d^3p\,\frac{1}{p^2}\mathrm{e}^{i\mathbf{p}\cdot\mathbf{R}}\,\rho^t_{\mu_1,\mu_2}(\mathbf{p})\rho^t_{\mu_3,\mu_4}(-\mathbf{p}), \tag{167}$$

where

$$\rho^t_{\mu_i,\mu_j}(\mathbf{p}) = \frac{1}{(2\pi)^{3/2}}\int d^3x\rho_{\mu_i,\mu_j}(\mathbf{x})\,\mathrm{e}^{-i\mathbf{p}\cdot\mathbf{x}} \tag{168}$$

and where

$$\mathbf{R} \equiv \mathbf{X}_{a'} - \mathbf{X}_a. \tag{169}$$

We will now show that when the densities are produced by products of Coulomb Sturmians, interelectron repulsion integrals of the type shown in (165) and (167) can be readily evaluated using Fock's relationship and the properties of hyperspherical harmonics. Suppose that

$$\rho_{\mu_1,\mu_2}(\mathbf{x}) = \chi^*_{\mu_1}(\mathbf{x})\chi_{\mu_2}(\mathbf{x}) = R_{n_1,l_1}(r)\, R_{n_2,l_2}(r)\, Y^*_{l_1,m_1}(\hat{\mathbf{x}})\, Y_{l_2,m_2}(\hat{\mathbf{x}}). \tag{170}$$

Then from the potential-weighted orthonormality relation (7), it follows that

$$\rho_{\mu_1,\mu_2}(\mathbf{x}) = \sum_{\mu} R_{n,l}(2r) Y_{l,m}(\hat{\mathbf{x}})\, \mathcal{C}_{\mu;\mu_1,\mu_2} \equiv \sum_{\mu} \chi_{\mu}(2\mathbf{x})\, \mathcal{C}_{\mu;\mu_1,\mu_2}, \tag{171}$$

where

$$\begin{aligned} \mathcal{C}_{\mu;\mu_1,\mu_2} &= \frac{n}{2}\int_0^\infty \mathrm{d}r\, r\, R_{n,l}(2r)\, R_{n_1,l_1}(r)\, R_{n_2,l_2}(r) \\ &\quad \times \int \mathrm{d}\Omega_3\;\; Y^*_{l,m}(\hat{\mathbf{x}})\, Y^*_{l_1,m_1}(\hat{\mathbf{x}})\, Y_{l_2,m_2}(\hat{\mathbf{x}}). \end{aligned} \tag{172}$$

The series in (171) terminates and the expansion is exact. The coefficients $\mathcal{C}_{\mu;\mu_1,\mu_2}$ form a large but very sparse matrix that can be precalculated and stored. What we have done here is to expand a product of two Coulomb Sturmians in terms of a single Coulomb Sturmian with double the k value. When this is done, the exponential part is automatically correct, and only the polynomial parts need to be taken care of. Hence, the sparseness of $\mathcal{C}_{\mu'',\mu',\mu}$. Then

$$\begin{aligned} J_{\mu_1,\mu_2,\mu_3,\mu_4} &\equiv \int d^3x \int d^3x' \rho_{\mu_1,\mu_2}(\mathbf{x} - \mathbf{X}_a)\frac{1}{|\mathbf{x} - \mathbf{x}'|}\rho_{\mu_3,\mu_4}(\mathbf{x}' - \mathbf{X}_{a'}) \\ &= \sum_{\mu',\mu} J_{\mu',\mu}\mathcal{C}_{\mu';\mu_1,\mu_2}\mathcal{C}_{\mu;\mu_3,\mu_4}, \end{aligned} \tag{173}$$

where

$$J_{\mu',\mu} \equiv 4\pi \int d^3p \frac{1}{p^2} \mathrm{e}^{i\mathbf{p}\cdot\mathbf{R}} \rho^t_{\mu'}(\mathbf{p}) \rho^t_{\mu}(-\mathbf{p}) \tag{174}$$

and where

$$\begin{aligned} \rho_{\mu'}(\mathbf{x}) &= R_{n',l'}(2r) Y_{l',m'}(\hat{\mathbf{x}}) \\ \rho_{\mu}(\mathbf{x}) &= R_{n,l}(2r) Y_{l,m}(\hat{\mathbf{x}}). \end{aligned} \tag{175}$$

Then from Fock's relationship, we have

$$J_{\mu',\mu} = 4\pi \int d^3p \frac{1}{p^2} \mathrm{e}^{i\mathbf{p}\cdot\mathbf{R}} \tilde{M}^2(p)(-1)^l Y_{\mu'}(\hat{\mathbf{w}}) Y_\mu(\hat{\mathbf{w}}), \tag{176}$$

where $Y_\mu(\hat{\mathbf{w}}) \equiv Y_{n-1,l,m}(\hat{\mathbf{w}})$ and

$$\hat{\mathbf{w}} = (w_1, w_2, w_3, w_4) = \left(\frac{4kp_1}{4k^2+p^2}, \frac{4kp_2}{4k^2+p^2}, \frac{4kp_3}{4k^2+p^2}, \frac{4k^2-p^2}{4k^2+p^2} \right). \tag{177}$$

In Fock's projection, we are now using double the value of k. Similarly, we now have

$$\tilde{M}(p) \equiv \frac{4(2k)^{5/2}}{(4k^2+p^2)^2}. \tag{178}$$

We can now go a step further by introducing the matrix

$$\tilde{c}_{\mu'',\mu',\mu} \equiv (-1)^l \int \mathrm{d}\Omega \; \mathrm{Y}^*_{\mu''}(\hat{\mathbf{w}}) Y_{\mu'}(\hat{\mathbf{w}}) Y_\mu(\hat{\mathbf{w}}), \tag{179}$$

which is also large but sparse, and which can also be precalculated and stored. Then

$$J_{\mu',\mu} = \sum_{\mu''} J_{\mu''} \, \tilde{c}_{\mu'';\mu',\mu}, \tag{180}$$

where

$$J_\mu \equiv 4\pi \int d^3p \frac{1}{p^2} \mathrm{e}^{i\mathbf{p}\cdot\mathbf{R}} \; \tilde{M}^2(p) Y_\mu(\hat{\mathbf{w}}). \tag{181}$$

The integral J_μ can be rewritten as

$$J_\mu = (4\pi)^2 k Y_{l,m}(\hat{\mathbf{R}}) \int_0^\infty \mathrm{d}p \; \tilde{M}(p) R^t_{n,l}(p) j_l(pR), \tag{182}$$

where

$$R^t_{n,l}(p) \equiv \sqrt{\frac{2}{\pi}} \int_0^\infty \mathrm{d}p \; p^2 j_l(pr) R_{n,l}(2kr). \tag{183}$$

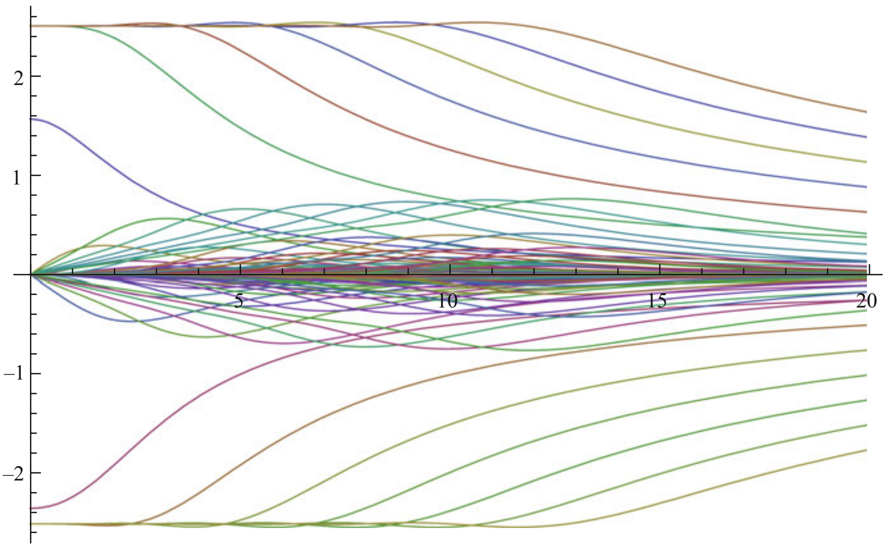

Fig. 3 The integrals $\int_0^\infty \mathrm{d}p\, \tilde{M}(p) R^t_{n,l}(p) j_l(pR)$ of (182) are shown here plotted as functions of $S \equiv kR$. There are 105 functions, corresponding $n = 1, 2, \ldots, 14$ and $l = 0, 1, \ldots, n - 1$

The integrals over dp in (182) are simple enough to be evaluated by Mathematica and they can conveniently be stored as functions kR in the form of interpolation functions. Notice that the integrals depend only on n and l, and there are therefore fewer of them than there would be if they also depended on m. The first 105 of these functions are shown in Fig. 3. Equations (173), (180), and (182) give us a very rapid and convenient way of evaluating integrals of the form shown in (173), where the densities are formed from products of Coulomb Sturmian basis functions located respectively on the two centers, a and a'. They constitute the largest contribution to the effects of interelectron repulsion.

6.3 3-Center and 4-Center Interelectron Repulsion Integrals

One also needs to calculate 3-center and 4-center integrals of the form

$$J_{\tau_1,\tau_2,\tau_3,\tau_4} = \int d^3x \int d^3x' \; \chi^*_{\tau_1}(\mathbf{x})\chi_{\tau_2}(\mathbf{x}) \frac{1}{|\mathbf{x} - \mathbf{x}'|} \chi^*_{\tau_3}(\mathbf{x}')\chi_{\tau_4}(\mathbf{x}'). \qquad (184)$$

Here, τ has the meaning defined by (65), where the index a is the index of the atom on which a Coulomb Sturmian basis function is located. In the case of a general 4-center integral, all the a values may be different from one another. Integrals of this type fall off rapidly with interatomic distances and they vanish as the overlap vanishes; but they are needed nevertheless, and we have developed a special type of Gaussian expansion method to evaluate them: Expressed in terms of the regular solid harmonics R_l^m, the Coulomb Sturmian basis functions can be written as [45]

$$\begin{aligned}\chi_{n,l,m}(\mathbf{x}) &= R_{n,l}(r)Y_{l,m}(\hat{\mathbf{x}})\\ &= \sqrt{\frac{2l+1}{4\pi}}R_{n,l}(r)s^{-l}\,\mathsf{R}_l^m(k\mathbf{x})\\ &\approx \sum_i \Gamma_{n,l,i}\mathrm{e}^{-a_i|k\mathbf{x}|^2}\mathsf{R}_l^m(k\mathbf{x}),\end{aligned} \tag{185}$$

where $s \equiv kr$ and where the coefficients $\Gamma_{n,l,i}$ are defined by the relationship

$$\sqrt{\frac{2l+1}{4\pi}}R_{n,l}(r)s^{-l} \approx \sum_i \Gamma_{n,l,i}\mathrm{e}^{-a_i s^2}. \tag{186}$$

Then

$$\chi_\tau(\mathbf{x}) = \chi_{n,l,m}(\mathbf{x}-\mathbf{X}_a) \approx \sum_i \Gamma_{n,l,i}\,\mathrm{e}^{-a_i|k\mathbf{x}-k\mathbf{X}_a|^2}\mathsf{R}_l^m(k\mathbf{x}-k\mathbf{X}_a). \tag{187}$$

In this expansion, the coefficients $\Gamma_{n,l,i}$ and a_i are universals that can be calculated once and for all, and that never have to be recalculated. When the basis functions scale with changing values of k, the expansion scales automatically too. Because the coefficients are universals, we can use many terms in the expansion and thus obtain especially good accuracy. The fact that the interelectron repulsion integrals divided by k are independent of k can be shown by arguments similar to those shown in (42)–(47). When divided by k, the interelectron repulsion integrals are pure functions of the parameters $\mathbf{s} \equiv k\mathbf{x}$ and $\mathbf{S}_a \equiv k\mathbf{X}_a$. Therefore, they scale automatically with changes of scale of the basis functions. The independence from k also implies that the molecular-Sturmian-based interelectron repulsion integrals can be pre-evaluated and stored.

6.4 Pilot Calculations

Since this method has been developed very recently, we have only begun to test it with a few pilot calculations. These are shown in Figs. 4 and 5. Our pilot calculations use very few basis functions, but nevertheless they yield quite accurate results. This seems to us to be a promising result, and we hope to develop the method further.

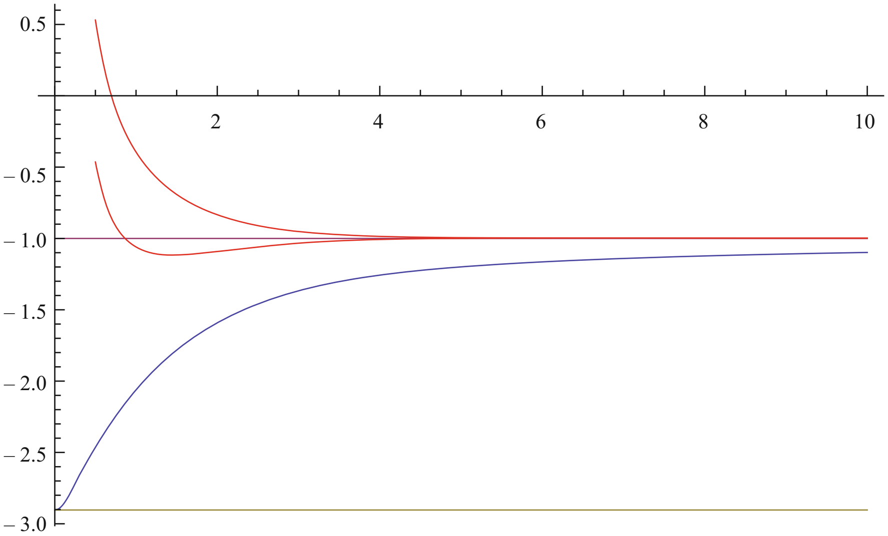

Fig. 4 This figure shows the results of a preliminary calculation on the dissociation of the hydrogen molecule using a very restricted basis set. Energies are shown in Hartrees as functions of the internuclear separation, measured in Bohrs. The *lowest curve* shows the ground-state electronic energy by itself, without internuclear repulsion. The two *upper curves* show the ground state and first singlet excited state electronic energies with nuclear repulsion added, i.e., the total energies of the two states. The calculated equilibrium bond length is 1.41 Bohrs, which can be compared with the experimental value, 1.40 Bohrs. It can be seen from the figure that at a separation of 5 Bohrs or more, the molecule is completely dissociated, and in fact the calculated wave function at that internuclear separation corresponds to two neutral hydrogen atoms, each with its own electron, while the total energy corresponds to that of two isolated hydrogen atoms

7 Discussion

This chapter is a review, and most of what is reported here can be found in our own books and papers and those of the authors whose works are cited. There are, however, some results that do not appear elsewhere. Among these are (42)–(47), that demonstrate that $T'_{\nu',\nu}$, the interelectron repulsion matrix based on Goscinskian congurations, is energy independent and consists of pure numbers when expressed in atomic units. Other new results include Table 3, and much of Sect. 4.4. Sects. 5.2–5.4 and much of the Appendix were previously reported only in the Ph.D. thesis of one of us and in works that are now in press.

Appendix: Angular and Hyperangular Integrations

In a 3-dimensional space, the volume element is given by $dx_1dx_2dx_3$ in Cartesian coordinates or by $r^2dr\ d\Omega$ in spherical polar coordinates. Thus, we can write

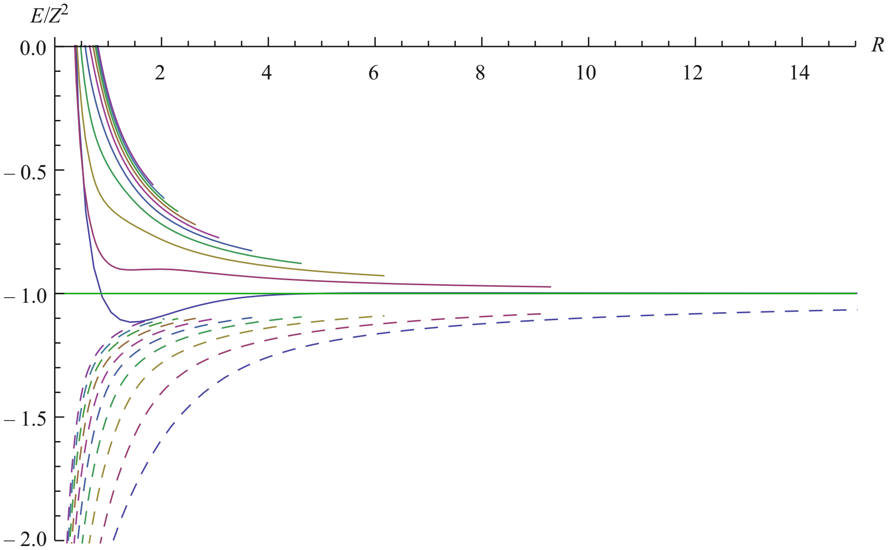

Fig. 5 This figure shows ground-state energies divided by Z^2 for the 2-electron isoelec-tronic series for homonuclear diatomic molecules, Z being the nuclear charges. The energies in Hartrees are shown as functions of the interatomic distance R, measured in Bohrs. The *dotted curves* are electronic energies alone, while the *solid curves* also include internuclear repulsion. For both the solid and dotted curves, the *lowest curve* corresponds to the smallest value of Z. As in Fig. 4, a very restricted basis set was used for the calculation

$$\mathrm{d}x_1\mathrm{d}x_2\mathrm{d}x_3 = r^2\mathrm{d}r\,\mathrm{d}\Omega, \tag{188}$$

where $\mathrm{d}\Omega$ is the element of solid angle. Similarly, in a d-dimensional space we can write

$$\mathrm{d}x_1\mathrm{d}x_2\cdots\mathrm{d}x_d = r^{d-1}\mathrm{d}r\,\mathrm{d}\Omega, \tag{189}$$

where r is the hyperradius and where $\mathrm{d}\Omega$ is the element of generalized solid angle. We will now prove a general theorem for angular and hyperangular integration [24]:

Theorem 1 (Angular integration theorem).
Let

$$I(\mathbf{n}) \equiv \int \mathrm{d}\Omega \left(\frac{x_1}{r}\right)^{n_1}\left(\frac{x_2}{r}\right)^{n_2}\cdots\left(\frac{x_d}{r}\right)^{n_d}, \tag{190}$$

where $x_1, x_2, \ldots, x_d$ are the Cartesian coordinates of a d-dimensional space, $\mathrm{d}\Omega$ *is the generalized solid angle, r is the hyperradius, defined by*

$$r^2 \equiv \sum_{j=1}^{d} x_j^2, \tag{191}$$

and where the n_j's are positive integers or zero. Then

$$I(\mathbf{n}) = \begin{cases} \dfrac{\pi^{d/2}}{2^{(n/2-1)}\Gamma\left(\frac{d+n}{2}\right)} \displaystyle\prod_{j=1}^{d} (n_j - 1)!! & \text{if all the } n_j'\text{s are even} \\ 0 & \text{otherwise,} \end{cases} \tag{192}$$

where

$$n \equiv \sum_{j=1}^{d} n_j. \tag{193}$$

Proof. Consider the integral

$$\int_0^\infty dr\, r^{d-1} e^{-r^2} \int d\Omega\, x_1^{n1} x_2^{n2} \cdots\, x_d^{nd} = \prod_{j=1}^{d} \int_{-\infty}^{\infty} dx_j\, x_j^{n_j} e^{-x_j^2}. \tag{194}$$

If n_j is zero or a positive integer, then

$$\int_{-\infty}^{\infty} dx_j\, x_j^{n_j}\, e^{-x_j^2} = \begin{cases} \dfrac{(n_j-1)!!\sqrt{\pi}}{2^{n_j/2}} & \text{if } n_j \text{ is even} \\ 0 & \text{if } n_j \text{ is odd,} \end{cases} \tag{195}$$

so that the right-hand side of (194) becomes

$$\prod_{j=1}^{d} \int_{-\infty}^{\infty} dx_j\, x_j^{n_j} e^{-x_j^2} = \begin{cases} \dfrac{\pi^{d/2}}{2^{n/2}} \displaystyle\prod_{j=1}^{d} (n_j - 1)!! & \text{if all the } n_j'\text{s are even} \\ 0 & \text{otherwise.} \end{cases} \tag{196}$$

The left-hand side of (5) can be written in the form

$$\int_0^\infty dr\, r^{d+n-1}\, e^{-r^2} \int d\Omega \left(\frac{x_1}{r}\right)^{n_1} \left(\frac{x_2}{r}\right)^{n_2} \cdots \left(\frac{x_d}{r}\right)^{n_d} = \frac{I(\mathbf{n})}{2} \Gamma\left(\frac{d+n}{2}\right). \tag{197}$$

Substituting (196) and (197) into (194), we obtain (192). Q.E.D.

Comments
In the special case where $d = 3$, (192) becomes

$$\int d\Omega \left(\frac{x_1}{r}\right)^{n_1} \left(\frac{x_2}{r}\right)^{n_2} \left(\frac{x_d}{r}\right)^{n_3} = \begin{cases} \dfrac{4\pi}{(n+1)!!} \displaystyle\prod_{j=1}^{3} (n_j - 1)!! & \text{all } n_j'\text{s even} \\ 0 & \text{otherwise.} \end{cases} \tag{198}$$

Let us now consider a general polynomial (not necessarily homogeneous) of the form:

$$P(\mathbf{x}) = \sum_{\mathbf{n}} c_{\mathbf{n}} \; x_1^{n_1} \; x_2^{n_2} \ldots x_d^{n_d}. \tag{199}$$

Then we have

$$\int \mathrm{d}\Omega \;\; P(\mathbf{x}) = \sum_{\mathbf{n}} c_{\mathbf{n}} \; \int \mathrm{d}\Omega \;\; x_1^{n_1} \; x_2^{n_2} \ldots x_d^{n_d} = \sum_{\mathbf{n}} c_{\mathbf{n}} \; r^n \; I(\mathbf{n}). \tag{200}$$

It can be seen that (192) can be used to evaluate the generalized angular integral of any polynomial whatever, regardless of whether or not it is homogeneous.

It is interesting to ask what happens if the n_j's are not required to be zero or positive integers. If all the n_j's are real numbers greater than -1, then the right-hand side of (194) can still be evaluated and it has the form

$$\prod_{j=1}^{d} \int_{-\infty}^{\infty} \mathrm{d}x_j \; x_j^{n_j} \mathrm{e}^{-x_j^2} = \prod_{j=1}^{d} \frac{1}{2} \left(1 + \mathrm{e}^{i\pi n_j}\right) \Gamma\left(\frac{n_j + 1}{2}\right). \tag{201}$$

Thus, (192) becomes

$$I(\mathbf{n}) = \frac{2}{\Gamma\left(\frac{d+n}{2}\right)} \prod_{j=1}^{d} \frac{1}{2} \left(1 + \mathrm{e}^{i\pi n_j}\right) \Gamma\left(\frac{n_j + 1}{2}\right) \qquad n_j > -1, \quad j = 1, \ldots, d. \tag{202}$$

This more general equation reduces to (192) in the special case where the n_j's are required to be either zero or positive integers.

References

1. Ballhausen CJ (1962) Introduction to Ligand Field Theory. McGraw-Hill, New York
2. Ballhausen CJ (1979) Molecular Electronic Structure of Transition Metal Complexes. McGraw-Hill, New York
3. Ballhausen CJ, Gray HB (1965) Molecular Orbital Theory. Frontiers in chemistry. W.A. Benjamin, New York
4. Ballhausen CJ, Gray HB (1980) Molecular Electronic Structures; An Introduction. W.A. Benjamin, New York
5. Avery JS, Dahl JP, Hansen AE (1987) Understanding Molecular Properties. Reidel, Dordrecht
6. Dahl JP (2001) Introduction to the Quantum World of Atoms and Molecules. World Scientific, Singapore
7. Dahl JP, Ballhausen CJ (1961) The electronic structure of ferrocene. Matematisk-Fysiske Meddelelser, Kongelige Danske Videnskabernes Selskab 33:1–23
8. Harris FE (1973) Computation methods in quantum chemistry. Preprint, Quantum Chemistry Group, Uppsala University
9. Harris FE, Michels HH (1967) Evaluation of molecular integrals for Slater-type orbitals. Adv Chem Phys 13:205

10. Pinchon D, Hoggan PE (2009) Gaussian approximation of exponential type orobitals based on b functions. Int J Quantum Chem 109:135–148
11. Steinborn EO (1983) On the evaluation of exponential (Slater) type integrals. In: Dierksen GHF, Wilson S (eds) Methods in Computational Molecular Physics. Reidel, Dordrecht
12. Weatherford CA Scaled hydrogenic sturmians as ETOs. In: Weatherford and Jones [40], pp. 29–34
13. Weatherford CA, Jones HW (eds) (1982) International Conference on ETO Multicenter Integrals. Reidel, Dordrecht, Netherlands
14. Weniger EJ, Steinborn EO (1983) The fourier transforms of some exponential-type basis functions and their relevance for multicenter problems. J Chem Phys 78:6121
15. Weniger EJ, Steinborn EO (1983) Numerical properties of the convolution theorems of B-functions. Phys Rev A28:2026
16. Shull H, Löwdin PO (1959) Superposition of configurations and natural spin-orbitals. applications to the He problem. J Chem Phys 30:617
17. Rotenberg M (1962) Ann Phys (New York) 19:262
18. Rotenberg M (1970) Theory and application of sturmian functions. Adv At Mol Phys 6:233–268
19. Avery JS (2003) Sturmians. In: Wilson S (ed) Handbook of Molecular Physics and Quantum Chemistry. Wiley, Chichester
20. Goscinski O (1968) Conjugate eigenvalue problems and the theory of upper and lower bounds. Research Report 217, Quantum Chemistry Group, Uppsala University
21. Goscinski O (2003) Conjugate eigenvalue problems and the theory of upper and lower bounds. Adv Quantum Chem 41:51–85
22. Avery JE, Avery JS (2006) Generalized Sturmians and Atomic Spectra. World Scientific. 256 pages, ISBN: 981-256-806-9
23. Avery JS (2000) Hyperspherical Harmonics and generalized Sturmians. Kluwer Academic Publishers, Dordrecht, p 196
24. Avery JS (1989) Hyperspherical Harmonics; Applications in Quantum Theory. Kluwer Academic Publishers, Dordrecht
25. Weniger EJ (1985) Weakly convergent expansions of a plane wave and their use in fourier integrals. J Math Phys 26:276
26. Avery JE (2006) libsturm: The generalized sturmian library. http://sturmian.kvante.org
27. Dahl JP, Avery JS (eds) (1984) Local Density Approximations in Quantum Chemistry and Solid State Physics. Plenum, New York
28. Gasaneo G, Colavecchia FD (2003) Two-body Coulomb wavefunctions as kernel for alternative integral transformations. J Phys A Math Gen 36(31):8443
29. Gasaneo G, Mitnik DM, Frapiccini AL, Colavecchia FD, Randazzo JM (2009) Theory of hyperspherical Sturmians for three-body reactions. The Journal of Physical Chemistry A 113(52): 14573–14582. DOI 10.1021/jp9040869. URL http://pubs.acs.org/doi/abs/10.1021/jp9040869. PMID: 19788257
30. Aquilanti V, Cavalli S, Coletti C, Grossi G (1996) Alternative sturmian bases and momentum space orbitals; an application to the hydrogen molecular ion. Chem Phys 209:405
31. Aquilanti V, Cavalli S, de Fazio D, Grossi G (1996) Hyperangular momentum: Applications to atomic and molecular science. In: Tsipis CA, Popov VS, Herschbach DR, Avery JS (eds) New Methods in Quantum Theory. Kluwer Academic Publishers, dordrecht, netherlands edn
32. Judd BR (ed) (1975) Angular Momentum Theory for Diatomic Molecules. AcademicPress, New York
33. Koga T, Matsuhashi T (1987) Sum rules for nuclear attraction integrals over hydrogenic orbitals. J Chem Phys 87(8):4696–4699
34. Koga T, Matsuhashi T (1988) One-electron diatomics in momentum space. v. nonvariational LCAO approach. J Chem Phys 89:983
35. Shibuya T, Wulfman C (1965) Molecular orbitals in momentum space. Proc Roy Soc A 286:376

36. Wulfman CE (1971) Dynamical groups in atomic and molecular physics. In: Loebel EM (ed) Group Theory and its Applications. Academic, New York
37. Wulfman CE (2011) Dynamical Symmetry. World Scientific, Singapore
38. Fock VA (1935) Z Phys 98:145
39. Fock VA (1958) Hydrogen atoms and non-euclidian geometry. Kgl. Norske Videnskab.Forh. **31**:138
40. Alliluev SP (1958) Sov Phys JETP 6:156
41. Bander M, Itzykson C (1966) Group theory and the H atom (i and ii). Rev Mod Phys 38(2):330–358
42. Avery JS, Herschbach DR (1992) Hyperspherical sturmian basis functions. J Quantum Chem 41:673
43. Caligiana A (2003) Sturmian orbitals in quantum chemistry. Ph.D. thesis, University of Perugia, Italy
44. Monkhorst HJ, Jeziorski B (1979) No linear dependence or many-center integral problems in momentum space quantum chemistry. J Chem Phys 71(12):5268–5269
45. Avery JS, Rettrup S, Avery JE (2011) Symmetry-adapted basis functions; automatic generation for problems in physics and chemistry. World Scientific (in press)

Struct Bond (2012) 143: 101–120
DOI: 10.1007/430_2011_44

Chemistry as a "Manifestation of Quantum Phenomena" and the Born–Oppenheimer Approximation?

Brian T. Sutcliffe

Abstract When considering the work of Carl Ballhausen on vibrational spectra, it is suggested that his use of the Born–Oppenheimer approximation is capable of some refinement and extension in the light of later developments. A consideration of the potential energy surface in the context of a full Coulomb Schrödinger Hamiltonian in which translational and rotational motions are explicitly considered would seem to require a reformulation of the Born–Oppenheimer approach. The resulting potential surface for vibrational motion should be treated, allowing for the rotational motion and the nuclear permutational symmetry of the molecule.

Keywords Born-Oppenheimer · Rotation-vibration spectra · Potential energy surface · Self-adjoint · Permutational symmetry

Contents

B.T. Sutcliffe (✉)
Service de Chimie Quantique et Photophysique, Université Libre de Bruxelles, 1050 Bruxelles, Belgium
e-mail: bsutclif@ulb.ac.be

1 Introduction

In a paper in 1979, Carl Ballhausen [1] expressed the belief that "today we realize that the whole of chemistry is one huge manifestation of quantum phenomena," but he was perfectly well aware of the care that had to be taken to express the relevant quantum theory appropriately. So in an earlier review [2] that he had undertaken with Aage Hansen, he scorned the usual habit of chemists in naming an experimental observation as if it was caused by the theory that was used to account for it. Thus in the review they remark that a particular phenomenon observed in molecular vibration spectra "is presently refered to as the Duchinsky effect. The 'effect' is, of course, just as fictitious as the Jahn–Teller effect." Their aim in the review was "to make a start towards rationalization" of the nomenclature and to specify the form of the molecular Hamiltonian implicit in any nomenclature. In an article that Jonathan Tennyson and I published in the festschrift to celebrate his sixtieth birthday in 1987 [3], we tried to present a clear account of a molecular Hamiltonian suitable for treating the vibration rotation spectrum of a triatomic molecule. In an article that I wrote that appeared in 1990 [4], I discussed the difficulty of deciding just how far the basic chemical idea of molecular structure could really be fitted into quantum mechanics.

The invitation to make a contribution to a volume that will celebrate Carl's life and achievements provides a welcome opportunity to develop the responses made so long ago and that is the burden of what follows.

2 Schrödinger's Equation in a Chemical Perspective

In [2], the authors concentrated on providing a clear and coherent account the way in which the words "Born–Oppenheimer" were used in the literature for they recognized that:

> . . . what constitutes the Born-Oppenheimer approximation to one scientist may nor necessarily mean the same approximation to another chemist.

and on the role that the various usages had in the interpretation of electronic spectra. One might say, using the nomenclature that Primas later uses [5], that the Born–Oppenheimer approximation is near to all schemes in the contextual topology of explanations, based on quantum mechanics, of molecular spectroscopy. This is because the Born–Oppenheimer approximation seems to provide a mechanism for incorporating the Eckart approach [6] to the interpretation of molecular spectra, which is based on classical mechanics and involves the choice of an equilibrium molecular geometry, into quantum mechanics. It is this approach in the quantum mechanical form provided by Watson [7] which forms what might be called the standard method of interpreting molecular spectra.

But in [1], Carl recognized that even though quantum mechanics was essential in describing spectra that:

> Each new generation of scientists works within a paradigm. For one thing this means that the manifold of performed experiments can be classified. However, after a shorter or longer time the old concepts are no longer capable of accommodating the accumulated evidence. A new, usually more abstract paradigm must take the place of the old before significant advances can be made again.

I should like to argue that it is now time to consider if new developments in the foundations of the Born–Oppenheimer approximation might not result in a new paradigm which alters the conceptual topology used in our interpretation of molecular spectra. I shall confine myself to considering just the Schrödinger Coulomb Hamiltonian and begin by looking at its formal mathematical structure. The Coulomb Hamiltonian for a system of N electrons and A atomic nuclei may be written as:

$$H = \sum_{g=1}^{A} \frac{p_g^2}{2m_g} + \frac{e^2}{8\pi\epsilon_o} \sum_{g,h=1}^{A}{}' \frac{Z_g Z_h}{r_{gh}} + \sum_{i=1}^{N} \left(\frac{p_i^2}{2m} - \frac{e^2}{4\pi\epsilon_o} \sum_{g=1}^{A} \frac{Z_g}{r_{ig}} \right) + \frac{e^2}{8\pi\epsilon_o} \sum_{i,j=1}^{N}{}' \frac{1}{r_{ij}}, \qquad (1)$$

where the individual terms have obvious classical interpretations; the charges and masses of the electrons and nuclei are regarded as parameters to be taken from experimental data. N and A are undetermined positive integers.[1]

2.1 The Clamped-Nuclei Approach

In 1951, Kato [9] established that the Coulomb Hamiltonian, H, is essentially self-adjoint.[2] This property, which is stronger than Hermiticity, guarantees that the time evolution

$$\Psi(t) = \exp(-iHt/\hbar)\Psi(0)$$

of a Schrödinger wave function is unitary and so conserves probability. This is not true for operators that are Hermitian but not self-adjoint. It is easy enough to construct examples of such operators; an example given by Thirring [10] is of the radial momentum operator $-i\hbar\partial/\partial r$ acting on functions $\phi(r)$, $\phi(0) = 0$ with $0 \leq r < \infty$.

All that is needed to remove the center-of-mass motion from the full molecule Hamiltonian is a linear point transformation symbolized by:

$$(\boldsymbol{t\xi}) = \boldsymbol{x}\boldsymbol{V}. \qquad (2)$$

---

[1] This Hamiltonian results from the standard canonical quantization of electrodynamics if it is assumed that particle speeds are negligible compared to the speed of light, and all charge–photon interactions are discarded; the Coulomb gauge condition must also be imposed [8].

[2] The work was completed in 1944 and was actually received by the journal in October 1948.

In (2), $\boldsymbol{t}$ is a 3 by $N_T - 1$ matrix ($N_T = N + A$), and ξ is a 3 by 1 matrix, so that the combined (bracketed) matrix on the left of (2) is 3 by N_T. $\boldsymbol{V}$ is an N_T by N_T matrix which, from the structure of the left side of (2), has a special last column whose elements are:

$$V_{iN_T} = {M_T}^{-1} m_i, \quad M_T = \sum_{i=1}^{N_T} m_i. \tag{3}$$

Hence, ξ is the standard center-of-mass coordinate:

$$\boldsymbol{\xi} = {M_T}^{-1} \sum_{i=1}^{N_T} m_i \boldsymbol{x}_i. \tag{4}$$

As the coordinates $\boldsymbol{t}_j$, $j = 1, 2, \ldots N_T - 1$ are to be translationally invariant,

$$\sum_{i=1}^{N_T} V_{ij} = 0, \qquad j = 1, 2, \ldots . N_T - 1 \tag{5}$$

on each remaining column of $\boldsymbol{V}$, and it is easy to see that (5) forces $\boldsymbol{t}_j \rightarrow \boldsymbol{t}_j$ as $\boldsymbol{x}_i \rightarrow \boldsymbol{x}_i + \boldsymbol{a}$, all i. Equivalently it means that the $\boldsymbol{t}_i$ must be linear combinations of the interparticle variables $\boldsymbol{x}_{jk}$. The Jacobian for the transformation is obviously a constant and providing that it is not zero, the transformation is a proper one and transforming yields a Hamiltonian of the form:

$$H = H'(\boldsymbol{t}) - \frac{\boldsymbol{\hbar^2}}{\boldsymbol{2M_T}} \nabla^2(\boldsymbol{\xi}). \tag{6}$$

Since the center-of-mass variable does not enter the potential energy term, the center-of-mass motion may be separated off completely so that the eigenfunctions of H are of the form:

$$T(\boldsymbol{\xi})\Psi(\boldsymbol{t}), \tag{7}$$

where $\Psi(\boldsymbol{t})$ is a wave function for the Hamiltonian $H'(\boldsymbol{t})$, (6), which will be referred to as the *translationally invariant* Hamiltonian. It should be emphasized that different choices of $\boldsymbol{V}$ are unitarily equivalent so that the spectrum of the translationally invariant Hamiltonian is independent of the particular form chosen for $\boldsymbol{V}$, provided that it is consistent with (3) and (5).

Kato considers just the translationally invariant part of the problem, and he actually uses a coordinate system in which the kinetic energy can be written in the form:

$$\frac{\hbar^2}{2}\sum_{i=1}^{N_T-1}\frac{1}{\mu_{ii}}\nabla^2(\boldsymbol{t}_i)+\frac{\hbar^2}{2\mu_0}\left|\sum_{i=1}^{N_T-1}|\vec{\nabla}(\boldsymbol{t}_i)\right|^2.$$

He points out that if μ_0 increases without limit, then something in the form of the original Hamiltonian is obtained but for one “particle” less, so that there is no loss of generality in choosing this form. But the finding is general. He specifies the potential energy in such a way as to include the usual Coulomb form.

It was pretty obvious to applied mathematicians that the kinetic energy operator alone is indeed self-adjoint because of their classical mechanical experience. It was shown by Stone in the 1930s that multiplicative operators of the coulomb kind are also self-adjoint, but it was entirely unobvious that the sum of the operators would be self-adjoint because the sum of the operators is defined only on the intersection of their domains.

What Kato showed in Lemma 4 of his amazing paper was that for a class of potentials including Coulomb ones and for any function f in the domain D_0 of the full kinetic energy operator T_0, the domain of full problem D_V contains D_0 and there are two constants a, b such that:

$$\|Vf\| \leq a\,\|T_0 f\| + b\|f\|,$$

and that a can be taken as small is liked. This result is often summarized by saying that the Coulomb potential is small compared to the kinetic energy.

Given this result he proved in Lemma 5 that the usual operator is indeed, for all practical purposes, self-adjoint and is bounded from below. The proof does not work unless there is a kinetic energy term in each of the particle variables that are involved in the potential energy expression.

It is often asserted that the Born–Oppenheimer approximation makes it possible when considering electronic motion to treat the nuclear masses as infinite and to determine the electronic wave function by finding solutions of the Hamiltonian

$$H^{elec}=\frac{e^2}{8\pi\in_o}\sum_{g,h=1}^{A}{}'\,\frac{Z_gZ_h}{r_{gh}}+\sum_{i=1}^{N}\left(\frac{p_i^2}{2m}-\frac{e^2}{4\pi\in_o}\sum_{g=1}^{A}\frac{Z_g}{r_{ig}}\right)+\frac{e^2}{8\pi\varepsilon_o}\sum_{i,j=1}^{N}{}'\,\frac{1}{r_{ij}}, \qquad (8)$$

which would result from the Hamiltonian (1) on making this choice. However, it is obvious that such a choice yields an operator which is not self-adjoint in the Kato sense because there are some potential terms in it which do not have kinetic operator partners. It thus cannot yield meaningful solutions in the context of the full problem. In practice, direct solutions to (8) are never attempted for the nuclei and are always regarded as clamped so that the first term in (8) is simply a constant, and the variables r_{ig} depend only on the electronic coordinates and are thus properly dominated by the electronic kinetic energy terms. A sequence of such clamped-nuclei calculations is then considered to define a potential in which nuclear motion can be considered and hence an approximate solution to the full problem can be constructed. It is in this context that it is appropriate to reconsider the Born– Oppenheimer approximation.

2.2 Looking for Molecules

In view of the discussion in the arguments advanced by Born and Oppenheimer [11], it may be helpful to express $H'(\boldsymbol{t})$ in terms of two sets of coordinates.[3] One set consists of $A - 1$ translationally invariant coordinates $\boldsymbol{t}_i^n$ expressed entirely in terms of the coordinates used originally to describe the nuclei, $\boldsymbol{x}_i^n$,

$$\boldsymbol{t}_i^n = \sum_{j=1}^{A} \boldsymbol{x}_j^n V_{ji}^n, \quad i = 1, 2, \ldots, A - 1. \tag{9}$$

Here $\boldsymbol{V}^n$ is a nonsingular matrix whose last column is special, with elements

$$V_{iA}^n = M^{-1} m_i, \qquad M = \sum_{i=1}^{A} m_i, \tag{10}$$

so that the coordinate $\boldsymbol{X}$, defined by its last column, is the coordinate of the center-of-nuclear mass. The elements in the first $A - 1$ columns of $\boldsymbol{V}^n$ each sum to zero, exactly as in the general case, to ensure translational invariance. The other set comprises N translationally invariant "electronic" coordinates defined in terms of the initially chosen electronic variables $\boldsymbol{x}^{\mathrm{e}}$ and whose origin is the center-of-nuclear mass

$$\boldsymbol{t}_i^e = \boldsymbol{x}_i^e - \boldsymbol{X}. \tag{11}$$

The inverse relations are:

$$\boldsymbol{x}_i^e = \boldsymbol{X} + \boldsymbol{t}_i^{\boldsymbol{e}}, \tag{12}$$

$$\boldsymbol{x}_i^n = \boldsymbol{X} + \sum_{j=1}^{A-1} \boldsymbol{t}_j^n ((\boldsymbol{V}^n)^{-1})_{ji}, \tag{13}$$

---

[3] The discussion below is aimed at the general polyatomic case. The cases A = 1, A = 2, A = 3 (the nuclear configurations that define, respectively, a point, a line, and a plane) may be dealt with by special techniques that are not considered here as it would deflect the main thrust of the argument.

with

$$((\boldsymbol{V}^n)^{-1})_{Ai} = 1, \qquad i = 1, 2, \ldots A, \tag{14}$$

while the inverse requirement on the remaining rows gives:

$$\sum_{i=1}^{A} ((\boldsymbol{V}^n)^{-1})_{ji} m_i = 0, \qquad j = 1, 2, \ldots A - 1. \tag{15}$$

With this choice of coordinates, the translationally invariant Coulomb Hamiltonian takes the form:

$$H'(\boldsymbol{t}) \to H^{\mathrm{e}}(\boldsymbol{t}^{\mathrm{e}}) + H^{n}(\boldsymbol{t}^{n}) + H^{\mathrm{e}n}(\boldsymbol{t}^{n}, \boldsymbol{t}^{\mathrm{e}}). \tag{16}$$

The part of the Hamiltonian which can be associated with electronic motion can be written as:

$$H^{e}(\boldsymbol{t}^{e}) = -\frac{\hbar^2}{2m}\sum_{i=1}^{N} \nabla^2(\boldsymbol{t}_i^{e}) - \frac{\hbar^2}{2M}\sum_{i,j=1}^{N} \vec{\nabla}(\boldsymbol{t}_i^{e}) \cdot \vec{\nabla}(\boldsymbol{t}_j^{e}) + \frac{e^2}{8\pi\in_0}\sum_{i,j=1}^{N}{}' \frac{1}{|\boldsymbol{t}_j^{e} - \boldsymbol{t}_i^{e}|}, \tag{17}$$

while the part that can be associated with nuclear motion is:

$$H^{n}(\boldsymbol{t}^{n}) = -\frac{\hbar^2}{2}\sum_{i,j=1}^{A-1} \frac{1}{\mu_{ij}^{n}} \vec{\nabla}(\boldsymbol{t}_i^{n}) \cdot \vec{\nabla}(\boldsymbol{t}_j^{n}) + \frac{e^2}{8\pi\in_0}\sum_{i,j=1}^{A}{}' \frac{Z_i Z_j}{r_{ij}(\boldsymbol{t}^{n})}, \tag{18}$$

$$r_{ij}(\boldsymbol{t}^{n}) = \left(\sum_{\alpha} \left(\sum_{k=1}^{A-1} ((V^{n-1})_{kj} - (V^{n-1})_{ki}) \boldsymbol{t}_{\alpha k}^{n} \right)^2 \right)^{1/2}, \tag{19}$$

and the inverse mass matrix is similarly specialized as:

$$1/\mu_{ij}^{n} = \sum_{k=1}^{A} m_k{}^{-1}\, V_{ki}^{n} V_{kj}^{n}, \quad i, j = 1, 2, \ldots A - 1. \tag{20}$$

The electronic and nuclear motions are coupled only via a potential term:

$$H^{\mathrm{e}n}(\boldsymbol{t}^{n}, \boldsymbol{t}^{e}) = -\frac{e^2}{4\pi\in_0}\sum_{i=1}^{A}\sum_{j=1}^{N} \frac{Z_i}{r'_{ij}(\boldsymbol{t}^{n}, \boldsymbol{t}^{e})}, \tag{21}$$

and the electron–nucleus distance expression becomes:

$$|\boldsymbol{x}_i^{n} - \boldsymbol{x}_j^{e}| \;\equiv\; r'_{ij} = \left| \sum_{k=1}^{A-1} \boldsymbol{t}_k^{n} (V^{n})_{ki}^{-1} - \boldsymbol{t}_j^{e} \right|. \tag{22}$$

If there is only a single nucleus and that is taken as the origin for the electronic coordinates, then the nuclear motion term (18) does not arise and so there is no need of explicit consideration of nuclear motion for an atom or atomic ion and such systems need not be considered further.

It might now be reasonably hoped that for some set of nuclei and electrons, there were discrete solutions of the form

$$H'(\boldsymbol{t})\Psi_n(\boldsymbol{t}) = E_n\Psi_n(\boldsymbol{t})$$

among which molecules might be identified. Here n is used to denote a set of quantum numbers ($J\,M\,p\,\boldsymbol{r}\,n$): J and M for the angular momentum state: p specifying the parity of the state: $\boldsymbol{r}$ specifying the permutationally allowed irreps within the groups of identical particles, and n to specify a particular energy value. For a given J, such solutions will be degenerate for all $2J + 1$ values of M, and the permutational irreps can be extensively degenerate too.

It might also be hoped that a first approximation to a solution of (16) could be constructed in terms of product functions in which one portion of each product was obtained from a problem in which the electronic motion was treated as primary, and the other portion described the nuclear motion in the electronic field derived from the first part of the product. This is the standard technique for treating a system of coupled differential equations in which one group of equations represent fast motions and another slow motions. Most chemists get their familiarity with this technique by considering the kinetics of sequential chemical reactions. It is this technique that underlies the Born and Oppenheimer program in which the electronic motion is approached in a frame fixed in the laboratory with an electronic Hamiltonian in which the nuclear motion is at first ignored. Thus, it is natural with the present coordinate choice to hope that functions of the form

$$\psi^{elec}(\boldsymbol{t}^e)\psi^{nuc}(\boldsymbol{t}^n, \boldsymbol{t}^e)$$

might prove effective approximations.

Although the Hamiltonian (16) has a complete spectrum, it should be remembered that when constructing approximate eigenfunctions, certain eigenfunctions may not be approximatable with a given functional form and a particular coordinate choice. If the region of the spectrum considered is one in which the system is dissociating into well-separated atoms, it is rather unlikely that the electronic motions can be effectively represented by a coordinate with origin at a remote center-of-nuclear mass. For reasons that are explained fully in [12], this form of the Hamiltonian is only really useful when the internuclear distances are relatively small, but since it is molecules that are being considered here, it is an appropriate form. It would not be very useful when considering a scattering problem.

So far it has not proved possible, except in some very simple diatomic cases to calculate eigenfunctions of the Hamiltonian (16) using methods in which the nuclei and electrons are treated on the same footing, and so it is essential to consider the status of the clamped-nuclei approach in this formulation as it, at present, forms the basis for all calculations.

By analogy, the electronic Hamiltonian arising from (16) on ignoring the nuclear motion is:

$$H^{elec}(\boldsymbol{t}^n, \boldsymbol{t}^e) = H^e(\boldsymbol{t}^e) + V^{en}(\boldsymbol{t}^n, \boldsymbol{t}^e) + \frac{e^2}{8\pi\epsilon_0} \sum_{i,j=1}^{A}{}' \frac{Z_i Z_j}{r_{ij}(\boldsymbol{t}^n)}. \tag{23}$$

It is the sum of (17) and (21) together with the last term from (18). Hence, the full Hamiltonian can now be written as:

$$H'(\boldsymbol{t}) = -\frac{\hbar^2}{2} \sum_{i,j=1}^{A-1} \frac{1}{\mu_{ij}^n} \vec{\nabla}(\boldsymbol{t}_i^n) \cdot \vec{\nabla}(\boldsymbol{t}_j^n) + H^{elec}(\boldsymbol{t}^n, \boldsymbol{t}^e). \tag{24}$$

If the $\boldsymbol{t}^n$ were assigned values, $\boldsymbol{b}$ say, based on choices $\boldsymbol{x}_g^n = \boldsymbol{a}_g$ in the laboratory-fixed frame, then this would be the translationally invariant form of the electronic Hamiltonian appropriate to a particular classical nuclear geometry and

$$H^{elec}(\boldsymbol{t}^n, \boldsymbol{t}^e) \to H^{elec}(\boldsymbol{b}, \boldsymbol{t}^e). \tag{25}$$

This Hamiltonian is very likely the usual clamped-nuclei one, but it is explicitly translationally invariant and has an extra term, the second term in (17), which is often called either the Hughes–Eckart or the mass-polarization term. Since this last term involves the reciprocal of the total nuclear masses, it is liable to be small. If it is neglected, the remaining part of $H^{\mathrm{elec}}(\boldsymbol{b}, \boldsymbol{t}^{\mathrm{e}})$ maps onto the usual clamped-nuclei form exactly, and the neglected part can be included as a first-order perturbation. This approach is often taken in electronic structure calculations and is usually called "including the diagonal BO corrections." The domain of $H^{\mathrm{elec}}(\boldsymbol{b}, \boldsymbol{t}^{\mathrm{e}})$ consists of functions on $\boldsymbol{R}^{3N}$ because the nuclear repulsion operator becomes a number multiplier and just determines an energy zero, and the electron–nucleus interaction terms have fixed origins.

It should be noted that because the eigenvalues of $H^{\mathrm{elec}}(\boldsymbol{b}, \boldsymbol{t}^{\mathrm{e}})$ do not depend on the way in which the geometry specified by $\boldsymbol{b}$ is oriented, in clamped-nuclei calculations a single orientation is always chosen and so the eigenvalue is always a function simply of the geometry. Thus, this eigenvalue is more properly regarded as the eigenfunction arising from a rotationally invariant formulation.

The Hamiltonian $H^{\mathrm{elec}}(\boldsymbol{t}^n, \boldsymbol{t}^{\mathrm{e}})$ has the same invariance under the rotation–reflection group O(3) as does the full translationally invariant Hamiltonian (6), and it has a somewhat extended invariance under nuclear permutations, since it contains the nuclear masses only in symmetrical sums. Since it contains the translationally invariant nuclear coordinates as multiplicative operators, its domain is of functions on $\boldsymbol{R}^{3N} \otimes \boldsymbol{R}^{3(A-1)}$. If the atomic and diatomic cases are not under consideration, then it is clear that the electronic Hamiltonian contains potential terms with no kinetic partners and so it cannot be self-adjoint, as explained earlier so presenting the electronic problem as if the potential for nuclear motion arose from:

$$H^{elec}(\boldsymbol{t}^n, \boldsymbol{t}^e)\Psi_p^{elec}(\boldsymbol{t}^n, \boldsymbol{t}^e) = E_p^{elec}(\boldsymbol{t}^n)\Psi_p^{elec}(\boldsymbol{t}^n, \boldsymbol{t}^e) \tag{26}$$

cannot be justified.

Progress can be made by noting that electronic Hamiltonian (23) commutes with each of the $A - 1$ nuclear position variables. Think now of the molecular bound state space $\mathcal{H}$ as the square integrable sections in the trivial fiber bundle $\boldsymbol{R}^{3A-6} \otimes \mathcal{L}^2(\boldsymbol{R}^{3N})$. In this case, the nuclear operator (which is the bare kinetic energy operator) acts in the base space, that is upon functions defined on $\boldsymbol{R}^{3A-6}$, and the electronic Hamiltonian acts only upon the fiber defined by the choice of $\boldsymbol{b}$. (In this case, the fiber is a vector space and so the fiber bundle in this context is often called a vector bundle.) Now write the full electronic Hamiltonian as a direct integral over the fibers:

$$H^{elec}(\infty, \boldsymbol{t}^e) = \int_{\oplus} H^{elec}(\boldsymbol{b}, \boldsymbol{t}^e)\, \mathrm{d}b, \tag{27}$$

where the $\boldsymbol{t}^n$ have been replaced by $\boldsymbol{b}$ within the integral, to emphasize that it is over fixed points that the "sum" is occurring and by ∞ on the left, to symbolize that this is the form that the electronic Hamiltonian would have were the nuclear masses allowed to increase without limit and the nuclear positions to cover all of $\boldsymbol{R}^{3A-3}$. This is, of course, to redefine the electronic Hamiltonian but in a perfectly reasonable way and one which avoids the pitfalls of trying to deal directly with (23). It is a perfectly decent operator, but there are some aspects of it that need a bit more discussion.

It should be noted that $\Psi^{\text{elec}}(\boldsymbol{b}, \boldsymbol{t}^e)$ as a solution to the Schrödinger equation (26) with $\boldsymbol{t}^n$ replaced by $\boldsymbol{b}$ is defined only up to a phase factor of the form:

$$exp\,[iw(\boldsymbol{b})],$$

where w is any single-valued real function of the $\boldsymbol{b}_k$ and can be different for different electronic states. Specific phase choices must therefore be made when tying this part to the nuclear part of the product wave function. It is only by making suitable phase choices that the electronic wave function is made a continuous function of the formal nuclear variables, $\boldsymbol{b}$, and the complete product function, made single valued. This is the origin of the Berry phase in clamped-nuclei calculations involving intersecting potential energy surfaces; for a discussion of these matters, see [13]. It is worth noting explicitly that notions of molecular Berry phases and conical intersections are tied to the clamped-nuclei viewpoint. They are only "observable" to the extent that experimental data are interpreted within that framework. According to quantum mechanics, the eigensolutions of (1) are single-valued functions by construction with arbitrary phases (rays); so one does not expect any Berry phase phenomena.

If it is decided to treat the system by specifying a set of three rotation angles and $3N_T - 6$ internal coordinates, then problems arise with the vector bundle idea. This is because such a separation requires that the vector space R^{3N_T-3} is decomposed into the manifold $\boldsymbol{S}^3 \otimes \mathbf{R}^{3N_T-6}$. But this manifold cannot be coordinatized globally, of course; so any account of electronic structure given in this way can at best be only local. The local Hamiltonian can describe only a subset of the states accessible in the full problem.

It is possible to decompose the full space leaving the electrons described in a vector space, if there are more than two nuclei, by splitting the whole space as $\boldsymbol{R}^{3N} \otimes \boldsymbol{S}^3 \otimes \boldsymbol{R}^{3A-6}$. Although with such a splitting the form of the electronic Hamiltonian remains unchanged, it couples the electronic motion to the angular motion and leaves the notion of the electronic Hamiltonian as a direct integral, a local idea. However, if the mass-polarization term is neglected, the resulting Hamiltonian can be mapped exactly on to clamped-nuclei electronic Hamiltonian with proper neglect of rigid rotations of the molecular frame defined by the choice of nuclear geometry.

If a solution of the electronic problem is to be used in a solution of the full problem, then the solution must be one invariant under the permutation of identical nuclei. The direct integral form is indifferent to whether individual nuclei are identified, and it is thus perfectly possible to regard formally identical nuclei as distinguishable particles simply by a suitable labeling of the points specified by $\boldsymbol{b}$. However, it is equally possible that the direct integral properly reflects the permutational symmetry by requiring that if $\boldsymbol{b}'$ results from a permutation of identical nuclei specified by $\boldsymbol{b}$ both sets be included in the same way in the direct integral.

3 The Status of the Born–Oppenheimer Approximation

The Born–Oppenheimer approximation consists of choosing a particular clamped-nuclei electronic state in terms of which the lower rotational and vibrational states of the full problem can be most closely approximated. What Born and Oppenheimer hoped that they were showing in their original paper was that by choosing the clamped-nuclei electronic state to be at a nuclear geometry that yielded the lowest electronic energy of all the states in the vicinity of that geometry, the nuclear motion could be treated as rotating the system almost as a rigid body while it was undergoing small vibrations and that the resulting set of rotation–vibration eigenvalues would be good approximations to the exact values provided. They expressed this by supposing that the clamped-nuclei electronic structure could be extended to provide a potential continuous in the geometrical variables around the chosen minimum, and that a good approximation might be expected if this minimum was isolated and deep. They started from an equivalent of (26) for a diatomic molecule and used ordinary perturbation theory. They give no fully explicit account of the polyatomic molecule problem at all.

The observations made above must make it clear that Born and Oppenheimer's original discussion cannot be mathematically sound, no matter how persuasive it may seem. However, Combes, Duclos, and Seiler [14], using the fiber bundle approach and singular perturbation theory about an assumed nondegenerate minimum in the potential $V^{\mathrm{elec}}(\boldsymbol{t}^{\mathrm{n}})$, showed in the 1970s that this approach for the diatomic molecule led in a mathematically sound way to *asymptotic solutions* for the full problem, just like those anticipated by Born and Oppenheimer. That is, they were able to show that asymptotically the energy could be written as the sum of an electronic, a vibrational, and rotational part. The electronic part was the value of the potential at the minimum, the vibrational part was given by the Harmonic oscillator eigenvalues with the force constant determined by the second derivative of the electronic energy at the potential minimum, and the rotational energies were given by those of a rigid rotor whose extension was the value of the internuclear separation at the potential minimum. That it is the Harmonic oscillator that provides the vibrational energies is, as the authors note, "a miracle" because the range of the internuclear distance operator is only $[0\infty)$, while that of the Harmonic oscillator variable is $(-\infty + \infty)$. But they show that this is justified if the vibrational eigenfunctions vanish quickly enough away from the equilibrium extension, and that such vanishing is a consequence of a potential minimum deep enough to validate the general argument.

Since it is possible to formulate the nuclear motion problem for a diatomic in terms of the spherical polar coordinates of the internuclear vector, it is possible to describe the rotational motion of the nuclei without leaving the Cartesian space $\boldsymbol{R}^3$. It was thus possible for Combes and Seiler to consider how this rotational motion approximated the rotational motion as a whole. However, it is not generally possible to do so, and for rotational motion to be considered explicitly, it is necessary to decompose to the manifold form discussed above. However, since the required kind of fiber bundle can be constructed only upon a Cartesian space that means that there is no single form for the electronic Hamiltonian but one for each of the possible bundles. This corresponds to approximating only that subset of states which are accessible in the chosen formulation. The fiber bundle structure here is thus nontrivial and is only generalizable locally. The nontrivial nature of the separated fiber bundle form has so far prevented a mathematically sound account of the Born–Oppenheimer approximation from being given with explicit consideration of rotational symmetry.

However, the fiber bundle structure on the translationally invariant space is trivial, and in 1992, however, it was shown by Klein et al. [15], treating the full translationally invariant problem in terms of a trivial fiber bundle, that if it is assumed that (25) has a discrete eigenvalue which has a minimum as a function of the $\mathbf{t}_g^n$ in the neighborhood of some values $\boldsymbol{t}_g^n = \boldsymbol{b}_g$, then because of the rotation– inversion invariance such a minimum exists on a three-dimensional sub-manifold for all $\boldsymbol{b}_g$ such that:

$$\boldsymbol{b}_g \to R\boldsymbol{b}_g, R \in O(3).$$

The $\boldsymbol{b}_g$ therefore defines the geometrical shape of the minimum in the usual way. If the minimum figure is a plane, then the potential well is diffeomorphic to SO(3), and if it is nonplanar, then it is diffeomorphic to O(3) and so the well is actually a symmetric double well. In either case, Klein et al. show that the eigenvalues and eigenfunctions for a polynuclear molecule can be obtained as WKB-type expansions to all orders[4] of the parameter κ. Hence, it is properly established that the Born–Oppenheimer approach leads to asymptotic solutions for the full problem but, interestingly, the potential is usually a double-well one.

Just as permutational symmetry was not considered in the work of Born and his collaborators, neither is it considered in the later work. With the choice of translationally invariant coordinates made above, it is a simple matter to incorporate electronic permutational symmetry and, without any diminution of mathematical generality, to require that the electronic part of the wave function includes spin and be properly antisymmetric. On this understanding, it is perfectly reasonable to assume that the potential at the minimum should not be degenerate. If it seems sufficient to treat the nuclei as distinguishable particles, then it can confidently be asserted that the Born–Oppenheimer approach offers a perfectly satisfactory account of molecular wave functions whose energy is close to a minimum in the potential.

At present there has been no direct consideration of the Born and Huang [16] approach by mathematicians. To remove the translational motion from the problem and so make possible the formal expansion at the heart of this method, while still allowing a useful approach as the nuclei became widely separated, seems a vain hope.[5] However, in the time-dependent coherent states (wave-packet) approach to a freely moving system, it is possible to use the laboratory-fixed coordinate system and hence to deal with all the asymptotes, while avoiding problems arising from the pure translational continuum. Among the first to use this approach on a molecule was Hagedorn [17]. For diatomics, he was able to show that, in the limit of large nuclear masses, the electrons move adiabatically and determine an effective potential in which the nuclei, treated as identifiable particles, move semi-classically if the potential surface is isolated. These results do not depend upon there being a minimum in the potential. The results of the Born and Oppenheimer work cited above would not be valid if there were not a minimum around which the wave function could be expanded. Hagedorn's work has not been formally extended to polynuclear molecules (but see [18]) though it certainly could be, by deploying the same sort of techniques that are used by Klein et al. [15] in their work on polynuclear systems. However, the approximation breaks down when the potential surface fails to remain isolated from the rest of the electronic energy spectrum. There is so far no mathematically satisfactory resolution of the general level-

---

[4] The eigenfunctions expand in integer powers of κ; most of the eigenvalues expand in even powers of κ.

[5] Although it seems very likely that the special case of this approach, called in [2] the Longuet–Higgins approach, in which the nuclei are regarded as fixed in the electronic problem and as variables in the nuclear motion problem could be treated as above.

crossing problem, but in a later paper [19] Hagedorn puts some aspects of the work that has been done here in the context of more chemically oriented level-crossing ideas. If it becomes possible to deal with level crossing, then what is usually done in quantum chemical calculations can be regarded as soundly based mathematically; however, to relate the product-like solutions obtained from such calculations to eigenfunctions of the Hamiltonian for the moving nucleus problem, it still remains to deal with nuclear permutational symmetry.

3.1 Permutational Invariance of the Effective Electronic Hamiltonian

If the nuclei are treated as identifiable particles and a particular set of nuclear coordinates is chosen, say $\boldsymbol{x}_g^n = \boldsymbol{a}_g$, then within the chosen set of translationally invariant coordinates this will generate the set $\boldsymbol{b}_g$ corresponding to the $\boldsymbol{t}_g^n$. A particular choice of nuclear coordinates will specify a geometrical figure **F** at whose vertices are placed the nuclei. Any choice of nuclear coordinates that can be obtained from a given choice by means of a rotation–reflection will generate the same geometrical figure. If the nuclear coordinate choice $\boldsymbol{a}$ generates a geometry **F**, then any nuclear coordinate choice that arises from a permutation of nuclei with the same charge will give rise to the same energy V^{elec}. However, two equivalent geometries so generated usually correspond to a different coordinate choice. Hence, regarding V^{elec} as specifying a particular point on a potential surface expressed in terms of the t_g^n is rather too restrictive. It actually corresponds to as many points as are generated by permutations of particles with identical charges. This observation was made at least as long ago as 1985 by Schmelzer and Murrell [20] and developed in a series of papers by Collins and his group [21]. The work of Schmelzer and Murrell has been further developed by Bowman and coworkers [22] and that of Collins by Cassam-Chenai and coworkers [23]. If the chosen point is located at a minimum on the potential surface, then it corresponds to a multiple minimum with as many wells as there are permuted positions.

It is perhaps useful to provide an example of what is meant here. Suppose that one was dealing with the molecule H_2O_2 and began by specifying four nuclear coordinates in the full problem as $\boldsymbol{x}_g^n$, $g = 1, 2, 3, 4$ with 1 and 3 as labels for the protons, and 2 and 4 for the oxygens. The internal coordinates might be chosen as:

$$\boldsymbol{t}_1^n = \boldsymbol{x}_2^n - \boldsymbol{x}_1^n,\ \boldsymbol{t}_2^n = \boldsymbol{x}_2^n - \boldsymbol{x}_4^n,\ \boldsymbol{t}_3^n = \boldsymbol{x}_4^n - \boldsymbol{x}_3^n$$

and thought of as one OH bond vector, an OO bond vector, and another OH bond vector, respectively. Now imagine a specific choice $\boldsymbol{a}$ made for the x^n, then such a choice would specify a point in the coordinate space. The permutation (13) would transform the OH bond vectors and produce new coordinates corresponding to crossed OH bonds vectors. These crossed forms would require a linear combination of all three of the original coordinates to express them. They would therefore, when the specific choice has been made, locate a different position in the coordinate space than that originally specified, but one at which the electronic energy had the same value.

Were there to be a minimum in the potential for some particular choice of the $\boldsymbol{b}$, then in this example there would be four minima simply as a result of permutational symmetry. If these minima occurred at a nonplanar configuration, there would be eight because of inversion symmetry. Any point group symmetry would be subsumed in the permutational symmetry. The nuclear motion problem tackled along the lines of the Born–Oppenheimer program would thus involve establishing that the usual solutions were asymptotic solutions to a problem with a many-well potential. It would also involve constructing permutationally allowed trial functions for nuclear motion. No mathematical work that attempts to follow the Born and Oppenheimer or the Born program along this path appears to have been done.

The work mentioned above is devoted to describing a potential surface in terms of coordinates that are invariant under permutations of identical nuclei and is not directly a help in the matters considered here. However, the use made of classical invariant theory as described in Weyl [24] in these discussions is very illuminating and may perhaps provide a way forward, as perhaps does the work of Helffer and Sjöstrand [25] dealing with multiple well potentials. The potentials considered in all of these works are invariant under the operations of the rotation–reflection group in three dimensions, O(3). The discussion given is thus at a level somewhat different from that given above, where only translational invariance has been considered explicitly. No matter which internal motion space is chosen, it will still be necessary to deal with both fermion and boson particles. Methods for dealing with spin $\frac{1}{2}$ fermions are well enough known, but the treatment of fermions with higher spins and bosons generally is much less studied. The work of Paldus and his colleagues [26] and that of Katriel [27] may perhaps provide a useful start here.

It should be pointed out that if one is considering potentials invariant under the operations of the rotation–reflection group in three dimensions, O(3), then it is possible that a permutation of identical particles may result in a redefinition of the Eulerian angles. Since the internal coordinates are defined in terms of scalar products of the translationally invariant coordinates, it is clear that a permutation of the original coordinates will transform any internal coordinate into, at most, a function of internal coordinates. However, since the Eulerian angles are defined by orienting a coordinate frame in the translationally invariant coordinate space, it is equally clear that, unless the orientation is such that all indistinguishable particles are treated symmetrically, a permutation will result in the Eulerian angles being transformed into functions of the original Eulerian angles *and* the internal coordinates. Thus, if the matrix $\mathbf{C}$ were chosen according to the Eckart prescription [6], which is the one generally used by molecular spectroscopists and does not usually involve all nuclei of equal mass symmetrically, then permutations often mix the Eulerian and internal coordinates. Nuclear motions in the Eckart prescription are defined in terms of displacements from a fixed nuclear geometry, and only permutations that correspond to point group operations for that geometry leave the Eulerian angles unchanged.

If it were possible to construct from a clamped-nuclei start, a very good approximate wave function for the whole system, having all the required symmetry properties and including nuclear motion, then it might be possible to consider in a proper manner in what sense it could be approximated by a wave function arising from the same clamped-nuclei start but leaving the nuclei identified and ignoring any nuclear permutation symmetry. This could be by means of an approach similar to that which is used in computing intermolecular forces within the clamped-nuclei approximation. Here, if one considers two interacting molecules, then the system of electrons formed by the two combined must be represented by an antisymmetric wave function. The system is a "super-molecule." But as the two molecules are separated, then the representation of the totally antisymmetric wave function by the product of two individually antisymmetric wave functions becomes perfectly adequate in energy terms. Thus, some consequences of the full symmetry requirements of the problem become unimportant from an energetic point of view. Of course if one were looking for Einstein–Podolsky–Rosen correlation effects, the full symmetry of the problem might well remain important in understanding the results of some experiment, even where it is unimportant energetically.

3.2 Rotation–Reflection Invariance

In the section on the Molecular Hamiltonian in [2], the authors begin by saying:

> The essential step in the construction[of the molecular Hamiltonian]is the removal of the ignorable coordinates corresponding to the overall translation and overall rotation of the molecule.

and although there is no doubt that translational motion is ignorable, the status of rotational motion, as has been seen, still remains more doubtful. In [28], it was argued that because the potential calculated from the standard clamped-nuclei electronic Hamiltonian is usually taken to be rotationally and translationally invariant, then any attempt to place this potential in the context of the full Schrödinger Coulomb Hamiltonian must be made with this Hamiltonian expressed in terms of translationally and rotationally invariant coordinates with the electronic coordinates explicit. Ways in which such a Hamiltonian might be constructed were discussed in [29, 30]. In what follows the account given in [30] will be used. Even though the mathematically sound arguments for the Born–Oppenheimer approximation do not allow for the explicit treatment of rotational motion, it is perfectly possible to construct an expression for the expected value of a wave function of electron–nucleus product form but with the rotational variables made explicit. In this approach, the approximating functions including angular momentum are taken to be of the form:

$$\psi_p(\boldsymbol{q}, z) \sum_{k=-J}^{+J} \Phi^J_{kp}(\boldsymbol{q}) |JMk>, \tag{28}$$

where $|JMk>$ is a symmetric-top eigenfunction expressed in terms of the nuclear coordinates and where the q_k are members of the set of $3A - 6$ internal coordinates invariant under rotation–reflections and z are the electronic coordinate in the molecular frame. J is the angular momentum quantum number, M its z-value along the axis fixed in space, k its z-value along the axis fixed in the molecule, and p denotes a chosen electronic state.

The effective nuclear motion Hamiltonian, depending only on the q, can be obtained by letting the Hamiltonian operator operate on functions of this kind and multiplying the resulting expression from the left by $\psi_{p'}(q, z)$ and integrating over the z. Doing this yields an equation with coupling between different electronic states, labeled by p. The effective internal motion operator is then:

$$\begin{aligned}
&<JMk'p'|H'|JMkp>_z \\
&\quad = \frac{\hbar^2}{4}(b_{+2}C^{+}_{Jk+1}C^{+}_{Jk}\delta_{k'k+2} + b_{-2}C^{-}_{Jk-1}C^{-}_{Jk}\delta_{k'k-2})\delta_{p'p} + \frac{\hbar^2}{4}(C^{+}_{Jk}(b_{+1}(2k+1) \\
&\qquad + \lambda_{+})\delta_{k'k+1} + C^{-}_{Jk}(b_{-1}(2k-1) + \lambda_{-})\delta_{k'k-1})\delta_{p'p} + \frac{\hbar^2}{4}(C^{+}_{Jk}\gamma^{+}_{p'p}(\boldsymbol{q})\delta_{k'k+1} \\
&\qquad + C^{-}_{Jk}\gamma^{-}_{p'p}(\boldsymbol{q})\delta_{k'k-1}) + \frac{\hbar^2}{2}((J(J+1) - k^2)b + b_0k^2 + \lambda_0 k)\delta_{k'k}\delta_{p'p} \\
&\qquad + \frac{\hbar^2}{2}\delta_{k'k}k\gamma^{0}_{p'p}(\boldsymbol{q}) + \delta_{p'p}\delta_{k'k}(K_A + E_p(\boldsymbol{q}) + V^n(\boldsymbol{q})) + \delta_{k'k}\gamma_{p'p}(\boldsymbol{q}). \qquad (29)
\end{aligned}$$

The definitions of the terms can be found in [30], but it is sufficient here to note that K_A represents the vibrational kinetic energy operator, E_p the electronic energy, V^n the nuclear repulsion operator, and the terms b and b_0 are elements of a matrix closely related to the inverse of the instantaneous inertia operator matrix. It should also be noted that the γ terms arise from the interaction of the rotational with the electronic motion and tend to couple electronic states, even those diagonal in k.

If it were the case that a single electronic state dominated in the energy range of interest and that within that state for a given J only a single value of k dominated then, to a first approximation the Hamiltonian

$$(K_A + E_p(\boldsymbol{q}) + V^n(\boldsymbol{q}))$$

would determine the vibrational motion and, since the b and b_0 values are simply multipliers, the Hamiltonian

$$\frac{\hbar^2}{2}((J(J+1) - k^2)b + b_0k^2)$$

would determine the rotational motion if any contribution from λ_0 can be ignored. This separation forms the basis for the standard description of vibration–rotation motion in which the vibrational levels are treated as primary levels having rotational sublevels. In the standard description of an oblate symmetric-top, for example, the expression becomes:

$$hc\,(BJ(J+1)+(C-B)k^2),$$

where B and C are the rotational constants expressed in cm^{-1}.

It is argued in [28], however, that it would be logical to regard this second term as a modification to the potential in the context of solving the full rotation–vibration problem for there is no particular indication that the second term is separable. Indeed, this is exactly what is done in the most accurate clamped-nuclei calculations on the hydrogen molecule. In [31], it is shown that for the hydrogen molecule dissociating into two hydrogen atoms in their ground states, the $J=0$ state supports 14 vibrational states, the state $J=15$ supports 10, and for $J=31$ only 1. In fact, there are just 301 states that can be associated with the lowest electronic state of the hydrogen molecule. Hence, it is clear that here the number of vibrational states possible is strongly associated with the rotational state. Furthermore, the energy levels are inter-twined. Thus, for example, in the ground vibrational state, the rotational state with $J=9$ has a higher energy than the $J=0$ state has in the second vibrational state. This approach to the potential has also been used in some calculations on H_3^+. In the case of $J=0$ in the chosen formulation, it is estimated that there are 1,280 vibrational states below dissociation [32]. It seems that 46 is the highest value of J for which at least one vibrational state exists [33], but these figures should be taken as indicative rather than definitive, for the electronic structure calculations from which they result, though among the best available, do not have quite the accuracy that the calculations on H_2 cited above do. What information there is would seem to indicate that for $J=11$ and above there will be overlap between the rotational states assigned to the lowest vibrational state and the $J=0$ states of the higher vibrational states, just like the inter-twining that occurs in the hydrogen molecule case.

It is clear, however, that the larger the nuclear masses become, the smaller must the variables b and b_0 become, for they depend on reciprocals of the nuclear masses. Thus, the rotational motion will have a decreasing effect upon the potential for vibrational motion as the nuclear masses increase. Hence, although it is not correct to treat rotational motion as an ignorable motion in the same sense that translational motion is, it seems nevertheless generally justifiable to neglect the effect of rotational motion when considering vibrational motion. The general arguments advanced in [2] would therefore seem to remain valid ones.

4 Conclusions

In [2], the authors clearly set out the way in which they saw quantum mechanics as being used to explain molecular spectra in a chemical context. They recognized that the Born–Oppenheimer approximation was central to the way in which the quantum mechanics was used to provide chemically relevant interpretations of spectra. Their particular interest was in the vibrational states and the vibrational structure on electronic transitions. They regarded the coordinates used to describe translations and rotations as ignorable in the context chosen and supposed that the arguments used by Born and Oppenheimer to separate rotational motion was sufficient for their purposes neither did they consider the problems that might be posed by the requirements of permutational invariance. In both these areas, there still remain unanswered questions. It is a source of great regret that we no longer have Carl among us to help to answer them.

Acknowledgments Some of this work developed as part of ESA contract 21790/08/NL/HE and was carried out at the Universite Libre de Bruxelles. I thank the Fonds National de la Recherche Scientifique (F.R.S.-FNRS, contracts FRFC and IISN), the Universite libre de Bruxelles, and the “Action de Recherches Concertees de la Communaute francaise de Belgique” for accommodation and the provision of library and computing facilities.

References

1. Ballhausen CJ (1979) J Chem Ed 56:357
2. Ballhausen CJ, Hansen AE (1972) Ann Rev Phys Chem 23:15
3. Sutcliffe BT, Tennyson J (1987) In: Avery JS, Dahl JP, Hansen AE (eds) Understanding molecular properties. Springer-Verlag, Berlin, p 449
4. Sutcliffe BT (1990) In: Maksic ZB (ed) Theoretical models of chemical bonding Part 1. Springer-Verlag, Berlin, p 1
5. Primas H (1998) Acta Polytechnica Scand 91:83
6. Eckart C (1935) Phys Rev 47:552
7. Watson JKG (1968) Mol Phys 15:479
8. Woolley RG (2003) In: Wilson S (ed) Handbook of molecular physics and quantum chemistry, Vol 1 fundamentals, Part 7, Chap 40. Wiley, London, p 679
9. Kato T (1951) Trans Am Math Soc 70:212
10. Thirring W (1987) In: Kilminster CW (ed) Schrödinger, centenary celebrations of a polymath. Cambridge University Press, Cambridge, p 65
11. Born M, Oppenheimer JR (1927) Ann Phys 84:457
12. Sutcliffe BT, Woolley RG (2005) Phys Chem Chem Phys 7:3664
13. Mead CA (1992) Rev Mod Phys 64:51
14. Combes JM, Duclos P, Seiler R (1981) In: Velo D, Wightman A (eds) Rigorous results in atomic and molecular physics. Plenum, New York, p 185
15. Klein M, Martinez A, Seiler R, Wang XP (1992) Commun Math Phys 143:607
16. Born M, Huang K (1955) Dynamical theory of crystal lattices. Oxford University Press, Oxford, Appendix 8
17. Hagedorn G (1980) Commun Math Phys 77:1
18. Hagedorn G, Joye A (2001) Commun Math Phys 223:583
19. Hagedorn G (1990) Theor Chim Acta 77:163
20. Schmelzer A, Murrell JN (1985) Int J Quant Chem 28:288
21. Collins MA, Parsons DF (1993) J Chem Phys 99:6756
22. Braams BJ, Bowman JB (2009) Int Rev Phys Chem 28:577
23. Cassam-Chenai P, Patras F (2008) J Math Chem 44:938
24. Weyl H (1946) The classical groups: their invariants and representations, 2nd edn. Princeton University, Princeton, p 75

25. Helffer B, Sjöstrand SJ (1984) Commun Partial Differ Equ 9:337
26. Katriel J, Paldus J, Pauncz R (1985) Int J Quant Chem 28:181
27. Katriel J (2001) J Mol Struct THEOCHEM 547:1
28. Sutcliffe BT (2010) Theor Chem Acc 127:121
29. Sutcliffe BT (1993) J Chem Soc Faraday Trans 89:2321
30. Sutcliffe BT (2000) Adv Chem Phys 114:1
31. Pachuki K, Komasa J (2009) J Chem Phys 130:164113
32. Henderson JR, Tennyson J, Sutcliffe BT (1993) J Chem Phys 98:7191
33. Miller S, Tennyson J (1988) Chem Phys Lett 145:117

Struct Bond (2012) 143: 121–148
DOI: 10.1007/430_2011_51

From Ligand Field Theory to Molecular Collision Dynamics: A Common Thread of Angular Momentum

Anthony J. McCaffery

Abstract Interest in, and appreciation of, the role played by angular momentum in chemical physics was first aroused by a Carl Ballhausen lecture early in the author's scientific career. Later came deeper understanding of the fundamental nature of angular momentum and the power of its formal algebraic expression. Spectroscopy using light of precisely defined energy and (*z*-component of) angular momentum represents a unique experimental probe with the potential to reveal the underlying physics of chemical processes. Experiments using circularly polarised emission of gas phase molecules led to new insights in the field of molecular collision dynamics. Further work, and that of others, suggested an alternative formulation of the mechanics of bimolecular collisions. A theoretical model was developed guided throughout by experiment. Its basis is linear-to-angular momentum conversion within the constraint of state-to-state energy conservation. An evolutionary process guided by experiment is described, with illustrations that demonstrate the power of the angular momentum theory of molecular collisions developed by the author and co-workers. Examples include very recent work on multicollision models of gas ensembles of potential value in, e.g., modelling planetary atmospheres.

Keywords Angular momentum · Energy transfer · Molecular collision dynamics

Contents

A.J. McCaffery (✉)
Department of Chemistry, University of Sussex, Brighton BN1 9QJ, UK
e-mail: A.J.McCaffery@Sussex.ac.uk

1 Introduction

My first encounter with Carl Ballhausen was at an Inorganic Group meeting in Oxford in the early 1960s when, as a second year graduate student working on optical activity in transition metal complexes, I heard Carl give an outstandingly clear exposition on why angular momentum (AM) eigenfunctions form an essential part of atomic, and hence coordination complex, theory and form the basis of atomic and molecular wave functions. David Buckingham had introduced Carl with the humorous aside that he (i.e., Carl) was the writer of a text [1] of great service to the inorganic community in making comprehensible the daunting volume by J. S.Griffith! [2] This of course it does; but from first publication Introduction to Ligand Field Theory was universally recognised as a major contribution to the theoretical basis of coordination chemistry. In the text and in his lecture, Carl lucidly explained how properly constructed AM eigenfunctions provide the essential description of many-electron systems of high symmetry, and he showed explicitly how to write suitable functions. These basic elements together with much insight into the theoretical and experimental basis of ligand field theory are set out at greater length in his book. I was greatly impressed by the clarity and rigour of this presentation so that a year later, when awarded a CIBA-GEIGY Fellowship, I opted to take it up in Copenhagen in the Ballhausen laboratory. This proved a very stimulating environment, right at the forefront of research on theoretical coordination chemistry and ligand field theory. Permanent staff and a large contingent of post-doctoral researchers from many different countries worked on experimental and theoretical aspects of coordination complex bonding theory and spectroscopy, creating a uniquely focussed and stimulating environment.

This introduction to the world of interactive theory and experiment, in which discoveries in one branch provided significant guidance for research in the other, was most influential. It was followed in my case by a very productive period working with Paul Schatz at University of Virginia and involved deeper immersion into the world of angular momentum theory, guided by expert tuition from Paul and from Philip Stephens. Also highly influential were the publications of Peter Day and other leading authors whose work illustrates vividly the elegance and power of Griffith's methods. As readers will be aware, the latter differ somewhat from the approach taken in Carl's book in their extensive use of Griffith's adaptation of formal angular momentum theory. This topic, previously the exclusive domain of theoretical physics, greatly speeds construction of symmetry adapted AM eigenfunctions for the electronic structure and symmetry of the molecule under consideration and in evaluating key matrix elements. The irreducible tensor method provides a very powerful and rigorous formalism for writing electronic structures of complexes of the transition metal ions and for describing their interaction with radiation and external electric and magnetic fields. In Paul Schatz's lab, experiments were designed to measure high-resolution magnetic circular dichroism in inorganic complexes at low temperature. Circularly polarised photons carry well-defined total, and *z*-component of, angular momentum and hence data analysis centres on how photons of precise energy and AM interact with molecules known to be in states defined in terms of AM eigenfunctions. This familiarity with the fundamental significance of angular momentum that began with the Ballhausen lecture was to have considerable influence in later developments.

2 Angular Momentum in Collision Dynamics

At first glance, the physics of molecular collisions in closed shell molecules might be thought to have little in common with vibronic transitions in complexes of the transition metal ions. However, the utility of AM eigenfunctions and the universality of AM algebra means that there are always potential common elements in formalism and concepts. Thus, angular momentum enters early on in the formal expression of quantum scattering theory for atom-rigid rotor collisions. In the coupled equations of Arthurs and Dalgarno [3], initial and final wave functions are written in terms of orbital ($l;m_\mathrm{l}$) and rotor ($j;m_\mathrm{j}$) AM and a single incoming momentum wave is scattered into a weighted sum of outgoing partial waves, each of well-defined ($l';m'_\mathrm{l}$); ($j';m'_\mathrm{j}$). The coupled equations are generally expressed in the total **J** basis in which the (vector) sum of $(l + j) = J = (j' + l')$, resulting in a set of close-coupled (CC) equations in which **J** is conserved as is its projection M. In the general atom–diatom scattering case, there are many coupled equations and determining the amplitudes of each scattered wave is a demanding task if a large number of *j* and *l* channels are open. The CC equations are diagonal in J and independent of M and the total *J* formulation could be seen as an application of the Wigner–Eckart theorem [4, 5], widely used in problems involving coordination chemistry [6]. Other forms of recoupling, the translation-internal coupling scheme, for example, allow the tensor properties of the T-matrix to be explicitly formulated [7, 8] and are particularly useful when the multipolar moments of the m_j distributions are required, as, for example, in experiments using polarised light or 2-photon excitation.

Despite the clarity contained within the AM formalism, current collision theories such as the CC method, briefly outlined above, or the numerous modifications of reduced rigour, insight into the relationship between initial conditions and the outcomes is often very hard to obtain. Calculations are highly computer intensive, since many ($l,m_\mathrm{l};j,m_\mathrm{j}$) channels must be summed over as the system traverses an intermolecular potential energy surface (PES). Furthermore, the PES must be accurately known for each collision pair. Scattering amplitudes are obtained but their relation to distinctive characteristics of the colliding species is rarely apparent and causal relationships are difficult to discern. Furthermore, any change in the collision partners, however small, requires a new PES appropriate to that pair, with results highly sensitive to PES details. Very few generalisations have emerged from many years of highly sophisticated experiment and theory, with few guiding principles or predictive principles for even the simplest of collision partners. Although computational packages now exist, scattering theory calculations of collision outcomes are still some distance from becoming an everyday tool of the practical chemist working in the field of chemical or physical change. Furthermore, this gap has not been filled by classical trajectory calculations, which also have given relatively little insight into the basic physics of change at the molecular level.

Experimental investigation of collision dynamics at the molecular level was revolutionised in the late 1960s and early 1970s by the introduction of commercial laser systems. These permitted quantum state-resolved transition probabilities to be measured with relative ease, rapidly creating a large database of state-to-state rate constants or cross-sections for inelastic transfer with rotational state resolution. Among these were a small number of experiments indicating that very simple theories, unrelated to the formal methods mentioned above, were capable of explaining the results of very sophisticated experiments. For example, Gentry and co-workers [9], following analysis of the rotational "rainbow" (i.e., angular distribution) of inelastic scattering of $ArCl_2$ in a difficult and lengthy molecular beam experiment, reported that the characteristic rainbow angle (distribution peak) was directly relatable to half the bond length of the Cl_2 molecule. They concluded that their "hard-won data had yielded little more than could have been predicted from a table of atomic radii". However, these authors also recognised the value of a direct link from a collision observable to a well-established, measurable, molecular property. Parmenter and coworkers [10] demonstrated that, in inelastic collisions between glyoxal and a wide range of partners, simple factors such as molecular mass of the partners were considerably more significant than the intermolecular potential. Most revealing were the 28 amu species CO, N_2 and C_2H_4. Each of these species has a very different PES of interaction with glyoxal, but the experimental inelastic data were found to be indistinguishable. Bosanac [11] had earlier reproduced the key elements of sophisticated molecular beam scattering experiments with a simple model based on linear-to-angular momentum conversion at the edge of a 2-D ellipse having the (A–B) dimension equal to half molecular bond length. In concluding a survey of atom–diatom collision data in 1992, Korsch and Ernesti [12] remarked ". . ..amazingly simple models allow very precise description of experimental rotational transfer results."

The author became interested in collision-induced state-to-state processes as a result of experiments in which narrow-line, circularly polarised laser radiation was used to excite fluorescence from diatomic molecules in collision cells. The laser excites known multipolar moments of m_j distribution among specific j states of an excited vibronic state. Wavelength and polarisation analysis of the emission allowed the population and orientation multipoles of m_j among states accessed by elastic and inelastic collisions to be determined from measured intensity and degree of circular polarisation. An example is shown in Fig. 1, from which it is evident that the initial asymmetric m_j distribution is maintained through elastic and inelastic collisions [13] even when substantial amounts of vibrational and rotational energy

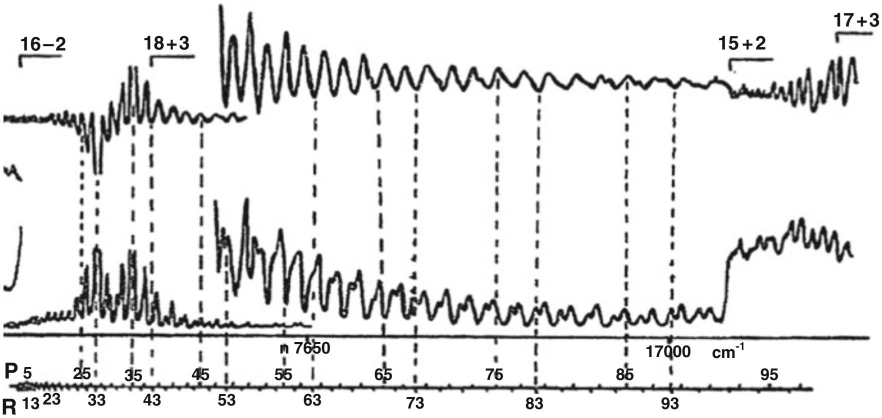

Fig. 1 Intensity (*lower spectrum*) and circular polarisation (*upper spectrum*) of emission from (B) $^3\Pi_{0u+}$ I_2 in a collision cell with He as partner gas. Initial excitation is to ($v = 16; j = 34$) of the B state and Fig. 1 shows the RT populations and circular polarisations monitored via the $16 \rightarrow 2$ vibrational transition. Note that VRT features $>\Delta v = 4$ are also strongly polarised

are exchanged. Subsequent experimental investigations [14, 15] demonstrated this to be a widespread phenomenon in diatomics that either are, light or heavy, do or do not possess dipole moments, do or do not have atoms possessing nuclear spin. Quantitative measurements indicate that reorienting (m_j changing) collisions have very small cross-sections for diatomic – rare gas partners [16]. In a detailed theoretical study of this phenomenon, Khare, Kouri and Hoffmann [17] concluded that the change in angular momentum causing a j changing collision must result from momentum change perpendicular to the direction of momentum change. This optimal condition for AM transfer, essentially Newtonian in nature, was later confirmed by experiment [18, 19].

The m_j components of a particular diatomic j state are $(2j + 1)$-fold degenerate. In an energy-based mechanics, such as the classical mechanics of Lagrange or Hamilton or quantum scattering theory, in which kinetic energy of relative motion is converted into rotational or other form of internal energy via anisotropies in the PES, very rapid interconversion between the m_j states in a j manifold would be anticipated. However, to those widely aware of the remarkable properties of angular momentum, such rapid changes might not be the first expectation in a body that, once set into motion, somewhat resembles a microscopic bicycle wheel. This indicator of an important role for angular momentum in collision dynamics led to further experimental discoveries, some described briefly below, where again the focus is on collision-induced *rotational* state change.

Angular momentum enters into the dynamics of collisions in two principal guises. It is created when the initial momentum of relative motion is converted, on impact, to orbital AM. This orbital AM is then partitioned between molecular rotation and recoil orbital AM. Molecular rotation plays a key role here since spectroscopic methods allow directly measurement of rotational energy and rotational AM both before and after collision and from such measurements, the key quantities of collision-induced change in energy and AM are obtained with high precision. This is important since the rotations, although small in energy magnitude, are the true building blocks of a theory of collision-induced change. Our principal interest is in the quantum state selectivity and probability of population transfer from precollision to post-collision species. This contains the critical information on the nature of the forces that govern physical and chemical change. Just as the sum of vibrational state populations gives that of a particular electronic state, the sum of rotational intensities within a given vibration state represents the population of that vibrational state. In momentum terms, collision-induced vibration state change simply represents an exchange of linear momentum and therefore could be seen in terms of a momentum and energy *threshold* that must be attained before rotations within that v-state may be accessed.

Diatomic molecules are favoured species for collision dynamics experiment and theory primarily because of their relative simplicity for theoretical and experimental investigation. Diatomics have a single vibrational mode and rotational motion about one axis so that data analysis is relatively simple. However, since rotational energy and rotational AM within a vibrational manifold increase and decrease together in diatomics, any differences between the role of AM change and of energy change are difficult to disentangle. This is particularly problematic if the diatomic is initially in its $j = 0$ level. The earliest and most detailed experiments were often performed on molecules in their lowest j states and thus any separation of the roles of the two variables mentioned above would not be apparent. However, this situation changes for rovibrational energy transfer from diatomics in high (v;j) states, and data from experiments of this kind [20, 21] have been used to demonstrate the dominant role of AM change in determining the probability of transition [22]. This separation is clearly apparent in, e.g., bent triatomic molecules. These species have complex energy level patterns arising from the asymmetric rotor quantisation condition in which total AM (j) and two projection quantum numbers (k_a and k_c) define each state. This effectively decouples the simple relation between energy and AM as the NH_2 energy level diagram shown in Fig. 2 illustrates. The diagram makes clear that, for example, transition between $j = 2$ and $j = 4$ (of $k_a = 0$ and 2, respectively) involve very small ΔE for $\Delta j = 2$, whereas the $\Delta j = 0$ transition from 3_{03} requires substantial ΔE. Thus, in asymmetric rotors, energy and AM changing events are readily decoupled.

Experimental [23, 24] probabilities for the many possible collision-induced transitions in this molecule show no apparent dependence on energy gap between initial and final state. However, the probabilities fall exponentially with the magnitude of the AM gap measured as shown in Fig. 3. This static model (Fig. 3) of an asymmetric top $j_{\mathrm{ka;kc}}$ AM vector is not wholly representative since the vector's natural precession creates an AM trajectory. Coupling of this vector to an external AM introduced on collision can cause the vector to hop to an adjacent trajectory of different $j_{\mathrm{ka;kc}}$ on the molecule's AM "surface." When this dynamical picture is considered, the conclusions above remain valid [24, 25]. The energy gap generally becomes more dominant as initial j state increases [25], an effect also found in

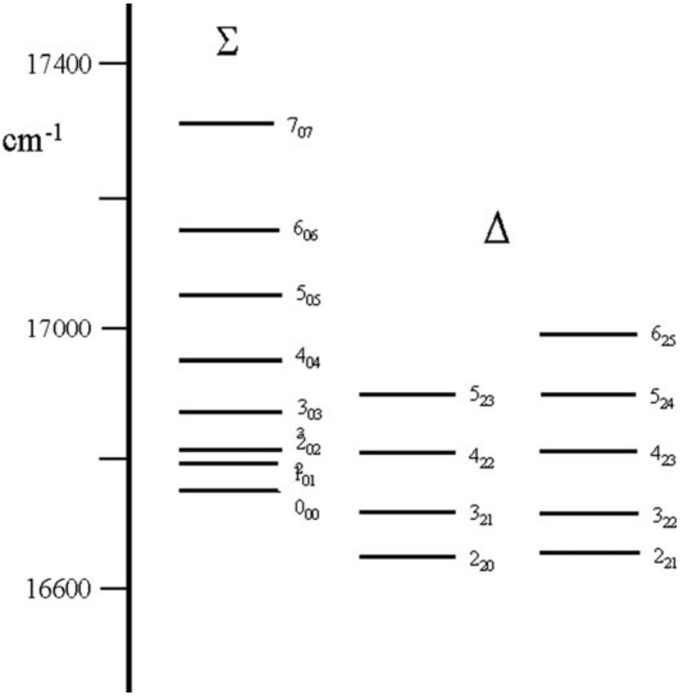

Fig. 2 Energy level diagram for the $k_a = 0, 2$ states of NH_2 in the (0,9,0) vibrational manifold of the (*upper*) $^2A_1$ state. Note that spin doublet states are not shown here

Fig. 3 AM vector diagram showing the length of the vector that couples $j_{ka;kc} = 3_{03}$ to 5_{23} in the fixed vector approximation

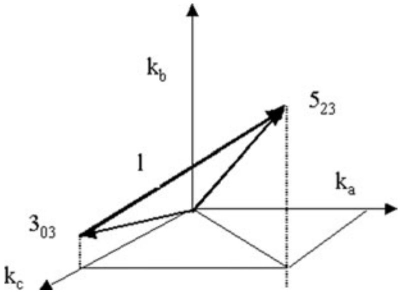

molecules generally [26]. This occurs because the energy conservation condition acts as a constraint on AM conversion as discussed in more detail below. Linear to-angular momentum conversion provides the primary motive force for change, although the manner in which energy conservation modifies the range of possible processes, each of which must simultaneously obey energy and AM conservation, leads to a wide variety of outcomes in collision experiments [27].

A third piece of experimental evidence came from double resonance measurements carried out in the author's laboratory using two narrow line tuneable dye lasers and a heated cell containing Li_2 molecules with Xe as collision partner. The first laser selects a known velocity subgroup of a single rovibrational state in $A(^1\Sigma^+)Li_2$ and a second narrow line laser, tuned to a different rotational state, measures intensity and line width of the transferred population. The line width is a measure of the reorientation of the velocity vector and can be directly transformed to give the differential scattering cross-section for the state-to-state process [28, 29]. Thus, this all-spectroscopic experiment gives a full description of the collision event namely the probability of transfer to a new rovibrational state for a selected relative velocity plus the most probable scattering angle for that relative velocity and its distribution. By tuning the excitation laser over the initial state Doppler profile a threefold change in magnitude of initial relative velocity was achieved [30, 31]. This highly detailed collision dynamics experiment yielded results that on analysis, corroborated the point made by Korsch and Ernesti [12], namely, that very simple models can reproduce the results of the most sophisticated of experiments. The most probable scattering angle could be predicted from a simple Newtonian vector model connecting initial relative velocity (v_r), threshold, or channel-opening velocity (v_{th}), a quantity readily calculated from ΔE for the transition, and sin θ where θ is the (measured) most probable scattering angle [32, 33]. The relationship is sin $\theta = v_{th}/v_r$ and as Fig. 4 demonstrates, this fits all data measured in the velocity selected double resonance experiment as well as data

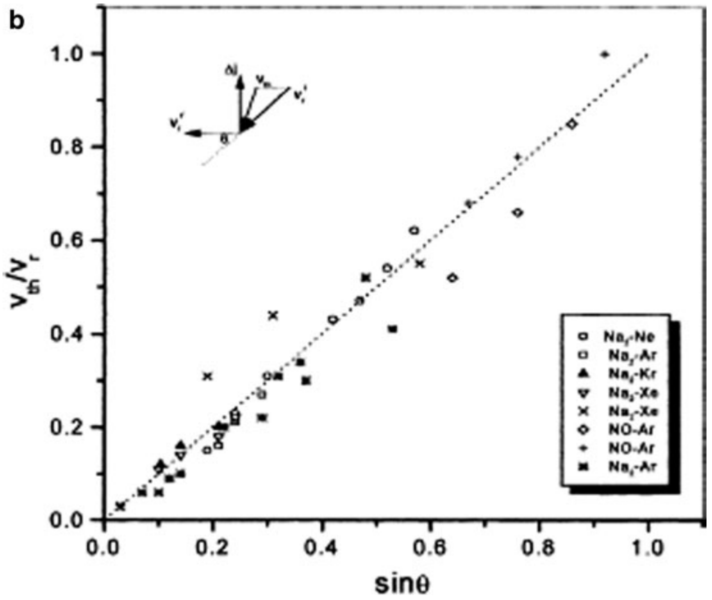

Fig. 4 Plot of sin θ, where θ is the most probable scattering angle, versus v_{th}/v_r where v_r is the most probable relative velocity and v_{th} the (calculated) threshold relative velocity for the particular state-to-state collision-induced transition

from a wide range of molecular beam scattering experiments on a number of different systems [24].

2.1 An Angular Momentum Model for Collision-Induced Transfer

These experimental results, and others similar in their conclusions, suggested to the author that an expression for predicting the quantum state-to-quantum state outcome of molecular collisions might be based on the (vector) momentum mechanics of Newton rather than the (scalar) energy mechanics of Lagrange and Hamilton. These differ fundamentally in their identification for the origin of the force that leads to change. This is attributed in Newtonian mechanics to momentum (p) change, i.e.,

$$F = ma = \mathrm{d}p/\mathrm{d}t. \tag{1}$$

The concept of energy in Newton's era was only partially formed and does not appear in his equations of motion. Ideas on energy only began to be sharpened following much later work on, e.g., the equivalence of heat and work by Joule and Rumford with experiments on the efficiency of the steam engine playing a particularly significant role. These led Lagrange to substitute expressions for kinetic (T) and potential (V) energy into (1) and in this new, energy-based mechanics, force is redefined in terms of the variation of the potential energy with distance or angle, i.e., $F = \mathrm{d}V/\mathrm{d}q$ where q is a generalised coordinate. Hamilton's later reformulation and the formal expression of the law of conservation of energy in the middle of the nineteenth century resulted in a very usable form of mechanics for macroscopic bodies that is generally known as classical mechanics, elements of which are evident in modern quantum mechanics. However, lost in the transformation is the inherent vector nature of Newton's mechanics with force and directionality now to be obtained from the variation of the scalar potential energy field with angle and/or distance.

Collision and reaction dynamics experiments on molecules in the laser era are considerably more sophisticated and detailed than those of the eighteenth and nineteenth centuries that resulted in the new forms of mechanics formulated by Lagrange and Hamilton. In addition to great improvements in the methods of preparing molecules prior to collision and probing them post-collision, there is the precision in our knowledge of the energy and angular momentum of molecules inherent in the molecule's quantum state description. Each molecule must start in a well-defined quantum state and end in another and thus the process has elements in common with spectroscopy. This analogy has its limitations but also has its uses. Photons have well-defined energy, AM and parity, all properties that place strict limitations on the destination state for a given initial state. In a collision dynamics experiment, the collision energy may be expressed with reasonable precision and so the initial orbital angular momentum generated on collision is moderately well defined. It may, however, be very large – up to 500 ħ or more for heavy atom – heavy molecule encounters, although frequently very much less. Nuclear spin change can generally be ruled out and so $\Delta j = \pm 2n$ propensities are commonly seen in homonuclear diatomics, but the ubiquitous and generally reliable $\Delta j = \pm 1$, 0 of spectroscopy is absent. The collision equivalent appears to be a Δj "transfer function" that is an exponential-like fall [34, 35] of transition probability as magnitude of Δj increases.

This "spectroscopic analogy" might seem an unpromising approach until the alternatives are considered of, e.g., summing over the many scattered partial waves following traversal over a PES with the partitioning of flux highly dependent on the accuracy of the surface and with little insight available as to the features of the surface that favour particular outcomes. The experimental factors described above led the author and co-workers to develop an alternative form of mechanics for collision-induced quantum state change that follows Newton but incorporates later discoveries, e.g., quantisation and the conservation of energy for each quantum state-to-quantum state transition. For the reasons given above on the special role of molecular rotations, the development begins from the equation for conversion of linear momentum of relative motion to angular momentum,

$$l = \mu v_{\mathrm{r}} b_{\mathrm{n}}, \tag{2}$$

where l is the orbital angular momentum generated initially on collision, μ is the reduced mass of the collision pair, v_{r} the relative velocity and b_{n} the effective impact parameter or molecular "*lever arm*" about which linear momentum is converted to angular momentum. Once created, l is then partitioned between molecular rotation change Δj and recoil orbital AM. Energy change (ΔE) on collision accompanies AM change and so, in the most general terms, the probability of collision-induced rotational state change could be written as a joint probability function $P(\Delta j;\Delta E)$. As experiment strongly suggests that momentum change provides the motive force, the probabilities (P) of simultaneous AM and energy change are assumed to be independent variables and can be written

$$P(\Delta j, \Delta E) = P(\Delta j)P(\Delta E). \tag{3}$$

To simplify the problem of calculation, $P(\Delta E)$ is assumed to be a delta function that allows state-to-state transitions strictly within the limit of available energy i.e.

$$P(\Delta j, \Delta E) = P(\Delta j)\delta(E_{\mathrm{tot}} - E'_{\mathrm{tot}})\delta(J - J'). \tag{4}$$

Using probability theory, the following expression was obtained as the basic rotational transfer function. In practice, this expression is summed over available velocities weighted by their individual probabilities.

$$P(j_\mathrm{f}|j_\mathrm{i}) = \int_0^{b_\mathrm{n}^\mathrm{max}} P(l|b_\mathrm{n})P(b_\mathrm{n})\delta(|E_\mathrm{tot} - E'_\mathrm{tot}|)\delta(|J_\mathrm{i} - J_\mathrm{f}|)b_\mathrm{n}db_\mathrm{n}dj_\mathrm{f}. \tag{5}$$

The energy conservation condition for each state-to-state process is

$$\tfrac{1}{2}\mu v_\mathrm{r}^2 = |\Delta E|, \tag{6}$$

where $\Delta E = E_\mathrm{f} - E_\mathrm{i}$ and the symbols i and f refer to initial and final quantum states, respectively, and the $j_\mathrm{i} - j_\mathrm{f}$ transition may take place within or between vibrational levels including those in different electronic states.

As Fig. 5 demonstrates, (5) is able to reproduce the exponential-like decay curve of rotational transfer probabilities and gives an excellent fit to a wide range of collision-induced rotational transfer (RT) data using $b_\mathrm{n}^\mathrm{max}$, the maximum value of the (molecular) torque- or lever arm, as a variable parameter. More precisely, an inverse-power dependence gave best results [36] although for many molecules, an exponential function provides a very reasonable fit. The data fit regularly returned $b_\mathrm{n}^\mathrm{max}$ = half bond length of a homonuclear diatomic or the equivalent distance from the centre-of-mass for a heteronuclear species, in good agreement with the very different experiment and analysis by Hoffbauer et al. [9].

However, (5) does not represent the most practical means of calculating state-to-state energy transfer rate constants or cross-sections. The process is readily computerised using a 3-dimensional ellipsoid or *Newton surface* to represent the molecule, in conjunction with a Monte Carlo set of many ($>10^6$) collision trajectories with the collision partner. This method was first used by Kreutz and Flynn [37] and is based on the simple 2-D ellipse kinematic relations first derived by Bosanac [11]. The function of the Newton surface, all dimensions of which are those of distance and are determined by the bond length of the target molecule, is to provide a realistic shape via which linear-to-(orbital) angular momentum conversion may be effected. The orbital AM is then partitioned between molecular rotation and recoil orbital AM with ellipsoid major (A) and minor (B) axis dimensions chosen so that (A–B) = half bond length = $b_\mathrm{n}^\mathrm{max}$. Relatively simple modifications allow heteronuclear species to be represented by an acentric ellipsoid. Bosanac [11] illustrates how a range of b_n values may be generated depending on the point of impact on the ellipse surface ranging from $b_\mathrm{n} = 0$ for end-on, or ellipse centre, impact or $b_\mathrm{n} = b_\mathrm{n}^\mathrm{max}$ for impact around 45°. Thus, the b_n value contains stereodynamical information.

This computational routine for predicting state-to-state probabilities has been shown to give quantitative agreement with experiment for a wide variety of collision-induced processes. These include rotational transfer (RT) [24, 26, 36, 38–40], i.e., state change *within* a vibrational manifold, vibration–rotation transfer (VRT) [41, 42], i.e., transitions between vibrational states and electronic energy transfer [43], i.e., transitions between discrete levels of different electronic states. An example is given in Fig. 6 in which the calculated data were computed using the

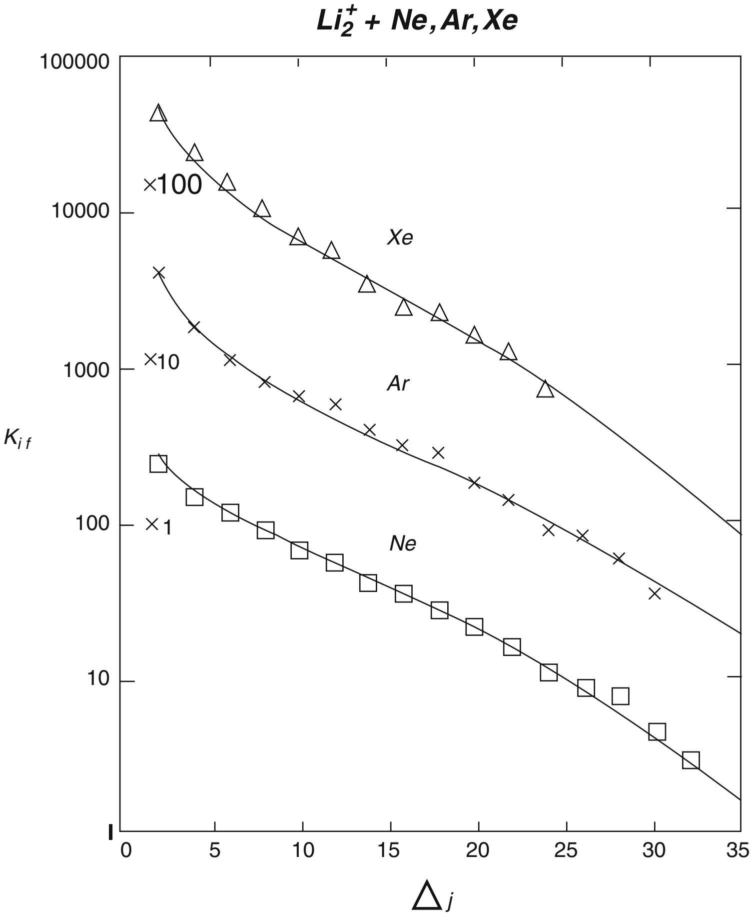

Fig. 5 Plot of rotational transfer rate coefficients for state-to-state collision-induced transfer in $A(^1\Sigma_u)$ Li_2 with Ne, Ar and Xe as collision partners from experiment (*symbols*) and via (5) (*full line*). Numerous other data sets on a wide range of molecules were found [36] to give fits of similar quality to (5)

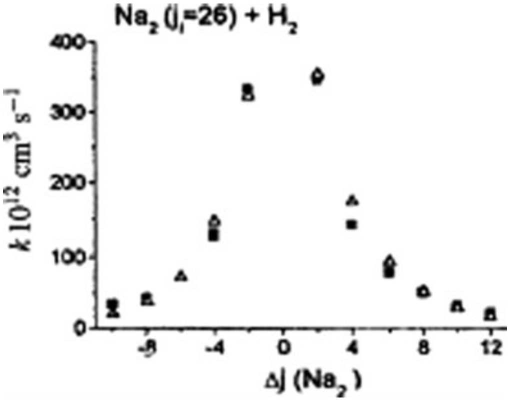

Fig. 6 Experimental (*filled squares*) and calculated (*open triangles*) rate constants for RT from $j = 26$ in Na_2* in collision with H_2. Experimental data from Brunner and Pritchard [35]. The figure illustrates that agreement between experiment and calculation is quantitative

diatomic–diatomic collision variant of the AM model [44]. The computation is based on (2) and the further conversion of l into Δj plus recoil with each trajectory subject to the state-to-state energy and overall energy conservation conditions of (4) and (6).

The use of classical mechanics to solve practical problems often involves development of an appropriate expression that combines simultaneous energy and AM conservation. This can be done for a limited number of cases of collision-induced transitions in molecular quantum states but rapidly becomes very complex when, for example, VRT or takes place. Furthermore, such equations often lack the transparency of the individual expressions for energy and AM conservation and key insights are lost. This is readily illustrated since the equations for ΔE and for Δj (in the limiting case $l = \Delta j$ so that $\Delta j = \mu\, v\, b_{\mathrm{n}}^{\max}$) may both be plotted as velocity or momentum as a function of Δj using $b_{\mathrm{n}}^{\max} =$ half bond length (HBL). This gives a clear picture of the very different effects energy– and AM– conservation constraints have on the state-to-state outcome of collisions. Some examples are given below. Particularly relevant are collisions involving diatomic hydrides such as HF, OH, HCl, etc., which have relatively large molecular mass and hence generate substantial AM on collision. However, the energy levels of these species are determined by their *reduced* mass, so that each unit of AM change requires substantial energy input, a feature that would not immediately be evident from a combined expression. This disjunction between energy and AM requirements has a significant influence on the dynamical properties of diatomic hydrides, explaining, e.g., why they are excellent candidates as the gain medium in chemical lasers.

3 Dynamical Properties of Atmospheric Molecules

The use of the AM theory to predict the results of processes of change at the molecular level such as inelastic collisions, molecular dissociation, etc. was mentioned above with appropriate references to publications where full detail is given. In this final section, the method is illustrated with reference to the collision dynamics of Earth's major atmospheric species N_2 and O_2 and, as a contrast to these collisionally "well-behaved" molecules, some aspects of the dynamical properties of the more eccentric OH molecule are discussed. To begin with, the behaviour in single, state-to-state inelastic collisions is described. This is followed by an outline of more recent work that utilises the speed and accuracy of the AM method to construct a rudimentary model of energy transfer in planetary atmospheres, plasmas or other gas ensembles. In this model, the fate of energy, initially located in a single $(v;j)$ state of a trace species, is followed through many hundreds of collisions in an ensemble of up to 10,000 particles. At each stage, the actual populations of each quantum state in the gas mixture may be obtained. This approach is found to give more insight into non-equilibrium ensemble behaviour than is obtained from statistical methods of describing quantum state populations.

In studies of global warming, much of the emphasis is on radiation balance and the ability of key species in the atmosphere to radiate excess energy through a narrow infrared "window." Also significant, but more difficult to study, is the redistribution of energy contained in "hot" molecules, by collision, to the abundant homonuclear species O_2 and N_2, each of which may act as a reservoir for excess energy. These molecules may transfer energy to or from Earth's surface and oceans, or to other atmospheric gases including the minority radiating species, but they themselves make no significant contribution to outgoing terrestrial radiation. Here some of the fundamental collision properties of N_2 and O_2 are discussed, and their similarities and differences highlighted. In addition, the energy transfer properties of the OH molecule are discussed. Although present only in trace quantities, OH plays a very important role as a cleansing agent in the troposphere [45] and is known to be an essential component in models of ozone layer concentrations [45]. Its presence in the upper atmosphere as a contributor to Earth's airglow has been known since the pioneering work of Meinel [46].

3.1 Rotational Transfer and Vibration–Rotation Transfer

Rotational transfer (RT) is the collision transfer process that involves exchange of the smallest quanta of energy, and is found to accompany many other forms of collision-induced physical and chemical change. This form of state-to-state transition is illustrated as process 1 in Fig. 7 where RT within rotational states of $v = 0$ of the N_2 molecule are shown. Collision-induced RT may take place from any rotational state that is populated. Often this will be from individual levels within a Boltzmann distribution among the lower rotational states, but might alternatively take place from a single rovibrational level populated, e.g., by a laser and hence highly specified. Many events involving physical and chemical change appear to be highly quantum state selective and almost invariably are accompanied by rotational state change. That this is inevitable follows from the fact that molecules

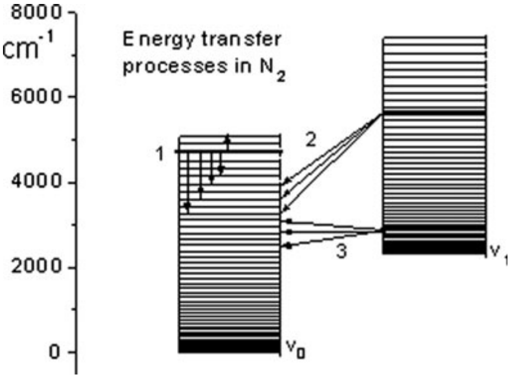

Fig. 7 Partial energy level diagram showing rotational states of $v = 0$, 1 of $(X)^1\Sigma_g^+$ N_2. Red, green and blue arrows illustrate the processes of rotational transfer (1), vibration rotation transfer (2) and quasi-resonant vibration rotation transfer (3) each of which is discussed in more detail in the text

Fig. 8 Collision-induced rotational transfer in collisions between Ar and $N_2(0;10)$ (*squares*), $O_2(0;12)$ (*circles*) and OH(0;3) (*triangles*). Collision conditions are Maxwell–Boltzmann distribution of velocities at 300 K. Note that there is a $\Delta j = 2n$ selection rule in collision-induced processes for homonuclear diatomic molecules

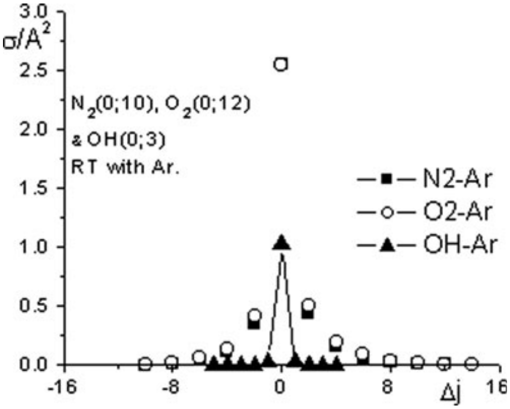

have a characteristic spatial distribution of mass and therefore generation of AM will usually occur when species collide due to the existence of lever arms within molecules. The value of constructing a view of energy transfer that begins with a quantitative description of rotational energy transfer was emphasised earlier.

Calculated cross-sections for RT in N_2, O_2 and OH in collisions with the rare gas Ar using the AM method are shown in Fig. 8. There are several interesting features in this figure. It is evident that the two principal components of Earth's atmosphere are quite similar in this basic aspect with calculated RT of N_2 and O_2 molecules almost identical. They have a very similar elastic ($\Delta j = 0$) cross-section and $\Delta j = \pm 2$ inelastic cross-sections that are of the order 0.4 $Å^2$ for each. It is well known that the transport properties of N_2 and O_2 in the troposphere are very alike, with little sign of gravitational separation until very high altitudes are reached [45], and this has its origin in the similarity in collision cross-sections for the two species. It is evident from Fig. 8 that transitions involving $\Delta j > \pm 4$ are of low probability with Ar as collision partner at 300 K. RT in the OH molecule is highly restricted under the same conditions (Ar partner, 300 K), with very low probability of rotational state change. A major cause of this inefficient conversion of linear to rotational AM in OH is the energy cost per AM unit. This aspect is discussed in more detail below.

There is greater differentiation in the behaviour of N_2 and O_2 when VRT is calculated. The data in Fig. 9 were computed for the processes $N_2(1,10) \rightarrow (0;\Delta j)$, $O_2(1,12) \rightarrow (0;\Delta j)$ and $OH(1,3) \rightarrow (0;\Delta n)$ at 1,200 K, 1,200 K and 300 K respectively, all with Ar as collision partner. As can be seen from Fig. 9, VRT cross-sections for O_2 exceed those for N_2 approximately by a factor of two. However, the individual state-to-state cross-sections for these two species are considerably smaller than those for RT. In addition, the overall shape of the VRT distributions for N_2 and O_2 are now much changed with the peak no longer at $\Delta j = 0$ but displaced to 16 and 15, respectively. The distribution shape, reminiscent to some extent of a rotational Boltzmann distribution, with Δj peak displaced by ≥ 15 units from the final state closest in energy to the initial quantum state, led early workers

Fig. 9 Vibration rotation transfer in $N_2(1,10) \rightarrow (0;\Delta j)$, (*squares*), $O_2(1,12) \rightarrow (0;\Delta j)$, (*circles*) and H(1,3) → (0;Δn), (*triangles*) collisions with Ar at 1,200 K, 1,200 K and 300 K respectively

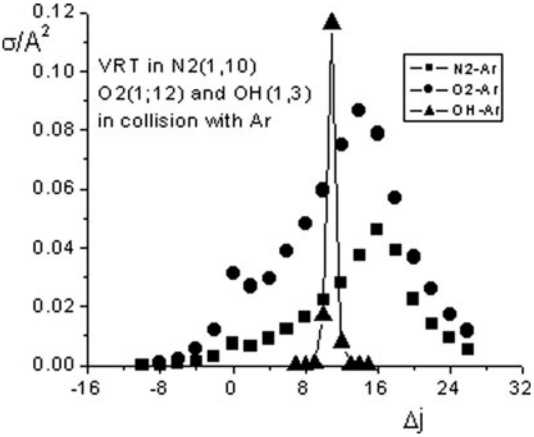

to assume complete thermalization occurs in this single collision event. However, rotational temperatures extracted from Boltzmann fits were often highly unphysical and clearly this interpretation is untenable. We show below that the shape and peak of VRT distributions are readily explained as the effect of energy and AM constraints on VRT process.

3.2 Understanding Collisions Through Velocity-AM Diagrams

In previous work, the author and co-workers have introduced, and made extensive use of, graphs in which relative velocity (or momentum) is plotted against change in rotational angular momentum [47]. This representation is very helpful in rationalising the disparate experimental observations that characterise the field of collision dynamics. The plots are of the two equations that form the basis of the above form of mechanics in their limiting forms and thus they indicate regions of velocity – AM space that are allowed or forbidden by the conservation of angular momentum and of energy.

The equations are:

$$\Delta j = \mu\, v_{\mathrm{rel}} b_{\mathrm{n}}^{\max} \quad (\mathrm{A-equation}). \tag{7}$$

The A-equation represents threshold condition for AM conservation in the process of linear-to-rotational AM conversion for each state-to-state transition. Thus, (7) expresses the limiting condition in which all incident linear momentum is converted to molecular rotation via the maximum lever arm ($b_{\mathrm{n}}^{\max}$) available from the molecule.

$$\Delta E = |E_{\mathrm{f}} - E_{\mathrm{i}}| = {}^1\!/_2\, \mu\, v_r^2 \quad (\mathrm{E-equation}). \tag{8}$$

Equation (8) is a statement of energy conservation for any collision-induced, state-to-state transition. Kinetic energy of relative motion is converted into internal energy within the molecule or vice versa. This might involve rotation state change alone or in conjunction with vibration state change and/or electronic state change. The velocity-AM diagrams are found to exist in a limited number of basic forms that have been found to be process-specific and, in addition, give strong indication as to the likely outcome of the collision. Examples below illustrate the power of these simple diagrams.

Figure 10 shows a $v_r - \Delta j$ diagram for RT and VRT for the N_2–Ar collision pair. The limiting linear-to-rotational AM condition (7) is represented by squares, whereas the energy conservation condition for RT within the $v = 0$ state is shown as circles with that for VRT from $v = 1 \rightarrow v = 0$ as triangles. The plot for O_2-Ar is very similar to this and so the general insights obtained from Fig. 10 will also apply to that system. Consider first the RT process. Any collision that results in quantum state change must occur with conservation of *both* energy and AM, and so the minimum permissible velocity available to open a specified Δj channel is the greater of the two obtained from computing solutions to (7) and (8). Figure 10 demonstrates that for transitions to most Δj channels for this collision pair, the limiting condition is generally that of energy conservation and those channels affected in this way are said to be *energy constrained*. Note, however, that the motive force for change in this model remains the momentum conversion process and for the Δj channels that are energy constrained, an adjustment to the value of $b_n^{\max}$ must be made so that the energy conservation condition is met. The diagram illustrates the A plot for the *maximum* value of b_n, the molecular lever arm, and it is evident that for all Δj channels that are energy constrained, a reduced maximum

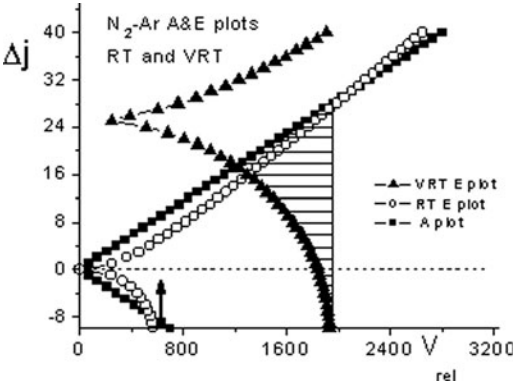

Fig. 10 Plots of (7) and (8) for RT within $v = 0$ from $N_2(0;10)$ and VRT N_2 $(1;10) \rightarrow (0;\Delta j)$. *Filled squares* represent the A-plot (7), *circles* the E-plot (8) for RT and *triangles* that for VRT. The *vertical arrow* indicates the mean relative speed at 300 K. From this it is evident that only velocities in the high-energy region of the MB distribution may open the VRT channels are hence the process is of low inherent probability. The *shaded region* indicates those channels and velocities for which energy and AM conservation are simultaneously conserved

value of b_n (lower than b_n^{max}) will conserve energy for all b_n up to this new maximum. This corrected, reduced, maximum b_n value is readily calculated for each Δj channel.

The link between b_n and point of impact was made above, and the effect of an energy constraint is to limit acceptable geometries for the atom–diatom collision to those that meet the new maximum b_n condition for the Δj channels concerned. This will of course reduce the number of successful trajectories and hence the probability of populating destination states that are energy constrained. The form of b_n reduction found in RT affects the efficiency of linear-to-angular momentum conversion, but does not change the essentially exponential-like decay of cross-section or rate constant with Δj. This characteristic shape results from the form of the $P(b_n)$ function for the ellipsoidal Newton surface used to represent the diatomic molecule, and is also exponential-like [36]. Other shapes have other, distinctive, forms of $P(b_n)$ function as demonstrated by Murrell and Bosanac [48]. The exponential-like decay of $P(\Delta j)$ with increasing Δj is the basic functional form from which other processes, with their characteristic energy constraint functions, are derived.

The N_2–Ar rotational transfer collisions (as with those between O_2–Ar) are relatively little constrained by energy conservation and so reasonably high RT probabilities are expected, and found, in collisions involving these molecules. The situation is very different for VRT, however, where, as Fig. 10 makes clear, all destination channels from $\Delta j = -12$ to +16 are energy limited, some very strongly so.

The overall shape of the E-plot is characteristic of vibrational energy transfer from high- to low-vibrational state, as portrayed in Fig. 7 (process 2), in which the largest energy gap is associated with the transition to the $j = 0$ rotational state of the lower vibrational level. This energy gap decreases as final j increases to a point around $j = 35$ ($\Delta j = 25$) when the energy gap is minimum, from which point it begins to increase. The near energy resonance with $j = 35$ in the lower state would, in some theoretical treatments, lead to the prediction that this j value should coincide with the peak of the rotational distribution following VRT. However, this is not the case and the peak is found at, or very close to, the Δj value at which the A- and the E-plots coincide. This is the case for both N_2 and O_2 with Ar and is found to be a widespread phenomenon in VRT and in the closely related process of vibrational predissociation [49–52].

The discussion above on reduction in maximum value of b_n to meet the energy conservation condition is particularly relevant here, and it is evident that all negative Δj, 0 and some low positive Δj channels are constrained strongly by energy conservation. They are further limited at 300 K by the magnitude of velocities required to open these channels so that only velocities in the high-energy tail of the MB distribution will suffice. The shaded region shows that part of velocity – AM space that is open for relative velocities greater than three times their mean value at 300 K (mean value indicated by the vertical arrow on the velocity axis of Fig. 10). The overall shape and peak of the resulting j state distribution in N_2 (0;Δj), following VRT from N_2 (1;10)–Ar collisions, are readily predicted from the $v_{rel} - \Delta j$ plot. The effect of the dominant energy constraint is to

Fig. 11 Plots of (7) and (8) for RT within $v = 0$ from OH (0;3) and VRT OH (1;3) → (0;Δj). *Squares* represent the A-plot (7), *circles* the E-plot (8) for RT and *triangles* represent the E-plot for VRT. The *vertical arrow* indicates mean relative speed at 300 K

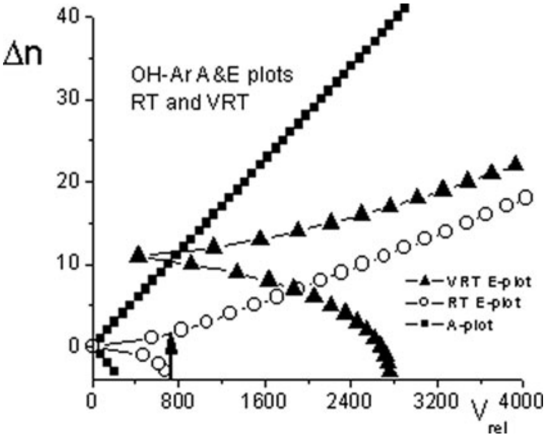

truncate strongly the −ve and low Δj region of the exponential-like decay. In addition to these insights concerning the rotational distributions, there is molecule frame directionality built in to this adapted form of vector mechanics via the b_n value. A simple illustration is that for $\Delta j = 0$, it is evident that $b_\mathrm{n} = 0$, implying impact either end-on, or directly in the middle of, a (homonuclear) diatomic. Other values of b_n are related to impact points on the Newton surface that represents a particular molecule for the key process of linear-to-angular momentum conversion.

The velocity-AM diagram for RT and VRT in OH–Ar collisions (Fig. 11) indicates that the energy conservation relation has a much more dramatic impact on the linear-to-angular momentum conversion process than was found with N_2 and O_2. This is a consequence of the very high rotational constant for OH – roughly an order of magnitude larger than those of N_2 and O_2. This results in an energy cost for each Δn collision-induced transition that is high and increases rapidly with the magnitude of Δn. The effect of this form of energy constraint is to focus the allowed collision-induced transitions into a narrow range of final n-states, as seen in Fig. 8. This constraint is highly effective, as the calculated RT cross-sections make clear. There is very little spread of Δn probabilities of the kind found in N_2 and O_2, and the exponential-like decay is very fast indeed.

A similar situation arises for VRT but now, because an inter-vibrational state change occurs, the peak is displaced to near energy-resonance with the initial OH (1;3) state. Again, access to other rotational states is limited by the energy cost of each Δn and at 300 K the focussing effect of flux into the new state is very marked. Thus, the molecule has been collisionally *pumped* to a narrow range of high n-states of $v = 0$. This is an example of process 3 in Fig. 7 and can be seen to represent a situation of some potential in gas laser gain-medium design. More valuable in this instance, however, would be to start with OH molecules in a high vibrational level, since the large anharmonic and centrifugal distortion constants for the hydrides and other light molecules mean that low Δn processes involving one or two Δv quanta occur quasi-resonantly. This quasi-resonant vibration–rotation transfer (QVRT) of low Δn transitions with small energy gaps can be very efficient indeed [20, 53–56], and the fact that it generally involves transitions between high n-states means that the energy constraint compresses transfer into a very small number of states. QVRT involves $-$ve Δv coupled with +ve Δn or vice versa and so population initially in high v and low n state may jump down in v but with increasing n. This effectively traps molecules in high n-states as the energy gaps for intra v-state relaxation become very large.

The above process is a key element in the operation of the gain medium in the HF chemical laser [57]. It is also thought to explain the remarkable persistence and exceptionally high rotational energy ($n \leq 32$) of OH emission in Earth's airglow which has been detected some 12 h after sunset and therefore cannot be the result of direct solar excitation [58]. In the final part of this contribution, the AM method is used to demonstrate how such effects might come about in a multicollision environment that represents a rudimentary model of Earth's atmosphere.

4 Equilibration of Gas Ensembles at the Quantum Level

The above discussion of the AM theory of collisions describes a theoretical approach to experiments designed to determine the quantum state outcome of single molecular collisions. These yield valuable data that allow theory to be tested and cross-sections or rate constants for elementary processes to be determined. However, real-life situations of physical and chemical change generally find molecules in environments where many collisions occur, and the single collision measurement may not always be a reliable guide to eventual outcomes. Examples of important gas ensembles include chemical reactors, industrial plasmas and planetary atmospheres. Furthermore, such gas ensembles often contain species that initially are highly excited. It would be very valuable to be able to model evolution towards equilibrium of such ensembles without recourse to the assumption of statistical behaviour, with consequent loss of potentially valuable information contained in the quantum state populations. Among the advantages of a full quantum state description of equilibration in multicollision environments are the possibility of (1) developing realistic models of chemical reactions in bulk that would allow process optimisation, (2) making positive use of known *non*-Boltzmann populations, e.g., in gas lasers, (3) intervening in the evolution of a non-equilibrium ensemble to achieve specific outcomes.

Obstacles to modelling the evolution of quantum state populations under multiple collisions primarily arise from the complexity of standard collision theory. An accurate PES is needed for all potential collision partners in a gas mixture and some species will be in highly excited states. State-to-state collision calculations are highly computer intensive for even the simplest of processes and, without a major increase in computational speed, are not suited to multiple, successive calculations. By contrast, the AM method is fast, accurate and calculations for atoms and/or diatomic molecules require only readily available data such as molecular bond length, atomic mass, spectroscopic constants and collision energy.

The author and coworkers have recently demonstrated [59–61] a quantitative, multicollision model of state-to-state equilibration in molecular gas ensembles containing up to 10,000 molecules. These are mixtures of atoms and/or diatomic molecules that generally contain one highly excited species in a bath gas of ground state atoms or molecules. Quantum state populations and (approximate) modal temperatures (T_{mode}) are computed for ensembles in which each constituent molecule undergoes successive cycles of single collision events of up to 1,000 or more collision cycles. T_{mode} values are obtained by assuming Boltzmann distributions. This is a poor approximation initially as all species begin in single (v;j) quantum states; however, T_{mode} values become much more reliable as equilibration proceeds. Plots of T_{mode} versus number of collision cycles undergone by the ensemble, the collision number (CN), give a useful pictorial guide to the equilibration process. The model also gives vibration and rotation quantum state population data at each stage in the ensemble's evolution and these yield greatest insight into the microscopic mechanism of ensemble equilibration. In our model, ensembles may consist of up to three different diatomic molecules, each initially in a specific (v;j) state ((v; n) in the case of OH) and in chosen proportions. Thus with further development, the method has the potential to model the microscopic processes of energy flow and the evolution towards local thermodynamic equilibrium (LTE) of gaseous environments that mimic aspects of the behaviour of, e.g., planetary atmospheres. Here, we illustrate use of the method to follow energy flow in the equilibration of a gas ensemble containing vibrationally excited OH (OH*) at the level of around 10% of total in a 4:1 mixture of N_2 + O_2.

OH is known to play a critical role in chemical, industrial and environmental contexts, although it frequently is only a minor component of the molecules present. An example is the combustion of hydrocarbon fuels [62]. Laser-induced fluorescence spectroscopy from OH is an important element in remote monitoring of the physical and chemical conditions during combustion. In Earth's troposphere, OH is a significant contributor to the oxidation, and eventual removal, of hydrocarbons and sulphur- or nitrogen-containing pollutants [45], and the role of OH in the balance of ozone creation and destruction is now well established [45]. The rotational spectra of OH have been used to measure mesosphere temperatures via ground, rocket or satellite-based measurements, as demonstrated by the recent work of Cosby and Slanger [63] based on the analysis of high-resolution Meinel band emission spectra. Excited OH is also found in comets, stellar atmospheres and interstellar clouds. In Earth's mesosphere, it is thought to be formed from the reaction $H + O_3 \rightarrow OH + O_2$ in a region around 8 km wide at ~87 km altitude. Laboratory studies [64, 65] have determined that the reaction is exothermic by $>$27,000 cm^{-1} with preferential population of OH vibrational states $v_{\mathrm{OH}} = 7$, 8 and 9.

A previous publication [59] contains a flowchart of the computational routine as well as a brief description of the method. For the calculations reported here, ensembles consist of (nominally) 8,000 molecules in the ratio excited species: bath gas molecule = 1:10. Choice of total number of molecules is determined by the balance between computational time and statistical reliability, given the small proportion of OH* molecules making up each ensemble. OH* is initially in the single rovibrational state $v;j = (8;3)$ with N_2 and O_2 bath gases in (0;10) and (0;12), respectively. Kinetic temperatures are set initially as a 250 K Maxwell–Boltzmann (M–B) distribution. These conditions, together with relevant spectroscopic data, are entered in the program which stores the initial ($v;j$) and velocities of all 8,000 molecules. Two molecules are then picked at random, weighted by size and velocity which, together with the starting ($v;j$) configurations, form the input to a diatom–diatom collision-induced RT and VRT calculation [44]. The molecules collide at random angle and the resulting new ($v;j$) states of the pair are stored in the appropriate location of the array. A fresh pair is picked and a new collision occurs with a new result, a process repeated many times until all members of the ensemble have (on average) undergone a single collision. This is repeated for as many single collision cycles as desired, here up to 1,000–1,500 collisions for each member of the ensemble (on average).

Following each round of collisions, which may be preset to consist of one, or any given number, of collisions for every molecule in the ensemble, the populations in each $v;j$ state of each component species are computed and presented as plots of population versus j for each v state or as population versus v, summed over j states for that v. Also available are plots of total j distribution (summed over v) for each species present. In addition, the v and j population data are fitted to Boltzmann expressions and results presented as vibrational, rotational and translational temperatures (T_v, T_r and T_t, respectively) for each of the three species present. Clearly the concept of a Boltzmann temperature assigned to an array of molecules entirely in single quantum state is not physically meaningful and it will be evident that modal temperatures are useful but not reliable in the early stages of ensemble. This situation improves later in the evolution, generally sometime after the early turbulent phase of rapid energy exchange has ended. Provided these caveats are borne in mind, the modal temperature plots provide a useful pictorial guide to the macroscopic equilibration process. However, the primary data are the quantum state populations that are available after each cycle of collisions undergone by the molecules of the ensemble.

Figure 12 shows a plot of modal temperatures versus number of collision cycles for an 8,000 molecule air-like ensemble containing approximately 10% excited OH. The figure illustrates how OH (8;3) is de-excited by exchanging vibrational, rotational and translational energy with the N_2 and O_2 bath gases. Note that in Fig. 12, the T_mode scale is truncated in order to display the variation of the low energy modes. Initially, T_v for OH exceeds 30,000 K and falls very rapidly with each collision cycle. Also, the collision number scale is terminated at CN = 500, although the computations were continued to CN = 1,000. Relatively minor changes are seen beyond 500 collisions. Several striking features stand out in the T_mode vs CN plot. Clearly the main initial cooling mechanism involves major exchange of vibrational energy between OH* and the two bath gases with the latter rising in modal temperature as the former falls. Detailed examination of quantum state populations in this early phase for this same system at 300 K indicate [66] the operation of fast vibration–vibration (V–V) exchange between OH* and N_2 and between OH* and O_2 [66]. These energy near-resonant vibrational state changes,

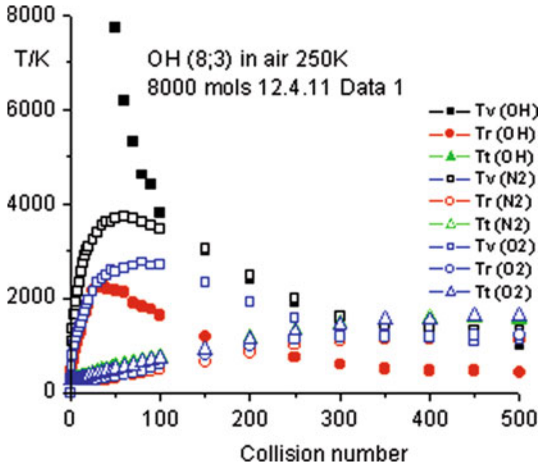

Fig. 12 Variation of modal temperatures of OH, initially in (v;n) = (8;3) with number of collision cycles (collision number) for a 1:10 mixture of OH (8;3) in a 4:1 mixture of N_2 (0;10) and O_2 (0;12) at 250 K. Total number of molecules is (nominally) 8,000. T_v (*squares*) represents vibrational temperature, T_r (*circles*) rotational temperature and T_t (*triangles*) translational temperature throughout. For OH and N_2 the symbols are *black*, *red* and *green* for T_v, T_r and T_t respectively and are solid for OH and open for N_2. The symbols for O_2 follow this same pattern but are *blue* for all three modal temperatures. As described in the text, the primary data are the quantum state populations. Modal temperatures are calculated assuming a Boltzmann distribution and thus T_v and T_r will not be meaningful at the outset and in the early stages of ensemble evolution

down in OH and up in N_2/O_2, will generally involve different numbers of quanta in each molecule because of differences in the characteristic vibrational frequencies of the three species. Near-resonance in this context means match to within ~200 cm^{-1} in the vibrational energies since the remainder may be taken up with rotational state change plus recoil. However, as Fig. 8 makes clear, the probability of fast V–V exchange falls off rapidly as the Δj requirement increases.

When excited and bath species are identical, *resonant* V–V exchange causes very rapid vibrational deactivation with very little rotational or translational energy involvement [61]. This can lead to a curious quasi-equilibrium of the vibrational modes in which translation and rotation remain cold [61]. Overall equilibration in these circumstances can then take many collisions. When excited and bath molecules have very different vibrational constants, the existence of near-resonant V–V pathways depends on such factors as the magnitude of anharmonicity and initial vibrational state and is highly partner specific. The mechanism can lead to rapid population of intermediate vibrational states in both excited and bath molecules from which there may only be very slow VRT pathways for relaxation, whereas in other instances, successive near-resonant paths can lead to a population cascade down to the lowest level. In the example shown above, N_2 has fewer near-resonant V–V pathways than O_2 on collision with OH (8;3) and so despite being the lesser partner in number density, O_2 is overall a more efficient relaxer of OH* than the more abundant N_2.

A second unusual feature of the T_{mode} versus CN plot is the rapid rise in T_{r} of OH as T_{v} for this species falls in the early stages of ensemble evolution. Examination of the rotational state populations during this phase [66] shows this to be due to the QVRT process described in more detail above (process 3 in Fig. 7). Very high n_{OH} states are populated during this phase with $n_{\mathrm{OH}} \geq 30$ being common. In air, this high level of rotational excitation does not last for many collision cycles and by $\mathrm{CN} = 150$, T_{r} for OH is very similar to rotational temperatures of both N_2 and O_2. The ensemble in our calculations represents a thermodynamically closed system from which energy and matter cannot migrate. This is not the case in Earth's atmosphere where airglow emission from $n_{\mathrm{OH}} > 30$ has been found and thought to originate from the exothermic H + O_3 reaction in the mesosphere [58] through the mechanism of QVRT. High n_{OH} molecules are calculated to survive more collisions in air as temperature is lowered.

The third unexpected observation from Fig. 12 is that modes other than T_{r} for OH have approximately equilibrated after 300 collisions and change little with further repeated collision cycles. T_{r} of OH; however, after an initial excursion to higher temperatures, drops to approximately 1,000 K below other modal temperatures following some 350 collision cycles and remains there, unchanged, to at least 2,000 collisions. This is an observation of some significance since the rotational spectrum of OH is widely used as a remote temperature sensor in the upper atmosphere [45, 63] and in combustion diagnostics [62]. It is generally assumed that the low frequency rotational modes will rapidly equilibrate and accurately reflect the kinetic temperature of an ensemble. In our closed system, there is only a very brief span in ensemble evolution when T_{r} for OH matches the translational (kinetic) temperature. Our calculations may not be a wholly reliable guide to the behaviour of an open system such as a planetary atmosphere in which gas transport is a significant feature. However, results on OH* relaxation in a range of bath gases indicate that low T_{r} may be a real phenomenon and one that perhaps is not inexplicable. It is evident from velocity-AM diagrams such as Fig. 11 that $-$ve Δn transitions will always be *energetically* favoured over +ve Δn because of the quadratic dependence of rotational state energy on quantum number. This is very pronounced with OH to the extent that once the QVRT phase has ended and the high n-state molecules have relaxed to a temperature near that of the other modes, relatively small +ve Δn transitions have become energetically inaccessible at the kinetic temperatures available. Other factors relating to the efficiency of the RT [27] process may become significant when many collisions take place. Further work is in progress to investigate in more detail the origin of this unexpected observation.

5 Conclusions

This contribution describes some of the experiments that led to and guided the formulation of a simple model for collisions in which motive force is momentum change. In the case of collision-induced energy exchange in molecules, the driving force is linear-to-angular momentum conversion. The formulation of this Angular Momentum model begins with two very simple equations. The first expresses the generation of angular momentum from linear momentum of relative motion via a lever arm of length determined by the molecular bond length. The second is a statement of energy conservation for each quantum state-to-quantum state transition. An expression for the probability of the first of these processes within limits set by the second proves highly successful in fitting known data, confirming the validity of the principle. A more practical model based on momentum conversion at a Newton surface is fast, accurate and reproduces known data quantitatively using only readily available input such as bond length, mass, velocity and spectroscopic constants. In addition to treating collision-induced transitions, the theory can be extended to the rovibrational products of dissociation experiments and to atom–diatom reactive collisions.

The two key equations both contain velocity and rotational angular momentum as variables, and so the threshold conditions for conservation of energy and of angular momentum may be separately displayed in a single velocity vs Δj plot. This graphical representation gives insight into causal factors. Thus, the origins of the widely differing rotational distributions observed from bimolecular collisions may readily be understood in terms of the state-to-state energy and angular momentum constraints that the diagrams reveal. As a result, the theory becomes transparent and although for practical purposes it is computerised, the velocity–angular momentum plots for a given process are generally able to connect outcomes to physical causes. This is also found to be the case in analysis of ensemble equilibration, a process that generally passes through a number of phases of differing relaxation mechanism and rate.

Examples are given to illustrate the power of the method in investigating energy transfer in molecules of atmospheric interest and velocity – AM diagrams are used to aid interpretation of these results in terms of molecular properties. The extension of the method is described to the more demanding task of modelling gas ensemble evolution while maintaining full quantum state information. An example is shown that illustrates the highly unusual quantum state behaviour of OH in a 4:1 nitrogen, oxygen mixture. The development of the theoretical approach outlined here was led throughout by experiment in which, in the case of those performed in the author's laboratory, the significance of angular momentum was always at the forefront. This keen awareness of the role of angular momentum as one of the cornerstones of molecular physics, began for the author, with a lecture by Carl Ballhausen nearly 50 years ago, and this contribution to the memorial issue is marks appreciation of this inspirational event and a very stimulating year spent in Carl's laboratory.

Acknowledgements The author wishes to thank all those co-workers who have played a part in the development of the ideas outlined above. This represents a large number of people, too large to list individually, but particular thanks go to Richard Marsh for his creation of tools that have made possible the successful application of the basic theory described here to a very wide range of physical problems.

References

1. Ballhausen CJ (1962) Introduction to ligand field theory. McGraw Hill, New York
2. Griffith JS (1961) The theory of the transition metal ions. Cambridge University Press, Cambridge
3. Arthurs AM, Dalgarno A (1960) Proc R Soc Lond A 256:540
4. Silver BL (1976) The irreducible tensor method. Academic Press, New York
5. Piepho SB, Schatz PN (1983) Group theory in spectroscopy. Wiley, New York
6. Edmonds AR (1960) Angular momentum in quantum mechanics. Princeton University Press, Princeton, NJ
7. Coombe DA, Snider RF (1979) J Chem Phys 71:4284, 72, 2445 (1980)
8. Orlikowski T, Alexander MH (1984) J Chem Phys 60:4133
9. Hoffbauer MA, Burdenski S, Giese CF, Gentry WR (1983) J Chem Phys 78:3832
10. Bosanac SD (1981) Phys Rev A26:816
11. Clegg SM, Burrill AB, Parmenter CS (1998) J Phys Chem A 102:8477
12. Korsch HJ, Ernesti A (1992) J Phys B 25:3565
13. Katô H, Clark R, McCaffery AJ (1976) Mol Phys 31:943
14. Jeyes SR, McCaffery AJ, Rowe MD (1978) Mol Phys 36:845
15. Katô H, Jeyes SR, Rowe MD, McCaffery AJ (1976) Chem Phys Lett 39:773
16. Rowe MD, McCaffery AJ (1978) Chem Phys 34:81; (1979) Chem Phys 43:35
17. Khare V, Kouri DJ, Hoffmann DK (1981) J Chem Phys 74:2275
18. Treffers MA, Korving J (1983) Chem Phys Lett 97:343
19. Mattheus A, Fischer A, Ziegler G, Gottwald E, Bergmann K (1986) Phys Rev Lett 56:712
20. Magill PD, Scott TP, Smith N, Pritchard DE (1989) J Chem Phys 90:7195
21. Stewart B, Magill PD, Pritchard DE (2000) J Phys Chem A 104:10565
22. McCaffery AJ, AlWahabi ZT, Osborne MA, Williams CJ (1993) J Chem Phys 90:7195
23. AlWahabi ZT, Harkin CG, McCaffery AJ, Whitaker BJ (1989) J Chem Soc Far Trans 2, 85:1003
24. AlWahabi ZT, Besley N, McCaffery AJ, Osborne MA, Rawi ZT (1995) J Chem Phys 102:7945
25. Dong F, Li X, Zhang M, Lou N (1999) J Chem Phys 111:10578
26. Clare S, Marks AJ, McCaffery AJ (2000) J Phys Chem A 104:7181
27. McCaffery AJ (2004) PCCP 6:1637
28. McCaffery AJ, Reid KL, Whitaker BJ (1988) Phys Rev Lett 61:2085
29. Collins TLD, McCaffery AJ, Wynn MJ (1993) Phys Rev Lett 70:3392
30. Reid KL, McCaffery AJ (1992) J Chem Phys 96:5789
31. McCaffery AJ, Richardson JP, Wilson RJ, Wynn MJ (1993) J Phys B 26:705
32. McCaffery AJ, Wilson RJ (1996) Phys Rev Lett 77:48
33. McCaffery AJ, Wilson RJ (1997) J Phys B At Mol Opt Phys 30:5773
34. Polanyi JC, Woodall KB (1972) J Chem Phys 57:1547
35. Brunner TA, Pritchard DE (1982) Adv Chem Phys 50:589
36. Osborne MA, McCaffery AJ (1994) J Chem Phys 101:5604
37. Kreutz TG, Flynn GW (1991) J Chem Phys 93:452
38. Osborne MA, Marks AJ, McCaffery AJ (1996) J Phys Chem 100:3888
39. Clare S, Marks AJ, McCaffery AJ (1999) J Chem Phys 111:9287
40. Marks AJ (1994) J Chem Soc Faraday Trans 90:2857
41. Marsh RJ, McCaffery AJ (2001) Chem Phys Lett 341:201
42. McCaffery AJ, Marsh RJ, Osborne MA, Lawrance WL, Waclawik ER (2004) J Chem Phys 121:169
43. McCaffery AJ, Marsh RJ (2001) J Chem Phys 115:9771
44. Marsh RJ, McCaffery AJ (2001) Chem Phys Lett 335:134
45. Wayne RP (2000) Chemistry of atmospheres, 3rd edn. Oxford University Press, Oxford
46. Meinel AB (1950) Astrophys J 112:555
47. Besley NA, McCaffery AJ, Osborne MA, Rawi Z (1998) J Phys B 31:4267

48. Murrell JN, Bosanac SD (1989) Introduction to the theory of atomic and molecular collisions. Wiley, Chichester
49. McCaffery AJ, Marsh RJ (2002) J Chem Phys 117:503
50. Pritchard M, Parr J, Li G, Reisler H, McCaffery AJ (2007) Phys Chem Chem Phys 9:6241
51. Parr J, Li G, Federov I, McCaffery AJ, Reisler H (2007) J Phys Chem A 111:7589
52. McCaffery AJ, Pritchard M, Reisler H (2007) J Phys Chem A 114:2983
53. Thompson DL (1981) J Chem Phys 75:1829; (1982) J Phys Chem 86:2538
54. Stewart B, Magill PD, Scott TP, Derouard J, Pritchard DE (1988) Phys Rev Lett 60:282
55. McCaffery AJ (1999) J Chem Phys 111:7697
56. Clare S, McCaffery AJ (2000) J Phys B At Mol Opt Phys 33:1121
57. Serkin ER, Pimentel GC (1981) J Chem Phys 75:604
58. Smith DR, Blumberg WHM, Nadille RM, Lipson SJ, Huppi ER, Wheeler NB (1992) Geophys Res Lett 19:593
59. Marsh RJ, McCaffery AJ (2002) J Chem Phys 117:503
60. McCaffery AJ, Marsh RJ (2002) J Chem Phys 132:074304
61. McCaffery AJ, Pritchard M, Turner JFC, Marsh RJ (2011) J Chem Phys 134:044317
62. Kohse-Höinghausen K, Jeffries JB (2002) Applied combustion diagnostics. Taylor and Francis, London
63. Cosby PC, Slanger TG (2007) Can J Phys 85:77
64. Klenerman D, Smith IWM (1987) J Chem Soc Faraday Trans 83:229
65. Charters PE, McDonald RG, Polanyi JC (1971) Appl Opt 10:1747
66. McCaffery AJ, Pritchard ME, Turner JFC, Marsh RJ (2011) J Phys Chem A 115:4169

Struct Bond (2012) 143: 149–220
DOI: 10.1007/430_2011_57

A Modern First-Principles View on Ligand Field Theory Through the Eyes of Correlated Multireference Wavefunctions

Mihail Atanasov, Dmitry Ganyushin, Kantharuban Sivalingam, and Frank Neese

Abstract Recent developments in AI methods for strongly correlated electronic systems and their implementations in highly efficient quantum chemistry programs allow one to calculate – from first principles – the spectroscopic and magnetic properties of transition metal complexes with open d- and f-shells. For a long time, this field was the domain of ligand field theory (LFT), subject to various assumptions and approximations which are solely justified by the success of using this theory for the interpretation of experimental data. Yet the chemical significance of the ligand field parameters, while being under intense debate, remains unclear as far as the roots of LFT in its relation to rigorous quantum chemistry are concerned. In the present review, we attempt to answer the question how well ligand field theory performs from the point of view of state-of-art first principle calculations and how to connect the two areas. To achieve this goal, energies of electronic states originating from d^n configurations of spectroscopically and structurally well-documented complexes of 3d metals from complete active space self-consistent field (CASSCF) wavefunctions and their improved energy eigenvalues from N-electron valence perturbation theory (NEVPT2) have been analyzed employing various ligand field parameterization schemes. Case studies include classical coordination compounds such as octahedral CrX_6^{3-} and tetrahedral CrX_4 complexes ($X = F, Cl, Br, I$), distorted tetrahedral to square planar $CuCl_4^{2-}$ complexes and the

---

M. Atanasov (✉)
Max-Planck Institute for Bioinorganic Chemistry, Stiftstr. 32-34, D-45470,
Mülheim an der Ruhr, Germany

Institute of General and Inorganic Chemistry, Bulgarian Academy of Sciences,
Acad. Georgi Bontchev Str. 11, 1113 Sofia, Bulgaria
e-mail: mihail.atanasov@mpi-mail.mpg.de

D. Ganyushin, K. Sivalingam, and F. Neese (✉)
Max-Planck Institute for Bioinorganic Chemistry, Stiftstr. 32-34, D-45470,
Mülheim an der Ruhr, Germany
e-mail: frank.neese@mpi-mail.mpg.de

distorted pseudotetrahedral $NiCl_4^{2-}$. In addition, bis and tris-chelate complexes of Ni^{II}, and M^{III} = Cr, Mn, respectively [$Ni(L\text{-}L)_2$, L-L = ethyldithiocarbamate (Et_2dtc^-), 2,2,6,6-tetramethylheptane-3,5-dionato (DPM^-), pentane-2,4 dionato ($acac^-$), and $M(acac)_3$ (M^{III} = Cr, Mn), all complex ligands possessing π-conjugate electronic systems] have been included in the analysis. Values of 10Dq, the energy difference between the *e*- and t_2-type orbitals in octahedral or tetrahedral complexes, identified as the energy of the first spin-allowed transition, in for example, octahedral Cr^{III} and Ni^{II} complexes, and the angular overlap parameters for σ and π metal 3d–ligand interactions (e_σ and e_π) for CrX_6^{3-} and CrX_4 (X^- = F, Cl, Br, I) compare nicely with their counterparts deduced from a fit to experimental d–d spectra. The expected variations of these parameters embodied in the well-known orderings of ligands, according to the spectrochemical series and two-dimensional maps accounting for the ligand σ- and π-functions toward the metal 3d orbitals (quantified by the parameters e_σ and e_π) are reasonably well reproduced and hence also justified by AI theory. In addition, the parameters of the covalently reduced d–d interelectronic repulsion *B* and *C* (the nephelauxetic series) are also well reproduced from a fit of these parameters to AI data, more specifically to NEVPT2 results. Being able to reproduce the AI data for all multiplets of a given d^n-complex using only three to four parameters, we conclude from these studies that the CASSCF and NEVPT2 AI methods and classical LFT are remarkably well compatible. A procedure of obtaining ligand field parameters from AI data described in this work opens the unique possibility to analyze numerical data from AI calculations. In turn, comparison between ligand field parameters, deduced from AI data and, independently, from available high-resolution electronic d–d absorption spectra can stimulate the validation and further development of multireference AI theory. Using this approach, the effects of π-bonding (in $Ni(L\text{-}L)_2$, L = Et_2dtc, acac, DPM and $Cr(acac)_3$) and the interplay between π-bonding and Jahn–Teller coupling in the case of $Mn(acac)_3$ on their optical spectra and the magnetic anisotropy (the zero-field splitting tensor) as studied by EPR spectroscopy are discussed. Finally optically detected transitions between the Zeeman levels of $Cr(acac)_3$ and $Mn(acac)_3$ have been analyzed in detail.

Contents

1 Introduction

Ligand field theory (LFT) has been initially developed as a model to explain the optical splittings of the multiplets of transition metal ions in ionic crystals (crystal field theory). The model has been set up qualitatively by Beckerel [1] and developed into a mathematically precise theory by H. Bethe. Bethe also discovered *all* group theoretical principles and basic tools governing the state and orbital splitting patterns [2]. The application of this theory to explain the magnetic moments of complexes of 3d transition metals by Van Vleck and Penney [3, 4], the calculation of the complete energy levels of chrome alum by Finkelstein and Van Vleck [5], and the discovery of the first spin-allowed d–d transition by Ilse and Hartmann [6, 7] laid down the experimental and theoretical framework for all subsequent studies of the spectroscopic and magnetic properties of transition metal complexes. A very important achievement toward the goal of understanding transition metal physical properties is the fusion of the ideas of Bethe [2] as well as Van Vleck and Penney [3, 4] with those of the molecular orbital theory by Mulliken [8] to eventually lead to [9] to what is known today as “ligand field theory” as documented in many excellent monographs and textbooks [10–14]. From all these, the two monographs authored Prof. C.J. Ballhausen [10, 11] served for a long time as a source of inspiration for researchers in the field (see also [15–17] for historical reviews).

The calculation of the ground state and excited state properties of transition metal complexes with open d shells, in particular, the nature of 10Dq – the energy separation between the e_g and t_{2g} orbitals in octahedral complexes of Cr(III) and Ni(II) – identified as the first spin-allowed d–d transition in their electronic d–d absorption spectra – has been a challenge for ab initio (AI) quantum chemistry since the early days of LFT and quantum chemistry [18, 19]. In order to describe electronic states of transition metal complexes stemming from nominally d^n electronic configurations, electronic correlation – both static correlation (related to the multiconfigurational character of the electronic states of the open d-shell) and dynamical correlation (reflecting the escaping tendency the electron cloud due to a pair of electrons with opposite spins) – has to be taken into account in a well-balanced way. During the past 15–20 years, significant progress has been made in the field of quantum chemistry applied to open-shell transition metal complexes. In fact, much of the progress has to be attributed to the success of density functional theory (DFT) to account for dynamic correlation effects [20–26]. DFT can also be applied to the calculation of excitation spectra within the time-dependent linear response formalism [27–32]. However, the TD-DFT method has not met with the same success that ground state applications of DFT have enjoyed

[33, 34]. Hybrids between ligand-field theory and DFT have been put forward for the calculation of multiplet structures of complexes of 3d- and 4f-metals and have also shown some success [35–37]. They do, however, not follow naturally from rigorous DFT theory and are therefore subjects to approximations which are sometimes out of control. Second, extremely efficient multireference (MR) approaches have been developed which, together with the enormous increase in available computer power, allow applications to transition metal complexes of significant size even on low cost personal computers. Pioneering work to this field have been made by Roos and co-workers who have developed the efficient complete active space self-consistent field method (CASSCF) together with the highly popular second-order perturbation correction for dynamic correlation (CASPT2). These methods have provided much insight into electron correlation effects in transition metal complexes. For reviews of these approaches and their application, see [38–44]. However, the development of new methods that provide a good balance between computational cost and reliable accuracy is still an important goal of quantum chemical method development.

During the past few years, we have been interested in the calculation and interpretation of transition metal optical spectra conducted in parallel to ongoing experimental studies. To this end, we have developed efficient computer codes to carry out such calculations [45]. In particular, a method called spectroscopy oriented configuration interaction (SORCI) was developed [46] and successfully tested in a number of applications [47–57] (for an extensive review on the these developments and their application, see [58]).

So far, we have briefly touched upon the ligand field approach and AI calculation on transition metal complexes. In our view, it is important to realize that these two approaches have fundamentally different goals. LFT aims at providing a conceptual framework which qualitatively describes the properties of a *class* of compounds in as-simple-as-possible terms. It is *not* meant to be a theory that lets one to predict the properties of a given compound accurately without any external input. Thus, using LFT, it is possible to predict how many absorption bands are expected in the UV–vis spectra of, say, high-spin d^3 systems, which of them are spin-allowed. Only *after* adjustment of certain parameters (to be described later), one can make semiquantitative estimates of the positions – and perhaps also the intensities – of these bands. However, importantly, LFT makes the statement that there are many properties that are *common* to the class of high-spin d^3 systems – or, in fact, that any d^n share a number of physical properties.

The aim of AI theory is completely different. These calculations are carried out on *individual* molecules and each and every molecule is treated as a completely new case. In fact, an unbiased quantum chemist will carefully explore the quality of his or her calculation for each and every molecule not taking anything for granted that was calculated for another molecule, no matter how similar it might have been to the present investigated system. These AI calculations do not aim at taking any external input, except perhaps for an initial geometry of the species under investigation. The aim is then to *predict* the physical properties of the compound under investigation “from scratch.” The ultimate goal would be to obtain precise results that are as close as possible to the one-particle and N-particle basis set limits under full inclusion of relativistic effects and as close as possible to the full four component Dirac–Coulomb–Breit relativistic wave equation.

As different the ligand field and AI approaches are, as different are the cultures of the respective proponents. It is very instructive to recall here a comment that Carl Ballhausen made in the preface of his wonderful book "Molecular Electronic Structures of Transition Metal Complexes" about the relation of LFT to microscopic first-principles physics; *"Unfortunately the temptation is to elaborate an approximate theory and to introduce an increasing number of loosely defined 'effects' in order to 'explain' the movements of the parameters . . . there is little reason to expect that deeper insight can be gained in this way."*

Being involved in both LFT and AI theories, we believe that it is timely and also important to discuss the connection between ligand field and AI theory from a somewhat broader perspective. It is obvious to us that better AI calculations will be performed if the underlying conceptual ligand field framework is known to the researcher. It is equally important to realize that LFT itself is a theory that is frustratingly wrong when taken literally. In fact, if one evaluates all integrals that occur in LFT precisely as written, the results are disastrously wrong. This just emphasizes that it would be a misunderstanding to treat LFT as a method to predict accurate numbers. LFT is, always has been and always will be, intimately related to semiempirical parameters. There are certainly better and worse sets of ligand field parameters. For example, the original LFT is formulated in terms of crystal field parameters: 10Dq, Ds, Dt, etc. The problem with these parameters is that they give little chemical insight and are not transferable between related systems. The angular overlap model (AOM) on the other hand tries to achieve just that. Both models treat the all-important interelectronic repulsion in a similar way by heavily relying on the insights provided by atomic spectra theory.

The natural question then arises what the connection between the parameters of LFT and the precise first-principles AI calculations is? Obviously, the connection is *not* to take the integrals of LFT literally. An earlier suggestion accompanied by a deep analysis shows the best answer to this problem lies in the theory of effective (or model) Hamiltonians [59].

Any quantum mechanical Hamiltonian operator has a spectrum of energy eigenvalues and eigenfunctions associated with it. If the Hamiltonian is the "true" first-principles microscopic Hamilton operator, i.e., the aforementioned Dirac–Coulomb–Breit (DCB) Hamiltonian, all available evidence point to the fact that its eigenspectrum coincides to very high precision with the best available measurements, without any known exception. Thus, when carried through in full consequence every experiment performed so far confirms that quantum mechanics correctly describes the behavior of all matter on an atomic scale. The nature of model Hamiltonians is to describe only a part of the full energy spectrum. As discussed at length by Primas, the nature of any model is to reduce complexity and only describe a part of reality with it [60]. Thus, models are "deliberately wrong" – and by doing so they create a language in terms of which scientists can communicate without facing the overwhelming complexity of the complete underlying many particle physics. LFT has clearly achieved this objective. The aim should then be to model the corresponding part of the true eigenspectrum qualitatively correctly (obtain the correct number of states and their order) and as precisely as possible. The question is then how good can a parameterization be in order to achieve this goal and how transparent is the connection of the parameters involved in the model to the true microscopic physics.

Obviously, effective Hamiltonians are extremely widespread in chemistry – each of them creating a field of investigation with an individual language that is based on the parameters occurring in the model. For "good" effective Hamiltonians, there is a clean and unambiguous definition of the parameters in terms of matrix elements of the microscopic operators. Such a "good" effective Hamiltonian is, for example, the spin-Hamiltonian used in EPR and NMR spectroscopy that is precisely defined in terms of many particle states and operators. A comparatively "bad" effective Hamiltonian is the Hückel Hamiltonian used to describe aromatic systems. Its prime parameter, the resonance integral, defeats a precise quantum chemical definition. Its value changes between systems and worse, even between different properties of the same system. The Anderson model for antiferromagnetism is another important effective Hamiltonian. When taken literally its predictions are plainly wrong and may be off by an order of magnitude or so. However, the physical picture it implies is an essentially correct one. What lacks from the Anderson model – as from any other model in chemistry – is dynamic electron correlation. It is this dynamic electronic correlation that is so overwhelmingly important to achieve good numerical predictions. Yet, it is something that is not amenable to human understanding (and it is difficult to calculate accurately).

Thus, the possibility to "hide" the effects of dynamic correlation in a small set of intuitively appealing semiempirical parameters is very attractive. This procedure to connect the microscopic and model physics through effective Hamiltonians brings a large amount of clarity and order into both theoretical and experimental results, which is a feature that, in our opinion, should not be underestimated in its importance – in particular, in modern times where the temptation to mistake numerical agreement between calculated and measured numbers for understanding appears to be widespread.

In terms of effective Hamiltonians LFT probably takes an intermediate position. Its parameters are, regrettably, not precisely defined in terms of matrix elements over the exact many particle eigenfunctions. However, the best point of connection between AI and LFT, in our opinion, is via the many particle eigenspectrum. A mathematically more precise formulation will be provided in Sect. 2. In fact, one of the biggest assets of LFT – next to its correct treatment of symmetry – is the fact that it has a well-defined many particle eigenspectrum. Thus, if one diagonalizes the ligand-field and interelectronic repulsion operators together over a complete basis of ligand field configuration state functions (CSFs, defined below) – subject to the ligand field parameterization of course – one can obtain a result that can be mapped onto the multiplets arising from the restricted part of eigenfunctions of the Born–Oppenheimer (BO) Hamiltonian that describes the d–d part of the spectrum. Likewise, when one includes spin–orbit coupling (SOC) or other spin- or magnetic field dependent effects, one can still diagonalize the ligand field plus relativistic and Zeeman Hamiltonians over a complete set of ligand field CSFs (or equivalently, a complete set of nonrelativistic ligand field eigenfunctions) and map the results one-to-one onto a part of the eigenspectrum of the DCB Hamiltonian. This procedure works as long as there is an identifiable part of the spectrum of the microscopic first-principle Hamiltonians that can be associated with a d^n manifold. That such a part exists is not self-evident. If the construction of the microscopic many particle spectrum is based on some sort of molecular orbitals (which is usually done, but not necessary in terms of fundamental theory), then this mapping is usually possible. In cases where it fails, a LFT cannot be defined [59, 61]. However, fortunately in very many, if not most, cases this mapping is possible. The general situation is sketched in Fig. 1. In general, the effective Hamiltonian will be designed to model a part of the eigenspectrum of the true Hamiltonian, quite typically the lowest energy eigenstates. Quite typically, the higher-energy eigenstates of the effective Hamiltonian are less well modeled than the lower eigenstates because there are stronger interactions with the "outer space" (the space not contained in the model space that is the isomorphic with the basis of the effective Hamiltonian) that are not modeled in the effective Hamiltonian. In case, the outer space and the model space overlap energetically, the effective Hamiltonian – depending on which formulation is chosen – may have accuracy or convergence problems. In this respect, Malrieu's theory of "intermediate Hamiltonians" that contain a "buffer space" to "protect" the model space from outer space intruders is an important concept [62].

In the case of LFT, this basic principle is readily illustrated. The model space for LFT is the manifold of the ground and d–d excited states. However, there are also intraligand, ligand-to-metal, metal-to-ligand, or ligand-to-ligand charge transfer states that may occur in the spectrum. As the d–d spectrum "runs into" the charge

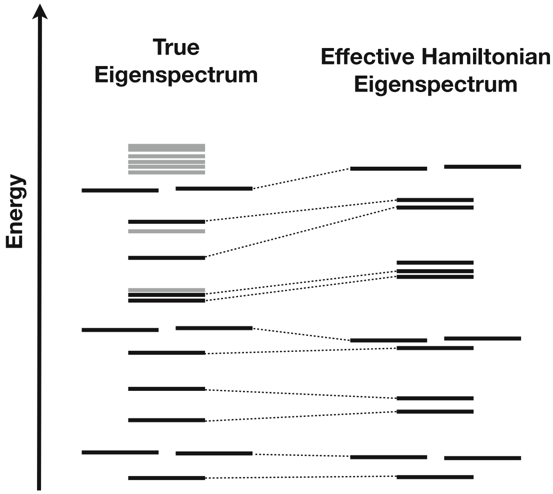

Fig. 1 Relationship between the eigenspectrum of the "true" Hamiltonian and an effective Hamiltonian. States that occur in the real spectrum but that are missing in the effective Hamiltonian eigenspectrum are printed in *gray* on the *left side*. States that correlate with each other are connected through *dashed lines*. It may occur, of course, that the order of states in the real and effective Hamiltonian eigenspectrum is different

transfer spectrum, the predictions of LFT for the d–d transitions become less accurate, and – obviously – the charge transfer states are not modeled at all in LFT. Quite typically, the overlap starts to occur for higher-energy d–d transitions because the lowest LMCT charge transfer states normally stem from electronic transitions from nonbonding ligand orbitals resulting in excited states which are only weakly mixed with the term manifold of the $3d^n$ configurations. By contrast, charge transfer states due to excitations from ligand orbitals which overlap strongly with metal 3d functions (e.g., those involved in σ metal–ligand bonds) are (even in the case of more covalent ligands such as S^{2-}, Se^{2-}, etc.) too high in energy. A nice example to illustrate this effect is shown in Fig. 2. Tetrahedral $FeO_4{}^{2-}$ with $Fe^{IV}(d^2)$ is involved in rather strong metal–ligand bonding to O^{2-}. It was possible to identify the low-lying d–d transitions corresponding to $^3A_2 \rightarrow {}^1E$, $^3A_2 \rightarrow {}^1A_1$, and $^3A_2 \rightarrow {}^3T_2$ and obtain the parameters $\Delta = 10Dq$, B, and C from a best fit to the

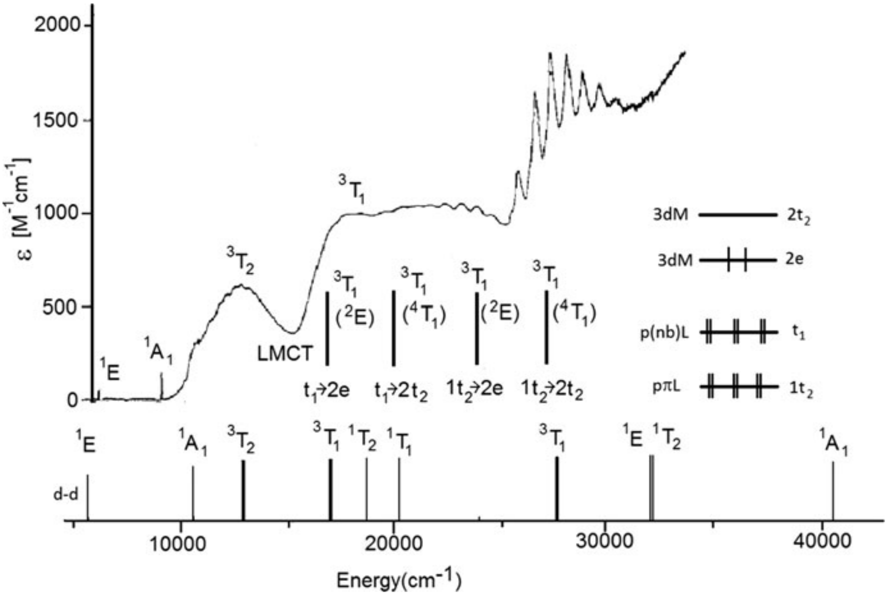

Fig. 2 The electronic absorption spectrum of Fe^{6+} doped into K_2SeO_4 (adopted from [63]), with the $^3A_2 \rightarrow {}^1E$ and $^3A_2 \rightarrow {}^1A_1$ spin–flip transitions within the e^2 electronic configuration, and the first spin-allowed $^3A_2(e^2) \rightarrow {}^3T_2(t_2{}^1e^1)$ d–d band. Theoretical values for all d–d transitions calculated using values of $\Delta = 12{,}940\ cm^{-1}$, $B = 375\ cm^{-1}$, $C = 1{,}390\ cm^{-1}$ (best fit values), and observed and calculated [189] LMCT energies are shown. The energy of the $1t_2 \rightarrow 2t_2$ transition has been calculated following the model of Vanquickenborne and Verdonck [189]. The Fe(V)(d^3) electronic states of the LMCT configuration, coupling with single hole on the t_1 and $1t_2$ oxygen-based orbitals are given in *parenthesis* (cf. *inset* showing the definition of orbitals involved in the CT along with the ground state electronic configuration of $FeO_4{}^{2-}$). Values of B and C much smaller than those of the Fe^{6+}-free ion ($B = 1{,}390$, $C = 5{,}560\ cm^{-1}$) reflect the very pronounced covalency of the Fe–O bond. The energy difference between the $^3T_1(^4T_1)$ and $^3T_1(^2E)$ excited CT states ($2{,}900\ cm^{-1}$) reflects the value of $\Delta = 10Dq$ ($12{,}940\ cm^{-1}$) reduced by the spin-pairing energy $7.6B[<S(S+1)> - S(S+1)]$ of $10{,}000\ cm^{-1}$

energy band maxima [63]. Higher lying ligand field excited states (Fig. 2) are however obscured by weak LMCT bands.

This discussion leads to the outline of the present chapter. We first describe computationally affordable approximations to the full eigenspectra of the BO and DCB Hamiltonians in terms of multireference self-consistent-field approaches supplemented with dynamic correlation and relativistic treatments. For the mentioned reasons, the AI methods of choice here are CASSCF and the *N*-electron valence perturbation theory (NEVPT2) as implemented in our computer program ORCA [45]. This allows for the calculation of electronic and magnetic properties of transition metal complexes of unprecedented size. We then describe in detail how this information can be used to determine a complete set of ligand field parameters using various model examples, for which spectroscopic data are also available. That these parameters are unique is by no means guaranteed of course. We have, in fact, severe doubts that a unique parameterization can exist. Two kinds of two ligand field models appear appealing to chemists. One of them, exploiting as much as possible the *symmetry of the whole complex* – the global parameterization, is more general and applicable in the case of high-symmetries – cubic point groups and their axial (trigonal and tetragonal) subgroups. Another parameterization, the AOM, rests on the concept of a functional group and the *pseudosymmetry of a given metal–ligand pair*. It then constructs the one-electron ligand field matrix of a ML_n complex as the sum over all metal–ligand pairs resulting in an additive or superposition model. We also present extensive numerical data to illustrate the possibilities and also the enormous utility that this approach has.

This work is structured as follows. After Sect. 2 setting up a rigorous and general procedure connecting AI and LFT, a short introduction into the multiconfigurational self-consistent field methods (MRSCF) and their simplified CASSCF and NEVPT2 variants providing wavefunctions and energies, respectively, in Sect. 3.1 and into the basic tools for calculations of magnetic properties using these results (the calculation of SOC and spin–spin coupling (SSC) and basic guidelines of applying quasidegenarate second-order perturbation theory, QDPT, Sect. 3.2). LFT and its model extensions are briefly outlined in Sect. 4. After a computational Sect. 5 describing basis sets, geometries, and the interfacing of ORCA with ligand field programs, applications are given in Sect. 6. Two different types of complexes have been encountered – classical coordination compounds such as octahedral $CrX_6{}^{3-}$ and tetrahedral (CrX_4, X = F, Cl, Br, I) (Sects. 6.1 and 6.2, respectively) and cases where the d–d only descriptions break down and need extensions (such as Jahn–Teller distorted $CuCl_4{}^{2-}$ and $NiCl_4{}^{2-}$, Sect. 6.3). Finally, in Sect. 6.4, we consider bis- and tris bidentate complexes of Ni^{II} and $M^{III} = Cr^{III}$ and Mn^{III} with complex ligands such as dithiocarbamete and acetylacetonate, and show how effects of π-bonding and the interplay of the latter with Jahn–Teller activity (in the case of $Mn(acac)_3$) affect their spectroscopic and magnetic properties including a planar paramagnetic complex of Ni(II) (Sect. 6.5) In Sect. 7 (Conclusions and Outlook), a summary is given of what we can learn from mapping AI results onto LFT.

2 Connection of Ab Initio and LFT

In this section, we provide a mathematical formulation of the connection between LFT and AI electronic structure theory. Let us start from an elementary and slightly abstract ligand field construction scheme. The exposition will be based on the strong-field coupling scheme which is the one that maps most readily onto AI theory. We give a construction scheme that cleanly connects the two areas. It is certainly not the only possible one but one that we find particularly transparent and illuminating. We stay at the nonrelativistic level in this section as the inclusion of relativistic effects brings in no new aspects.

In LFT, the five d-orbitals d_i ($i = 1$–5) are the basic one-electron objects. There are n_d-electrons to be distributed over these orbitals. A *configuration I* is defined by the occupation number of each orbital. Thus, there are N_{CFG} configurations with occupation vectors $\mathbf{n}^{(I)}$ ($I = 1, ..., N_{CFG}$). If the point group is Abelian, each individual configuration transforms under one of the irreducible representations of the point group. For non-Abelian groups, linear combination of configurations must be taken in order to transform correctly. In general, one will need two additional quantum numbers Γ to denote the irreducible representation (irrep) and γ to denote the particular column of the irrep under which a given configuration transforms.

In each configuration, there can be unpaired electrons ($n_i = 1$). A CSF is defined by a configuration and a spin-coupling pattern μ among the SOMOs of that configuration to a given total spin S. For a given number of open-shells (n, number of unpaired electrons) and given total spin S, there are n_μ spin-couplings with:

$$n_\mu = \begin{bmatrix} n \\ \frac{1}{2}n - S \end{bmatrix} - \begin{bmatrix} n \\ \frac{1}{2}n - S - 1 \end{bmatrix}. \quad (1)$$

A good way to construct the different spin-couplings is based on the branching diagram technique as elaborated into a constructive algorithm by Grein and coworkers˙[64] (Fig. 3). We cannot go into details here (Table 1).

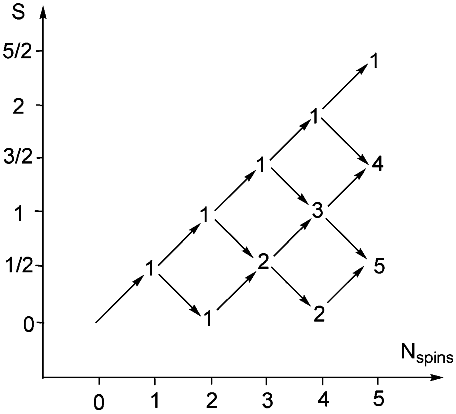

Fig. 3 Yamanouchi–Kotani branching diagram governing the spin-levels of d^N for $N = N_{spin} = 1, 2, 3, 4, 5$ (see Ref. 19, p. 44)

Table 1 The number of spin-functions for number of d-electrons in the five d-orbitals $n_{\mathrm{d}} = 1$–9^{a}

Nel	1,9	2,8	3,7	4,6	5
	5S=1/2(1)	10S=1(1,1)	10S=3/2(1,1,1)	5S=2(1,1,1,1)	1S=5/2(1,1,1,1,1)
		10S=0(1,1)	20S=1/2(1,1,1)	15S=1(1,1,1,1)	4S=3/2(1,1,1,1,1)
		5S=0(2)	20S=1/2(1,2)	10S=0(1,1,1,1)	5S=1/2(1,1,1,1,1)
				30S=1(2,1,1)	20S=3/2(1,1,1,2)
				30S=0(2,1,1)	40S=1/2(1,1,1,2)
				10S=0(2,2)	30S=1/2(1,2,2)

[a] Type of configuration vectors are given in parenthesis

To each CSFs of spin S, there are $2S + 1$ magnetic sublevels with quantum number $M = S, S - 1, ..., -S$. Thus, a ligand field CSF is defined by $|^{\mathrm{LFT}}\mathbf{n}_I \mu \Gamma \gamma SM\rangle$. As long as one treats spin-independent properties, it is only necessary to treat the "principle" components with $M = S$ because all $2S + 1$ members of the multiplet are degenerate. For simplicity, lets us enumerate the totality of the ligand field CSFs by $|I^{\mathrm{LFT}}\rangle$. Obviously, there are $N_{\mathrm{CSF}} > N_{\mathrm{CFG}}$ ligand field CFSs.

The time-independent Schrödinger equation in this basis is:

$$\mathbf{H}^{\mathrm{LFT}}\mathbf{C}^{\mathrm{LFT}} = \mathbf{E}^{\mathrm{LFT}}\mathbf{C}^{\mathrm{LFT}}. \tag{2}$$

With

$$H_{IJ}^{\mathrm{LFT}} = \left\langle I^{\mathrm{LFT}} | H^{\mathrm{LFT}} | J^{\mathrm{LFT}} \right\rangle. \tag{3}$$

On a most elementary level, the CSFs can be reduced to sums over Slater determinants and then the Slater–Condon rules can be used to calculate the actual matrix elements. Recipes to do this are readily found in the literature.

Given the set of $\{|I^{\mathrm{LFT}}\rangle\}$ is complete, the solutions to this eigenvalue equation are the exact nonrelativistic ligand field states

$$\left|\Psi_I^{\mathrm{LFT}}\right\rangle = \sum_J C_{JI} \left|J^{\mathrm{LFT}}\right\rangle \tag{4}$$

with associated energies E_I^{LFT}. Since the coefficients $\mathbf{C}^{\mathrm{LFT}}$ and the eigenenergies $\mathbf{E}^{\mathrm{LFT}}$ result from a linear eigenvalue problem, the information they contain is identical to the information content of the ligand field Hamiltonian matrix $\mathbf{H}^{\mathrm{LFT}}$. Thus, the connection between AIT and LFT can be made most readily by fitting either of the two quantities. The matrix $\mathbf{H}^{\mathrm{LFT}}$ is a function of the ligand field parameters that can be collectively summarized in a vector $\mathbf{p}$ with elements p_k with $k = 1...N_p$ where N_p is the number of such parameters. There are two types of ligand field parameters: (1) The parameters that describe the ligand field. They enter the one-electron matrix. In the AOM model, these are the various e_σ^L and e_π^L parameters for each ligand L. (2) The parameters that enter the calculation of the interelectronic repulsion, normally expressed in terms of the Slater–Condon parameters F^0_{dd}, F^2_{dd}, and F^4_{dd} or, equivalently, the Racah parameters A, B, and C. "Fancy" refinements would include molecular anisotropy into account by scaling different interelectronic repulsion parameters differently as a result of anisotropic covalency. Over-parameterization of the model is a danger. It is interesting to note that all of these parameters enter the matrix $\mathbf{H}^{\mathrm{LFT}}$ in a linear fashion. Thus, one might as well write this matrix as:

$$\mathbf{H}^{\mathrm{LFT}}(\mathbf{p}) = \mathbf{H}^{\mathrm{LFT};(0)} + \sum_{k=1}^{N_p} p_k \mathbf{H}^{\mathrm{LFT};(k)}, \tag{5}$$

where $\mathbf{H}^{\mathrm{LFT};(k)}$ is the part of the matrix $\mathbf{H}^{\mathrm{LFT}}$ that is linearly dependent on p_k and $\mathbf{H}^{\mathrm{LFT};(0)}$ is the part that does not depend on any of the parameters.

We now turn to AI theory. While it is not strictly necessary, it is extremely convenient to base the discussion on some sort of molecular orbitals $\{\psi_i\}$. The precise form of these orbitals and how to obtain them are discussed below. This set of orbitals will be divided into three classes: (a) the internal orbitals (labels i, j, k, l), (b) the active orbitals (labels p, q, r, s), and (c) the inactive or virtual orbitals (labels a, b, c, d). A natural connection to LFT arises, when the active orbitals are of dominantly metal d-character.

Obviously, it is now possible to distribute *all* of the n_{el} electrons of the systems among *all* of the available orbitals and couple spins in the same way as in the ligand field case to obtain the AI CSFs. This then defines the full configuration interaction (FCI) many particle space. This space is gigantically large and grows factorially with the number of electrons. If one diagonalizes the BO Hamiltonian over the entire set of FCI CSFs, one can obtain the FCI wavefunction. In practice, one is forced to expand the MOs in terms of basis functions ($\psi_i(\mathbf{x}) = \sum_\nu c_{\nu i}\varphi_\nu(\mathbf{x})$, with $\varphi_\nu(\mathbf{x})$ being a member of a finite set of basis functions, $c_{\nu i}$ is a molecular orbital coefficient, and $\mathbf{x}$ collectively denotes the spin-and-space variables of the single electron). The FCI wavefunction and its associated energy approaches the exact nonrelativistic solution of the Schrödinger equation as the one-particle basis set $\{\varphi_\nu\}$ is approaching mathematical completeness.

The FCI wavefunction, while being completely impractical, still serves well for illustrative purposes. For the discussion, it is necessary that a single CSF or a class of CSFs dominates the many particle ground state wavefunction $\Psi_0(x_1, ..., x_{n_{el}})$ – these are the configurations with n_d electrons in the active space orbitals. If it possible to identify such a class, then n_d is fixed and one can cleanly divide the CSFs in the FCI space into two categories: (a) the "model space" ("a" space) CSFs. These are *all* CSFs with exactly n_d electrons in the active, metal-d-based orbitals and (b) the "outer space" that contains *all* other CSFs.

It is obvious that there are *exactly* as many AI CSFs in the "a" space as there are LF CSFs for n_d electrons. Their number is never exceeding a few hundred and hence this is a very attractive model space to work with. It is now exceedingly easy to diagonalize the BO Hamiltonian over the model "a" space. However, this does not lead to accurate results as the coupling with the "outer" space brings in the dynamic correlation. If one is aiming at an AI effective Hamiltonian, one wants to incorporate the effects of the outer space while still keeping the model space at exactly the ligand field space. Thus, one needs an effective equation that only involves the "a" space. The simplest possible approach is based on writing the FCI equation in partitioned form:

$$\begin{pmatrix} \mathbf{H}^{aa} & \mathbf{H}^{ab} \\ \mathbf{H}^{ba} & \mathbf{H}^{bb} \end{pmatrix} \begin{pmatrix} \mathbf{C}^{a} \\ \mathbf{C}^{b} \end{pmatrix} = E \begin{pmatrix} \mathbf{C}^{a} \\ \mathbf{C}^{b} \end{pmatrix}, \tag{6}$$

which can be readily re-arranged to an equation involving only $\mathbf{C}^a$:

$$\underbrace{\left\{ \mathbf{H}^{aa} - \mathbf{H}^{ab}\left(\mathbf{H}^{bb} - \mathbf{1}E\right)^{-1}\mathbf{H}^{ba} \right\}}_{\mathbf{H}^{\text{eff}}(E)} \mathbf{C}^{a} = E\mathbf{C}^{a}. \tag{7}$$

Thus, the term in curly brackets defines an effective Hamiltonian that operates only on the "a" space while incorporating the effects of the "b" space. This equation is exactly equivalent to the FCI equations. The re-arrangement came, however, at a significant cost, namely, the fact that the effective Hamiltonian is energy dependent. There are various ways to reconcile this and we will not enter a detailed discussion as this section is only meant to lay out the principles. For the purposes pursued here, it is sufficient to argue that one seeks solutions close to ground state. Thus, one can replace E by E_0, the lowest solution of the $\mathbf{H}^{aa}$ eigenvalue problem. Furthermore, a more practical equation is obtained by approximating $\mathbf{H}^{bb}$ by its diagonal in which case the inversion is trivial and one can obtain an equation that is correct to second order:

$$H_{IJ}^{\text{eff}} = H_{IJ}^{aa} - \sum_{K \in b} \frac{\langle I^a | H | K^b \rangle \langle K^b | H | J^a \rangle}{H_K^{bb} - E_0}. \tag{8}$$

No matter which approximations are made (or none), one can obtain a matrix $\mathbf{H}^{\text{eff}}$ that is of the same dimension as the ligand field matrix. It is this matrix that one tries to approximate in AI LFT. Thus, in order to determine the LF parameters, one should form the root mean square difference:

$$R(\mathbf{p}) = \sum_{I,J} \left(H_{IJ}^{\text{LFT}}(\mathbf{p}) - H_{IJ}^{\text{eff}}\right)^2. \tag{9}$$

Thus:

$$\begin{aligned} R(\mathbf{p}) = & \sum_{I,J} \left(H_{IJ}^{\text{LFT};(0)}\right)^2 + \left(H_{IJ}^{\text{eff}}\right)^2 + 2\sum_k p_k H_{IJ}^{\text{LFT};(k)} \left(H_{IJ}^{\text{eff}} + H_{IJ}^{\text{LFT};(0)}\right) \\ & + \sum_{kl} p_k p_l H_{IJ}^{\text{LFT};(k)} H_{IJ}^{\text{LFT};(l)} = R_0 + 2\sum_k p_k \sum_{IJ} H_{IJ}^{\text{LFT};(k)} \left(H_{IJ}^{\text{eff}} + H_{IJ}^{\text{LFT};(0)}\right) \\ & + \sum_{kl} p_k p_l \sum_{IJ} H_{IJ}^{\text{LFT};(k)} H_{IJ}^{\text{LFT};(l)}. \end{aligned} \tag{10}$$

With

$$R_0 = \sum_{I,J} (H_{IJ}^{\mathrm{LFT};(0)})^2 + (H_{IJ}^{\mathrm{eff}})^2 \tag{11}$$

and minimize it:

$$\frac{\partial R}{\partial p_k} = 0 = \sum_{IJ} H_{IJ}^{\mathrm{LFT};(k)} (H_{IJ}^{\mathrm{eff}} + H_{IJ}^{\mathrm{LFT};(0)}) + \sum_{l} p_l \sum_{IJ} H_{IJ}^{\mathrm{LFT};(k)} H_{IJ}^{\mathrm{LFT};(l)}, \tag{12}$$

Which is written in the form:

$$\mathbf{Ap} = -\mathbf{b}, \tag{13}$$

$$A_{kl} = \sum_{IJ} H_{IJ}^{\mathrm{LFT};(k)} H_{IJ}^{\mathrm{LFT};(l)}, \tag{14}$$

$$b_k = \sum_{IJ} H_{IJ}^{\mathrm{LFT};(k)} (H_{IJ}^{\mathrm{eff}} + H_{IJ}^{\mathrm{LFT};(0)}) \tag{15}$$

and has a unique solution:

$$\mathbf{p} = \mathbf{A}^{-1}\mathbf{b}. \tag{16}$$

Thus, this solution defines the exact AI parameterization of the ligand field Hamiltonian. To the best of our knowledge, this is a new result. In practice, of course, the FCI equations cannot be solved for even the smallest transition metal complex. Hence one has to resort to approximation that still define an effective Hamiltonian or at least its energies. We next turn our attention to such approximations.

3 Ab Initio Theory

3.1 Multiconfigurational Self-Consistent Field

The self-consistent field Hartree–Fock (HF) method is the foundation of AI quantum chemistry. In this simplest of approaches, the n_{el}-electron ground state function $\Psi(\mathbf{x}_1, ..., \mathbf{x}_N)$ is approximated by a single Slater determinant built from antisymmetrized products of one-electron functions $\psi_i(\mathbf{x})$ (molecular orbitals, MOs, $\mathbf{x}_i$ includes space, $\mathbf{r}_i$, and spin, $\sigma_i = \pm 1/2$ variables). MOs are orthonormal single electron wavefunctions commonly expressed as linear combinations of atom-centered basis functions $\{\varphi\}$ as $\psi_i(\mathbf{x}) = \sum_\mu c_{\mu i}\varphi_\mu(\mathbf{x})$. The MO expansion coefficients $c_{\mu i}$ are determined variationally according to the Rayleigh Ritz theorem. This leads to the Hartree–Fock (HF) method. Owing to the single Slater determinantal form, it does of course not coincide with the exact wavefunction. Physically speaking, the electrons are moving in the field of the nuclei and the average field of the remaining electrons in HF theory. Already at this level of theory, often 99% of the exact total energy is reproduced. The missing energy fragment, known as the correlation energy, can be recovered if the n_{el}-electron state function is expanded in the full CI space. If one starts from a single HF determinant, the FCI space is usually spanned by singly, doubly, triply, etc. excited determinants. The wavefunction depends implicitly on the molecular orbital, and explicitly on the configuration coefficients C that determine the n_{el}-electron state function

$$\Psi(\mathbf{c},\mathbf{C}) = C_{\mathrm{HF}}\Psi_{\mathrm{HF}} + \sum_{ia} C_a^i \Psi_i^a + \tfrac{1}{4}\sum_{ijab} C_{ab}^{ij}\Psi_{ij}^{ab} + \tfrac{1}{36}\sum_{ijkabc} C_{abc}^{ijk}\Psi_{ijk}^{abc} + \cdots. \tag{17}$$

Based on the technique used to estimate the C-coefficients, three principle approaches arise. If they are derived variationally, one can obtain the method of configuration interaction (CI). Alternatives are many body perturbation theory (MBPT) and coupled cluster (CC) theory. Due to the systematic construction of determinants in the wavefunction Ansatz, these methods strongly rely on the validity of the reference determinant. Although many chemical questions can be successfully addressed with these approaches, cases, where the reference is degenerate or nearly degenerate, cannot be described even qualitatively correct. Examples, where such degeneracy appears, are multiplet structures, d–d excited states of transition metal compounds, or even simply bond formation and breaking processes. Single references electron correlation theories have come a long way and presently have been fully developed. They are, however, not the method of choice when it comes to the connection between LFT and AIT.

The generalization of the HF methods toward degenerate or nearly degenerate systems is known as multiconfigurational self-consistent field (MCSCF). In this method, the MCSCF wavefunction is initially expanded in a set of many particle basis functions $\{\Phi\}$ (Slater determinants or CSFs) [65].

$$\Psi_{\mathrm{MCSCF}}(\mathbf{c},\mathbf{C}) = \sum_I C_I \Phi_I. \tag{18}$$

The configuration expansion coefficients $\mathbf{C}$ and MO coefficients $\mathbf{c}$ are determined simultaneously using the variational principle. The selection of CSFs is, however, anything from straightforward. Experience has shown, however, that one is well advised with a construction that is known as CASSCF [66, 67]. In CASSCF, the orbitals are partitioned into three classes; internal orbitals i, j, k, l that are doubly occupied in all CSF; virtual orbitals a, b, c, d that are unoccupied in all CSF; the active orbitals p, q, r, s spanning the space in between and the generic orbitals, t, u, v, and w. Respecting spin and spatial symmetry, CSFs are constructed such that *n* electrons are distributed among the *m* active orbitals corresponding to a FCI in the subspace. This is abbreviated as CASSCF (*n*, *m*). Although, this approach is not the most economic as many of the CSFs have little contribution to the energy, CASSCF also has many advantages. The most noteworthy advantage is the orbital invariance within the three subspaces. Usually, the computation of many states is performed in a state-averaged CASSCF (SA-CASSCF), where a single set of orbitals minimizes the average energy. Nowadays, CASSCF is routinely applied to many challenging questions. Molecules with up to 2,000 basis functions can be computed using modern computational techniques [68, 69]. Despite recent progress in approximate FCI theory [70], calculations with more than 14 orbitals still remain challenging. Notwithstanding the CI size, CASSCF is not designed to obtain exact energies, but a qualitatively correct picture by covering degeneracy effects and correct multiplet structures. It is therefore a good starting point for the treatment of dynamic correlation.

One particular defect of CASSCF, the bias toward high-spin states also inherent in HF, is lifted upon inclusion of dynamic correlation. For detailed information on CASSCF and its application to transition metal chemistry, we refer to the pertinent literature and references therein [42, 71].

While the CASSCF wavefunction accounts for degeneracy effects (static correlation), accuracy requires the inclusion of CSF outside the CAS-CI. The computational most attractive approach to improve on the CASSCF description is through perturbation theory, which is motivated by the enormous success of Møller–Plesset perturbation theory (MP2) [72]. Various extensions toward multireference perturbation theory have been proposed as the partitioning of the Born Oppenheimer Hamiltonian into a zero Hamiltonian and a perturbation is not unique [73–81]. The most widely used approach so far is the CASPT2 approach of Roos and co-workers [82], which has been extensively applied to transition metal chemistry. Here we report on a similar multireference perturbation theory named *n*-electron valence state perturbation theory (NEVPT2) that was devised by Angeli and co-workers [74, 83–88]. While it has many attractive features in common with CASPT2, other important properties such as exact size consistency and absence of intruder state are specific to NEVPT2. Early calibration studies have revealed an accuracy comparable to CASPT2 [85]. NEVPT2 has further matured by extension to a third-order treatment [88] and its quasidegenerate formulation [87, 89].

Let us start with some general considerations. In second-order perturbation theory, the first-order wavefunction $|1\rangle$ is expanded in a set of many particle CSFs Ψ_I that are excited with respect to the CSFs in the CAS-CI:

$$|1\rangle = \sum_{I \notin CAS} C_I^{(1)} \Psi_I. \tag{19}$$

Due to the fact that at most single and double excitations can directly interact through the BO Hamiltonian with the zero-order wavefunction $|0\rangle$, it is sufficient to terminate the expansion at this level known as “first-order interacting space”

(FOIS) [90]. Comparing with the single reference counterpart, the multireference FOIS is by the factor *number of references* larger. Thus, calculations with larger CAS-CI spaces quickly become intractable. The success of CASPT2 is based on an approximation proposed by Siegbahn and Meyer known as internal contraction [91, 92]. Here, the FOIS is spanned by excitations acting on the entire zero-order wavefunction instead of the references therein, e.g.,

$$\Psi_{ij}^{ap} = E_i^a E_j^p |0\rangle, = E_i^a E_j^p \sum_I C_I \Phi_I, \tag{20}$$

where the C_I coefficients are fixed by the proceeding CASSCF. We used the notation $E_w^v = a_{v\alpha}^\dagger a_{w\alpha} + a_{v\beta}^\dagger a_{w\beta}$ for the replacement operators in second quantization; here $a_{\mu\sigma}^\dagger$ and $a_{v\sigma}$ are operators that annihilate and create one electron of spin σ on orbitals v and μ, respectively. However, these functions are generally not orthogonal or linear independent, thus a transformation into a suitable set is necessary. Despite this complication, the internal contraction leads to substantial time saving as the FOIS is reduced to the same dimension as the single reference counterpart. The introduced error is negligible [93, 94]. There are some cases, where the perturbation causes strong mixing in the reference space, e.g., conical intersection. Then a quasi-degenerate formulation is necessary [87, 89, 95]. NEVPT2 comes in three flavors: uncontracted, partially contracted, and strongly contracted [74]. The uncontracted and partially contracted variants are very similar to the previously discussed representation of the FOIS. The reader is encouraged to consult the original papers on this topic for details [74]. In the following, we focus on the strongly contracted version, which goes beyond the common internal contraction. Excitation operators are averaged (contracted) in the active space before acting on the contracted CAS-CI wave function. The resulting functions are defined just by the internal and virtual excitation labels. In principle, the BO Hamiltonian

$$H_{\mathrm{BO}} = \sum_{tu} h_{tu} E_u^t + \tfrac{1}{2} \sum_{tuvw} (tu|vw) \left[E_u^t E_w^v - \delta_{uv} E_w^t \right], \tag{21}$$

$$h_{tu} = \int \varphi_t^*(\mathbf{x}) \hat{h} \varphi_u(\mathbf{x}) \mathrm{d}\mathbf{x}, \tag{22}$$

$$(tu|vw) = \int \varphi_t^*(\mathbf{x_1}) \varphi_u(\mathbf{x_1}) \hat{G}(\mathbf{x_1}, \mathbf{x_2}) \varphi_v^*(\mathbf{x_2}) \varphi_w(\mathbf{x_2}) \mathrm{d}\mathbf{x_1} \mathrm{d}\mathbf{x_2}, \tag{23}$$

where $\hat{h}$ and $\hat{G}(\mathbf{x_1}, \mathbf{x_2}) = 1/|\mathbf{r_1} - \mathbf{r_2}|$ are the one-electron Hamiltonian and the two-electron repulsion operators, respectively, contains the very same single and double excitation operators that are involved in the definition of the internally contracted CSFs, but they are contracted with integrals. The strongly contracted NEVPT2 utilizes this contraction to define a new set of functions in the FOIS. They are generated by acting with just the parts of the Hamiltonian on the contracted wavefunction, that involve the respective internal and virtual excitation labels, e.g., a function (class) for the excitations of two internal into a virtual orbital is [83]

$$\Psi_{ij}^{a} = \bar{\delta}_{ij} \sum_{p} \left[(aj|pi) E_{j}^{a} E_{i}^{p} + (ai|pj) E_{i}^{a} E_{j}^{p} \right] |0\rangle \equiv \hat{V}_{ij}^{a}, \tag{24}$$

with $\bar{\delta}_{ij} = 1 - (1/2)\delta_{ij}$. Here, we introduced the effective excitation operator $\hat{V}_{ij}^{a}$. The so defined averaging of the excitation operators is physically motivated through the inherent integrals coupling. In fact, calibration studies by Havenith et al. show a negligible difference between the partially and strongly contracted NEVPT2 despite the compactness of the FOIS in the latter scheme [85]. As a second important consequence, the functions are exactly orthogonal, and thus once properly normalized, they are perfectly suited for a wavefunction expansion. We define the normalized FOIS functions

$$\Psi_{I}' = \frac{1}{\sqrt{N_I}} \Psi_{I}, \tag{25}$$

where $N_I = \langle \Psi_I | \Psi_I \rangle$ is the norm.

Having defined the FOIS, we construct the zero-order Hamiltonian such that

$$\hat{H} = \hat{H}_0 + \hat{V}, \tag{26}$$

where the direct sum of previously defined effective excitations exactly span the perturbation

$$\hat{V} = \sum_{I \in \mathrm{FOIS}} \hat{V}_{I}. \tag{27}$$

In multireference perturbation theory, defining a proper zero-order Hamiltonian is anything but straightforward. The reference wavefunction, in general, is not an eigenfunction of the zero-order Hamiltonian. A second complication arises as interactions between the FOIS functions and zero-order wavefunction through the zero-order Hamiltonian cannot be excluded. Therefore, projection techniques are commonly employed. In NEVPT2, the zero-order Hamiltonian takes the form

$$\hat{H}_0 = \hat{P}\hat{H}\hat{P} + \sum_{I \in \mathrm{FOIS}} \left| \Psi_{I}' \right\rangle E_{I}' \left\langle \Psi_{I}' \right|, \tag{28}$$

where $\hat{P} = |0\rangle\langle 0|$ is the projector into the CAS-CI space and E_I are energies of the FOIS functions defined as expectation values

$$E_{I}' = \left\langle \Psi_{I}' | \hat{H} | \Psi_{I}' \right\rangle. \tag{29}$$

Usually, the full Hamiltonian is approximated with a computationally more attractive and less complex counterpart. In NEVPT2, the Dyall Hamiltonian [96] H^D is employed

$$\hat{H}^D = \hat{H}^D_{ie} + \hat{H}^D_v, \tag{30}$$

$$\hat{H}^D_{ie} = \sum_i \varepsilon_i E^i_i + \sum_a \varepsilon_a E^a_a + C, \tag{31}$$

$$\hat{H}^D_v = \sum_{pq} h^{\mathrm{eff}}_{pq} E^p_q + \tfrac{1}{2} \sum_{pqrs} (pq|rs) \left[E^p_q E^r_s - \delta_{qr} E^p_s \right]. \tag{32}$$

with $\hat{H}^D_{ie}$ and $\hat{H}^D_v$ denoting the internal–external (ie) and the valence (v) Hamiltonians, respectively. The constant C in (31) is chosen as $C = 2\sum_i h_{ii} + \sum_{ij} [2(ii|jj) - (ij|ij)] - 2\sum_i \varepsilon_i$ to satisfy

$$\hat{H}^D|0\rangle = E^{(0)}|0\rangle \tag{33}$$

The orbitals with energies $\varepsilon_i, \varepsilon_a$ are canonical in the internal and external space with respect to Fock operator

$$F_{mn} = h_{mn} + \sum_i [2(ii|mn) - (im|in)] + \sum_{pq} \gamma^p_q \left[(mn|pq) - \tfrac{1}{2}(mp|nq) \right], \tag{34}$$

where $\gamma^p_q = \left\langle 0|E^p_q|0 \right\rangle$ is the first-order reduced density matrix.

Applying standard Rayleigh-Schrödinger perturbation theory, the first-order wave function and second-order energy correction $E^{(2)}$ are

$$|1\rangle = \sum_{I \in \mathrm{FOIS}} |\Psi'_I\rangle \frac{\left\langle \Psi'_I|\hat{V}|0 \right\rangle}{E^{(0)} - E'_I} = \sum_{I \in \mathrm{FOIS}} |\Psi'_I\rangle \frac{\sqrt{N_I}}{E^{(0)} - E'_I}, \tag{35}$$

$$E^{(2)} = \sum_{I \in \mathrm{FOIS}} \frac{N_I}{E^{(0)} - E_{I'}}. \tag{36}$$

By construction in (28), the reference wave function cannot interact with FOIS functions at zeroth order. Thus, no linear equation system has to be solved, as it would otherwise be the case.

In many multireference perturbation theories, the energy spectrum computed with the approximated Hamiltonian is ill conditioned. Functions outside the reference space become artificially degenerate with reference wavefunction. The phenomenon is known in the literature as “intruder state,” and it results in unphysical energy corrections and spurious bumps along a potential energy surface. Several schemes, such as ad hoc level shift parameter, have been proposed [97–100], yet none of the schemes is entirely convincing [101]. The inclusion of the full two-electron interaction within the active space in (30) guarantees the absence of intruder states in the NEVPT2 formulation, since energies of the FOIS functions are computed at the same level as the zero-order CAS-CI wave function.

3.2 Calculation of Magnetic Properties

The starting point for the introduction of the SOC and SSC interactions is a calculation of matrix elements over multiconfigurational wave functions

$$\Psi_I^{SS}(\mathbf{x}_1, ..., \mathbf{x}_N) = \sum_J C_{JI}^{SS} \Phi_J^{SS}(\mathbf{x}_1, ..., \mathbf{x}_N) \tag{37}$$

of a CASSCF or a multireference configuration interaction (MRCI) type. Here Φ_I^{SS} symbolizes a CSF with spin quantum number S and spin projection quantum number $M_S = S$, and C_I^{SS} represents a CI coefficient.

3.2.1 Spin–Orbit Coupling

In order to include the SOC effects, a suitable many-electron Hamiltonian should be introduced. We employed a widely used in calculations Breit–Pauli spin–orbit Hamiltonian:

$$\hat{H}_{\mathrm{BP}} = \hat{H}_{\mathrm{BP}}^{(1)} + \hat{H}_{\mathrm{BP}}^{(2)}, \tag{38}$$

$$\hat{H}_{\mathrm{BP}}^{(1)} = \frac{\alpha^2}{2} \sum_i \sum_A Z_A r_{iA}^{-3} \hat{\mathbf{l}}_{iA} \hat{\mathbf{s}}_i, \tag{39}$$

$$\hat{H}_{\mathrm{BP}}^{(2)} = \hat{H}_{\mathrm{SSO}}^{(2)} + \hat{H}_{\mathrm{SOO}}^{(2)} = -\frac{\alpha^2}{2} \sum_i \sum_{j \neq i} r_{ij}^{-3} \hat{\mathbf{l}}_{ij} \hat{\mathbf{s}}_i - \sum_i \sum_{j \neq i} \alpha^2 r_{ij}^{-3} \hat{\mathbf{l}}_{ij} \hat{\mathbf{s}}_j. \tag{40}$$

Here $\hat{H}_{\mathrm{SSO}}^{(2)}$ and $\hat{H}_{\mathrm{SOO}}^{(2)}$ denote the spin–same orbit (SSO) and spin–other-orbit (SOO) contributions. $\hat{\mathbf{l}}_\mathbf{i}$ and $\hat{\mathbf{s}}_\mathbf{i}$ stand for the orbital momentum and the spin momentum operators of the ith electron, and $r_{iA} = |\mathbf{r}_i - \mathbf{R}_A|$ is the distance between the electron i and the nucleus A. The angular momentum operator of the electron i calculated with respect to the nucleus A at the position $\mathbf{R}_A$ is defined as $\hat{\mathbf{l}}_{iA} = (\mathbf{r}_i - \mathbf{R}_A) \times \hat{\mathbf{p}}_i$. Similarly, $r_{ij} = \left|\mathbf{r}_i - \mathbf{r}_j\right|$ represent the distance between the electrons i and j; $\hat{\mathbf{l}}_{ij} = \left(\mathbf{r}_i - \mathbf{r}_j\right) \times \hat{\mathbf{p}}_i$ symbolizes the orbital momentum operator of the electron i with respect to the position of the electron j. Boldface printed operators conventionally have three Cartesian components x, y, z; $\alpha = 1/c$ in atomic units is the fine structure constant (~1/137).

The Breit–Pauli SOC Hamiltonian contains a one-electron and two-electron parts. The one-electron part describes an interaction of an electron spin with a potential produced by nuclei. The two-electron part has the SSO contribution and the SOO contribution. The SSO contribution describes an interaction of an electron spin with an orbital momentum of the same electron. The SOO contribution describes an interaction of an electron spin with the orbital momentum of other electrons. However, due to a complicated two-electron part, the evaluation of the Breit–Pauli SOC operator takes considerable time. A mean field approximation was suggested by Hess et al. [102] This approximation allows converting the complicated two-electron Breit–Pauli Hamiltonian to an effective one-electron spin–orbit mean-field form

$$\hat{H}_{\text{SOMF}} = \sum_i \hat{\mathbf{z}}(i)\hat{\mathbf{s}}(i), \tag{41}$$

where $\hat{\mathbf{z}}_i$ is an appropriate effective (Hermitian but purely imaginary) spacial operator, which incorporates the bulk of the two-electron effects. Omitting the full derivation and employing the following notations (see [103] for details):

$$\hat{\mathbf{h}}_i^{\text{1el}-\text{SOC}} = \frac{\alpha^2}{2}\sum_A Z_A r_{iA}^{-3}\hat{\mathbf{l}}_{iA}, \tag{42}$$

$$\hat{\mathbf{g}}^{\text{SOC}} = -\frac{\alpha^2}{2}\hat{\mathbf{l}}_{ij} r_{ij}^{-3}, \tag{43}$$

the final working equation in a set of atomic basis functions $\{\varphi\}$

$$\phi_i = \sum_\mu c_{\mu i}\varphi_\mu, \tag{44}$$

for our SOMF implementation can be written as [103]:

$$\begin{aligned} \langle\varphi_\mu|\hat{\mathbf{z}}|\varphi_\nu\rangle = {} & \left\langle\varphi_\mu\middle|\hat{\mathbf{h}}^{\text{1el}-\text{SOC}}\middle|\varphi_\nu\right\rangle + \left(\varphi_\mu\varphi_\nu\middle|\hat{\mathbf{g}}^{\text{SOC}}\middle|\rho\right) - \frac{3}{2} \\ & \times \sum_{\kappa\tau} P_{\kappa\tau}\left[\left(\varphi_\mu\varphi_\kappa\middle|\hat{\mathbf{g}}^{\text{SOC}}\middle|\varphi_\tau\varphi_\nu\right) + \left(\varphi_\tau\varphi_\nu\middle|\hat{\mathbf{g}}^{\text{SOC}}\middle|\varphi_\mu\varphi_\kappa\right)\right]. \end{aligned} \tag{45}$$

Here

$$P_{\mu\nu} = \sum_j n_j c_{\mu j} c_{\nu j} \tag{46}$$

represents the electron density in an atomic basis where n_j refers to the occupation number of the jth molecular orbital, and

$$\rho(\mathbf{r}) = \sum_{\mu,\nu} P_{\mu\nu}\phi_\mu(\mathbf{r})\phi_\nu(\mathbf{r}) \tag{47}$$

stands for the electron density.

The SOMF operator was successfully employed in various calculations as implemented in the ORCA [103], MOLPRO [104], and AMFI [105] integral programs. Several additional approximations can be optionally employed in the ORCA program such as a one-center approximation and utilization of atomic densities (in line with the AMFI code) as well as utilization of the RI approximation for the Coulomb-like (second) term of (45) [103]

3.2.2 Spin–Spin Coupling

The dipole coupling between two spins is described by the Breit–Pauli spin–spin Hamiltonian [106]

$$\hat{H}_{\mathrm{SS}} = \frac{g_e^2\alpha^2}{8}\sum_{i\neq j}\left[\frac{\hat{\mathbf{s}}(i)\hat{\mathbf{s}}(j)}{r_{ij}^3} - 3\frac{\left(\hat{\mathbf{s}}(i)\mathbf{r}_{ij}\right)\left(\hat{\mathbf{s}}(j)\mathbf{r}_{ij}\right)}{r_{ij}^5}\right]. \tag{48}$$

Here g_e represents the g-factor of a free electron, α is a fine structure constant, $\mathbf{r}_{ij} = \mathbf{r}_i - \mathbf{r}_j$, and $r_{ij} = \left|\bar{r}_i - \bar{r}_j\right|$, and $\hat{\mathbf{s}}(i)$, $\hat{\mathbf{s}}(j)$ are spin operators for electrons i, j.

It is convenient to represent the SSC Hamiltonian in the form of a product of two second-rank irreducible tensor operators in order to take an advantage of using symmetry of a spin [106].

$$\hat{H}_{\mathrm{SSC}} = -\frac{3g_e^2\alpha^2}{8}\sum_{m=0,\pm1,\pm2}\sum_{i\neq j}\frac{(-1)^m}{r_{ij}^5}\left[\mathbf{r}_{ij}\times\mathbf{r}_{ij}\right]_{-m}^{(2)}\left[\hat{\mathbf{s}}(i)\times\hat{\mathbf{s}}(j)\right]_m^{(2)}. \tag{49}$$

Here $[\hat{\mathbf{s}}(i)\times\hat{\mathbf{s}}(j)]_m^{(2)}$ stands for a linear combinations of spin operator products $\hat{s}_k(i)\hat{s}_l(j)$ transforming like spin eigenfunctions with quantum numbers S, M [107].

3.2.3 Quasi-Degenerate Perturbation Theory

In the basis of precalculated spin-free states of the BO Hamiltonian, SOC and SSC effect could be treated in the most accurate way using quasi-degenerate perturbation theory. This method implies construction and diagonalization of the matrix representations of $\hat{H}_{\mathrm{BO}} + \hat{H}_{\mathrm{SOC}} + \hat{H}_{\mathrm{SSC}} + \hat{H}_Z$.

$$\begin{aligned}\left\langle \Psi_I^{SM}\middle|\hat{H}_{\mathrm{BO}}+\hat{H}_{\mathrm{SOC}}+\hat{H}_{\mathrm{SSC}}+\hat{H}_Z\middle|\Psi_J^{S'M'}\right\rangle &= \delta_{IJ}\delta_{SS'}\delta_{MM'}E_I^{(S)}\\ &+\left\langle \Psi_I^{SM}\middle|\hat{H}_{\mathrm{SOC}}+\hat{H}_{\mathrm{SSC}}+\hat{H}_Z\middle|\Psi_J^{S'M'}\right\rangle.\end{aligned} \tag{50}$$

The resulting matrix has a typical size of ~100 which depends on the number of spin-free roots taken into the treatment. After diagonalization, the resulting eigenvalues yield the fine structure splitting along with the Zeeman splitting. The complex eigenvectors can be employed later for calculations of properties. Thus, the main effort consists in computation of SOC and SSC matrix elements using multiconfiguration wavefunctions each containing several million CSFs.

Employing the standard tensor algebra notations for tensor spherical components

$$\hat{J}_0=\hat{J}_z,\quad \hat{J}_{+1}=-\frac{1}{\sqrt{2}}\left(\hat{J}_x+i\hat{J}_y\right),\quad \hat{J}_{-1}=\frac{1}{\sqrt{2}}\left(\hat{J}_x-i\hat{J}_y\right). \tag{51}$$

The SOMF operator can be rewritten as

$$\hat{H}_{\mathrm{SOMF}}=\sum_{m=0,\pm1}(-1)^m\sum_i \hat{z}_{-m}(i)\hat{s}_m(i). \tag{52}$$

It is highly useful to employ symmetry relations and selection rules of angular momentum operators for SOC matrix elements [108, 109]. The Wigner–Eckart theorem (WET) allows calculations of just a few matrix elements of manifold S,M,S',M' in order to obtain all other matrix elements. The WET states that the dependence of the matrix elements on the M,M' quantum numbers can be entirely represented by a Clebsch–Gordan coefficient $\left(\begin{array}{cc|c} S' & 1 & S\\ M' & m & M\end{array}\right)$ (CGC). Thus, a general spin-dependent matrix element can be written as [110]:

$$\left\langle \Psi_I^{SM}\middle|\sum_i \hat{s}_m(i)\middle|\Psi_J^{S'M'}\right\rangle=\left(\begin{array}{cc|c} S' & 1 & S\\ M' & m & M\end{array}\right)\left\langle \Psi_I^{S}\middle\|\hat{S}\middle\|\Psi_J^{S'}\right\rangle. \tag{53}$$

Here $\left\langle \Psi_I^{S}\middle\|\hat{S}\middle\|\Psi_J^{S'}\right\rangle$ denotes so-called a reduced matrix element (RME) which depends only on the quantum numbers S,S'. Because the CI wavefunction employed in our spin-free calculations is a linear combination of CSFs which are eigenfunctions of S_z, so that $M_S=S$, it is advantageous to evaluate the RMEs only for the states $M_S=S$.

Application of the WET to the case of SOMF operator yields:

$$\left\langle \Psi_I^{SM}\middle|\sum_{m=0,\pm1}(-1)^m\sum_i \hat{z}_{-m}(i)\hat{s}_m(i)\middle|\Psi_J^{S'M'}\right\rangle=\sum_{m=0,\pm1}(-1)^m\left(\begin{array}{cc|c} S' & 1 & S\\ M' & m & M\end{array}\right)Y_{IJ}^{SS'}. \tag{54}$$

Here $Y_{IJ}^{SS'}$ symbolizes the RMEs needed to be computed. For three possible cases $S - S' = 0, \pm 1$, one can obtain the following matrix elements [109, 111]

$$Y_{IJ}^{SS}(m) = \frac{\sqrt{S(S+1)}}{S} \left\langle \Psi_I^{SS} \middle| \sum_i \hat{z}_m(i)\hat{\mathbf{s}}_0(i) \middle| \Psi_J^{SS} \right\rangle, \tag{55}$$

$$Y_{IJ}^{SS-1}(m) = \left\langle \Psi_I^{SS} \middle| \sum_i \hat{z}_m(i)\hat{\mathbf{s}}_{+1}(i) \middle| \Psi_J^{S-1S-1} \right\rangle, \tag{56}$$

$$Y_{IJ}^{SS-1}(m) = \sqrt{\frac{2S+3}{2S+1}} \left\langle \Psi_I^{SS} \middle| \sum_i \hat{z}_m(i)\hat{\mathbf{s}}_{-1}(i) \middle| \Psi_J^{S+1S+1} \right\rangle. \tag{57}$$

In order to develop computationally manageable expressions for the RMEs, second quantization form of the SOMF operator is usually employed in actual calculations. As described elsewhere [112], the SOMF operator in the second quantization approach written in the basis of the one-electron orbitals p, q used to construct the CSFs is given by:

$$\hat{H}_{\text{SOMF}} = \frac{1}{2} \sum_{pq} z_{pq}^{-} \hat{a}_p^{\dagger} \hat{b}_q + z_{pq}^{+} \hat{b}_p^{\dagger} \hat{a} + z_{pq}^{0} \left[\hat{a}_p^{\dagger} \hat{a}_q - \hat{b}_p^{\dagger} \hat{b}_q \right]. \tag{58}$$

Here $\hat{a}_p^{\dagger}, \hat{a}_p$ symbolizes the creation and annihilation of a spin-up electron p, and $\hat{b}_p^{\dagger}, \hat{b}_p$ the creation and annihilation of a spin-down electron p. The operator $\hat{S}_{pq}^{(z)} = 1/2\left[\hat{a}_p^{\dagger} \hat{a}_q - \hat{b}_p^{\dagger} \hat{b}_q \right]$ corresponds to the spin-density operator; operators $\hat{S}_{pq}^{(+1)} = -(1/\sqrt{2})\hat{a}_p^{\dagger}\hat{b}_q$ and $\hat{S}_{pq}^{(-1)} = (1/\sqrt{2})\hat{b}_p^{\dagger}\hat{a}_q$ represent the spin-rising and spin-lowering operators. Combining (44) and (45), $z_{pq}^{\pm} = z_{pq}^{x} \pm i z_{pq}^{y}$ and z_{pq}^{0} are calculated as:

$$z_{pq}^{i} = \sum_{\mu,\nu} c_{\mu p} c_{\nu q} \langle \varphi_\mu | \hat{z}^i | \varphi_\nu \rangle (i = x, y, z). \tag{59}$$

The evaluation of the SSC matrix elements is analogous to the treatment of the SOC matrix elements with exception that the SSC Hamiltonian of (49) is a product of two irreducible second-rank tensors operators. Because SSC has nonvanishing contribution in the first order, it is usually sufficient to neglect contributions from states of different multiplicities. Application of the WET theorem to SSC Hamiltonian of (49) reads ($S = S'$):

$$\left\langle \Psi_I^{SM} \middle| \hat{H}_{\text{SSC}} \middle| \Psi_J^{SM'} \right\rangle = -\frac{3g_e^2\alpha^2}{8} \sum_{m=0,\pm1,\pm2} (-1)^m \begin{pmatrix} S & 2 & S \\ M' & m & M \end{pmatrix} X_{IJ}^{SS}(-m). \tag{60}$$

The RME for the SSC Hamiltonian takes the form:

$$X_{IJ}^{SS}(m) = \frac{\sqrt{(S+1)(2S+3)}}{\sqrt{S(S+1)}} \left\langle \Psi_I^{SS} \middle| \sum_{i \neq j} r_{ij}^{-5} \left[\mathbf{r}_{ij} \times \mathbf{r}_{ij}\right]_{-m}^{(2)} [\hat{\mathbf{s}}(i) \times \hat{\mathbf{s}}(j)]_0^{(2)} \middle| \psi_J^{SS} \right\rangle \tag{61}$$

Where the Cartesian components of the spin part of the Hamiltonian read:

$$\left[\hat{\mathbf{s}}(i) \times \hat{\mathbf{s}}(j)\right]_0^{(2)} = \frac{1}{\sqrt{6}} \left(2\hat{s}_z(i)\hat{s}_z(j) - \hat{s}_y(i)\hat{s}_y(j) - \hat{s}_x(i)\hat{s}_x(i)\right) \tag{62}$$

and the spatial part [108]

$$\left[\mathbf{r}_{ij} \times \mathbf{r}_{ij}\right]_0^{(2)} = \frac{1}{\sqrt{6}} \left[2\left(r_{ij}\right)_z^2 - \left(r_{ij}\right)_y^2 - \left(r_{ij}\right)_x^2\right], \tag{63}$$

$$\left[\mathbf{r}_{ij} \times \mathbf{r}_{ij}\right]_{\pm 1}^{(2)} = \mp\left[\left(r_{ij}\right)_z \left(r_{ij}\right)_x \pm i\left(r_{ij}\right)_z \left(r_{ij}\right)_y\right], \tag{64}$$

$$\left[\mathbf{r}_{ij} \times \mathbf{r}_{ij}\right]_{\pm 2}^{(2)} = \left[\left(r_{ij}\right)_x^2 - \left(r_{ij}\right)_y^2 \pm 2i\left(r_{ij}\right)_x \left(r_{ij}\right)_y\right]. \tag{65}$$

Similar to the evaluation of the SOC matrix element, it is convenient to employ second quantization technique to compute SSC matrix elements over a wavefunction of a MRCI type. In the second quantized formulation, the RMEs of the SSC operator reads:

$$X_{IJ}^{SS}(m) = \frac{\sqrt{(S+1)(2S+3)}}{\sqrt{S(2S-1)}} \sum_{pqrs} D_{pqrs}^{(m)} \left\langle \Psi_I^{SS} \middle| Q_{pqrs}^{(0)} \middle| \Psi_J^{SS} \right\rangle. \tag{66}$$

Here, the spin part $Q_{pqrs}^{(0)}$ represents the quintet spin-density operator:

$$Q_{pqrs}^{(0)} = \frac{1}{4\sqrt{6}} \left\{ E_{pq}\delta_{sr} - S_{ps}^z S_{rq}^z + \frac{1}{2}\left(S_{pq}^z S_{rs}^z - E_{pq}E_{rs}\right) \right\}, \tag{67}$$

here, $S_{pq}^{(z)} = \hat{a}_p^\dagger \hat{a}_q - \hat{b}_p^\dagger \hat{b}_q$ represent the spin density operator.

The spatial part represents the two-electron field gradient integrals. Employing the notation for the Cartesian components

$$D_{pqrs}^{kl} = \int\int \varphi_p(r_1)\varphi_q(r_2) \frac{(r_{12})_k (r_{12})_l - (1/3)\delta_{kl} r_{12}^2}{r_{12}^5} \varphi_q(r_1)\varphi_s(r_2) \mathrm{d}r_1 \mathrm{d}r_2 \tag{68}$$

the compound tensor operators read:

$$D_{pqrs}^{(0)} = \frac{1}{\sqrt{6}} \left(2D_{pqrs}^{(zz)} - D_{pqrs}^{(xx)} - D_{pqrs}^{(yy)}\right), \tag{69}$$

$$D_{pqrs}^{\pm 1} = \mp \left(D_{pqrs}^{(zx)} \pm iD_{pqrs}^{(zy)} \right), \tag{70}$$

$$D_{pqrs}^{(\pm 2)} = D_{pqrs}^{(xx)} - D_{pqrs}^{(yy)} \pm 2iD_{pqrs}^{(xy)}, \tag{71}$$

Thus, the computation of the SSC Hamiltonian matrix element requires calculations of six (five if one employs the fact that the SSC operator is traceless) Cartesian components of two-electron integrals. Those two-electron SSC integrals can be evaluated using an RI approximation [113].

Finally, the Zeeman contribution can be included into QDPT treatment in the form:

$$\hat{H}_z = \frac{\mu_B g_e}{2} \left(\hat{\boldsymbol{l}} + 2\hat{\boldsymbol{s}} \right) \boldsymbol{B} \tag{72}$$

Here $\hat{\boldsymbol{l}} = \sum_i \hat{\boldsymbol{l}}(i)$ and $\hat{\boldsymbol{s}} = \sum_i \hat{\boldsymbol{s}}(i)$ represent the total angular momentum operator and the total spin operator, μ_B is the Bohr magnetron, in atomic units $\mu_B = \alpha/2 = 1/2c$. $\boldsymbol{B}$ represents the applied magnetic field. It affects the calculated SOC and SSC energy levels in two different ways. First, it splits the degenerate level such as Kramers pairs changing the energy levels and Boltzmann distribution. Second, the applied magnetic field mixes M_S components of initial and final states.

The Zeeman Hamiltonian is multiplied by a correction factor $g_e/2$ which arises from a treatment of the interaction of between an electron and the electromagnetic field according to quantum electrodynamics [114].

4 Ligand Field Parameterization Schemes

In Sect. 2, we have outlined a general procedure of mapping the AI Hamiltonian H_{IJ}^{eff} onto a parameterized ligand field Hamiltonian $H_{IJ}^{\mathrm{eff}}(\mathbf{p})$ which we have let unspecified up to now. We should recall here, that in difference to H_{IJ}^{eff}, which in complexes without symmetry implies strong mixing between $|\mathrm{d}_i\rangle (i = \mathrm{d_{xy}}, \mathrm{d_{yz}}, \mathrm{d_{z2}}, \mathrm{d_{xz}}, \mathrm{d_{x2-y2}})$ orbitals, the effective ligand field Hamiltonian $V_{\mu\nu}^{\mathrm{eff}}(\mathbf{p})$ is build up in a basis of CFS with configurations constructed *from pure* $|\mathrm{d}_i\rangle$ orbitals defined in the chosen Cartesian axis molecule frame and arranged, for convenience, in a given standard order. Denoting these CSF by $\left|\Phi_\mu^{\mathrm{LFT}}\right\rangle$ ($\mu = 1, N_{\mathrm{CSF}}$), we can transform $V_{\mu\nu}^{\mathrm{eff}}(\mathbf{p})$ into the desired $H_{IJ}^{\mathrm{eff}}(\mathbf{p})$ form of (5) as follows. Using the projection operator technique, we express $|I^{\mathrm{LFT}}\rangle$ of (2)–(3) in terms of $\left|\Phi_\mu^{\mathrm{LFT}}\right\rangle$:

$$\left|I^{\mathrm{LFT}}\right\rangle = \sum_{\mu=1}^{N_{\mathrm{CSF}}} \left|\Phi_\mu^{\mathrm{LFT}}\right\rangle T_{\mu,I}, \tag{73}$$

with $T_{\mu,I}$ given by

$$T_{\mu,I} = \left\langle \Phi_{\mu}^{\mathrm{LFT}} \middle| I^{\mathrm{LFT}} \right\rangle. \tag{74}$$

We should note here, that by construction, the matrix $\mathbf{T}$ is neither orthogonal nor normalized; deviations from orthonormality are particularly pronounced in complexes with highly covalent metal–ligand bonds, as for example in Fe–S clusters. However, denoting the overlap matrix $\mathbf{S} = \mathbf{T}^{\mathrm{T}} \cdot \mathbf{T}$, Löwdin's procedure (75) is used to obtain an orthogonal matrix $\mathbf{C}$. Using this matrix $V_{\mu\nu}^{\mathrm{eff}}(\mathbf{p})$ is transformed into $H_{IJ}^{\mathrm{eff}}(\mathbf{p})$ of (5) as given by (76).

$$\mathbf{C} = \mathbf{T}.\mathbf{S}^{-(\mathbf{1/2})} \tag{75}$$

$$\mathbf{H}^{\mathrm{LFT}}(\mathbf{p}) = \mathbf{C}^{\dagger}(\mathbf{V}^{\mathbf{eff;(0)}} + \sum_{k=1}^{N_p} p_k \mathbf{V}^{\mathbf{eff;(k)}})\mathbf{C}. \tag{76}$$

After having explained the relation between AIT and the LFT formalism, we now turn to a brief outline of the various parameterizations of $V_{\mu\nu}^{\mathrm{eff}}(\mathbf{p})$. The effective ligand field Hamiltonian (77) consists of one-electron terms, the one-electron ligand field Hamiltonian ($\hat{v}_{\mathrm{LF}}(i)$), and two-electron terms ($\hat{G}(i,j)$), which take account of the Coulomb interactions between the d-electrons; summations is carried out over the d-electrons $i < j = 1, N_d$. In difference to crystal field theory, these operators are left unspecified. Various LF models differ in the way they approximate the matrix elements of these operators. When acting on CSF $\left| \Phi_{\mu}^{\mathrm{LFT}} \right\rangle$, the operators $\hat{v}_{\mathrm{LF}}(i)$ and $\hat{G}(i,j)$ lead to one- (h_{ab}) and two-electron (G_{abcd}) matrix elements (a, b, c, d – d-orbitals). Common to all ligand models is expressing the G_{abcd} integrals:

$$\hat{H}_{\mathrm{LF}} = \sum_{i} \hat{v}_{\mathrm{LF}}(i) + \sum_{i<j} \hat{G}(i,j), \tag{77}$$

(without symmetry there are 120 independent integrals of this type) in terms of parameters pertaining to the spherical symmetry. These are the Slater–Condon (F_o, F_2, and F_4), or alternatively, the Racah parameters (A, B, and C), reduced by covalency from the values of the free atom or ion. Of these, only the parameters (F_2, F_4) or ($B = F_2 - 5F_4$, $C = 35F_4$) contribute to the multiplet splittings. The latter parameters are common to all ligand field models. What makes the various models different is the parameterization of the matrix elements h_{ab} ($a, b = d_{xy}$, d_{yz}, d_{z2}, d_{xz}, d_{x2-y2}, there are 15 independent parameters, from which only 14 contribute to the multiplet splittings). For complexes with C_4 and C_3 symmetry axes, the h_{ab} matrix takes a very simple form. Thus, in octahedral or tetrahedral complexes, there is only one nonzero matrix element of h_{ab} – the energy difference between the t_2 and e type orbitals ($\Delta = 10\mathrm{Dq}$). On lowering the symmetry to $D_{4\mathrm{h}}$ or $D_{2\mathrm{d}}$, the t_2 and

e orbitals split into e and b_2 and a_1 and b_1, respectively and this leads to three diagonal parameters (Δ, $\Delta_{t_2} = e(e) - e(b_2)$, and $\Delta_e = e(a_1) - e(b_1)$). Finally, trigonal distortions of O_h and T_d complexes impose a splitting of t_2 into $e + a_1$, and this leads again to three ligand field parameters, two diagonal (Δ, $\Delta_{t_2} = e(e) - e(a_1)$) and one off-diagonal matrix element. The latter accounts for the mixing between $e(t_2)$ and $e(e)$. An advantage of these parameterizations (LFModel 1) is that, being based on symmetry, they are quite general and model independent. A drawback is that being global (referring to the whole complex) these parameters are not transferable and not easy to interpret. However, when being extracted from AI post-Hartree–Fock calculations, these parameters allow for the use of symmetry principles to deduce d-orbital energy differences.

In difference to the global symmetry based parameterization, the AOM considers the nonspherical ligand-field potential as consisting of spacially discrete nonoverlapping parts, each associated with a separate ligand or donor group, in such a way that the LF matrix in the basis of the five d-orbitals and axes of quantization reflecting the local metal–ligand pseudosymmetry is diagonal. With a local $C_{2\mathrm{v}}$ pseudosymmetry, taking a M-pyridine bond, for example, we choose the N lone pair pointing along the Z axis and the Cartesian axes X and Y lying in and perpendicular to the pyridine plane. We then have the following nonzero matrix elements in this local frame:

$$\begin{aligned}\langle d_{z2}|v_\mathrm{LF}|d_{z2}\rangle &= e_\sigma,\\ \langle d_{xz}|v_\mathrm{LF}|d_{xz}\rangle &= e_{\pi c},\\ \langle d_{yz}|v_\mathrm{LF}|d_{yz}\rangle &= e_{\pi s},\end{aligned} \tag{78}$$

with parameters e_σ, $e_{\pi c}$, and $e_{\pi s}$ describing σ (e_σ), π in-plane ($e_{\pi c}$), and out-of-plane ($e_{\pi s}$), respectively, and matrix elements for δ bonding interactions (for $\mathrm{d_{xy}}$ and $\mathrm{d_{x2-y2}}$) which are usually either neglected or are subsumed in e_σ, $e_{\pi c}$, and $e_{\pi s}$. In a second step, one expresses the LF matrix in a global molecular frame and sums contribution from each metal–ligand interactions. One then arrives at the master equation for a matrix element of the AOM given by (79) (LFModel 2). It is a great merit of the AOM that it uses structural data to define the coordinates and the orientation of a given ligand in space (defined by the Euler angles $\theta_L, \varphi_L, \psi_L$) and energy parameters $e_{\lambda,L}; \lambda = \sigma, \pi s, \pi c$ describing the chemical nature of a given ligand independently of the angular geometry. When adjusted from spectra or AI data, these parameters bear important chemical content and are largely transferable between analogous complexes. Excellent reviews on the AOM, its extensions, and application are found in literature [115–118] which the reader can refer.

$$h_{ab} = \sum_L \sum_\lambda F_{\lambda a}(\theta_L, \varphi_L, \psi_L) F_{\lambda b}(\theta_L, \varphi_L, \psi_L) e_{\lambda,L}; \quad \lambda = \sigma,\ \pi s,\ \pi c \tag{79}$$

5 Computational Details

In this work, we have computed and analyzed hexa- and tetradentate complexes of Cr(III)(d^3) and Cr(IV)(d^2), respectively, and bis-chelate complexes of Ni(II)(d^8) with structures depicted schematically in Fig. 4.

Calculations of the full manifold of the electronic states spanned by these configurations have been done on structures obtained from DFT geometry optimizations using the Perdew–Becke–Ernzerhof (PBE) functional [119, 120], empirical van der Waals corrections [121] for the DFT energy, the scalar relativistic zero-order regular approximation (ZORA) [122], and the scalar relativistically recontracted (SARC) [123] version of the def2-TZVP basis set [124].

Ground and excited state energies based on CASSCF wavefunctions were calculated using the CASSCF module of ORCA (to account for static correlation) together with the NEVPT2 [74, 83, 84] (to account for dynamic correlation). Reasonably extensive basis sets have been used – def2-TZVP, along with corresponding auxiliary basis functions needed to apply the resolution of identity method for the evaluation of molecular integrals. In all calculations, only the metal d-orbitals were included in the active space. Better results can be obtained by also including ligand orbitals or a second d-shell. However, here we want to demonstrate what can be achieved on the basis of an "ab initio" version of LFT. As initial guess for the CASSCF calculations, spin-unrestricted Kohn–Sham DFT orbitals were

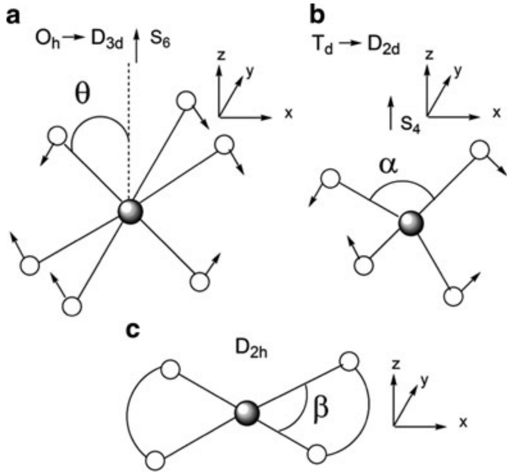

Fig. 4 Octahedral (**a**) and tetrahedral (**b**) complexes and the angles $\theta = 60^\circ$ and $\alpha = 120^\circ$ defining $O_h \rightarrow D_{3d}$ and $T_d \rightarrow D_{2d}$ distortions employed in determining AOM parameters of CrX_6^{3-} and CrX_4 complexes based on AI (CASSCF and NEVPT2) results; (**c**) bis-bidentate chelate complexes with the chelate bite angle β used to analyze the effect of geometry and π-bonding anisotropy (Orgel effect) in $Ni(dtc)_2$, $Ni(Et_2dtc)_2$, $Ni(acac)_2$, and $Ni(DPM)_2$ planar complexes (*dtc* dithiocarbamate, *Et₂dtc* diethyldithiocarbamate, *acac* acetylacetonate, *DMP* 2,2,6,6-tetramethylheptanedionato)

converted to quasi restricted orbitals. In some cases, reordering using the rotation option of ORCA was necessary in order to ensure that the orbitals of dominantly d-character are in the active space. To identify symmetries of CASSCF eigenstates, we used the symmetry options of ORCA following a descent of symmetry, say from O_h into the corresponding Abelian subgroup (D_{2h}). For highly negatively charged CrX_6^{3-} (X^- = F, Cl, Br, I) species, a charge compensating polarizable continuum using the conductor like solvent model (COSMO) with dielectric parameters for water (dielectric constant $\varepsilon = 80$) have been chosen, both in the DFT and in the correlated calculations. All calculations have been done with the program ORCA [45] (DFT and AI) interfaced with the ligand field program AOMX [125] allowing to fit ligand field parameters from the AI energy eigenvalues. Parameter optimizations using Powell's parallel subspace algorithm [126] and a subsequent multivariate error analysis [127] allowed to refine ligand field parameters and to obtain the associated error bars.

6 Applications and Analysis

6.1 *The Ligand Field Spectra of $Cr^{III}X_6^{3-}$ (X^- = F, Cl, Br, I)*

Electronic absorption spectra due to d–d transitions of CrF_6^{3-} in solution [128] and various solids – $(NH_4)_3CrF_6$ [129], K_3CrF_6 [130], and K_2NaCrF_6 [131, 132] – served for a long time to test and validate AI methods. Theoretical studies on CrF_6^{3-} have been done in the framework of simple Roothaan restricted open-shell HF SCF method, limited CI and CASSCF [133–149] including also analysis of second coordination sphere effects [150]. With three unpaired electrons in the $^4A_{2g}$ ground state, absorption spectra of the CrF_6^{3-} complex ion in various ionic solids display three broad bands due to spin-allowed quartet–quartet transitions with band maxima showing small (but essential, see [150]) changes in dependence on the surrounding cations. The three d–d bands in increasing order of energy have been assigned to the single ($t_{2g}^3 \rightarrow t_{2g}^2 e_g^1$):$^4A_{2g} \rightarrow {}^4T_{2g}$ and $^4A_{2g} \rightarrow {}^4T_{1g}(1)$, and double ($t_{2g}^3 \rightarrow t_{2g}^1 e_g^2$):$^4A_{2g} \rightarrow {}^4T_{1g}(2)$ electron excitations, all three multiplets originating from the ground ^4F and excited ^4P electronic terms of the free Cr^{3+} ion. In addition to these broad bands, sharp electronic absorptions due to the formally forbidden spin–flip transitions $^4A_{2g} \rightarrow {}^2E_g$, $^2T_{1g}$ and $^4A_{2g} \rightarrow {}^2T_{2g}$ within the t_{2g}^3 ground state configuration have been observed [128–132]. Being rather close, respectively, to the $^4A_{2g} \rightarrow {}^4T_{2g}$ and $^4A_{2g} \rightarrow {}^4T_{1g}(1)$ bands, these spin forbidden transitions gain intensity from the spin-allowed ones by mixing via SOC. In Table 2, we list the experimental energies for K_3CrF_6 [130] along with the corresponding (CASSCF and NEVPT2) AI values. In Table 3, we compare our results with published AI data on the same complex including various levels of theory – the simple, state-specific ROHF SCF method, CASSCF(3,5) employing atomic natural orbital (ANO) basis sets and the singles and doubles configuration

Table 2 Energies of d–d transitions (ground state $^4A_2$ is taken as energy reference) of octahedral CrX_6^{3-} ($X = F, Cl, Br, I$) complexes[a] from CASSCF and NEVPT2 calculations and their values[b] resulting from a AILFT calculation (LFModel 1) with $\Delta = 10Dq$, B, and C obtained from a best fit to the AI results

	CrF_6^{3-}		$CrCl_6^{3-}$		$CrBr_6^{3-}$		CrI_6^{3-}	
	CASSCF	NEVPT2 exp.[c]	CASSCF	NEVPT2 exp.[d]	CASSCF	NEVPT2 exp.[e]	CASSCF	NEVPT2
$^4T_2$	13,380 (−20)	15,365 (−111) **15,200**	11,055 (−113)	14,465 (−354) **12,800**	9,972 (−95)	13,959 (−416) **13,400**	9,255 (4)	14,263 (−730)
$^4T_1(1)$	21,424 (−42)	23,449 (−533) **21,800**	18,018 (−210)	22,145 (−1,072) **18,200**	16,498 (−251)	21,510 (−1,323) **17,700**	15,541 (−251)	21,801 (−1,801)
$^4T_1(2)$	34,778 (−16)	35,307 (439) **35,000**	30,447 (−605)	32,716 (47) **28,400**	28,706 (−735)	31,507 (−127)	27,542 (−911)	31,603 (−523)
$^2E(1)$	19,409 (−64)	17,579 (−283) **16,300**	18,800 (−427)	17,030 (−723) **14,435**	18,714 (−569)	16,986 (−855) **13,900**	18,584 (−790)	16,934 (−1,004)
$^2T_1(1)$	20,430 (−38)	18,681 (−575) **16,300**	19,760 (−447)	18,058 (−1,050) **15,050**	19,636 (−581)	18,009 (−1,224)	19,466 (−800)	17,965 (−1,418)
$^2T_2(1)$	27,372 (−85)	25,288 (−119) **23,000**	25,735 (−316)	24,616 (−931) **~20,100**	25,041 (−250)	24,801 (−1,451) **19,200**	24,280 (−124)	25,450 (−2,355)
$^2A_1$	29,674 (25)	30,022 (−156)	26,811 (−196)	28,607 (−614) **~24,800**	25,676 (−251)	28,064 (−712)	24,823 (−270)	28,286 (−1,078)
$^2T_2(2)$	32,664 (88)	32,979 (−527)	29,153 (268)	30,516 (−210)	27,975 (219)	29,388 (167)	27,080 (170)	28,651 (683)
$^2T_1(2)$	33,736 (20)	33,800 (−678)	30,495 (−127)	31,903 (−1,019)	29,265 (−139)	31,219 (−1,119)	28,238 (−92)	31,249 (−1,408)
$^2E(2)$	36,009 (10)	35,316 (−151)	32,854 (−323)	33,434 (−617)	31,667 (−404)	32,790 (−776)	30,715 (−471)	32,861 (−1,134)
$^2T_1(3)$	39,668 (90)	39,324 (−694)	35,181 (440)	36,541 (−702)	33,505 (582)	35,571 (−746)	32,057 (820)	35,269 (−843)
$^2T_2(3)$	46,237 (−24)	45,791 (−797)	40,380 (591)	42,875 (−1,353)	38,094 (821)	41,549 (−1,316)	36,286 (1,133)	41,187 (−1,576)
$^2T_1(4)$	46,546 (89)	48,689 (−767)	40,734 (162)	45,470 (−885)	38,475 (142)	44,064 (−811)	36,897 (142)	43,935 (−942)
$^2A_2$	51,121 (−4)	47,612 (−480)	46,802 (−421)	44,328 (−996)	45,320 (−446)	43,272 (−1,337)	43,882 (−472)	42,783 (−1,599)
$^2T_2(4)$	52,510 (−11)	49,902 (762)	47,811 (−385)	45,807 (1,220)	46,283 (−500)	44,520 (1,119)	44,898 (−631)	43,947 (1,292)
$^2E(3)$	55,140 (−166)	55,611 (−1,017)	48,519 (−296)	52,782 (−2,301)	45,914 (−411)	51,406 (−2,503)	44,342 (−755)	51,367 (−3,052)
$^2T_1(5)$	58,744 (52)	57,144 (−123)	52,244 (164)	52,548 (55)	49,947 (204)	50,771 (89)	48,035 (264)	49,993 (229)
$^2E(4)$	77,494 (22)	72,471 (2,014)	70,648 (−181)	66,146 (3,127)	68,540 (−349)	64,017 (3,389)	66,686 (−586)	62,777 (3,976)
$^2T_2(5)$	80,221 (−1)	74,569 (824)	71,792 (947)	67,428 (2,242)	69,044 (1,251)	64,860 (2,751)	66,401 (1,640)	62,831 (3,799)
σ	61	726	402	1,284	513	1,451	680	1,856

[a] Calculated using Cr–X bond distances R from a DFT geometry optimization using a PBE functional: R (in Å)1.942 (Cr–F), 2.386 (Cr–Cl), 2.559 (Cr–Br), and 2.801 (Cr–I)

[b] Given in brackets as deviations of the AILFT value from the AI one: $E(\text{AILFT}) - E(\text{CASSCF})$ or $E(\text{AILFT}) - E(\text{NEVPT2})$

[c] Values from experiment listed in boldface type in the column for NEVPT2 column taken from [130], pertaining to K_3CrF_6

[d] [191]

[e] [190]

Table 3 Differences (in cm^{-1}) between calculated (AI or LFDFT) and experimental (K$_3$CrF$_6$, [130]) energies of d–d transitions of CrF$_6{}^{3-}$

	SCF [149][a]	CASSCF [149][b]	MRCI [149][c]	MRCI [149][d]	CASSCF [this work]	NEVPT2 [this work]	LFDFT [35]
$^4A_{2g} \rightarrow {}^4T_{2g}$	−1,410	−1,780	−1,830	−980	−1,820	165	−1,631
$^4A_{2g} \rightarrow {}^2E_g$	5,770	3,470	1,820	2,410	3,109	1,279	−3,803
$^4A_{2g} \rightarrow {}^2T_{1g}$	5,750	4,470	3,120	3,320	4,130	2,381	−3,256
$^4A_{2g} \rightarrow {}^4T_{1g}(1)$	4,974	−460	−990	150	−376	1,649	−2,357
$^4A_{2g} \rightarrow {}^2T_{2g}$	13,433	4,690	1,430	2,389	4,372	2,288	−4,372
$^4A_{2g} \rightarrow {}^4T_{1g}(2)$	−4,592	120	−1,910	100	222	307	−4,661

[a] HF-Roothaan calculation: basis set Cr:15s11p6d/[9s6p4d]; F: 9s5p/[5s3p]

[b] Atomic natural orbitals (ANO) basis sets: Cr:16s12p8d/[7s5p3d]; F:14s9p/[5s3p]

[c] MRCI: CASSCF(3,5) + 8(Cr: 3s, 3p)

[d] MRCI: CASSCF(3,5) + 10(F: bonding e_g, t_{2g})

interaction (multireference CI, MRCI) on top of precalculated CASSCF wavefunctions, where in addition to the 3d^3 electrons, the (3s^2, 3p^6) electrons of Cr^{III}, or alternatively, electrons on the fully occupied bonding e_g and t_{2g} orbitals (dominated by 2p functions of F$^-$ – $e_g{}^4t_{2g}{}^6$) have been correlated. Energies of the electronic transitions within the $t_{2g}{}^3$ ground state configuration ($^4A_{2g} \rightarrow {}^2E_g, {}^2T_{1g}, {}^2T_{2g}$, Table 3, second column), which are 5,000–6,000 cm^{-1} higher in energy than experiment, show that HF methods largely overestimate open-shell repulsion effects (DFT calculations drastically underestimates them, see Table 3, eighth column). While the value of 10Dq, identified with the $^4A_{2g} \rightarrow {}^4T_{2g}$ band maximum energy is readily reproduced already at the ROHF level of theory (the error is merely −1,400 cm^{-1}), the two $^4A_{2g} \rightarrow {}^4T_{1g}(t_{2g}{}^2e_g{}^1)$ [$^4A_{2g} \rightarrow {}^4T_{1g}(t_{2g}{}^1e_g{}^2)$] transitions are found about 5,000 cm^{-1} larger and lower, respectively, in energy compared to experiment. This artifact is largely due to the neglect of configuration interaction between states of the same symmetry. Hence, this discrepancy is already largely removed when accounting for static correlation (Table 3, results for CASSCF(3,5), third column). The CASSCF method also leads to an improvement of the energies of the intraconfigurational $t_{2g}{}^3$ quartet–doublet transitions; the ^2E_g, $^2T_{1g}$, and $^2T_{2g}$ states due to this configuration mix with states of the same symmetry originating from excited $t_{2g}{}^{3-x}e_g{}^x$ (x = 1, 2, 3) configurations which leads to decrease of the energies of the former states. Not unexpectedly, this effect is larger for the $^2T_{2g}$ state, being higher lying in energy, than for the lower lying ^2E_g and $^2T_{1g}$ (cf. Table 2, second column). Calculated energies of the lowest ^2E_g, $^2T_{1g}$, and $^2T_{2g}$ states are further improved when, in addition to the three 3d Cr(III) electrons, eight (3s^{2}3p^6) or ten ($t_{2g}{}^6e_g{}^4$) electrons on Cr^{III} or F$^-$, respectively, are correlated. Dynamical correlation introduced in this way leads to a further energy lowering of ^2E_g, $^2T_{1g}$, and $^2T_{2g}$ as the MRCI results clearly show (Table 2, columns 3 and 4). We note in passing that, in spite of the quite different basis sets and implementations of the CASSCF method in MOLCAS [151] and ORCA [45], CASSCF results from [149] (Table 2, second column) and the ones reported here (Table 2, fifth column) are almost identical. Further account for dynamic correlation using NEVPT2 (Table 3, column 7) leads to further improvement and results which are actually *best* among all AI data reported so far. We also calculated electronic multiplets for the analogous CrX_6^{3-} ($X = Cl^-$, Br^-, I^-) complexes which are listed in Table 2, where for $X = Cl^-$ and Br^- energies of d–d transitions from electronic absorption spectra are included for comparison. We should note here, that in difference to CrF_6^{3-}, agreement between experimental and theoretical values of these energies are less good for the more covalent $CrCl_6^{3-}$ and $CrBr_6^{3-}$. More specifically, the energies of the lowest two spin-allowed transitions $^4A_2 \rightarrow {}^4T_2$ and $^4A_2 \rightarrow {}^4T_1(1)$ are now found by CASSCF(NEVPT2) by −1,745 (1,665) and −182 (3,945) for $CrCl_6^{3-}$ and −3,428 (559) and −1,202 (3,810) for $CrBr_6^{3-}$ smaller (larger) compared to experimental values. Positive corrections to the energies of d–d transitions brought in by the NEVPT2 method are due to stronger stabilization of the ground state compared to the excited states. However, going from the rather ionic Cr–F to the more covalent Cr–Cl and Cr–Br bonds, this effect becomes artificially enlarged (Table 2), a feature shared by all methods based on second-order perturbation theory. In spite of this, the experimental trend of 10Dq values, decreasing in the order X = F, Cl, Br and I is well reproduced, both by CASSCF and the NEVPT2 results (Fig. 5).

Let us now turn to the question of how consistent are various LF parameterization schemes with rigorous AI calculations. Here, we focus on the *total manifold* of states originating from a given d^n configuration of a transition metal in a complex. In Table 2, we analyze this point taking *all multiplets* stemming from the nominal d^3 configuration of Cr(III). In a first step, we focus on the simple LFModel 1 with parameters 10Dq, B, and C. A least squares fit to the energies of the 3 quartet–quartet and the 16 quartet–doublet transitions yields parameter values (Table 4) with deviations between calculated (AILFT) vs. CASSCF–NEVPT2 energies and standard deviations (σ) listed in Table 2. We observe from these results that the LFModel 1 is remarkably well consistent with both the CASSCF and NEVPT2, not unexpectedly, agreement being better with data from SA-CASSCF.

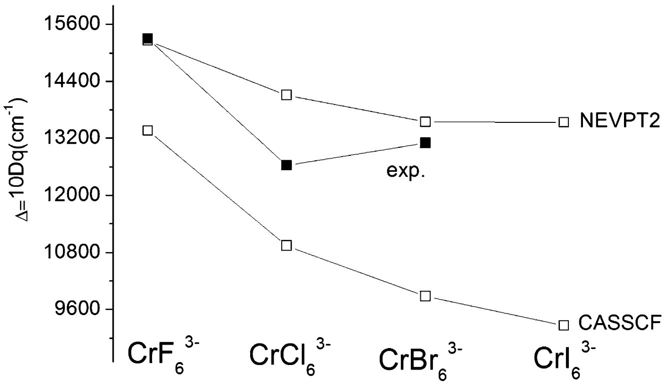

Fig. 5 Values of 10Dq ($^4A_{2g} \rightarrow {}^4T_{2g}$ transition energy) from CASSCF and NEVPT2 AI results of octahedral CrX_6^{3-} complexes and their comparison with data deduced from spectroscopic d–d-transitions

Deviations between AILFT and CASSCF–NEVPT2 energies are getting larger upon introduction of dynamic correlation (NEVPT2) and this becomes increasingly pronounced with increasing covalency in the series F $<$ Cl $<$ Br $<$ I (Table 2). Along the same lines, lowering of interelectronic repulsion, as reflected by the changes of the parameter B across the series (referred to as the nephelauxetic effect [128]) is well reproduced by the AI results (Table 4). Also included in Table 4 are values of 10Dq, B and C that result from a fit to experimental spectral data. From a comparison of between these values and the AILFT ones, one can infer that dynamic correlation accounted for by NEVPT2 leads to a great improvement of B and C over the CASSCF results. A refined parameterization of interelectronic repulsions considers the fact that σ-antibonding $e_g(d_{z2}, d_{x2-y2})$ orbitals undergo a larger expansion than the π-antibonding $t_{2g}(d_{xz}, d_{yz}, d_{xy})$ ones. Hence, different B parameters B_{33}, B_{55}, and B_{35} for interelectronic repulsion between electrons on e_g–e_g, t_{2g}–t_{2g}, and e_g–t_{2g} pairs of orbitals are introduced (LFModel 3) [152, 153]. In this parameterization, the C/B ratios are assumed to retain their free ion values, because covalency is thought to affect B and C to about the same extent (but see [154, 155]). One therefore introduces weighting factors in the molecular repulsion integrals "t" and "e" for electrons occupying the t_{2g} and e_g orbitals and takes these parameters along with 10Dq as adjustable starting with the values of the free ion B_o and C_o. Results from such a fit to the AI results (NEVPT2) are listed in Table 5. From the fit data, the expected order $t > e$ is nicely confirmed by the AI calculations. Values of B_{33}, B_{55}, and B_{35} calculated in this way have been included in the plot of Fig. 6. As judged by the values of σ (the standard deviation between AILFT and NEVPT2 energies, Table 5), electronic transitions calculated using best fit parameters (Table 5) are approaching the AI results even more closely than the results of LFModel1 (Table 4).

Let us now analyze AI results in terms of the additive parameterization scheme offered by the AOM (LFModel2). In terms of this model 10Dq $= 3e_\sigma - 4e_\pi$, which makes it impossible to fix the two parameters for an octahedral complex. To do that we employed a fixed but otherwise arbitrary distortion ($\theta = 60^\circ$, trigonal compression, see Fig. 4 for the definition of this angle; $\theta = 54.73^\circ$ for the octahedron). The trigonal field leads to splitting of the t_{2g} orbitals into a_{1g} and e_g and to mixing of the latter orbital with the one of the e_g parent symmetry described by (80) and (81).

a_1:

$$|d_{z2}\rangle : \left(\frac{9}{2}\right) e_\pi \sin^2 2\theta + \left(\frac{3}{8}\right) e_\sigma (1 + 3\cos 2\theta)^2, \tag{80}$$

e:

$$\begin{array}{cc} |d_{yz(xz)}\rangle & |d_{x2-y2(xy)}\rangle \\ \left[\begin{array}{c} 3e_\pi(\cos^2\theta + \cos^2 2\theta) + (9/4)\sin^2 2\theta e_\sigma \\ (3/2)(4e_\pi - 3e_\sigma)\cos\theta \sin^3\theta \end{array}\right. & \left.\begin{array}{c} (3/2)(4e_\pi - 3e_\sigma)\cos\theta \sin^3\theta \\ [3e_\pi(1+\cos^2\theta) + (9/4)\sin^2\theta e_\sigma]\sin^2\theta \end{array}\right]. \end{array} \tag{81}$$

Table 4 AILFT parameters Δ, *B*, and *C* (LFModel 1) for octahedral CrX_6^{3-} (X = F, Cl, Br, I) complexes and their values deduced from optical d–d transitions[a] from literature

	CrF_6^{3-}			$CrCl_6^{3-}$			$CrBr_6^{3-}$			CrI_6^{3-}	
	CASSCF	NEVPT2	Exp.	CASSCF	NEVPT2	Exp.	CASSCF	NEVPT2	Exp.	CASSCF	NEVPT2
Δ = 10Dq	13,359	15,255	15,297	10,941	14,109	12,630	9,876	13,542	13,089	9,258	13,533
B	1,071	863	734	988	767	632	972	729	471	943	699
C	4,018	3,720	3,492	3,907	3,605	3,180	3,886	3,631	3,249	3,841	3,627
C/*B*	3.75	4.31	4.76	3.95	4.70	5.03	4.00	4.98	6.90	4.07	5.18

[a] Denoted as "exp." and obtained from a best fit to experimentally reported energies of d–d transitions, see Table 2

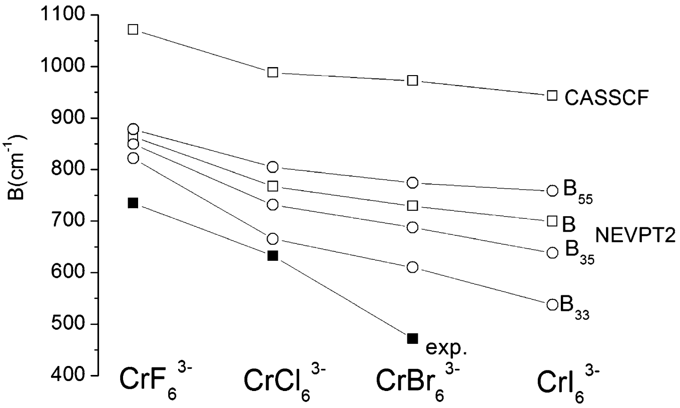

Fig. 6 Variation of the parameter B across the CrX_6^{3-} series (nephelauxetic effects due to central field covalency) and Jørgensens' B_{33}, B_{35}, and B_{55} (differential covalency or symmetry restricted covalency: B_{33} (e_g–e_g), B_{35} (e_g–t_{2g}), B_{55}(t_{2g}–t_{2g}))

Table 5 AILFT ligand field parameter values for octahedral CrX_6^{3-} complexes allowing for anisotropic covalence (LFModel 3)[a]

	CrF_6^{3-}	$CrCl_6^{3-}$	$CrBr_6^{3-}$	CrI_6^{3-}
$\Delta = 10Dq$	15,150	13,944	13,383	13,389
t	0.968	0.947	0.938	0.933
e	0.952	0.903	0.884	0.856
$B_{55} = t^4B$	878	804	774	758
$B_{35} = t^2e^2B$	849	731	687	638
$B_{33} = e^4B$	821	665	610	537
σ	641	921	970	1,106

[a]Based on a reference value of $B = 1{,}000$ and values of $C/B = 4.31$ (CrF_6^{3-}); 4.70 ($CrCl_6^{3-}$); 4.98 ($CrBr_6^{3-}$); 5.18 (CrI_6^{3-}) from Table 4 (values for NEVPT2)

Thus, the octahedral $^4T_2$ term splits into $^4A_1 < {}^4E$, and $^4T_1(1)[^4T_1(2)]$ into $^4E < {}^4A_2[^4A_2 < {}^4E]$ with order of energies as indicated. In Table 6, we list their values for CrX_6^{3-} (X = F, Cl, Br, I). Parameters of e_σ, e_π, and B resulting from a best fit to both the CASSCF and NEVPT2 data are listed in Table 7. Focusing on e_σ, e_π we find that these values compare well with values from the literature (included also in Table 7). From these results, we can deduce the following: First of all, and more importantly, the dynamic correlation covered by NEVPT2 introduces a significant increase of both e_σ and e_π as comparison between the CASSCF and NEVPT2 AILFT values shows. Thus, taking e_σ, we find e_σ(NEVPT2) − e_σ(CASSCF) to increase in from F (1,404 cm^{-1}) to Cl (1,700 cm^{-1}) to Br (1,891 cm^{-1}) to I (2,121 cm^{-1}), i.e., with increasing covalency. Here, we convey to usual interpretations of the AOM parameters using perturbation theory being a sum of two terms ((82), cellular ligand field model (CLF) [115–118]).

Table 6 CASSCF and NEVPT2 energies of d–d transitions (in cm^{-1}) and their best fit AILFT values[a] showing the effect of trigonal distortions ($\theta = 60^{\circ}$) on the parent octahedral quartet states[b]

	CrF_6^{3-}		$CrCl_6^{3-}$		$CrBr_6^{3-}$		CrI_6^{3-}	
	CASSCF	NEVPT2	CASSCF	NEVPT2	CASSCF	NEVPT2	CASSCF	NEVPT2
$^4A_1[^4T_2]$	12,880 (87)	14,603 (26)	10,888 (30)	13,706 (−14)	9,874 (40)	13,323 (−36)	9,278 (75)	13,484 (−121)
$^4E[^4T_2]$	13,536 (−172)	15,227 (−28)	11,160 (−174)	13,921 (−13)	10,080 (−123)	13,467 (−2)	9,411 (−51)	13,558 (−59)
$^4E[^4T_1(1)]$	20,511 (−308)	22,097 (−649)	17,424 (−273)	20,577 (−801)	15,990 (−263)	20,064 (−889)	15,170 (−278)	20,150 (−990)
$^4A_2[^4T_1(1)]$	23,264 (360)	24,919 (−332)	19,483 (343)	22,901 (−441)	17,861 (279)	22,316 (−551)	16,920 (218)	22,295 (−622)
$^4A_2[^4T_1(2)]$	31,626 (35)	31,508 (227)	28,640 (36)	29,589 (301)	27,195 (31)	28,692 (350)	26,347 (27)	28,683 (428)
$^4E[^4T_1(2)]$	36,496 (−60)	36,357 (406)	31,753 (−49)	32,840 (513)	29,942 (−31)	31,694 (600)	28,797 (−18)	31,461 (697)
σ^c	211	353	195	446	166	513	150	585

[a] Given in brackets as deviations of the AILFT form the AI one: E(AILFT) – E(CASSCF) of E(AILFT) – E(NEVPTZ)

[b] Listed in square brackets in the first column

[c] Standard deviation in cm^{-1}

Table 7 Angular overlap parameters e_σ and e_π for Cr–X bonds and B from AILFT (LFModel 2) along with their values deduced from optical d–d transitions (denoted here as “exp.”) taken from literature[a]

	CrF_6^{3-}			$CrCl_6^{3-}$			$CrBr_6^{3-}$			CrI_6^{3-}		
	CASSCF	NEVPT2	Exp. [156, 192, 193]	CASSCF	NEVPT2	Exp. [156, 192, 193]	CASSCF	NEVPT2	Exp. [156, 192, 193]	CASSCF	NEVPT2	Exp. [156, 192, 193]
e_σ	6,868	8,272	7,400	4,730	6,430	5,500	4,223	6,114	4,900	3,855	5,976	4,300
e_π	1,755	2,375	1,700	715	1,270	900	596	1,142	600	469	1,023	600
$\Delta = 3e_\sigma - 4e_\pi$	13,584	15,316	15,400	11,330	14,210	12,900	10,285	13,774	12,300	9,689	13,836	10,500
B	1,092	829	–	1,050	752	–	1,052	730	–	1,030	713	–

[a] (NEVPT2 – CASSCF)/NEVPT2 (in %) for e_σ (e_π) are as follows: CrF_6^{3-}: 17(26); $CrCl_6^{3-}$: 26(43); $CrBr_6^{3-}$: 31(48); CrI_6^{3-}: 35(54)

$$e_\lambda \approx \langle d_\lambda|h|d_\lambda\rangle + \sum_\lambda \frac{\langle d_\lambda|h'|\chi_\lambda\rangle\langle\chi_\lambda|h'|d_\lambda\rangle}{\varepsilon_d - \varepsilon_\chi}; \quad \lambda = \sigma, \pi, \tag{82}$$

(h and h' – properly defined as one-electron operators, see [118] for a review). The first-order term (referred to as the static contribution) is ascribed to a direct electrostatic influence of the ligand, a term which is formally similar to electrostatic matrix element considered in crystal field theory. At the level of interpretation using AI results, we can associate this term with the CASSCF values for e_σ and e_π (e.g., e_σ(CASSCF) = 6,868 (F), 4,730 (Cl), 4,222 (Br), and 3,855 (I)). We see that this term diminishes with increasing metal–ligand distance and orbitals getting more and more diffuse in the given sequence. The second-order term, called dynamical contribution, is covalent in nature; simple overlap considerations (Wolfsberg–Helmholz approximation) might be used to rewrite it in the form of (83). With the AI data at hand, we can associate this terms with the e_σ(NEVPT2) − e_σ(CASSCF)

$$\Delta\varepsilon_{\text{antibonding}} = e_\lambda \approx \frac{S_{ML}^2(\lambda)\varepsilon_L^2}{\varepsilon_M - \varepsilon_L}; \quad \lambda = \sigma, \pi \tag{83}$$

difference which we find to increase from F (1,404 cm^{-1}) to Cl (1,700 cm^{-1}) to Br (1,891 cm^{-1}) to I (2,121 cm^{-1}). Due to the more diffuse ligand orbitals and favorable overlap in the given sequence, this term counteracts the increase of the metal–ligand distance. The overall effect of the two effects – the electrostatic and covalent – is apparently in favor of the first one. Arguments have been presented claiming that the static term is considerably smaller than the dynamic one, especially so for $\lambda = \pi$ rather than σ. This is not supported by our AI data; for the systems considered here, the term e_σ(CASSCF) is found to be dominant in all complexes and responsible for the trend in e_σ. However, the larger relative importance of dynamic correlation effects for π than for σ (leading to contributions of 26 (F), 44 (Cl), 48 (Br), and 54 (I) % of the total e_π, compared to 17, 26, 31, and 35 for e_σ) finds full support in our AI data. We should also note here that (82) is a one-electron analog of the rigorous (8), which carries essentially the same information being based on a many-electron formulation of the problem, however. What is different between (8) and (82), is that in the chosen basis and being based on canonical orbitals, the second term in (8) is solely governed by electrostatic forces described by *two-electron repulsion matrix elements rather than one-electron hopping integrals as the simple (82) implies.*

Finally, concluding this section we should note that the two-dimensional spectrochemical series, i.e., the order of the ligands with regard to their values of e_σ vs. e_π, subject to many analysis of spectroscopic results [118, 156] finds full support in our AI studies, both in the $\text{Cr}^{\text{III}}\text{X}_6{}^{3-}$($\text{d}^3$) and in the $\text{Cr}^{\text{IV}}\text{X}_4$ (d^2) series (see next section) of complexes (Fig. 7).

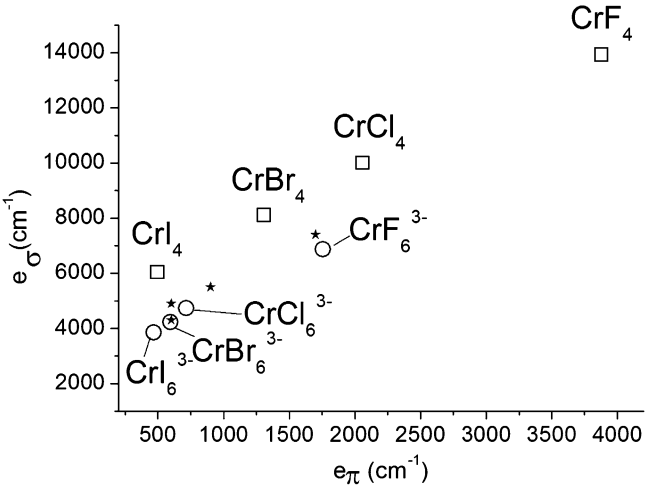

Fig. 7 Two-dimensional spectrochemical series for Cr–X (X = F, Cl, Br, I) tetrahedral and octahedral complexes from AILFT results based on SA-CASSCF calculations. Values reported from AOM interpretations of d–d absorption spectra of $Cr(NH_3)_5X^{2+}$ complexes are given by starts (adopted from D. W. Smith, Structure and Bonding, 35, 87–118 (1978), p. 92, Table 1)

6.2 Ligand Field Spectra and Multiplet Structures of CrX_4 (X = F, Cl, Br, I)

Tetrahedral CrX_4 and the analogous isoelectronic VX_4^- complexes (X = F, Cl, Br, I), with a $^3A_2(e^2)$ ground state on Cr^{IV} and V^{III} have attracted much attention as model complexes appropriate for DFT-based ligand field analysis [36, 157–159]. Imposing a D_{2d} distortion on the parent tetrahedron (D_{2d}: $\alpha = 120^\circ$, T_d: 109.47°, see Fig. 4), nonadditive and additive ligand field models have been used to derive 45 equations (corresponding to the same number of spin-unprojected Slater determinants) linear in the LF parameters to allow a least squares fit of these parameters to the corresponding DFT Kohn–Scham eigenvalues [157–159]. For each complex, a "data" reduction from three (Δ, $\Delta_{t_2} = e(e) - e(b_2)$, and $\Delta_e = e(a_1) - e(b_1)$, see Sect. 4) to two parameters (e_σ and e_π) was possible to afford values of e_σ and e_π reproducing nicely the two-dimensional spectrochemical series of the AOM σ and π-parameters [157–159]. Using the same training set of complexes, a general DFT-based LF model has been described [35, 36]. It is therefore interesting to compare these DFT-based results with CASSCF–NEVPT2 calculations on the same systems. In Tables 8 and 9, we list multiplet energies and parameter values for the T_d and D_{2d} distorted complexes. All four compounds with a CrX_4 composition are known. Solid CrF_4 is composed of $CrF_2F_{4/2}$ chains implying a sixfold coordination of Cr^{IV}, $CrCl_4$ is a solid build up from $CrCl_4$ tetrahedra, while tetrahedral species $CrBr_4$ and CrI_4 are only stable in the gas phase [160]. Out of all possible d–d transitions (Table 8), only two bands have been reported for

$CrCl_4$ [$CrBr_4$] and assigned to the $^3A_2 \rightarrow {}^3T_2$, 7,200 [10,000], and $^3A_2 \rightarrow {}^3T_1(1)$, 6,700 [11,000] cm^{-1} transitions [194]. They are listed in Table 8 and compared with the CASSCF(NEVPT2) energies of the same transitions. Due to covalency which is much more pronounced in $Cr^{IV}X_4$ than in $Cr^{III}X_6{}^{3-}$ (reflected also in much shorter Cr–X bond distances for CrX_4), agreement between NEVPT2 and experiment is poor. Differential dynamic correlation which largely overstabilizes (by as much as 6,000 cm^{-1} for $CrCl_4$ and $CrBr_4$), the π-type $^3A_2(e^2)$ ground state against the excited states is responsible for these results. As we shall see below, the situation changes completely when going to complexes such as $NiCl_4{}^{2-}$ and $CuCl_4{}^{2-}$ with σ-type ground states. We should also note here that due to error compensation and in difference to $CrX_6{}^{3-}$, CASSCF energies of the two transitions are closer to experiment than NEVPT2. For the mentioned reason, we focus the LF analysis of the AI data mostly on the CASSCF results. It was possible to consistently fit the full manifold of multiplet energies of tetrahedral CrX_4 complexes given by the CASSCF–NEVPT2 method using LFModel 1; 10Dq, B, and C values are included in Table 8. Standard deviations between AI and AILFT values of the energies of d–d transitions for CrX_4 are larger than for $CrX_6{}^{3-}$ and they increase from CASSCF to NEVPT2 and from F to I. Also, against expectations, values of B (C/B) increase(decrease) from CASSCF to NEVPT2. All this implies violations from the picture given by LFT in high-valent Cr^{IV} when ligand-to-metal charge transfer states approach localized d-multiplets (increasing metal ligand covalency). As for $CrX_6{}^{3-}$ $(10Dq)T_d$ values are found to decrease in the order F, Cl, Br, and I, however.

Turning now to LFModel 2, we consider D_{2d} distorted CrX_4 complexes. Focusing on tetragonal compressions ($\alpha = 120^\circ$) and restricting to the triplet state manifold, we consider the ground $^3A_2$ and the $^3T_2$ and the $^3T_1(1)$ and $^3T_1(2)$ excited states, splitting into ^3E, $^3B_2$ and ^3E, $^3A_2$ sublevels, respectively. Their energies are listed in Table 9. Using these splittings, the parameters e_σ, e_π, and B have been deduced from a least squares fit to the CASSCF results (included in Table 9). It is remarkable that AILFT values of e_σ and e_π are quite consistent with ones reported independently from ligand field DFT-based analysis [157–159] (included in square brackets in Table 9). They closely follow the two-dimensional spectrochemical series reported for $CrX_6{}^{3-}$(Fig. 6) but, owing to the shorter Cr–X distances, exceed considerably the corresponding values for $CrX_6{}^{3-}$ (Table 7).

6.3 s–d Mixing in Jahn–Teller Distorted $MCl_4{}^{2-}$ (M^{II} = Cu, Ni)

In Sects. 6.1 and 6.2, we considered complexes of Cr^{III} and Cr^{IV} with orbitally nondegenerate ground states. Small geometrical distortions of the complexes away from the cubic symmetry have been used to fix the AOM parameters from AI data. Here, we consider tetrahedral complexes $CuCl_4{}^{2-}$ and $NiCl_4{}^{2-}$ with $^2T_2$ and $^3T_1$ ground states. With one and two holes on the antibonding $t_2(d_{xz}, d_{yz}, d_{xy})$ orbital, these complexes are geometrically unstable. Tetragonal compression (for $CuCl_4{}^{2-}$)

Table 8 Energies of d–d transitions (ground state $^3A_2$ is taken as energy reference) of tetrahedral CrX_4 (X = F, Cl, Br, I) complexes[a] from CASSCF and NEVPT2 calculations and their values[b] resulting from a AILFT calculation (LFModel 1) with Δ = 10Dq, *B*, and *C* obtained from a best fit to the AI results

	CrF_4		$CrCl_4$		$CrBr_4$		CrI_4	
	CASSCF	NEVPT2	CASSCF	NEVPT2	CASSCF	NEVPT2	CASSCF	NEVPT2
$^3T_2$	11,459 (−382)	14,455 (−906)	9,066 (−484) [7,200]^c	15,015 (−1,880) [7,200]^c	8,057 (−448) [6,700]^c	16,226 (−2,719) [6,700]^c	6,606 (−262)	19,836 (−4,845)
$^3T_1(1)$	18,301 (−232)	22,002 (−876)	14,936 (−668) [10,000]^c	22,286 (−1,709) [10,000]^c	13,635 (−865) [11,000]^c	23,690 (−2,441) [11,000]^c	11,955 (−1,183)	27,424 (−4,033)
$^3T_1(2)$	30,361 (80)	31,909 (1,484)	25,129 (312)	30,458 (2,188)	23,310 (392)	31,158 (2,680)	20,884 (497)	34,219 (2,772)
$^1E(1)$	15,226 (−304)	13,408 (−798)	13,825 (−902)	12,294 (−1,593)	13,631 (−1,172)	12,288 (−2,017)	13,404 (−1,638)	12,492 (−2,716)
$^1A_1(1)$	25,663 (−540)	23,707 (−1,408)	22,958 (−1,232)	22,018 (−2,396)	22,403 (−1,572)	22,342 (−3,126)	21,676 (−2,159)	23,585 (−4,824)
$^1T_2(1)$	26,096 (−526)	27,021 (−1,178)	21,696 (−624)	26,015 (−2,500)	20,168 (−546)	26,852 (−3,419)	17,961 (−309)	29,836 (−5,421)
$^1T_1$	30,225 (374)	30,725 (−505)	25,243 (542)	28,664 (−773)	23,625 (675)	29,233 (−1,172)	21,154 (1,101)	31,813 (−2,534)
$^1E(2)$	38,060 (1,085)	41,156 (200)	31,266 (866)	38,610 (21)	28,986 (788)	38,734 (319)	25,995 (625)	40,860 (731)
$^1T_2(2)$	40,414 (−840)	42,588 (−316)	33,191 (−626)	39,548 (−596)	30,795 (−576)	39,906 (−508)	27,684 (−607)	42,095 (−152)
$^1A_1(2)$	64,245 (262)	59,720 (1,603)	53,574 (662)	51,779 (2,843)	50,510 (795)	50,168 (3,700)	46,302 (972)	48,257 (6,714)
σ^d	544	1,072	733	1,866	854	2,480	1,099	3,994
Δ = 10Dq	11,076 (10)	13,548 (10)	8,581 (10)	13,135 (10)	7,608 (10)	13,507 (10)	6,344 (10)	14,991 (10)
B	1,019 (3)	925 (3)	931 (2)	921 (3)	910 (2)	971 (3)	875 (2)	1,027 (3)
C	3,649 (9)	2,786 (10)	3,016 (9)	1,850 (10)	2,887 (8)	1,450 (10)	2,706 (8)	980 (10)
C/*B*	3.58	3.01	3.24	2.01	3.17	1.49	3.09	1.05

[a] Calculated using Cr–X bond distances *R* from a DFT geometry optimization using a PBE functional: *R* (in Å)1.717 (Cr–F), 2.111 (Cr–Cl), 2.262 (Cr–Br), and 2.488 (Cr–I)

[b] Given in brackets as deviations of the AILFT value from the AI one: *E*(AILFT) − *E*(CASSCF) or *E*(AILFT) − *E*(NEVPT2)

[c] Values from experiment reported by Studer [186]

[d] Standard deviation in cm^{-1}

Table 9 CASSCF energies of triplet states of D_{2d} distorted CrX_4 complexes[a,b] used to deduce AOM parameters e_σ and e_π for the Cr–X bond and B and their AILFT values[c]

	CrF_4	$CrCl_4$	$CrBr_4$	CrI_4
$^3B_1[^3A_2]$	0	0	0	0
$^3E[^3T_2]$	9,570 (−211)	7,727 (81)	6,636 (224)	5,192 (606)
$^3B_2[^3T_2]$	14,625 (159)	12,292 (−41)	10,936 (−191)	9,546 (−471)
$^3A_2[^3T_1(1)]$	17,685 (89)	14,513 (122)	12,998 (176)	11,374 (161)
$^3E[^3T_1(1)]$	16,959 (−36)	14,753 (−17)	12,982 (−16)	10,992 (9)
$^3E[^3T_1(2)]$	30,973 (−41)	26,483 (−123)	24,076 (−139)	21,945 (−239)
$^3A_2[^3T_1(2)]$	31,772 (0)	26,870 (59)	24,422 (72)	22,055 (180)
σ	116	84	154	343
e_σ	13,931 ± 161 [12,970 ± 15][d]	10,003 ± 161 [8,190 ± 18][d]	8,109 ± 159 [7,060 ± 19][d]	6,037 ± 146
e_π	3,878 ± 114 [4,020 ± 11][d]	2,058 ± 115 [2,070 ± 13][d]	1,306 ± 114 [1,680 ± 14][d]	495 ± 106
e_π/e_σ	0.28[0.31][d]	0.20[0.25][d]	0.16[0.24]	0.08
B	982 ± 4	887 ± 4	850 ± 4	838 ± 3

[a] $\theta = 60^\circ$ (θ – the S_4–Cr–X angle, for a tetrahedron without distortions $\theta = 54.74^\circ$)
[b] Tetrahedral parent terms are given in square brackets in the first column
[c] Given in brackets as deviations of the AILFT value from the AI one: $E(\text{AILFT}) - E(\text{CASSCF})$
[d] DFT results for e_σ, e_π and e_π/e_σ taken from [157] are listed in square brackets

or elongation (for $NiCl_4^{2-}$) along the one of the three S_4 axes of the tetrahedron leads to splittings of the t_2 and e orbitals into $b_2 + e$ und $a_1 + b_1$ and correspondingly changes the $^2T_2$ and $^3T_1$ states to lead to nondegenerate $^2B_2(a_1{}^2b_1{}^2e^4b_2{}^1)$ and $^3A_2(a_1{}^2b_1{}^2b_2{}^2e^2)$ ground states and doubly degenerate $^2E(a_1{}^2b_1{}^2e^3b_2{}^2)$ and ^3E $(a_1{}^2b_1{}^2e^3b_2{}^1)$ excited states (Jahn–Teller effect). The stabilization energy (Jahn–Teller stabilization energy E_{JT}) is the driving force for possible static distortions (static Jahn–Teller effect). In Fig. 8, we illustrate this by plotting NEVPT2 energies for the $^2B_2(CuCl_4^{2-})$ and $^3A_2(NiCl_4^{2-})$ ground states vs. the distortion given by the angle α (Fig. 4), where for the sake of comparison, the corresponding curves calculated using DFT (PBE functional) are also included. Well-developed minima at angles $\alpha = 127\ (141)^\circ$ and stabilization energies of 1,082 (2,303) cm^{-1} for $CuCl_4^{2-}$, NEVPT2 (DFT), and $\alpha = 103.5\ (98.5)^\circ$ and 225 (819) cm^{-1} for $NiCl_4^{2-}$, respectively, are obtained. The NEVPT2 geometry of $CuCl_4^{2-}$ with 127.4° is very close to the X-ray structure of $CuCl_4^{2-}$ ($\alpha = 129.2 \pm 2^\circ$) in Cs_2CuCl_4 [161]. The clear tendency of DFT toward larger distortions and energy stabilizations when compared with NEVPT2 emerges from these results. We implicitly stress here that the dynamic correlation accounted for by both NEVPT2 and DFT is the sole cause for the distortion; for $NiCl_4^{2-}$ CASSCF results did not show up in any JT-stabilization, while $CuCl_4^{2-}$ did distort but with a very small stabilization energy ($\alpha = 120^\circ$, $E_{JT} = 201\ cm^{-1}$). It is interesting to note that $CuCl_4^{2-}$ distorts stronger than $NiCl_4^{2-}$. It has been shown for tetrahedral complexes of Ni^{II} that configurational mixing between the $^3T_1(1)$ ground state

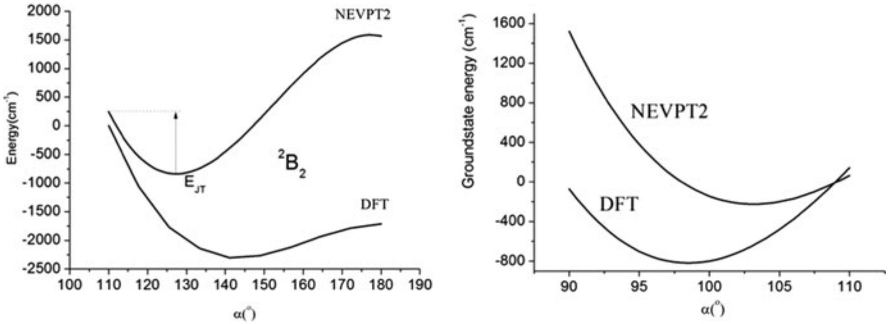

Fig. 8 Dependence of the ground state energy of $CuCl_4^{2-}$ (*left*) and $NiCl_4^{2-}$ (*right*) on the angle α using NEVPT2 in comparison with DFT (PBE functional). The Jahn–Teller stabilization energy E_{JT} is indicated. Numerical values for the minima of the curves are: $CuCl_4^{2-}$: $\alpha = 127^{\circ}$, $E_{JT} = 1{,}082\ \mathrm{cm}^{-1}$ (NEVPT2), $\alpha = 141^{\circ}$, $E_{JT} = 2{,}303\ \mathrm{cm}^{-1}$; $NiCl_4^{2-}$: $\alpha = 103^{\circ}$, $E_{JT} = 225\ \mathrm{cm}^{-1}$ (NEVPT2), $\alpha = 98.5^{\circ}$, $E_{JT} = 819\ \mathrm{cm}^{-1}$. The plots have been constructed from energies calculated at discrete values of α and the points in-between have been interpolated using a third-order polynomial (bond distances used throughout have been fixed at values of 2.25 Å for Cu–Cl and 2.267 Å for Ni–Cl)

with the $^3T_1(2)$ excited state having an opposite sign of the distortion is responsible for Jahn–Teller activity being weaker for the Ni(II) than for Cu(II) [162].

The plots of Fig. 8 pertain to isolated negative species where electrostatic perturbations from surrounding counter ions have been accounted for by a polarizable solvent continuum (COSMO). Calculations using periodic DFT and model clusters where a second coordination shell of $CuCl_4^{2-}$ was explicitly taken into account did show that energy minima positions can be widely tuned in geometry and energy by counter ions and H-bonds [163]. Thus, it was possible to synthesize and spectroscopically characterize as much as 62 complexes of $CuCl_4^{2-}$ covering the whole range of geometries from tetrahedral to square planar [164]. Energies of d–d transitions (NEVPT2 results) of $CuCl_4^{2-}$ in dependence on the angle α are plotted in Fig. 9. These energies shift to higher values starting with a small value of 10Dq (T_d) and approaching the square planar structure. Therefore, d–d spectra are sensitive probe for changes in geometry. d–d Transition energies from AI CASSCF, NEVPT2 results and from experiment for two representative examples – distorted tetrahedral [165] and square planar [166] $CuCl_4^{2-}$ – are listed in Table 10. Comparing CASSCF with NEVPT2 results, we can deduce, similar to CrX_6^{3-} (vide supra), that dynamic correlation brought in by NEVPT2 plays an important role. At the same time, agreement with experiment is greatly improved when comparing with the CASSCF results. For the same reason, one can find LFDFT values for the energies of the d–d transition (included in Table 10) close to the NEVPT2 results. Energy expressions given by the AOM for the energies of the d–d transitions (84)

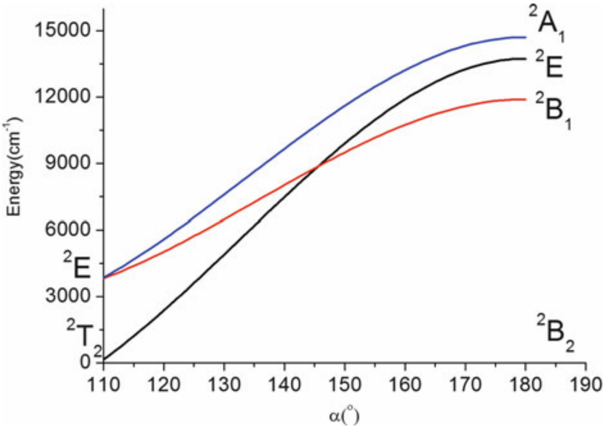

Fig. 9 Dependences of the energies of the d–d transitions (NEVPT2 results) for $CuCl_4^{2-}$ on the angle α (Fig. 4) describing the tetrahedral to square planar interconversion

Table 10 AI and experimental energies (in cm^{-1}) of d–d transition of pseudotetrahedral ($\alpha = 127.4^\circ$) and square planar $CuCl_4^{2-}$ ($\alpha = 180^\circ$)

	$\alpha = 127.4^\circ$				$\alpha = 180^\circ$			
	CASSCF	NEVPT2	LFDFT [163]	Exp. [165]	CASSCF	NEVPT2	LFDFT [163]	Exp. [166]
$^2B_2 \rightarrow {}^2E$	2,885	4,200	4,438	5,200	9,380	13,728	13,231	14,450
$^2B_2 \rightarrow {}^2B_1$	3,770	6,097	7,435	7,900	7,452	11,897	13,252	12,500
$^2B_2 \rightarrow {}^2A_1$	4,702	7,077	7,671	9,050	10,117	14,700	16,391	17,000

have been used to analyze the AI data (Fig. 9). In D_{2d} symmetry, the d_{z2}, d_{xy} and d_{yz}, d_{xz} orbitals transform as a_1, b_2, and e and can mix with

$$\Delta E(^2B_2 \rightarrow {}^2E) = 3\sin^2(\alpha/2)[1 - 3\cos^2(\alpha/2)]e_\sigma + [1 - 3\cos^2\alpha - \cos^2(\alpha/2)]e_\pi,$$

$$\Delta E(^2B_2 \rightarrow {}^2B_1) = 3\sin^4(\alpha/2)e_\sigma + [\sin^2\alpha - 4\sin^2(\alpha/2)]e_\pi - 13.3\sin^4(\alpha/2)\cos^2(\alpha/2)e_{pd\sigma},$$

$$\Delta E(^2B_2 \rightarrow {}^2A_1) = 2[6\sin^2(\alpha/2) - 3\sin^4(\alpha/2) - 2]e_\sigma - 2\sin^2\alpha.e_\pi + 4[2 - 3\sin^2(\alpha/2)]^2e_{ds} - 13.3\sin^4(\alpha/2)\cos^2(\alpha/2)e_{pd\sigma}, \quad (84)$$

4s, $4p_z$, and $4p_x$,p_y orbitals, respectively. Therefore, two new parameters, e_{sd} and e_{pd} are introduced to account for such mixings (84). In D_{4h} ($\alpha = 180^\circ$), e_{pd} vanishes for symmetry reason and we obtain:

Table 11 AILFT parameters[a] for $CuCl_4^{2-}$ and $NiCl_4^{2-}$ (additive LFModel 2, AOM)[b]

	e_σ	e_π	e_{sd}	e_{pd}	σ
$NiCl_4^{2-}$	4,877 [4,980]	666 [1,594]	1,090 [3,402]	927 [−]	94 [−]
$CuCl_4^{2-}$	4,832 [4,259]	663 [−134]	1,234 [1,708]	879 [739]	206 [143]

[a] Computed from a least squares fit to the energies of the d–d transitions from NEVPT2 calculation; data set for $CuCl_4^{2-}$ $\alpha(^\circ)$, $\Delta_e(^2B_2 \rightarrow {}^2E)$, $\Delta_{b_1}(^2B_2 \rightarrow {}^2B_1)$, $\Delta_{a_1}(^2B_2 \rightarrow {}^2A_1)$ (energies are given in cm^{-1}): 112, 549, 4,028, 4,161; 120, 2,418, 5,059, 5,627; 130, 4,907, 6,490, 7,619; 138, 6,971, 7,710, 9,231; 140, 7,466, 8,006, 9,635; 150, 9,887, 9,486, 11,588; 160, 11,932, 10,768, 13,258; 180, 13,728, 11,897, 14,700; data set for $NiCl_4^{2-}$, the angle $\alpha(^\circ)$, and parameters Δ_e, Δ_{b_1}, Δ_{a_1} (in cm^{-1}) deduced from a fit of the triplet state energies using LFModel 1 as follows: 90, −3,376, 1,585, 671; 92, −3,075, 1,754, 909; 95, −2,604, 2,001, 1,274; 98, −2,113, 2,256, 1,659; 99, −1,944, 2,346, 1,794; 100, −1,773, 2,434, 1,929; 103.5, −1,207, 2,929, 2,595; 107, −493, 3,098, 2,952; 109, −100, 3,306, 3,270

[b] Data from LFDFT taken from [163] for $CuCl_4^{2-}$ and [169] for $NiCl_4^{2-}$ are listed in square brackets

$$\begin{aligned} \Delta E(^2B_{2g} \rightarrow {}^2E_g) &= 3e_\sigma - 2e_\pi \\ \Delta E(^2B_{2g} \rightarrow {}^2B_{1g}) &= 3e_\sigma - 4e_\pi \\ \Delta E(^2B_{2g} \rightarrow {}^2A_{1g}) &= 2e_\sigma + 4e_{ds}. \end{aligned} \tag{85}$$

An excellent fit to the AI data base including geometries with angles α ranging from 112° to 180° varying in steps of 10° (Fig. 9) with an unique set of AOM parameters was possible (Table 11). These parameters compare well with values adjusted directly to spectroscopic results ($e_\sigma = 5{,}120\ cm^{-1}$, $e_\pi = 910\ cm^{-1}$, $e_{sd} = 930\ cm^{-1}$, $e_{pd} = -20\ cm^{-1}$, extracted from spectroscopic data for $CuCl_4^{2-}$ complexes with α angles ranging between 129.2° and 146.6° [163]) and also with parameters from a DFT-based ligand field study (Table 11) [163]. In being able to reproduce energies of d–d transitions of $CuCl_4^{2-}$ with different geometries but with the same ligand, the transferability of parameters postulated for the AOM finds strong support by AI theory. AI results also support the important role that s–d mixing plays in square planar complexes. Due to such a mixing d_{z2} orbital, which is otherwise a σ-antibonding becomes nearly nonbonding, thus placing $^2B_2 \rightarrow {}^2A_1$ transitions in d–d spectra of square planar complexes of Cu^{2+} highest in energy (Fig. 9) [156, 167].

The electronic spectrum of $NiCl_4^{2-}$ (Fig. 10) shows a mostly cubic appearance with spin-allowed transitions from the $^3T_1$ ground state into the $^3T_2$, $^3A_2$, and $^3T_1$ excited states and band maxima at about 4,000, 6,900, and 14,500 cm^{-1}, respectively, with low symmetry splittings seen in the $^3T_2$ and $^3T_1$ bands in agreement with the tiny D_{2d} distortions ($\alpha = 103.5^\circ$, Figs. 8 and 12) predicted by theory. A spectrum of $NiCl_4^{2-}$ (as a bis(tetraethylammonium salt)) in high resolution [168] displays a very rich fine structure with electronic and vibronic origins and vibronic side bands that deserve a separate analysis. Focusing on the geometry corresponding to the energy minimum in Fig. 8 ($\alpha = 103.5^\circ$) in Table 12, we list

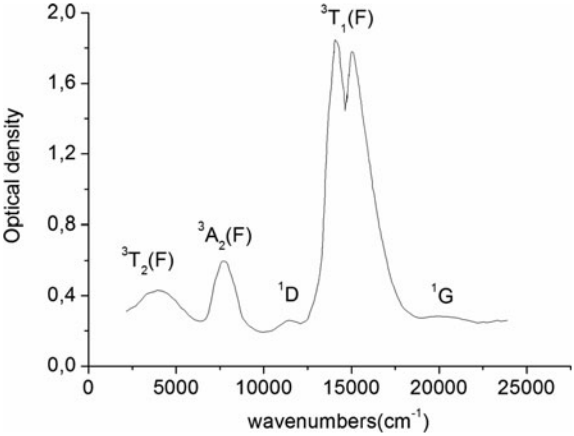

Fig. 10 Electronic spectrum of tetrahedral NiCl$_4^{2-}$ with effects of low-symmetry due to a weak $^3T_1 \otimes \varepsilon$ Jahn–Teller coupling (adopted from [190] after digitalization)

Table 12 AI (CASSCF and NEVPT2) energies of d–d transitions of NiCl$_4^{2-}$ (in cm^{-1}), their AILFT (nonadditive LF Model 1) values adjusted to the NEVPT2 results[a] and experimentally reported ones

$^3A_2[^3T_1(1)]$ →	CASSCF	NEVPT2	AILFT	Exp.
→$^3E[^3T_1(1)]$	538	834	846	–
→$^3E[^3T_2]$	2,057	3,233	3,224	3,972
→$^3B_2[^3T_2]$	2,685	4,189	4,180	4,442
→$^3B_1[^3A_2]$	4,549	7,101	7,109	6,865
→$^3E[^3T_1(2)]$	20,249	18,178	18,180	14,250
→$^3A_2[^3T_1(2)]$	21,068	19,279	19,277	15,240
→$^1B_2[^1T_2(1)]$	16,388	14,561	15,317	11,694
→$^1E[^1T_2(1)]$	16,625	14,991	15,841	12,222
→$^1B_1[^1E(1)]$	16,811	15,044	15,907	12,469
→$^1A_1[^1E(1)]$	17,637	16,327	17,166	–
→$^1E[^1T_2(2)]$	25,236	23,625	23,252	18,184
→$^1B_2[^1T_2(2)]$	25,260	23,821	23,538	–
→$^1E[^1T_1]$	26,050	24,934	24,457	19,620
→$^1A_1[^1E(2)]$	26,364	25,536	25,018	22,152
→$^1B_1[^1E(2)]$	26,623	26,163	25,877	–
→$^1A_2[^1T_1]$	27,206	26,460	25,902	–
→$^1A_1[^1A_1(1)]$	27,438	26,880	26,450	–
→$^1A_1[^1A_1(2)]$	61,667	53,446	57,311	–

[a] Best fit parameters and standard deviations are given in Table 13

the full manifold of triplet and singlet states of NiCl$_4^{2-}$ from CASSCF and NEVPT2 AI calculations along with their values from spectra in high resolution [168]. Comparison between CASSCF and NEVPT2 results shows again substantial contribution from dynamical correlation which in difference to CASSCF improves agreement with experiment. Dynamical correlation also improves (lowers) the energies of the spin-forbidden transitions. However, NEVPT2 energies still remain by 3,000–4,000 cm^{-1} higher than the experimental ones. Utilizing the nonadditive

Fig. 11 Symmetry-based parameterization (nonadditive ligand field model, LFModel 1) for tetragonally distorted $CuCl_4^{2-}(d^9)$ and $NiCl_4^{2-}(d^8)$, the parameters should be taken with a sign minus when going to orbitals (d^1); term notations pertain to $CuCl_4^{2-}(d^9)$

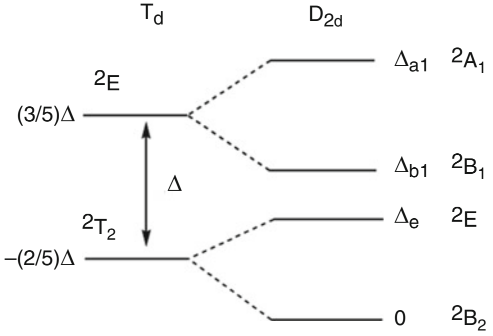

Table 13 AILFT parameters (in cm^{-1}) for $NiCl_4^{2-}$ fitting the NEVPT2 results; nonadditive model (LFModel 1) fit to triplet states[a]

Δ_{a_1}	Δ_{b_1}	Δ_e	B	σ[b]
2,595	2,929	−1,207	1,039	8

[a] $C = 4{,}460\ cm^{-1}$; obtained adopting the given parameters, and adjusting C to the energies of spin-forbidden transitions, $\sigma = 602\ cm^{-1}$

[b] Standard deviations NEVPT2–AILFT values

LFModel 1 with parameters $\Delta_{a_1}, \Delta_{b_1}$, and Δ_e (see Fig. 11 for their definition), we have analyzed the NEVPT2 results. Within this model, the energies of the triplet states are given in (86). A least squares fit to the energies of the spin-allowed transition resulted in $\Delta_{a_1}, \Delta_{b_1}$, Δ_e, and B values listed in Table 13.

$$\begin{array}{l}
\begin{array}{ccc}
|^3E[^3T_2(t_2e)]\rangle & |^3E[^3T_1(t_2e)]\rangle & |^3E[^3T_1(t_2^2)]\rangle \\
\end{array} \\
\left[\begin{array}{ccc}
-8B+\Delta_e+(3/4)\Delta_{b_1}+(1/4)\Delta_{a_1} & (\sqrt{3}/4)(\Delta_{a_1}-\Delta_{b_1}) & 0 \\
(\sqrt{3}/4)(\Delta_{a_1}-\Delta_{b_1}) & 4B+\Delta_e+(3/4)\Delta_{a_1}+(1/4)\Delta_{b_1} & 6B \\
0 & 6B & -5B+\Delta_e
\end{array}\right], \\
\begin{array}{cc}
|^3A_2[^3T_1(t_2e)]\rangle & |^3A_2[^3T_1(t_2^2)]\rangle,
\end{array} \\
\left[\begin{array}{cc}
4B+\Delta_{b_1} & 6B \\
6B & -5B+2\Delta_e
\end{array}\right], \\
|^3B_2[^3T_2(t_2e)]\rangle : -8B+\Delta_{a_1}, |^3B_1[^3A_2(e^2)]\rangle -8B+\Delta_{a_1}+\Delta_{b_1}.
\end{array} \tag{86}$$

From the former three parameters, we deduce orbital order of energies $e(t_2) < b_2(t_2) < a_1(e) < b_1(e)$ (tetrahedral parentages are given in parenthesis). Notice that splittings of the t_2 and e orbitals for $NiCl_4^{2-}$ have just the opposite sign of $CuCl_4^{2-}$. The value of B resulting from the fit ($B = 1{,}039\ cm^{-1}$) is nearly that of the gaseous ion Ni^{2+} ($B = 1{,}084\ cm^{-1}$ [12]) and thus distinctly larger than the one resulting from a direct fit to the observed d–d bands ($B = 725\ cm^{-1}$, $C = 3{,}262\ cm^{-1}$,

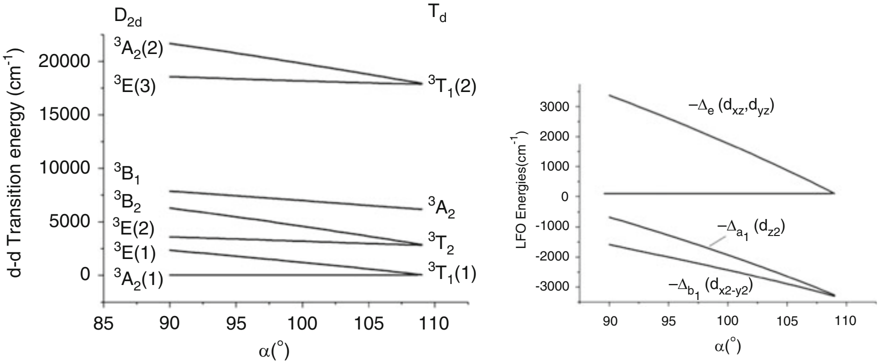

Fig. 12 Dependences on the angle α of energies of spin-allowed d–d transitions in $NiCl_4^{2-}$ (NEVPT2 results, *left*) and energies of ligand field orbitals resulting from a least squares fit to the NEVPT2 results using LFModel 1 (*right*); numerical data base for the calculations: *Right*: $\alpha(^{\circ})$, $^3A_2 \rightarrow {}^3E(1)$ (cm^{-1}), $^3A_2 \rightarrow {}^3E(2)$ (cm^{-1}), $^3A_2 \rightarrow {}^3B_2$ (cm^{-1}), $^3A_2 \rightarrow {}^3B_1$ (cm^{-1}), $^3A_2 \rightarrow {}^3E(3)$ (cm^{-1}), $^3A_2 \rightarrow {}^3A_2$ (cm^{-1}): 109, 69, 2,823, 2,882, 6,176, 17,877, 17,965; 107, 338, 2,900, 3,271, 6,356, 17,939, 18,382; 103.5, 786, 3,036, 3,936, 6,673, 18,059, 19,104; 100, 1,220, 3,192, 4,585, 6,995, 18,190, 19,813; 99, 1,333, 3,233, 4,766, 7,084, 18,226, 20,011; 98, 1,454, 3,273, 4,944, 7,174, 18,265, 20,206; 95, 1,799, 3,397, 5,467, 7,442, 18,383, 20,780; 92, 2,138, 3,521, 5,973, 7,708, 18,504, 21,334; 90, 2,348, 3,593, 6,300, 7,868, 18,583, 21,690; *Left*: numerical values for the parameters $\Delta_e, \Delta_{b_1}, \Delta_{a_1}$ are listed in Table 11

10Dq = 3,850 cm^{-1}, room temperature data for Ni^{2+}-doped Cs_2ZnCl_4). This is a drawback shared by all post-HF methods (however, with $B = 521$ cm^{-1} for $NiCl_4^{2-}$ [169], LFDFT largely underestimates this energy). As illustrated in Fig. 12 (left) and similar to $CuCl_4^{2-}$ (Fig. 9), d–d transition energies of $NiCl_4^{2-}$ are sensitive probe for the molecular geometry which may be used for structure–spectra correlation. The essential information of the dependence between spectra and structure is hidden in the parameters $\Delta_{a_1}, \Delta_{b_1}$, and Δ_e which may be used to analyze the Ni–Cl bond since the structure (here α) is known. Parameters $\Delta_{a_1}, \Delta_{b_1}$, and Δ_e obtained from least squares fit to the electronic transitions in Fig. 12 (left) are depicted in Fig. 12 (right). They can be analyzed by applying the AOM expressions (84) in the same way as this was done for $CuCl_4^{2-}$. Again a unique set of parameters is achieved (Table 11) reproducing consistently all d–d transitions in the entire range of α values (Fig. 12 (left)) illustrating once more parameter transferability. Not unexpectedly for Ni(II) and Cu(II) being neighbor ions in the periodic table, the AOM parameter values for the two complexes are very close.

6.4 Anisotropic Bonding and Magnetic Anisotropy in Chelate Complexes

Frontier orbitals of chelating ligands are frequently part of an extended π-network. In such complexes, perturbations from *all bonding and antibonding delocalized*

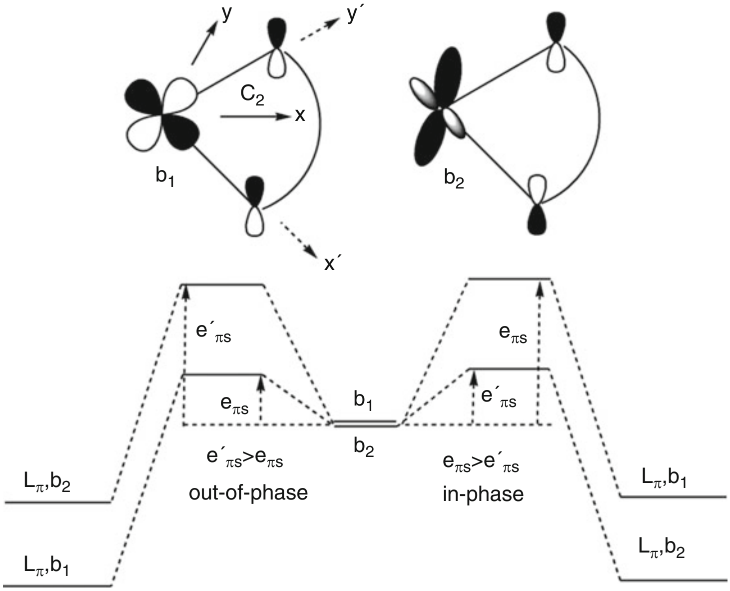

Fig. 13 Splitting of the d-orbitals d_{xz} and d_{yz} depending on the topology of ligand frontier orbitals, *left* HOMO/LUMO out-of-phase/in-phase (out-of-phase coupling), *right* HOMO/LUMO in-phase/out-of-phase (in-phase coupling); the z-axis is taken perpendicular to the chelate plane

ligand π-MOs, rather than separate and independent ligator functions governs the ligand field splittings. This effect was predicted by Orgel [170] and later parameterized and included in the AOM by Ceulemans et al. [171–173] Manifestation and analysis of the effect in d–d spectra of 3d chelate complexes of Cr(III) have been reported [174–175, 179]. The effect is most simply illustrated considering the interaction between a transition metal (M) chelated by a bis-bidentate ligand (L-L). We restrict to frontier HOMO–LUMO orbitals of π-type (Fig. 13). With coordinate choice of Fig. 13 and the C_{2v} symmetry of the complex, the $d_{xz}(b_1)$ and $d_{yz}(b_2)$ orbitals are perturbed solely by the in-phase and out-of-phase ligand π-orbitals of the same symmetry. The LF matrix $V_{\pi s}$ in this representation is diagonal (87). $e_{\pi s}(e'_{\pi s})$ are effective energies reflecting *the overall effect of all in-phase (out-of-phase) donor (occupied) and acceptor (empty) ligand π orbitals*. With π-donor ligands (as is usually the case) and restricting to the

$$\begin{array}{cc} & |d_{b1}\rangle \quad |d_{b2}\rangle \\ V_{\pi s} = & \begin{bmatrix} e_{\pi s} & 0 \\ 0 & e'_{\pi s} \end{bmatrix}. \end{array} \tag{87}$$

HOMO, the splitting pattern of the b_1 and b_2 metal centered MOs is solely governed by the ligand topology (i.e., the number of ligand atoms involved in π-conjugate system). Thus with ligands possessing in-phase (ψ)[out-of-phase (χ)]

HOMOs, an energy splitting pattern with $e_{\pi s} > e'_{\pi s}$ ($e_{\pi s} < e'_{\pi s}$) is derived (Fig. 13). Accounting for the energy effect from the LUMOs does not qualitatively alter the results; since LUMOs usually have opposite phases compared to the HOMOs, the energetic effect they are expected to cause even increases the spitting; e.g., ligands with HOMOs/LUMOs of ψ/χ type would lead to positive (negative) $e_{\pi s}(e'_{\pi s})$ parameters and therefore to an increase of the difference $e_{\pi s} - e'_{\pi s}$(and vice versa). In the general case, no simple relation between the parameters $e_{\pi s}$ and $e'_{\pi s}$ and ligand frontier orbital π-orbitals can be given. In the following, we will regard these parameters as effective ones, and using representative examples we will try deduce their values from theory and, independently, from experiment and compare the results.

6.4.1 Planar Bis-Chelate Complexes of Ni(II)

Here, we consider bis-didentate complexes $Ni(Et_2dtc)_2$ and $Ni(DPM)_2$ representing $Ni^{II}S_4$ and $Ni^{II}O_4$ cores and structures depicted in Fig. 14a (Et_2dtc^- and DPM^- are abbreviations for *N*,*N*-diethyldithiocarbamato and 2,2,6,6-tetramethylheptane-3,5-dionato, i.e., derivatives of the well-known dithiocarbamato (dtc) and acetylacetonato (acac) anions). Based on the definitions given by Figs. 13 and 15, the latter illustrating the frontier HOMO and LUMO orbitals, we can assign the two ligands as being, correspondingly of out-of-phase and in-phase type. With two holes in the antibonding $b_{1g}(d_{xy})$ orbital both complexes are diamagnetic (^1A_g ground state, symmetry assignments follow notations for the irreducible representations of the idealized D_{2h} symmetry point group). Both complexes posses center of symmetry and week d–d absorption in the visible spectral range ($Ni(Et_2dtc)_2$ [176], Ni $(DPM)_2$ [177]). Focusing on $Ni(Et_2dtc)_2$, polarized d–d spectra along with vibronic selection rules based on a β_{2u} intensity promoting mode (implying movements of the two entire *S–S* chelate rings against each other) have been used to *tentatively* assign the band maxima of the d–d bands to transitions from the ^1A_g ground state into $^1B_{2g}(b_{3g}$, $d_{yz} \rightarrow b_{1g})$ 17,000 cm^{-1}, $^1B_{1g}(a_g \rightarrow b_{1g})$ 15,900 cm^{-1}, $^1B_3(b_{2g}$, $d_{xz} \rightarrow b_{1g})$ 19,000 cm^{-1}, and $^1B_{1g}(a_g \rightarrow b_{1g})$ 21,000 cm^{-1} excited states with electron excitations as indicated (the two a_g orbitals are mixtures of d_{z2}–d_{x2-y2} orbitals with the higher(lower) in energy dominated by d_{z2} and d_{x2-y2}, respectively) [176].[1] NEVPT2 results for multiplets with energies lower that 30,000 cm^{-1} are listed in Table 14 (states at higher energy are omitted because of their overlap with S → Ni charge transfer states starting already with 23,000 cm^{-1} [176]). With exception of the assignment of the lowest two transitions (NEVPT2 yields a reverse order for the lowest two excited singlet states), the assignment of [176] is supported by the NEVPT2 results. There is also a nice numerical agreement between computational

---

[1] A different assignment based on transition energies of 15,900 cm^{-1} ($d_{z2} \rightarrow d_{xy}$), 16,300 ($d_{x2-y2} \rightarrow d_{xy}$), 16,400 ($d_{xz} \rightarrow d_{xy}$), and 18,100 ($d_{yz} \rightarrow d_{xy}$) (given by the extended Hückel model) has been proposed in [177] (however notice the energy order of d_{xz} and d_{yz} being the same as the one provided by our AI data).

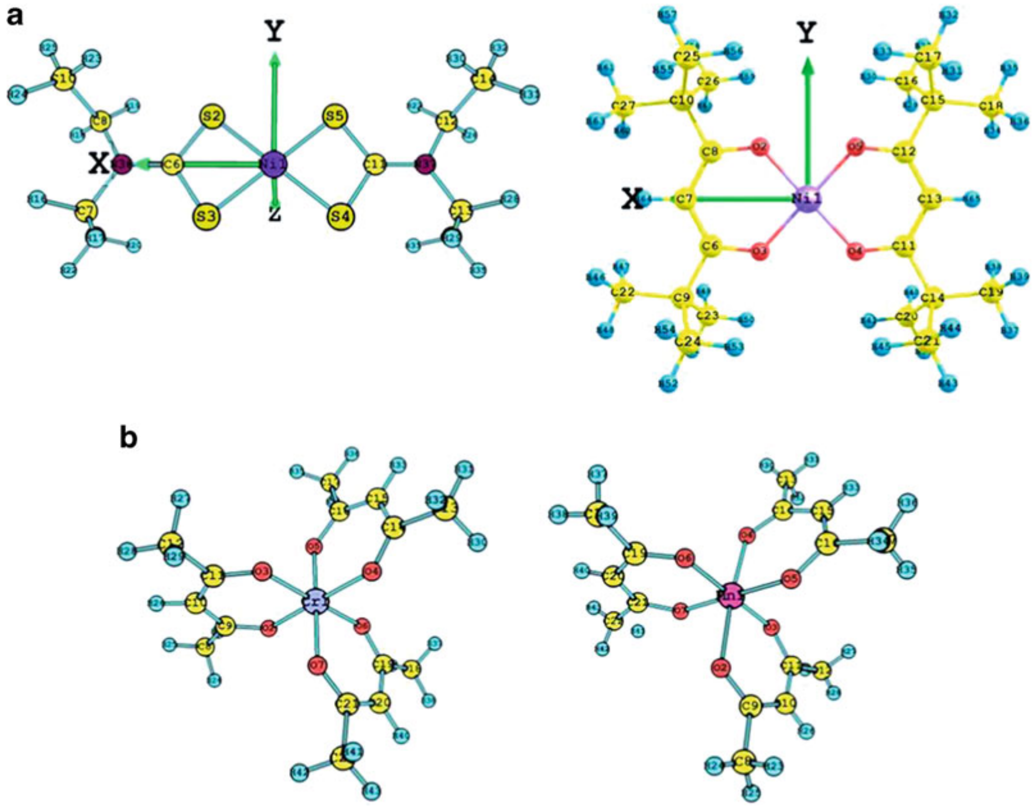

Fig. 14 Bis-chelate complexes of Ni^{II} (**a**) and tris-chelate complexes of $M^{III}(acac)_3$ ($M^{III} = Cr^{III}$ and Mn^{III}) (**b**) used in the AILFT analysis of the effect of π-orbital phase coupling (Orgel effect) on their electronic spectra and magnetic anisotropy; Et_2dtc, DPM, and acac – stand for the anionic forms of the following ligands: *Et_2dtc* diethyldithiocarbamate, *DPM* 2,2,6,6,-tetramethylheptane-3,5-dionato, *acac* pentane-2,4 dionato. Calculations have been done on structures optimized using DFT leading to the following selected bond distances and bond angles: $Ni(Et_2dtc)_2$: Ni–S_2, Ni–S_4: 2.211 Å, Ni–S_3, Ni–S_5: 2.209 Å, S_2NiS_3, S_4NiS_5: 79°; C–N: 1.341 Å; Ni–S–C 85.7°; $Ni(DPM)_2$: Ni–O: 1.847 Å, O_2NiO_3, O_4NiO_5: 95.1°; NiOC 126.1°; $Cr(acac)_3$: Cr–O 1.964 Å, OCrO bite angles $\beta = 91.1°$; $Mn(acac)_3$: Mn–O_2 2.114, Mn–O_3 1.937, Mn–O_4 2.112, Mn–O_5, 1.965 Mn–O_6, 1.928, Mn–O_7 1.967 Å; O_2MnO_3 87.9°; O_4MnO_5 88.0°; O_6MnO_7 91.9°

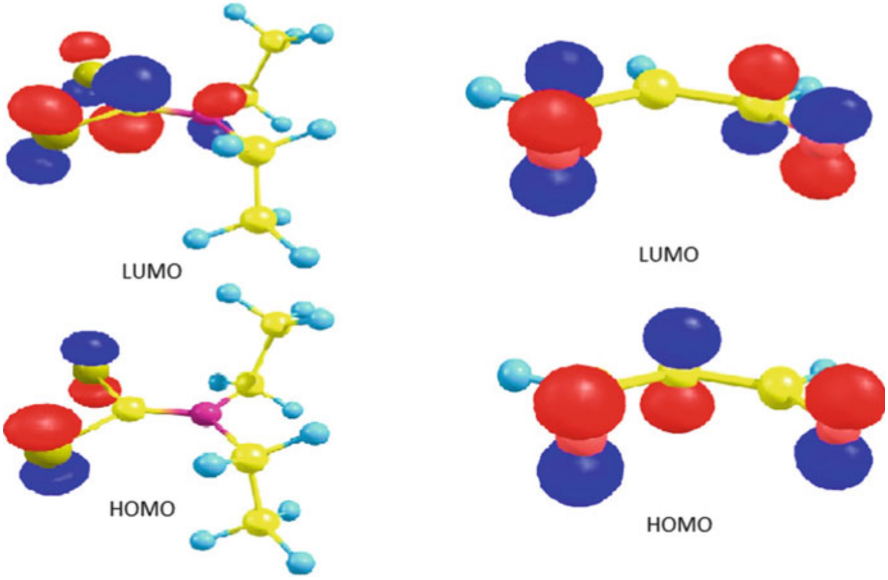

Fig. 15 The HOMO and LUMO orbitals of the anionic ligands Etdtc$^-$ (*left*) and DPM$^-$ (DPM$^-$ 2,2,6,6-tetramethylheptane-3,5-dioanto), (*right*) here for the sake of simplicity plotted as truncated propane-3,5-dionato anion

Table 14 Energies of d–d transitions (NEVPT2 results) of Ni(dtc)$_2$ and Ni(Et$_2$dtc)$_2$, values reported from d–d absorption spectra[a] and calculated using AILFT and best fit parameters from Table 15

	Ni(dtc)$_2$		Ni(Et$_2$dtc)$_2$							
	NEVPT2	AILFT	NEVPT2	AILFT						
				Energy	Orbital populations					
					d_{xy}	d_{xz}	d_{yz}	d_{x2-y2}	d_{z2}	Exp.[a]
$^1A_g(1)$	0	0	0	0	0.08	1.98	1.98	2.00	1.97	
$^3B_{2g}(1)$	2,703	1,836	3,200	2,282	1.03	1.97	1.03	1.99	1.98	
$^3B_{1g}(1)$	2,788	2,875	3,254	3,373	1.00	2.00	2.00	2.00	1.00	
$^3B_{3g}(1)$	4,026	3,606	4,401	3,974	1.03	1.03	1.97	1.99	1.97	
$^3B_{1g}(2)$	13,599	12,469	14,156	13,100	1.19	1.81	1.81	1.19	2.00	
$^1B_{2g}(1)$	16,564	15,610	17,028	15,975	1.02	1.98	1.02	1.99	2.00	17,000
$^1B_{1g}(1)$	17,551	17,510	17,991	17,933	1.03	1.97	1.97	2.00	1.03	15,750
$^1B_{3g}(1)$	17,943	17,396	18,265	17,679	1.02	1.02	1.98	1.98	1.99	19,000
$^1B_{1g}(2)$	23,661	22,614	24,109	23,143	1.00	2.00	2.00	1.00	2.00	21,000
$^3B_{3g}(2)$	23,597	23,211	24,490	24,121	2.00	2.00	1.00	1.28	1.72	
$^3B_{2g}(2)$	24,320	25,442	25,227	26,327	2.00	1.00	2.00	1.26	1.74	
$^3A_g(1)$	25,727	26,533	26,686	27,565	2.00	2.00	2.00	1.00	1.00	
$^3B_{1g}(3)$	26,514	27,701	27,232	28,422	1.81	1.19	1.19	1.81	2.00	
σ[b]	–	815		803						

[a] [176]

[b] σ – standard deviation AILFT – NEVPT2

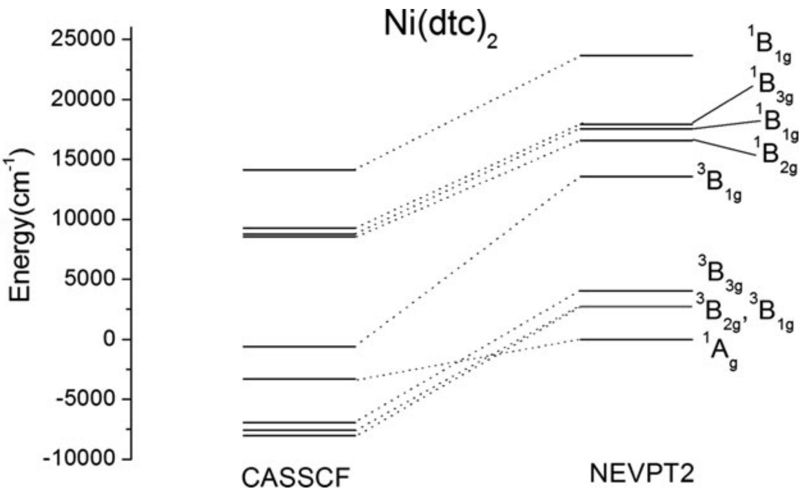

Fig. 16 Importance of the inclusion of dynamic correlation when going from CASSCF to NEVPT2 multiplet levels for the correct prediction of the spin-ground state and d–d absorption spectra of Ni(dtc)$_2$

NEVPT2 and experimental data (Table 14). However, this is distinctly not the case with results from CASSCF which also predicts a wrong ($^3B_{2g}$) ground state. Figure 16 impressively illustrates the crucial role played by dynamic correlation neglected by CASSCF but accounted for by NEVPT2. For Ni(Et$_2$dtc)$_2$ with rather covalent Ni–S bond accounting for dynamic correlation is mandatory, yielding a good agreement with both spectral data and correctly reproducing the diamagnetic ground state. We also studied the effect of the ethyl substituents on the energies of the d–d transitions. Comparison between these energies for Ni(Et$_2$dtc)$_2$ with those for Ni(dtc)$_2$ complex (Table 14) shows that d–d transitions get shifted to higher energy (~500 cm^{-1}) from Ni(dtc)$_2$ to Ni(Et$_2$dtc)$_2$. Within the AOM, d-orbital energies can be analyzed introducing one more parameter into the AOM expressions according to (87). With the set of (88), the problem of overparameterization in the AOM starts to emerge; there are five energy parameters but only four accessible energy differences. This does not allow us to fix all five parameters

$$\begin{array}{l}
a_1: \quad \begin{array}{cc} \left|\mathrm{d}_{z2}\right\rangle & \left|\mathrm{d}_{x2-y2}\right\rangle, \\ \end{array} \\
\begin{bmatrix} e_\sigma - 4e_{sd} & \sqrt{3}\cos\beta(-e_\sigma + 4e_{sd}) \\ \sqrt{3}\cos\beta(-e_\sigma + 4e_{sd}) & 4e_{\pi c}\sin^2\beta + 3(e_\sigma - 4e_{sd})\cos^2\beta \end{bmatrix}, \\
b_3: \left|\mathrm{d}_{yz}\right\rangle : 4e'_{\pi s}\sin^2(\beta/2), \\
b_2: \left|\mathrm{d}_{xz}\right\rangle : 4e_{\pi s}\cos^2(\beta/2), \\
b_1: \left|\mathrm{d}_{xy}\right\rangle : 4e_{\pi c}\cos^2\beta + 3e_\sigma\sin^2\beta,
\end{array} \tag{88}$$

Table 15 AILFT parameters (in cm^{-1})[a] and the angle β (in degree) from AI CASSCF and NEVPT2 calculations of planar bis-chelate complexes of Ni(II) with dtc, Etdtc, acac and DPM ligands

Parameter[b]	Ni(dtc)_2		$\text{Ni(Et}_2\text{dtc)}_2$	Ni(acac)_2	Ni(DPM)_2
	CASSCF	NEVPT2	NEVPT2	NEVPT2	NEVPT2
e_σ	4,630 (8)	8,202 (8)	8,394 (8)	7,318 (29)	7,871 (31)
e_{sd}	1,365 (9)	1,898 (8)	1,920 (8)	1,818 (12)	1,844 (15)
$e_{\pi s}(\text{in} - \text{phase})$	−112 (68)	730 (64)	838 (63)	1,454 (44)	1,798 (50)
$e'_{\pi s}(\text{out} - \text{of} - \text{phase})$	388 (32)	2,230 (36)	2,338 (37)	630 (30)	1,044 (36)
B	1,197 (3)	992 (4)	995 (4)	1,103 (2)	1,078 (2)
C	4,205 (12)	3,638 (16)	3,589 (16)	3,931 (9)	3,872 (10)
β	79.0	79.0	79.0	96.0	94.5

[a] Standard deviations for the parameters are given in parenthesis

[b] The parameter $e_{\pi c}$ for in-plane Ni–ligand bonds was set to 0 for Ni(dtc)_2 and Ni(Etdtc)_2 and $e_{\pi c}/e^{\text{o}}_{\pi s} = 0.6$, $e^{\text{o}}_{\pi s} = (e_{\pi s} + e'_{\pi s})/2$, in the case of Ni(acac)_2 and Ni(DPM)_2

from spectra or from AI results. To reduce the number of parameters, the value of $e_{\pi c}$ describing π-bonding within the chelate plane was set to zero [178]. Least squares fit to AI results affords parameter values listed in Table 15 and AILFT results which reproduce well the AI data (included Table 14). An orbital occupation analysis of the CI wavefunctions from the AILFT treatment allows one to judge the multiconfigurational character of the various states. Typical deviations of the occupation numbers from 0, 1, and 2 are about 2–4%. These deviations are small but still significant for the energy. In Table 15, we compare the AOM parameters deduced from CASSCF and NEVPT2 results for Ni(dtc)_2. We conclude that dynamic correlation introduces considerable and positive corrections to e_σ, e_{sd} and it turns the sign of the parameter $e_{\pi s}$ from negative to positive, implying as expected π-donor character of the S ligand. The π-type anisotropy predicted by the Orgel concept is nicely reflected by the out-of-phase coupling parameter ($e_{\pi s} = 2{,}230\ \text{cm}^{-1}$) exceeding largely that of the in-phase type energy ($e'_{\pi s}$=730 cm^{-1}). As usual, we verify the (slight) improvement of the parameters B and C getting smaller when going from CASSCF to NEVPT2. Comparing NEVPT2 results between Ni(dtc)_2 and $\text{Ni(Et}_2\text{dtc)}_2$, we notice the small yet nonnegligible increase of the parameters e_σ and e_π when replacing H by ethyl groups. Finally, AOM parameters from a best fit to NEVPT2 results (Table 15) compare well with values obtained from a direct fit to spectroscopic data ($e_\sigma = 9{,}030\ \text{cm}^{-1}$, $\bar{e}_{\pi s} = (e_{\pi s} + e'_{\pi s})/2 = 2{,}670\ \text{cm}^{-1}$, $e_{sd} = 1{,}662\ \text{cm}^{-1}$) [178].[2]

The polarized electronic spectrum of the diamagnetic Ni(DPM)_2 displays three d–d transitions hidden under a broad band envelope, with energies at 16,000, 18,500, 20,000 cm^{-1} which could only be resolved using polarized light with

---

[2] Because of a different choice of coordinate axes and different definitions, parameters σ_{sd} and $e_{\pi c}$ in the given reference should be compared with $4e_{sd}$ and $(e_{\pi s} + e'_{\pi s})/2$ calculated with the values in Table 15. Because no distinction between $e_{\pi s}$ and $e'_{\pi s}$was possible at that time, comparison with the average of these parameters of Table 15 and the cited values is only possible.

intensities in the y and/or z, x and x directions, respectively (see Fig. 14a for axes definitions) [177]. With a center of symmetry, intensity of d–d transitions is borrowed by mixing with charge transfer states via off-centric vibrations. Assuming (in analogy to Ni(Et$_2$dtc)$_2$ vide supra) an intensity promoting mode of β_{2u} symmetry, the three bands are assigned to $^1B_{3g}(b_{2g}, d_{xz} \rightarrow b_{1g})$ (z), $^1B_{1g}(a_g \rightarrow b_{1g})$, and $^1B_{1g}(a_g \rightarrow b_{1g})$, respectively, [$^1B_{2g}(b_{2g}, d_{yz} \rightarrow b_{1g})$ remains forbidden by this mechanism and is possibly hidden under the absorption to the first d–d transition]. NEVPT2 results (Table 16) lend support of this assignment yielding also a good agreement with the experimental energies. NEVPT2 results yield the $^1B_{3g}$ state at 15,373 with $^1B_{2g}$ at 1,000 cm^{-1} higher energy, implying an orbital energy order $d_{xz} > d_{yz}$. With the value of the bite angle $\beta = 94.5^\circ$ and neglecting π-bonding anisotropy, an opposite order is expected ((84), $e_{\pi s} = e'_{\pi s} > 0$). This is a clear manifestation of DPM functioning as a in-phase coupling ligand (see Fig. 15) yielding a positive $E(^1B_{2g}) - E(^1B_{3g})$ energy contribution ($=2(e_{\pi s} - e'_{\pi s})$ for $\beta = 90^\circ$), overcompensating by far the effect of the geometry ($\beta = 94.5^\circ$, $E(^1B_{2g}) - E(^1B_{3g}) < 0$). In Table 16, results for Ni(DPM)$_2$ are compared with those for Ni(acac)$_2$ illustrating the effect of the replacement of the tertiary butyl

Table 16 Energies of d–d transitions (NEVPT2 results) of Ni(acac)$_2$ and Ni(DPM)$_2$, values reported from d–d absorption spectra[a] and calculated using AILFT and best fit parameters listed in Table 15

	Ni(acac)$_2$		Ni(DPM)$_2$							
	NEVPT2	AILFT	NEVPT2	AILFT						
				Energy	Orbital populations					
					d_{xy}	d_{xz}	d_{yz}	d_{x2-y2}	d_{z2}	Exp.[a]
$^1A_g(1)$	0	733	0	0	0.09	1.97	1.97	2.00	1.96	
$^3B_{3g}(1)$	741	0	1,159	582	1.04	1.04	1.96	1.99	1.98	
$^3B_{1g}(1)$	338	558	1,294	1,390	1.00	2.00	2.00	2.00	1.00	
$^3B_{2g}(1)$	1,676	1,117	2,300	1,569	1.04	1.96	1.04	1.99	1.97	
$^3B_{1g}(2)$	7,175	8,128	7,706	8,543	1.17	1.83	1.83	1.17	2.00	
$^1B_{3g}(1)$	15,862	15,082	16,367	15,372	1.03	1.03	1.97	1.98	1.99	16,000
$^1B_{2g}(1)$	16,835	16,205	17,096	16,360	1.04	1.96	1.04	1.97	1.99	–
$^1B_{1g}(1)$	16,382	16,501	17,431	17,068	1.03	1.97	1.97	2.00	1.03	18,500
$^1B_{1g}(2)$	18,410	19,227	18,901	19,175	1.00	2.00	2.00	1.00	2.00	20,000
$^3B_{2g}(2)$	18,270	17,803	19,483	19,244	2.00	1.00	2.00	1.19	1.81	
$^3B_{3g}(2)$	18,921	19,029	19,989	20,409	2.00	2.00	1.00	1.19	1.81	
$^3A_g(1)$	18,954	19,825	20,294	21,482	2.00	2.00	2.00	1.00	1.00	
$^3B_{1g}(3)$	25,638	24,896	26,710	25,932	1.83	1.17	1.17	1.83	2.00	
$^1A_g(2)$	32,921	32,411	34,106	33,717	2.00	1.30	1.61	1.52	1.56	
$^1A_g(3)$	33,792	34,788	34,829	35,774	1.99	1.93	1.79	0.49	1.81	
$^3B_{2g}(3)$	33,780	33,800	34,867	35,227	1.96	1.04	1.96	1.82	1.22	
$^3B_{3g}(3)$	35,119	34,905	36,506	36,111	1.97	1.97	1.03	1.82	1.21	
σ[b]	–	630		656						

[a] [177]

[b] σ – standard deviation AILFT – NEVPT2

with methyl substituents. From Ni(DPM)$_2$ to Ni(acac)$_2$[3], d–d transitions shift by 200–1,000 to lower energies, reflecting the effect of the bulkier substituent which increase the donor character of the oxygen ligators. The parameterization of (88), with $e^o_{\pi s}/e_{\pi c} = 0.6$, $e^o_{\pi s} = (e_{\pi s} + e'_{\pi s})/2$, following [174], was used to reproduce the NEVPT2 energies (see Table 16 for AILFT results and standard deviations) yielding also LF parameters (Table 15). AOM parameter values implying σ and π donor character, similar to Ni(Et$_2$dtc)$_2$ but with $e_{\pi s} > e'_{\pi s}$ reflecting the in-phase out-of-plane π-character of DPM$^-$ are obtained. The increase of the Lewis basicity when going from Ni(acac)$_2$ to Ni(DPM)$_2$ both in σ and the out-of-plane π-functions of the ligands become now quantified by the best fit values of e_σ and the parameters $e_{\pi s}$and $e'_{\pi s}$, respectively.

Finally, ligand field parameters adjusted to correlated electronic structure results provide a way to define an orbital energy functional. As illustrated in Fig. 17, orbital energies calculated from AOM parameters calibrated to NEVPT2 results yields results which differ completely from ones obtained using SA-CASSCF[4] calculations. The obvious reason is dynamic correlation, which different to any set orbitals provided by quantum chemistry, becomes embodied in one-electron quantities such d-like ligand field orbitals (cf. (82)). Unfortunately, such type of energy functional is not uniquely defined but depends on the adopted LF

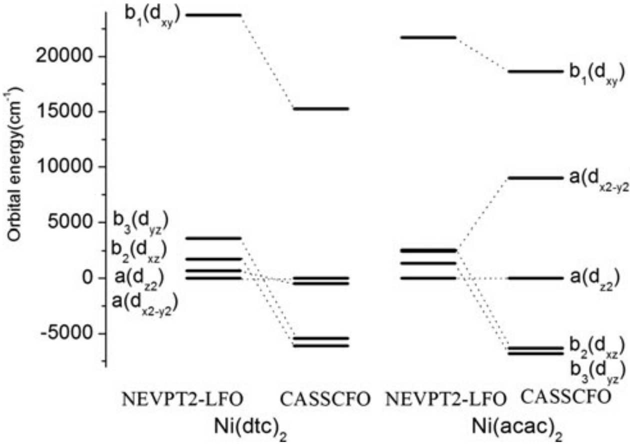

Fig. 17 NEVPT2-based AILFT d-orbital levels schemes in comparison with those from SA-CASSCF for Ni(dtc)$_2$ and Ni(acac)$_2$ reflecting the Orgel effect with $d_{yz} > d_{xz}$ for out-of-phase (dtc$^-$) and the $d_{xz} > d_{yz}$ in-phase (acac$^-$); the energy of d_{z2} was taken as the energy reference

---

[3] In solid Ni(acac)$_2$, three Ni(acac)$_2$ moieties assemble to a trimer yielding sixfold coordination around each of three Ni^{II} centers (see [198]). Because of the bulky *tert*-butyl substituents in solid Ni (DPM)$_2$ [199] this does not occur, resulting in a crystal build up from discrete Ni(DPM)$_2$ units.

[4] Not unexpectedly, orbital energies from SA-CASSCF calculations are very close to ones obtained using AILFT and AOM parameters adjusted to CASSCF results.

parameterization scheme. In Fig. 17, we compare results for Ni(dtc)$_2$ and Ni(acac)$_2$. In both complexes, results are affected by dynamic correlations to the same extent leading to an overall increase of ligand field splittings and changing dramatically the orbital energy sequence. However, we pleasingly find that irrespective of the level of approximation, the energy order of $b_2(\mathrm{d}_{xz})$ and $b_3(\mathrm{d}_{yz})$ strictly follows the one predicted by the Orgel concept [170].

6.4.2 Tris-Acetylacetonate Complexes of Cr(III) and Mn(III)

The intrinsic π-bonding anisotropy of the acetylacetonate ligand finds intriguing manifestations in the spectra and magnetic behavior of paramagnetic Cr(acac)$_3$ and Mn(acac)$_3$ complexes. The first complex is almost trigonal with β angles of the three Cr(acac) moieties close to 90°(Fig. 14b). This implies a local geometry of the CrO$_6$ core close to octahedral. However, as we have shown, the symmetry imposed on Ni(acac)$_2$ by the π-electron system of acac is $D_{2\mathrm{h}}$ rather than $D_{4\mathrm{h}}$ even when the β angle in each of the two M(acac) fragments is 90°. For Ni(acac)$_2$, this $D_{4\mathrm{h}} \rightarrow D_{2\mathrm{h}}$ symmetry lowering causes a splitting of the $^1\mathrm{E_g}(\mathrm{d}_{xz}, \mathrm{d}_{yz})$ excited state into $^1\mathrm{B_{2g}}$ and $^1\mathrm{B_{3g}}$. In trigonal Cr(acac)$_3$ (D_3 symmetry), the three in-phase coupled functions [Fig. 13 (right)] give rise to species of e and a_2 symmetry. From these only the e-combination interacts with the Cr part of the same symmetry ($e(D_3)$ from $t_2(O_\mathrm{h})$); the a_1 component of the t_2-orbital has no counterpart from the ligand and thus remains nonbonding in this approximation. This leads to a splitting of the O_h $t_{2\mathrm{g}}$ orbital in D_3 into $a_1 < e$, $[\Delta_{t_2} = (3/2)(e_{\pi\mathrm{s}} - e'_{\pi\mathrm{s}})]$ and to a corresponding splitting of the $^4\mathrm{A}_2 \rightarrow {}^4\mathrm{T}_2$ octahedral spin-allowed transition (10Dq) ($\Delta(^4\mathrm{A}_2 \rightarrow {}^4\mathrm{T}_2) = (3/4)(e_{\pi s} - e'_{\pi s})$, CI neglected). The polarized electronic absorption spectrum of Cr(acac)$_3$ shows one band with maximum at 18,100 cm^{-1} and one shoulder under the charge transfer band of raising intensity with maximum (deduced upon deconvolution) at 22,700 cm^{-1}. Using polarized light, two transitions have been assigned on the basis of their polarizations (parallel (z) and perpendicular (x, y) to C_3 axis) to the band maxima at 17,700 cm^{-1} ($^4\mathrm{A}_2 \rightarrow {}^4\mathrm{A}_1$) and 18,500 ($^4\mathrm{A}_2 \rightarrow {}^4\mathrm{E}$), respectively [174]. High-resolution polarized emission spectra of Cr^{3+}-doped Ga(acac)$_3$ allowed further to resolve the $^4\mathrm{A}_2$ ground state splitting ($2|D| = 1.1$–1.2 cm^{-1}) and analysis of the intensity have shown that D is negative [$E(M_\mathrm{s} = \pm 3/2) < E(M_\mathrm{s} = \pm 1/2)$] [175]. The lowest excited emitting state $^2\mathrm{E}$ state was experimentally located at 12,940 cm^{-1}. CASSCF and NEVPT2 results for a selected set of low-lying multiplets are listed in Table 17. While the sign of the splitting of the $^4\mathrm{A}_2 \rightarrow {}^4\mathrm{T}_2$ 10Dq transition, $^4\mathrm{A}_1[^4\mathrm{T}_2] < {}^4\mathrm{E}[^4\mathrm{T}_2]$, is well reproduced by the AI results, its magnitude (800 cm^{-1}) is underestimated by a factor of 2–3 by both CASSCF (264 cm^{-1}) and NEVPT2 (381 cm^{-1}). Similar CASSCF results (320 cm^{-1}) have been reported previously [180]. However, with 1,320 cm^{-1} reported in [180], dynamic correlation given by CASPT2 was found to overestimate this difference. Results from a previous LFDFT work (included in Table 17) are similar to the NEVPT2 with the only difference of placing the two $^4\mathrm{A}_2 \rightarrow {}^4\mathrm{T}_2$ transitions by $\approx$4,000 cm^{-1} higher in energy than experiment [181]. We have been

Table 17 AI and AILFT 3d^3 multiplet energies (in cm^{-1}) of Cr(acac)$_3$ and values deduced from the polarized absorption and emission spectra in high resolution[a]

D_3 [O]	CASSCF	CASSC-AILFT[b]	NEVPT2	NEVPT2-AILFT[b]	Exp.[c,d]
$^4A_2(1)[^4A_2]$	0	0	0	0	0 ($E_{3/2}$) 1.2 ($E_{1/2}$)
$^4A_1[^4T_2]$	16,340	16,224	18,826	18,686 [21,306]	17,700
$^4E(1)[^4T_2]$	16,604	16,590	19,207	19,806 [22,655]	18,500
$^4E(2)[^4T_1(1)]$	25,142	25,535	27,159	27,149 [28,748]	22,700
$^4A_2(1)[^4T_1(1)]$	25,870	24,903	27,823	26,543 [26,742]	–
$^4A_2(2)[^4T_1(2)]$	38,629	39,291	40,181	41,674	–
$^4E(3)[^4T_1(2)]$	40,327	39,837	42,265	42,356	–
$^2E(1)[^2E(1)]$	19,152	19,040	17,797	17,706	13,200 ($E_{1/2}$) 12,940 ($E_{3/2}$)
$^2A_2(1)[^2T_1(1)]$	19,962	20,125	18,717	18,497	–
$^2E(2)[^2T_1(1)]$	20,246	20,057	18,956	18,443	–
$^2E(3)[^2T_2(1)]$	27,608	27,787	25,163	26,547	–
$^2A_1(1)[^2T_2(1)]$	28,186	27,618	25,967	26,378	–
$^2A_1(2)[^2A_1]$	32,384	32,461	33,757	34,002	–
$^2A_1(3)[^2T_2(2)]$	35,011	35,366	36,544	36,368	–
$^2E(3)[^2T_2(2)]$	35,402	35,481	37,096	36,461	–
$^2E(4)[^2T_1(2)]$	36,154	36,314	37,352	37,059	–
$^2A_2(2)[^2T_1(2)]$	36,537	36,517	37,955	37,229	–
σ	–	385		681	–

[a] Results from a previous LFDFT study are listed in square brackets [181]

[b] Ligand-field parameters from a best fit of AILFT are listed in Table 18

[c] [174]

[d] [175]

Table 18 AILFT parameters[a] (in cm^{-1}) deduced from fits to CASSCF and NEVPT2 calculations of Cr(acac)$_3$ and Mn(acac)$_3$

	Cr(acac)$_3$		Mn(acac)$_3$	
	AILFT-CASSCF	AILFT-NEVPT2	AILFT-CASSCF	AILFT-NEVPT2
e_σ	5,887 ± 14	6,983 ± 14	5,402 ± 10	6,408 ± 10
$e_{\pi s}$	536 ± 26	583 ± 22	990 ± 15	1,194 ± 14
B	1,035 ± 3	810 ± 3	785 ± 8	829 ± 7
C	3,949 ± 6	3,935 ± 6	4,894 ± 11	4,544 ± 10

[a] $e_{\pi c}/e_{\pi s} = 0.60; e'_{\pi s} = 0; \Delta e_{\pi s} = e_{\pi s}; e^{o}_{\pi s} = e_{\pi s}/2$ [174]

able to reproduce consistently both the CASSCF and NEVPT2 results (Table 17) with AILFT and best fit parameters listed in Table 18. Based on earlier considerations, perturbations from the out-of-phase π-orbitals of acac have been neglected ($e'_{\pi s} = 0$) and, further, using overlap considerations the ratio $e_{\pi c}/e_{\pi s}$ has been fixed at 0.6 [174]. Comparison between CASSCF and NEVPT2 results shows that dynamic correlation contributes to an essential increase of the parameter e_σ (from 5,887 to 6,983 cm^{-1}), the NEVPT2 value comparing well with the one that results from a direct fit to experimental results ($e_\sigma = 7{,}292$ cm^{-1} [174]). However, reported values $e_{\pi s}$ (B), 1,400–2,000 (500 cm^{-1}) [174] show that NEVPT2 underestimates(overestimates) the corresponding energy effects.

Table 19 Sublevels of the $^4A_2$ ground state and of the ^2E spin–flip octahedral excited state split by spin–orbit coupling from NEVPT2 calculations and their AILFT equivalents adopting a model of anisotropic spin–orbit coupling[a] (A) and their shifts by reduction of the values of B and C from those of a NEVPT2 treatment to effective values [b] deduced from high-resolute d–d absorption and emission spectra of Cr(acaca)$_3$[c] (B)

$D_3^*(D_3)$ [O]	NEVPT2	(A)	(B)	Exp.
$E_{3/2}(^4A_2)[^4A_2]$	0.0	0.0	0.0	0
$E_{1/2}$ $(^4A_2)[^4A_2]$	0.63	0.23	0.66	1.2[b/c]
$E_{3/2}(^2E)[^2E]$	17,711	17,631	13,989	12,940[d]
$E_{1/2}(^2E)[^2E]$	17,737	17,657	14,012	–

[a] $k_{xy} = 0.864$; $k_z = 0.409$, $\zeta = 294\ \mathrm{cm}^{-1}$

[b] $B = 810 \rightarrow 500\ \mathrm{cm}^{-1}$; $C = 3{,}935 \rightarrow 3{,}400\ \mathrm{cm}^{-1}$

[c] [195–197]

[d] [175]

Table 20 AI zero-field splitting tensor parameters for Cr(acac)$_3$ and Mn(acac)$_3$

	Cr(acac)$_3$		Exp.	Mn(acac)$_3$		Exp.[a]
	CASSCF SOC + SSC(SOC)	NEVPT2 SOC + SSC(SOC)		CASSCF SOC + SSC (SOC)	NEVPT2 SOC + SSC (SOC)	
D	−0.38 (−0.30)	−0.36 (−0.29)	−0.60	−4.20 (−3.86)	−4.32 (−3.84)	−4.52
E	–	–	–	−0.43 (−0.38)	−0.49 (−0.44)	−0.25

[a] [182]

Fine structure effects in Cr(acac)$_3$ have been long time a challenge for both LF and AI theory [180]. In Table 19 (second column), we include the sublevels split by SOC of the $^4A_2(t_{2g}{}^3)$ ground state and the $^2E(t_{2g}{}^3)$ spin–flip excited states as given by the NEVPT2 results. Using these data, ground state ZFS parameters are listed in Table 20. While the negative sign of the ground state splitting $2D$ is well reproduced, its value $2D = -0.63\ \mathrm{cm}^{-1}$ is about half the one observed experimentally. Direct SSC yields an essential contribution ($-0.15\ \mathrm{cm}^{-1}$) to the total $2D = -0.75\ \mathrm{cm}^{-1}$. The latter value has been calculated introducing SSC at the same time as the SOC into the CI procedure (see Sect. 3.2). Otherwise, as it emerges from the results (Table 20), the two contributions – from SOC ($2D_{\mathrm{SOC}} = -0.63\ \mathrm{cm}^{-1}$) and SSC ($2D_{\mathrm{SS}} = -0.15\ \mathrm{cm}^{-1}$) – are not additive, having different orientations than the complete $2D$ tensor ($-0.75\ \mathrm{cm}^{-1}$). However, even with SSC included comparison with the experimental ($-1.2\ \mathrm{cm}^{-1}$) $2D$ is not perfect. A reason is that the absolute positions of the doublet states are still by 4,000–5,000 cm^{-1} overestimated by NEVPT2 (see result for ^2E in Table 17). It has been shown [180] that the ground state splitting arises mainly from its interaction with the components of $^4T_2$ and $^2T_2$ excited states, both states contributing approximately to the same extent to this splitting. Turning now to the AILFT calculation of $2D$ and utilizing parameters from Table 18 and a SOC energy $\zeta = 294\ \mathrm{cm}^{-1}$ (adjusted to the relativistic AI results, Table 19), one realize that LF is not able to reproduce $2D$ (a negligibly small value of $2D = -0.04\ \mathrm{cm}^{-1}$ results). It has been suggested that anisotropic SOC (relativistic nephelauxetic effect) between the t_{2g}–e_g is responsible for the rather large experimental value of $2D = -1.2\ \mathrm{cm}^{-1}$ [175, 179]. In support of this, introducing differential reduction factors $k_{xy} = 0.864$, $k_z = 0.409$ to account for such effect (Table 19, column

A) and further shifting the doublet excited states downwards in energy (controlled by a reduction of B, Table 19, column B) improves the result against experiment. However, even so, agreement with experiment is far from being perfect. NEVPT2 results also reproduce the sign of ^{2}E splitting ($E_{3/2} < E_{1/2}$, Table 19) however again, not its magnitude [$E(E_{1/2}) - E(E_{3/2}) = 220$–$290\ \mathrm{cm}^{-1}$ [175]].

Mn(acac)$_3$ is a high-spin d^4 complex which, in difference to Cr(acac)$_3$, possess one extra electron on the e_g orbital. The Jahn–Teller active ^{5}E ground state is unstable and distorts leading to a tetragonally elongated octahedron with two long (axial, $R_\mathrm{ax} = 2.113 \pm 0.001$ Å) and four short (equatorial, $R_\mathrm{eq} = 1.949 \pm 0.020$ Å) Mn–O bonds (Fig. 14b, right). High-precision measurements have lead to the ZFS tensor with values $D = -4.52\ \mathrm{cm}^{-1}$ and $E/D = 0.05\ \mathrm{cm}^{-1}$ [182]. Three d–d bands in the absorption spectrum of Mn(acac)$_3$ with band maxima at 9,250, 17,900, and 21,500 cm^{-1} have been reported and assigned to transitions from the $^5\mathrm{B}_{1\mathrm{g}}(b_{2\mathrm{g}}{}^1 e_\mathrm{g}{}^2 a_{1\mathrm{g}}^1)$ ground state into the $^5\mathrm{A}_{1\mathrm{g}}(a_{1\mathrm{g}} \rightarrow b_{1\mathrm{g}})$, $^5\mathrm{B}_{2\mathrm{g}}(b_{2\mathrm{g}} \rightarrow b_{1\mathrm{g}})$, and $^5\mathrm{E}_\mathrm{g}(e_\mathrm{g} \rightarrow b_{1\mathrm{g}})$ excited states, where symmetry has been approximated as $D_{4\mathrm{h}}$ [182]. However, in a strict sense, the interplay between Jahn–Teller coupling (due to Mn$^{\mathrm{III}}$(d^4), leading to $D_{4\mathrm{h}}$ symmetry) and the π-electron orbital phase coupling (due to acac, imposing D_3 symmetry) makes the symmetry very low (C_1) to preclude any neat ligand field analysis based on symmetry arguments. These experimental observations have been subject to a deep AI analysis [48] which the reader can refer. In Table 21, we present energies for the lowest transitions from CASSCF and NEVPT2 calculations, where because of the low symmetry and in order to avoid ambiguity, term notations for the parent O_h symmetry were given. It follows from Table 21 that the AI methods yield consistent set of excitation energies which agree within 1,000–2,000 cm^{-1} with the experimental values. In particular, agreement of theoretical values with the first spin-allowed transition (9,250 cm^{-1}), the ^{5}E(O_h) ground state Jahn–Teller splitting becomes better when including dynamic correlation (NEVPT2, cf. Table 21). Along the same lines and as expected, the energy of the spin–flip $^5\mathrm{E} \rightarrow {}^3\mathrm{T}_1$ transitions shift by 3,500 cm^{-1} to lower energies from CASSCF to NEVPT2. The latter results are also comparable in quality with those resulting from more sophisticated treatments, such as SORCI and DDCI2 [48].

Table 21 Energies of quintet states and the lowest excited triplet state (parent octahedral term notations) of Mn(acac)$_3$ calculated using SA-CASSCF and NEVPT2 and reproduced using AILFT and reported from optical d–d absorption spectra

O	CASSCF	CASSC-AILFT[a]	NEVPT2	NEVPT2-AILFT[a]	Exp.[b]
^{5}E	0	0	0	0	0
^{5}E	6,658	5,080	7,423	6,025	9,520
$^5\mathrm{T}_2$	16,057	16,252	19,202	19,219	17,900
$^5\mathrm{T}_2$	17,429	16,586	20,690	19,623	21,500
$^5\mathrm{T}_2$	17,833	17,985	21,290	21,308	21,500
$^3\mathrm{T}_1$	14,982	14,027	11,526	10,450	–
$^3\mathrm{T}_1$	15,220	15,436	11,850	12,171	–
$^3\mathrm{T}_1$	16,034	15,553	12,981	12,349	–
σ		615	–	692	–

[a] Ligand-field parameters from a best fit of AILFT are listed in Table 18

[b] Experimental values are taken from Krzystek et al. [182]

As reflected by the energies $^5T_2$ and $^3T_1$ octahedral parent terms (Table 21) each splitting into three nondegenerate components, the symmetry of Mn(acac)$_3$ is very low and only coarsely described as D_{4h}. Even so, with the energy splitting patterns given by 16,057 and 17,631 ± 202 [for $^5T_2(O_h) \rightarrow {}^5B_2(D_{4h})$ and $^5E(D_{4h})$] and 15,101 ± 119 cm^{-1} and 16,034 cm^{-1} [for $^3T_1 \rightarrow {}^3E(D_{4h})$ and $^3A_2(D_{4h})$] – CASSCF and 19,202, 20,990 ± 300 cm^{-1} and 11,688 ± 162, 12,981 – NEVPT2, respectively, the dominant axial component of the ligand field (D_{4h}) is clearly discernible being superimposed by a much smaller low-symmetry component. Not unexpectedly, Jahn–Teller coupling being a stronger σ-effect (tolerating D_{4h}) dominates over the acac-phase coupling being a weaker π-effect (tolerating D_3 symmetry). Under the combined action of SOC and low symmetry, the $^5A(C_1)$ ground state of Mn(acac)$_3$ splits into five sublevels with the lowest taken as reference (energy 0) and four excited states at 0.140 [0.171], 10.026 [10.778], 12.295 [13.364], 14.956 [16.183] –CASSCF [NEVPT2]. Solutions of the spin-Hamiltonian problem for $S = 2$ (89) from [183] (90) have been used to extract D and E from the given eigenvalues.

$$\hat{H}^{\text{eff}}_{ZFS} = D\left[\hat{S}_z^2 - \frac{S(S+1)}{3}\right] + E(\hat{S}_x^2 - \hat{S}_y^2), \tag{89}$$

$$\begin{gathered} |2^s\rangle = a^+\frac{|+2\rangle + |-2\rangle}{\sqrt{2}} + a^-|0\rangle \quad E_{2s} = \text{sign}(D)2\sqrt{D^2+3E^2}, \\ |2^a\rangle = (|+2\rangle - |-2\rangle)/\sqrt{2} \quad E_{2a} = 2D, \\ |1^s\rangle = \frac{|+1\rangle + |-1\rangle}{\sqrt{2}} \quad E_{1s} = -D + 3E, \\ |1^a\rangle = \frac{|+1\rangle - |-1\rangle}{\sqrt{2}} E_{1a} = -D - 3E, \\ |0'\rangle = a^-\frac{|+2\rangle + |-2\rangle}{\sqrt{2}} - a^+|0\rangle \quad E_{0'} = -\text{sign}(D)2\sqrt{D^2+3E^2}, \end{gathered} \tag{90}$$

where

$$a^{\pm} = \frac{1}{\sqrt{2}}\left(1 \pm \frac{D}{\sqrt{D^2+3E^2}}\right)^{\frac{1}{2}} \tag{91}$$

Thus, using the eigenvalues resulting from the diagonalization of the SOC-CI matrix, D and E can be determined as

$$D = \pm\frac{1}{4}\sqrt{\Delta^2 - \frac{4}{3}\delta^2}, \tag{92}$$

$$E = \frac{\delta}{6},$$

with $\Delta = |E_{0'} - E_{2s}|$ and $\delta = |E_{1s} - E_{1a}|$; the sign of D is negative if $E_{0'} > E_{2s}$ and positive if $E_{0'} < E_{2s}$ which immediately follows inspecting the eigenfunctions of the SOC-CI matrix. Further by convention $\mathrm{sign}(E) = \mathrm{sign}(D)$ and $0 < E/D < 1/3$. If $E/D = 1/3$, the sign of D is indeterminate. In determining D and E using (92), we ignore quadratic term of the ZFS Hamiltonian. However, for Mn(acac)$_3$ such terms are of the order of 0.1 cm^{-1} and thus can be neglected. In Table 20, computed D and E values compare well with those reported experimentally. In difference to the term energies themselves (Table 6), D and E turn out to be not sensitive to dynamic correlation, but undergo a significant improvement (in particular, D) when accounting SSC. Analysis from a previous work [48] shows that mixing with $^3T_1$(62%) rather than $^5T_2$(32%) dominates the magnitude of D.

Finally, using AILFT, we have fitted CASSCF and NEVPT2 results (Table 21) utilizing the LF model for Cr(acac)$_3$ where in addition a $1/R^6$ dependence of the AOM parameters on distance has been allowed. Best fit parameters (Table 18) have been used to consistently reproduce the AI data from Table 21. AOM parameters compare well with the corresponding Cr(III) showing at the same time coupling between the 3d and πs orbitals for Mn(III) being about twice larger than those for Cr(III). We are now also in a position to analyze the contributions of the Jahn–Teller distortions and of the π-anisotropy on D and E. Technically this is possible by excluding one effect or the other using proper manipulations of the LF parameters. Thus, taking simply reference AOM parameters from Table 18 (pertaining to an average Mn–O distance of 2.004 Å) and not accounting for their variation with the distance, the sole effect of the πs-anisotropy is studied. Alternatively, assuming isotropic $e_{\pi s} = e'_{\pi s}$ parameters but allowing for the alteration of the Mn–O bond lengths, the net effect of Jahn–Teller distortion is studied. Result from these analysis are collected in Table 22. From these results, we infer that the two effects provide competitive but strongly nonadditive effects in D and E. Thus, switching from one effect to the other, while not changing the values of D and E dramatically leads to a rotation of the ZFS tensor from the tetragonal (D_{4h}, Jahn–Teller regime) to the trigonal direction (D_3, πs-anisotropy). Unfortunately, no single crystal measurements were made to experimentally locate the axes of the magnetic anisotropy. Based on a preliminary results, we predict that D and E will predominantly follow the anisotropy axis due to the stronger Jahn–Teller interaction (vide supra).

Table 22 AILFT analysis of the contributions to D(SOC) (in cm^{-1}) of Mn(acac)$_3$ from anisotropic π-bonding (phase coupling) and Jahn–Teller (JT) distortions

	NEVPT2 (SOC)	AILFT-NEVPT2 (SOC)		
		π-anisotropy + JT-distortions	JT-distortions (ease axis ∥ C_4)	π-anisotropy (ease axis ∥ C_3)
D	−3.84	−3.93	−3.74	−5.00
E	−0.44	−0.55	−0.52	−0.63

6.5 Unusual Spin-States: Square Planar Paramagnetic Ni^{II} Complexes

Due to the large destabilization of the antibonding d_{x2-y2} orbital, square planar complexes of Ni^{II} invariably possess a low-spin ground states and are therefore diamagnetic. In Sect. 6.4.1, we considered such examples with two bis-bidentate complexes of Ni^{II}, where it was shown that dynamic correlation brought in by the NEVPT2 leads to a low spin ground state. But are planar complexes of Ni^{II} always diamagnetic? Results in Table 14 (see also Fig. 16) for $Ni(Et_2dtc)_2$ show that the $^3B_{2g}{-}^1A_g$ energy difference is only 3,200 cm^{-1} and gets even smaller (by 500 cm^{-1}) when going from the more to the less donating ligands $Et_2dtc \rightarrow dtc$.

As follows from the dependence of the energies of the in-plane d_{xy} (d_{x2-y2}) orbitals ($3e_\sigma \sin^2\beta$ and $3e_\sigma \cos^2\beta$, respectively, see (88)) on the geometry, the low-lying triplet excited state can be qualitatively ascribed to the small chelate bite angle $\beta = 79°$ deviating significantly from the direction of maximal metal–ligand $\sigma(\pi)$ overlap ($\beta = 90°$) an thus narrowing the $d_{xy}{-}d_{x2-y2}$ HOMO–LUMO gap. One can imagine that further lowering of this angle will lead to switching from a singlet to a triplet ground state. This is exactly what takes place in the planar bis-chelate complex $Ni[(tBu_2)PON(iPr)_2]_2$ ($[(tBu_2)PON(iPr)_2]$ is the monoanion *P*,*P*-di-*tert*-butylphosphinic-*N*-isopropyl-amidato-*N*,*O*) with an even smaller value of the angle $\beta = 74.2°$ (Fig. 18) [184]. CASSCF and NEVPT2 values for multiplet energies of the complex are listed in Table 23 with the result that both the CASSCF and NEVPT2 now correctly reproduce

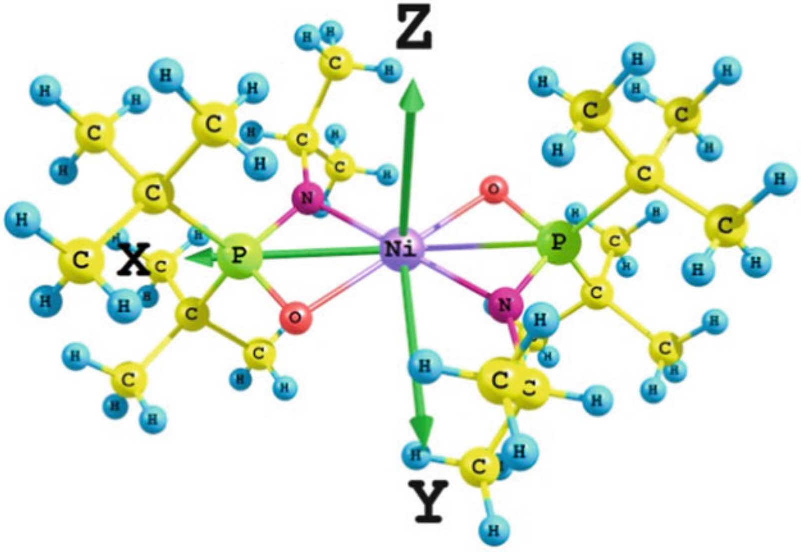

Fig. 18 The paramagnetic planar bis-chelate $Ni[tBu_2PON(iPr)]_2$; geometry from experimentally reported structure: Ni–O 2.103 Å, Ni–N 1.903 Å, P–O 1.516 Å, P–N 1.604 Å, ONiN bite angle β 74.2°, NiOP 89.6°, OPN 101.7°

Table 23 CASSCF and NEVPT2 energies (in cm^{-1}) of d–d transitions of the planar paramagnetic $Ni[(tBu_2)PON(iPr)]_2$ and their values reported from d–d absorption spectra[a] and calculated using AILFT-NEVPT2 and best fit parameters given in Table 24

	CASSCF	NEVPT2	AILFT(NEVPT2)						Exp[a]
			State energy[b]	Orbital occupations					
				d_{xy}	d_{xz}	d_{yz}	d_{x2-y2}	d_{z2}	
$^3B_3(1)$	0	0	0	1.04	1.04	1.96	1.99	1.97	
$^3B_2(1)$	976	2,140	1,901 (−238)	1.06	1.94	1.06	1.98	1.96	
$^3B_1(1)$	1,578	2,899	2,356 (−542)	1.00	2.00	2.00	2.00	1.00	
$^1A(1)$	10,725	6,236	6,597 (361)	0.15	1.94	1.96	2.00	1.94	
$^3B_1(2)$	5,980	8,181	7,926 (−254)	1.35	1.65	1.65	1.36	2.00	7,300
$^3B_2(2)$	9,168	13,257	13,779 (522)	2.00	1.00	2.00	1.19	1.81	
$^1B_3(1)$	17,134	15,030	15,217 (187)	1.04	1.04	1.96	1.97	1.99	–
$^3B_3(2)$	10,648	15,641	15,276 (−364)	2.00	2.00	1.00	1.21	1.79	17,300
$^3A(1)$	11,090	16,493	17,117 (624)	2.00	2.00	2.00	1.00	1.00	
$^1B_2(1)$	18,370	17,395	17,177 (−218)	1.07	1.93	1.07	1.95	1.99	
$^1B_1(1)$	18,445	17,667	18,072 (405)	1.07	1.93	1.93	1.98	1.09	
$^3B_1(3)$	21,113	21,170	20,805 (−364)	1.65	1.35	1.35	1.65	2.00	
$^1B_1(2)$	21,877	21,447	21,020 (−427)	1.00	2.00	2.00	1.02	1.98	
$^3B_2(3)$	27,289	27,776	28,226 (450)	1.94	1.06	1.94	1.83	1.23	
$^1A(2)$	26,520	28,675	28,328 (−347)	2.00	1.04	1.53	1.70	1.73	
σ[c]			399						

[a] [184, 185]

[b] Differences between NEVPT2 and AILFT values are enclosed in parenthesis

[c] σ – standard deviation AILFT – NEVPT2

Table 24 Best fit parameters (in cm^{-1}) deduced from d–d transitions of the planar paramagnetic $Ni[(tBu_2)PON(iPr)]_2$ calculated using NEVPT2

e_σ	e_{sd}	$e_{\pi s}$	$e_{\pi c}$	B	C
6,344 ± 17	1,369 ± 7	1,979 ± 22	790 ± 15	1,026 ± 2	4,261 ± 10

the spin ground state. However, it is only the NEVPT2 method which yields transition energies comparing well with the two reported d–d bands (7,300 and 17,300 cm^{-1}) [185]. In Table 23, we also include AILFT energies calculated with parameters obtained from a least squares fit to the NEVPT2 data (Table 24). When modeling the AI data and to avoid overparameterization common parameters, AOM parameters for the O and N donor atoms have been used. From best fit values (Table 24), we infer that the geometry is not the only cause for the stabilization of a triplet ground state. Apparently, the relatively low bonding strength of σ-type reflected by the relatively small value of e_σ (in comparison with Table 15) contributes to the inverted order placing the ^1A_g state by 6,000 above the triplet. Responsible for this might be the rather high electron withdrawing (contrapolarizing) phosphine lowering the donor character of the directly attached N and O ligating atoms (for a detailed discussion of such effects and their spectroscopic manifestations see [186]). The analysis of this issue was subject to controversy which is not completely resolved yet [185, 187, 188].

7 Conclusions and Outlook

Calculation of spectroscopic and magnetic properties of complexes with open d shells from first principles is still a rather rapidly developing field. In this review, we have outlined the basic principles for the calculations of these properties within the framework of the complete active space self-consistent field (CASSCF) and the NEVPT2 serving as a basis for their implementation in ORCA. Furthermore, we provided a link between AI results and LFT using various parameterization schemes. More specifically, we used effective Hamiltonian theory describing a recipe allowing one to relate AI multiplet theory with LFT on a 1:1 matrix elements basis.

Using a recently developed AI-based ligand field approach (AILFT), AI results on selected spectroscopically and magnetically well-characterized octahedral CrX_6^{3-} and tetrahedral CrX_4, (X = F, Cl, Br, I) complexes have been mapped onto LFT giving first access to ligand field parameters from first principles; values of 10Dq and the angular overlap parameters for σ- and π-metal 3d–ligand interactions (e_σ and e_π) computed in such a way are found to compare well with their counterparts deduced experimentally from the interpretation of d–d spectra. The expected variations of these parameters embodied in the well-known orderings of the ligands according to the increase of their 10Dq values (the spectrochemical series) and two-dimensional maps accounting for the ligand σ and π functions toward the metal 3d-orbitals (quantified by the parameters e_σ and e_π) are well reproduced and thus justified by AI theory. In addition, the reduction of the parameters of d–d interelectronic repulsion B and C reduced by metal–ligand covalence with respect to their values for a free atom or ion (the nephelauxetic series) could be reproduced from a fit of these parameters to AI data, more specifically to NEVPT2. Being able to reproduce the AI data for all multiplets of a given d^n-complex using only three to four parameters, we can conclude from these studies that the CASSCF and NEVPT2 AI methods and classical LFT are remarkably well compatible. This opens a perspective for applications in two directions:

(1) Interpretations and analysis of AI results using LFT in the way the later has been used for years for the interpretation of experimental data. To recover the ligand field picture from AI data is truly useful in the interpretation of both experiments and correlated AI calculations. This is important because otherwise correlated AI calculations are often difficult to interpret in simple chemical terms.
(2) Comparing parameters from a AI results with such from highly resolved spectroscopic data is rather stimulating for the validation and further improvements (developments) of wavefunctions based methods.

In the second part of this review, we have focused on systems which can be treated equally well by AI theory as Werner type complexes, but for which classical LFT breaks down or at least needs to be extended. These are systems with orbitally degenerate ground states such as tetrahedral $CuCl_4^{2-}$(d^9, $^2T_2$) and $NiCl_4^{2-}$(d^8, $^3T_1$).

The Jahn–Teller effect and the implied geometrical distortions and symmetry breaking from T_d to D_{2d} and further to D_{4h} (for $CuCl_4^{2-}$) leads to a significant mixing between the d_{z2} and 4s (D_{2d}, D_{4h}) and between $d_{yz,xz,xy}$ and $4p_{x,y,z}$ (T_d, D_{2d}) orbitals. Using AI results as numeric experimental data base, we were able to quantify these effects demonstrating again the striking compatibility between the AI results and the angular overlap parameterization of the ligand field when accounting additionally for the effects of 4s–3d and 4p–3d mixing in terms of two additional parameters e_{ds} and e_{dp}. Surprisingly enough, it has been proven that for any given parameterization scheme the values of the ligand field parameters are uniquely determined from the AI data through the solution of a linear equation system. Furthermore, parameter transferability could be demonstrated by theory (allowing for various geometries using the same complex) and by experimental structural and spectroscopic data.

The basic assumptions of LFT are violated if ligand donor atoms are parts of a complex ligand with a π-conjugated system. Here, contributions to the ligand field from metal–ligand π-interactions cannot be considered as additive. These terms depend on the ligand topology and can lead to specific level splittings in complexes with partly filled t_{2g} shells. It has been recognized as early as in 1961 by L. Orgel that orbital-phase coupling in conjugated π-systems could be responsible for the spectra and magnetism of complexes involving such ligands, as was found in $Ti(bipy)_3$ (bipy = 1,1′-bipyridyl) and $V(bipy)_3^+$ (both complexes are d^4) being low and high spin, respectively. To reconcile these effects with the basic formalism of LFT, an extension of the latter has been proposed, again at the expense of one additional parameter. NEVPT2 calculations on bis-chelate complexes of Ni^{II} with the bidentate ligands bis-ethyl dithiocarbamate (Et_2dtc^-) and DMP^- 2,2,6, 6-tetramethylheptane-3,5-dionato have been employed assigning these ligands to the out-of-phase and in-phase coupling type, respectively. Excellent agreement between calculated and experimentally reported energies and orderings of the d–d transitions (from polarized spectra) lends further support of the phase coupling concept.

By comparing the CASSCF to NEVPT2 calculations, it was consistently found that introducing dynamic correlation leads to an essential lowering of the parameters of interelectronic repulsion B and C in all considered systems. This is physically sensible of course, as dynamic correlation reduces the interelectronic repulsion energy that is necessarily overestimated by mean-field approaches. For Ni$(Et_2dtc)_2$ and $Ni(DPM)_2$, this has the important consequence that the CASSCF ground state is a triplet, while the NEVPT2 one is a singlet (which is also the experimental finding). However being only 2,000–3,000 cm^{-1} above the ground state, excited triplet states are close lying. We interpret this result (similar to [187]) as originating from the very acute value of the SNiS bite angle β (only 79°). It lowers the metal ligand σ overlap and thus reduces (increases) the energies of the empty d_{xy} (doubly occupied d_{x2-y2}) orbitals thus lowering the HOMO–LUMO gap. One can imagine that further lowering of β will lead to a switch to a triplet ground state. This is exactly what happens in $Ni[(tBu_2)PON(iPr)]_2$ – a planar paramagnetic Ni^{II} complex ($\beta = 74°$). NEVPT2 results nicely reproduce the triplet ground state and the d–d transitions reported experimentally by other authors [185, 187, 188].

π-Type anisotropy and in-phase coupling in a Cr(acac)$_3$ complex have been found to be responsible for both the trigonal splitting of the $^4A_2 \rightarrow {}^4T_2$ band revealed by the polarized absorption and the large and negative zero-field splitting ($2D = -1.2\ \mathrm{cm}^{-1}$) of the $^4A_2$ ground state [$E(\pm 3/2) < E(\pm 1/2)$]. This is largely supported by NEVPT2 calculations yielding ligand field parameters in good agreement with ones obtained by a fit to polarized absorption and emission spectra and optically detected excited state Zeeman splittings (ODMR). An exciting case where Jahn–Teller and orbital-phase couplings interfere is illustrated using Mn(acac)$_3$ (d^4 high-spin ground state) as example; here NEVPT2 results agree well with experimental spin-allowed quintet transitions and the large and negative zero-field splitting D. Employing further AILFT as a tool for the analysis, we could show that Jahn–Teller coupling and π-phase coupling effects yield comparable but nonadditive contributions to D. Thus, switching one or the other effect on or off leads to re-orientation of the main direction of D from one parallel to the C_4 axis (Jahn–Teller effect on, no-phase coupling) to C_3 (phase coupling on, Jahn–Teller coupling off). We therefore suggest single-crystal EPR measurements to experimentally probe the interplay between the two opposing effects.

References

1. Becquerel J (1929) Z Phys 58:205
2. Bethe H (1929) Ann Phys 3:135
3. van Vleck JH (1932) Theory of magnetic and electric susceptibilities. Oxford University Press, Oxford
4. van Vleck JH, Penney WG (1934) Phil Mag 17:961
5. Finkelstein R, van Vleck JH (1940) J Chem Phys 8:790
6. Ilse FE, Hartmann H (1951) Zeit f Phys Chem 197:239
7. Ilse FE, Hartmann H (1951) Z Naturforschg 6a:751
8. Mulliken RS (1932) Phys Rev 40:55
9. van Vleck JH (1935) J Chem Phys 3:407
10. Ballhausen CJ (1962) Introduction to ligand field theory. McGraw-Hill, New York
11. Ballhausen CJ (1979) Molecular electronic structures of transition metal complexes. McGraw-Hill, New York
12. Griffith JS (1971) The theory of transition-metal ions. Cambridge University Press, Cambridge
13. Sugano S, Tanabe Y, Kamimura H (1970) Multiplets of transition-metal ions in crystals. Academic, New York
14. Figgis BN, Hitchman MA (2000) Ligand field theory and its applications. Wiley, New York
15. Ballhausen CJ (1979) J Chem Educ 56:215
16. Ballhausen CJ (1979) J Chem Educ 56:294
17. Ballhausen CJ (1979) J Chem Educ 56:357
18. Dahl JP, Ballhausen CJ (1968) Adv Quant Chem 4:170
19. Berthier G (1974) Adv Quant Chem 8:183
20. Koch W, Holthausen MC (2000) A chemist's guide to density functional theory. Wiley, Weinheim
21. Chermette H (1998) Coord Chem Rev 178–180:699
22. Lovell T, Himo F, Han W-G, Noodleman L (2003) Coord Chem Rev 238–239:211
23. Ciofini I, Daul CA (2003) Coord Chem Rev 238–239:187

24. Autschbach J, Ziegler T (2003) Coord Chem Rev 238–239:83
25. Bickelhaupt FM, Baerends EJ (2000) In: Lipkowitz KB, Boyd DB (eds) Reviews in computational chemistry. Wiley, New York, p 1
26. Diedenhofen M, Wagener T, Frenking G (2001) In: Cundari TR (ed) Computational organometallic chemistry. Marcel Dekker, New York, p 69
27. Gross EKU, Kohn W (1990) Adv Quant Chem 21:255
28. Casida ME (1995) In: Chong DP (ed) Recent advances in density functional methods. World Scientific, Singapore, p 155
29. Bauernschmitt R, Ahlrichs R (1996) Chem Phys Lett 256:454
30. Bauernschmitt R, Häser M, Treutler O, Ahlrichs R (1997) Chem Phys Lett 264:573
31. Dobson JF (1998) In: Dobson JF et al (eds) Electronic density functional theory: recent progress and new directions. Plenum, New York
32. Furche F (2001) J Chem Phys 114:5982
33. Grimme S, Parac M (2003) Chem Phys Chem 3:292
34. Dreuw A, Head-Gordon M (2005) Chem Rev 105:4009
35. Atanasov M, Daul CA, Rauzy C (2004) Struct Bond 106:97
36. Atanasov M, Daul CA, Rauzy C (2003) Chem Phys Lett 367:737
37. Atanasov M, Comba P (2009) In: Köppel H, Barentzen H, Yarkony DR (eds) The Jahn-Teller effect: fundamentals and implications for physics and chemistry, vol 97. Springer Series in Chemical Physics, Berlin
38. Andersson K, Malmqvist PA, Roos BO, Sadlej AJ, Wolinski K (1990) J Phys Chem 94:5483
39. Andersson K, Malmqvist PA, Roos BO (1992) J Chem Phys 96:1218
40. Andersson K (1995) Theor Chim Acta 91:31
41. Andersson K, Roos BO (1995) In: Yarkony D (ed) Modern electronic structure theory. World Scientific, Singapore, p 55
42. Pierloot K (2001) In: Cundari TR (ed) Computational organometallic chemistry. Marcel Dekker, New York, p 123
43. Roos BO, Andersson K, Fülscher MP, Malmquist PA, Serrano-Andres L, Pierloot K, Merchan M (1996) In: Prigogine I, Rice SA (eds) Advances in chemical physics, vol. XCIII. Wiley, New York, p 219
44. Roos BO, Andersson K, Fülscher MP, Serrano-Andres L, Pierloot K, Merchan M, Molina V (1996) J Mol Struct (Theochem) 388:257
45. Neese F (2005) ORCA—an ab initio, density functional and semi-empirical program package. Max-Planck institute for Bioinorganic Chemistry, Mülheim an der Ruhr, Germany
46. Neese F (2003) J Chem Phys 119:9428
47. Neese F (2006) J Inorg Biochem 100:716
48. Neese F (2006) J Am Chem Soc 128:10213
49. Wanko M, Hoffmann M, Strodel P, Thiel W, Neese F, Frauenheim T, Elstner M (2005) J Phys Chem B 109:3606
50. Schöneboom J, Neese F, Thiel W (2005) J Am Chem Soc 127:5840
51. Ray K, Weyhermüller T, Neese F, Wieghardt K (2005) Inorg Chem 44:5345
52. Fouqeau A, Casida ME, Lawson LM, Hauser A, Neese F (2005) J Chem Phys 122:044110
53. Blanchard S, Neese F, Bothe E, Bill E, Weyhermüller T, Wieghardt K (2005) Inorg Chem 44:3636
54. Neese F (2004) Magn Reson Chem 42:S187
55. Fouqueau A, Mer S, Casida ME, Daku LML, Hauser A, Mieva T, Neese F (2004) J Chem Phys 120:9473
56. Bill E, Bothe E, Chaudhuri P, Chlopek K, Herebian D, Kokatam S, Ray K, Weyhermüller T, Neese F, Wieghardt K (2004) Chem Eur J 11:204
57. Petrenko T, Ray K, Wieghardt K, Neese F (2006) J Am Chem Soc 128:4422
58. Neese F, Petrenko T, Ganyushin D, Olbrich G (2007) Coord Chem Rev 251:288–327
59. Gerloch M, Harding JH, Wooley RG (1981) Struct Bond (Berlin) 46:1–46
60. Primas H (1981) Chemistry, quantum mechanics and reductionism: perspectives in theoretical chemistry, vol 24. Lecture Notes in Chemistry, Springer Verlag, Berlin

61. Orgel LE (1960) An introdction to transition to transition-metal chemistry: ligand-field theory. Methuen & CO, London, Wiley, New York
62. Zaitsevskii A, Malrieu J-P (1995) Chem Phys Lett 233:597–604
63. Brunold TC, Hauser A, Güdel HU (1994) J Lumin 59:321–332
64. Grabenstetter JE, Tseng TJ, Grein F (1976) Int J Quant Chem 10:143–149
65. Pauncz R (1979) Spin eigenfunctions: construction and use. Plenum, New York
66. Roos BO, Taylor PR, Siegbahn PEM (1980) Chem Phys 48:157
67. Siegbahn PEM, Almlöf J, Heiberg A, Roos BO (1981) J Chem Phys 74:2384
68. Aquilante F, Pederson TB, Lindh R, Roos BO, Sánches de Meras A, Koch H (2008) J Chem Phys 129:024113
69. Vahtras O, Almlöf J, Feyereisen MW (1993) Chem Phys Lett 213:514
70. White SR, Martin RL (1999) J Chem Phys 110:4127
71. Roos BO (2008) In: Shukla MK, Leszczynski J (eds) Radiation induced molecular phenomena in nucleic acids, vol 5. Springer, Netherlands, pp 125–156
72. Møller C, Plesset MS (1934) Phys Rev 46:618
73. Cimiraglia R (1996) Int J Quant Chem 60:167
74. Angeli C, Cimiraglia R, Evangelisti S, Leininger T, Malrieu JP (2001) J Chem Phys 114:10252
75. Wolinski K, Pulay P (1989) J Chem Phys 90:3647
76. Davidson ER, Jarzecki AA (1999) In: Hirao K (ed) Recent advances in multireference methods. World Scientific, Singapore, p 31
77. Kozlowski PM, Davidson ER (1994) J Chem Phys 100:3672
78. Murhphy RB, Messmer RP (1991) Chem Phys Lett 183:443
79. Hirao K (1992) Chem Phys Lett 190:374
80. Nakana H (1993) J Chem Phys 99:7983
81. Malrieu JP, Heully JL, Zautsevskii A (1995) Theor Chim Acta 90:167
82. Andersson K, Malmqvist PA, Roos BO, Sadlej AJ, Wolinski K (1990) J Phys Chem 94:5483
83. Angeli C, Cimiraglia R, Malrieu J-P (2002) J Chem Phys 117:9138
84. Angeli C, Cimiraglia R, Malrieu J-P (2001) Chem Phys Lett 350:297
85. Havenith RWA, Taylor PR, Angeli C, Cimiraglia R, Ruud K (2004) J Chem Phys 120:4619
86. Angeli C, Pastore M, Cimiraglia R (2007) Theor Chim Acta 117:743
87. Angeli C, Borini S, Cestari M, Cimiraglia R (2004) J Chem Phys 121:4043
88. Angeli C, Bories B, Cavallini A, Cimiraglia R (2006) J Chem Phys 124:054108
89. Angeli C, Borini S, Cavallini A, Cestari M, Cimiraglia R, Ferrighi L, Sparta M (2006) Int J Quant Chem 106:686–691
90. McLean AD, Liu B (1973) J Chem Phys 58:1066
91. Siegbahn PEM (1977) Chem Phys 25:197
92. Meyer W (1977) In: Schaefer HF III (ed) Methods of electronic structuretheory. Plenum Press, New York, p 413
93. Werner H-J, Knowles PJ (1990) Theor Chim Acta 78:175
94. Angeli C, Calzado CJ, Cimiraglia R, Malrieu J-P (2006) J Chem Phys 124:234109
95. Finley J, Malmqvist P-Å, Roos BO, Serrano-Andrés L (1998) Chem Phys Lett 288:299
96. Dyall KG (1995) J Chem Phys 102:4909
97. Roos BO, Andersson K (1995) Chem Phys Lett 245:215
98. Ghigo G, Roos BO, Malmqvist P-A (2004) Chem Phys Lett 396:142
99. Forsberg N, Malmqvist P-Å (1997) Chem Phys Lett 274:196
100. Witek HA, Choe Y-K, Finley JP, Hirao K (2002) J Comput Chem 23:957
101. Camacho C, Cimiraglia R, Witek HA (2010) Phys Chem Chem Phys 12:5058
102. Hess BA, Marian CM, Wahlgren U, Gropen O (1996) Chem Phys Lett 251:365
103. Neese F (2005) J Chem Phys 122:034107
104. Berning A, Schweizer M, Werner HJ, Knowles PJ, Palmieri P (2000) Mol Phys 98:1823
105. Schimmelpfennig B (1996) AMFI – an atomic mean field integral program. University of Stockholm, Stockholm, Sweden
106. McWeeny R (1992) Methods of molecular quantum mechanics. Academic, London

107. McWeeny R (1965) J Chem Phys 42:1717
108. Marian CM (2001) In: Lipkowitz KB, Boyd DB (eds) Reviews in computational chemistry, vol 17. Wiley, New York
109. Neese F, Solomon EI (2003) In: Miller JS, Drillon M (eds) Magnetoscience – from molecules to materials, vol IV. Wiley, Weinheim, p 345
110. Rose ME (1967) Elementary theory of angular momentum. Wiley, New York
111. Neese F, Solomon EI (1998) Inorg Chem 37:6568
112. Ganyushin D, Neese F (2006) J Chem Phys 125:024103
113. Ganyushin D, Gilka N, Taylor PR, Marian CM, Neese F (2010) J Chem Phys 132:144111
114. Harriman JE (1978) Theoretical Foundations of Electron Spin Resonance. Academic Press, London
115. Gerloch M, Guy Woolley R (1984) Progr Inorg Chem 31:371
116. Schönherr T (1997) Top Curr Chem 191:87–152
117. Bridgeman AJ, Gerloch M (1997) Progr Inorg Chem 45:179
118. Schönherr T, Atanasov M, Adamsky H (2003) In: Comprehensive coordination chemistry, vol II. Elsevier, pp 433–455
119. Perdew JP, Burke K, Ernzerhof M (1996) Phys Rev Lett 77:3865
120. Perdew JP, Burke K, Ernzerhof M (1997) Phys Rev Lett 78:1396 (Erratum)
121. Grimme S (2006) J Comput Chem 27:1787
122. van Wüllen C (1998) J Chem Phys 109:392
123. Pantazis DA, Chen XY, Landis CR, Neese F (2008) J Chem Theory Comput 4:908
124. Weigend F, Ahlrichs R (2005) Phys Chem Chem Phys 7:3297
125. Adamsky H. with contributions from Hoggard PE, Atanasov M, Eifert K AOMX, http://www.aomx.de
126. Powell MJD (1964) Comput J 7:155–162
127. Clifford AA (1973) Multivariate error analysis. Applied Science, London
128. Jørgensen CK (1962) Absorption spectra and chemical bonding in complexes. Pergamon, Oxford
129. Schläfer HL, Gaussman H, Zander HU (1967) Inorg Chem 6:1528
130. Allen GC, El-Sharkawy GAM, Warren KD (1971) Inorg Chem 10:2538
131. Ferguson J, Knox K, Wood DL (1971) J Chem Phys 54:504
132. Dubicky L, Ferguson J, Van Oosterhout B (1980) J Phys C 13:2791
133. Richardson JW, Vaught DM, Saules TF, Powell RR (1969) J Chem Phys 50:3633
134. Gladney HM, Veillard A (1969) Phys Rev 180:385
135. Wachters AJH, Nieuwpoort WC (1972) Phys Rev B5:4291
136. Demuynck J, Veilard A, Wahlgren U (1973) J Am Chem Soc 95:5563
137. Pueyo JW, Richardson JW (1977) J Chem Phys 67: 3577–3582 and 3583–3591
138. Smit TJM, Haas WC, Nieuwpoort WC (1977) Theor Chim Acta (Berlin) 43:277
139. Miyoshi E, Obara S, Takada T, Kashiwagi H, Ohno K (1981) Int J Quant Chem 19:481
140. Miyoshi E, Obara S, Takada T, Kashiwagi H, Ohno K (1983) Int J Quant Chem 23:1753
141. Gutiérrez Orellana S, Pueyo L (1984) J Solid State Chem 55:30
142. Vanquickenborne LG, Haspeslagh L, Hendricks M, Verhulst J (1984) Inorg Chem 23:1677
143. Bauschlicher CW, Bagus PS (1984) J Chem Phys 81:5889
144. Florez M, Seijo L, Pueyo L (1986) Phys Rev B34:1200
145. Broer R, Aissing G, Nieuwpoort WC (1986) Int J Quant Chem 29:1059
146. Čársky P, Dedieu A (1986) Chem Phys 103:265
147. Vanquickenborne LG, Hendricks M, Postelmans D, Hyla-Kryspin I, Pierloot K (1988) Inorg Chem 27:900
148. Pierloot K, Verhulst J, Verbeke P, Vanquickenborne LG (1989) Inorg Chem 28:3059
149. Pierloot K, Vanquickenborne LG (1990) J Chem Phys 93:4154
150. Pierloot K, Van Praet E, Vanquickenborne LG (1992) J Chem Phys 96:4163
151. MOLCAS, Electronic Structure Software, Almlöf J, Blomberg M, Karlström G, Malmqvist P-Å, Roos BO, Sadlej AJ, Siegbahn PEM, Widmark P-O

152. Jørgensen CK (1966) Struct Bond (Berlin) 1:3
153. Atanasov M, Adamsky H, Reinen D (1996) Chem Phys 202:155–165
154. Ferguson J, Wood DL (1970) Aust J Chem 23:861
155. Schmidtke H-H (2004) Struct Bond (Berlin) 106:19–35
156. Smith DW (1978) Struct Bond 35:87–118
157. Anthon C, Bendix J, Schäffer CE (2004) Inorg Chem 43:7882–7886
158. Anthon C, Bendix J, Schäffer CE (2003) Inorg Chem 42:4088–4097
159. Anthon C, Bendix J, Schäffer CE (2004) Struct Bond (Berlin) 107:207–301
160. Holleman AF, Wiberg E (1995) Lehrbuch der Anorganischen Chemie, 101 edn. Gruyter
161. McGinnety JA (1972) J Am Chem Soc 94:8406–8413
162. Reinen D, Atanasov M, St. Nikolov G (1988) Inorg Chem 27:1678
163. Atanasov M, Delley B, Reinen D (2010) Z Anorg Allg Chem 636:1740–1750
164. Halvorson KE, Patterson C, Willet RD (1990) Acta Crystallogr B 46:508
165. Ferguson J (1964) J Chem Phys 40:3406
166. Hitchman MA, Cassidy PJ (1979) Inorg Chem 18:1745
167. Smith DW (1977) Inorg Chim Acta 22:107
168. Koester VJ, Dunn TM (1975) Inorg Chem 14:1811
169. Atanasov M, Rauzy C, Baettig P, Daul C (2005) Int J Quant Chem 102:119–131
170. Orgel LE (1961) J Chem Soc 3683.
171. Ceulemans A, Dendooven M, Vanquickenborne LG (1985) Inorg Chem 24:1153
172. Ceulemans A, Dendooven M, Vanquickenborne LG (1985) Inorg Chem 24:1159
173. Ceulemans A, Debuyst R, Dejehet F, King GSD, Vanhecke M, Vanquickenborne LG (1990) J Phys Chem 94:105–113
174. Atanasov MA, Schönherr T, Schmidtke H-H (1987) Theor Chim Acta 71:59–73
175. Atanasov M, Schönherr T (1990) Inorg Chem 29:4545–4550 (and cited ESR and ODMR references)
176. Dingle R (1971) Inorg Chem 10:1141
177. Cotton FA, Wise JJ (1967) Inorg Chem 6:917
178. Atanasov M, St. Nikolov G (1983) Inorg Chim Acta 68:15–23
179. Schönherr T, Atanasov M, Hauser A (1996) Inorg Chem 35:2077–2084
180. Ribbing C, Pierloot K, Ceulemans A (1998) Inorg Chem 37:5227–5232
181. Atanasov M, Daul CA (2005) CR Chimie 8:1421–1433
182. Krzystek J, Yeagle GJ, Park J-H, David Britt R, Meisel MW, Brunel L-C, Telser J (2003) Inorg Chem 42:4610–4618
183. Hendrich MP, Debrunner PG (1989) Biophys J 56:489
184. Frömmel T, Peters W, Wunderlich H, Kuchen W (1992) Angew Chem Int Ed Engl 31:612
185. Mink H-J, Schmidtke H-H (1994) Chem Phys Lett 231:235–240
186. Reinen D, Atanasov M, Lee S-L (1998) Coord Chem Rev 175:91–158
187. Bridgeman AJ, Gerloch M (1995) Chem Phys Lett 247:304–309
188. Mink H-J, Schmidtke H-H (1995) Chem Phys Lett 247:310–312
189. Vanquickenborne LG, Verdonck E (1976) Inorg Chem 15:454–461
190. Lever ABP (1984) Inorganic electronic spectroscopy, 2nd edn. Elsevier, Amsterdam, The Netherlands
191. Schwartz RW (1976) Inorg Chem 15:2817–2822
192. Barton TJ, Slade RC (1975) J Chem Soc Dalton Trans 650
193. Glerup J, Monsted O, Schäffer CE (1976) Inorg Chem 15:1399
194. Studer P (1975) Optical studies on chromium (IV) halide complexes, Ph.D. Thesis, University of Fribourg, Switzerland
195. Fields RA, Heindl E, Winscom CJ, Khan ZH, Plato M, Möbius K (1984) J Chem Phys 80:3082
196. Elbers G, Remme S, Lehmann G (1986) Inorg Chem 25:896
197. Andriessen WTM (1976) J Phys Chem Solids 37:189
198. Bullen GJ, Mason R, Pauling PP (1965) Inorg Chem 4:456–462
199. Cotton FA, Wise JJ (1966) Inorg Chem 5:1200–1207

Struct Bond (2012) 143: 221–230
DOI: 10.1007/430_2011_56

The Phase Rule: Beyond Myopia to Understanding

R. Stephen Berry and Boris M. Smirnov

Abstract The Gibbs phase rule relating the number of degrees of freedom f of a system to the number of components c and the number of coexisting phases p is a central, universally used relation, expressed by what is probably the simplest formula in the natural sciences, $f = c - p + 2$. Research into the behavior of small systems, notably atomic clusters, has shown in recent years that the phase rule is not as all-encompassing as is often assumed. Small systems can show coexistence of two or more phases in thermodynamic equilibrium over *bands* of temperature and pressure (with no other forces acting on them). The basis of this apparent violation of the phase rule, seeming almost like violation of a scientific law, is in reality entirely understandable, consistent with the laws of thermodynamics, and even allows one to estimate the upper size limit of any particular system for which such apparent violation could be observed.

Keywords Coexistence · Mass action · Phase equilibrium · Phase rule

Contents

R.S. Berry (✉)
Department of Chemistry, The University of Chicago, Chicago, IL 60637, USA
e-mail: berry@uchicago.edu

B.M. Smirnov
Institute for High Temperatures of Russian Academy of Sciences, 127412 Moscow, Russia
e-mail: bmsmirnov@gmail.com

1 Introduction and Background

In 1876, Gibbs [1] introduced the relation between the number of controllable degrees of freedom, f, the number of chemically distinguishable components, c, in a system, and the number of phases, p, coexisting in thermodynamic equilibrium. It is this rule, $f = c - p + 2$, that tells us that we can vary the temperature and pressure of a liquid composed of a single substance, but that if we require that liquid to be in equilibrium with a solid of the same substance, we can vary only the temperature or the pressure, and that the value of the other variable will be fixed by our physical requirement. The rule of course applies just when the only control variables we have are temperature and pressure; the number “2” changes if we add such variables as applied electric or magnetic fields. The work was virtually unknown until Roozeboom recognized and publicized it in 1887 [2]. The concept became much more widely known when Wilhelm Ostwald translated and published Gibbs’ papers in German in 1892. It became a central focus of some physical chemists, notably Wilder Bancroft, soon after the turn of the twentieth century [3].

The history of the phase rule is the subject of a review written for its centenary [4]; that history need not concern our discussion here because it reviews the applications and the controversies over the derivation of the rule. Here, we concern ourselves with the *deviations and apparent violations* of the phase rule, a topic essentially untouched until computer simulations of small systems suggested that the phase rule might, after all, not be so universal.

2 Observations of Apparent Violations

The first indications that certain systems might violate the phase rule came from computer simulations of small clusters of atoms. A number of studies revealed clearly defined solid-like and liquid-like forms [5–14]. These embraced both molecular dynamics and Monte Carlo simulations, and explored a variety of clusters. These included several based on atomic models with interparticle Lennard-Jones forces, which mimic rare gas clusters rather well. There were also models of alkali halide clusters. Hence, the existence of solid and liquid forms for such small systems seemed not only plausible but general, not restricted to any one kind of system. Shortly after these studies appeared, another, of a 55-atom cluster with Lennard-Jones interparticle forces, showed not only solid and liquid forms but also a form in which the surface of the cluster (with icosahedral structure) is liquid and the core is solid [15]. Simulations of metal clusters followed, and also showed solid and liquid forms [16, 17].

Experimental evidence for solid and liquid forms of clusters began to appear soon thereafter [18–21]. At that time, simply demonstrating the existence of the two phase-like forms for small clusters was a primary goal. Later, as we shall note shortly, more detailed and precise information came from experiments.

One particularly remarkable phenomenon seemed to appear in the early simulations. The observation of solid and liquid phases led Briant and Burton to make the tentative suggestion that even the small Lennard-Jones clusters that they were simulating could have a first-order phase transition [10]. However, Hill had argued in his monograph [22] that very small systems would have to have smooth passage between phases. But the simulations appeared to indicate that, at the molecular level in time evolution and in spatial structure, the solid and liquid forms are clearly distinguishable, with no indication, at least for many kinds and sizes of clusters, that there is no smooth, intermediate kind of behavior. Some of the simulations suggested that perhaps they showed dynamical coexistence of solid and liquid phases at more than one energy or temperature, with the simulated pressure constant, typically at zero.

In short, small clusters showed tantalizing kinds of behavior that did not seem to fit conventional concepts of how such systems should behave. This was a puzzle awaiting explanation.

3 Fundamental Explanation

3.1 *Local Stability of Phases*

The first step toward that explanation came from a rationalization of the simulation results of Briant and Burton [10] and of Etters and Kaelberer [11–13]. In this approach [23], one constructs quantum-mechanical models of the densities of states of rigid and highly nonrigid forms, i.e., solid and liquid forms, of the cluster of interest, and, from these, one can estimate partition functions and free energies of the two forms. The model uses a harmonic, rigid rotor model for the rigid form and an Einstein vibrator model for the nonrigid case. This is enough to specify the symmetry groups for the two limits, and hence to construct the correlation diagram between the two. (For N particles, the solid form has symmetry $SO(3) \times SO(3) \times U(3N - 6)$ and the liquid form has symmetry $U(3N - 3)$.) In this model, the parameter that varies from the solid extreme to the liquid extreme is simply some unspecified measure of the degree of nonrigidity. Such measures are available, but were not needed for the analysis of [23]. From the correlation diagrams and densities of states, it is straightforward to show that at low energies or temperatures, where only the low-lying levels are populated, only the rigid form has a minimum in its Helmholz or Gibbs free energy. At sufficiently high temperatures, only the nonrigid or liquid form has a minimum in its free energy. That is, at sufficiently low temperatures, only the solid is stable, and at sufficiently high temperatures, only the liquid is stable. However, there is an intermediate range of temperatures in which, according to this model, *both the rigid solid and the nonrigid liquid have local minima in their free energies.*

Within this model, there is a lowest temperature at which there is a minimum in the free energy in the region of the nonrigid limit, and another temperature that is the highest for which there is a free energy minimum in the region of the rigid, solid form.

From this point, several fruitful directions open. This result has told us that there is a distinct lower bound of temperature below which no liquid form is locally stable, and, correspondingly, a distinct upper bound of temperature above which no solid form is locally stable. These temperatures presumably depend on pressure, but that aspect has yet to be investigated. Whether those sharp bounds can be observed in real experiments is not clear, because of the question of whether fluctuations would hide or appear to smooth them. We refer to the lower limit of stability of the liquid as the *freezing limit* and the upper limit of stability of the solid as the *melting limit.*

3.2 The Coexistence of Phases

The next question is a very important one, perhaps the one most central to the issue of the relation between the phase rule and the behavior of small systems. This is the question of how the equilibrium between solid and liquid forms of small systems can be described in a manner that links that behavior to the behavior of macroscopic systems. It is, in fact, straightforward to address in traditional, classical thermodynamic terms.

We begin by writing the chemical *equilibrium constant* K_{eq} for the equilibrium between solid and liquid, $K_{\mathrm{eq}} = [\mathrm{liquid}]/[\mathrm{solid}]$. This quantity is determined by the difference between the free energies ΔF of the two forms, $K_{\mathrm{eq}} = \exp[-\Delta F/k_{\mathrm{B}}T]$, where k_{B} is the Boltzmann constant and T is the absolute temperature. But ΔF is the difference in the chemical potentials $\Delta\mu$, multiplied by N, the number of particles in each system. We know that the traditional condition for equilibrium of two phases, e.g., solid and liquid, is the equality of the free energies or chemical potentials of the two forms. This is what sets the conditions for the coexistence curves required by the phase rule.

Now suppose we are dealing with a small but macroscopic system of, say, 10^{20} particles, much less than a millimole. And suppose the system is not quite at the traditional equilibrium point of $\Delta\mu = 0$; suppose that there is a deviation of $\pm 10^{-10}$ from the exact equality in $\Delta\mu/k_{\mathrm{B}}T$. This means that the *exponent* determining the equilibrium constant is $\pm 10^{10}$, so $K_{\mathrm{eq}} = \exp[\pm 10^{10}]$. This tells us something we already knew from the phase rule, that even at such tiny deviations from exact equality of the chemical potentials, the amount of the unflavored phase, whichever it is, is present in unobservable tiny amounts.

But now let us apply this reasoning to small systems. Suppose we take $N = 20$; then if, for example, $\Delta\mu/k_{\mathrm{B}}T = \pm 0.01$, then $K_{\mathrm{eq}} = \exp[\pm 0.2]$, i.e., 1.22 or 0.81. In words, this means that the unflavored or minority form, whether solid or liquid, is present in almost as large an amount as the more stable form. *This way of approaching solid–liquid equilibria shows that the phase rule is strictly a consequence of large numbers, and that its range of validity is that of macroscopic systems.*

That range is something we examine later.

Because the equilibrium constant K_{eq} ranges from zero, when the system is all solid, to infinity, when it is all liquid, (strictly, one should include vaporization, neglected here) it is convenient to introduce another related function, a ratio we call D (for distribution), which contains the same information but ranges from -1 to $+1$: $D = (K_{\mathrm{eq}} - 1)/(K_{\mathrm{eq}} + 1)$. This allows us to portray graphically the behavior of a system in terms of the amount of each of two phases as a function of temperature. This is done in Fig. 1, for a small system (a), a mid-size system (b), and a large but not truly macroscopic system (c). However, even case (c) in this figure does not

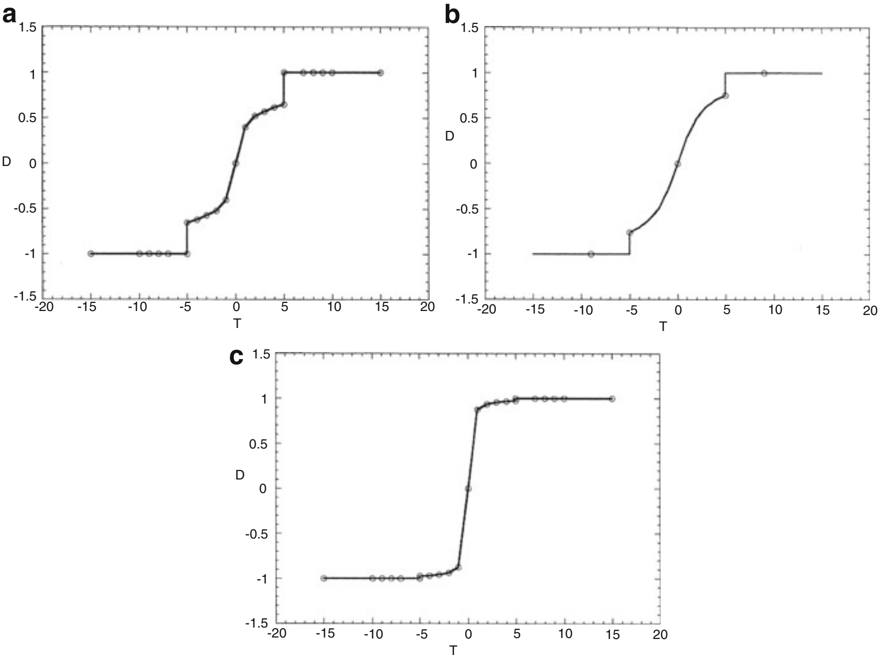

Fig. 1 Schematic behavior of two-phase systems as functions of temperature T. (**a**) A small system, with relatively large jumps in the distribution D at the freezing and melting limits, and a gradual change in D between these two limits, (**b**) a somewhat larger system, with smaller jumps and a steeper variation in D with temperature, and (**c**) a still larger system, for which the jumps in D are not discernable and its variation from -1 to $+1$ is very steep

make the change of D from -1 to $+1$ nearly as sharp as it is for any truly macroscopic system; for any system large enough to be visible to the naked eye, the change would be via a vertical line.

One important point that is virtually hidden in the argument showing that, for a small system, two phases can coexist over a range of temperature and pressure is this: the argument applies equally to more than two phases! So long as their free energies have sufficiently similar values, observable amounts of several phases can indeed coexist.

One particularly vivid example is the cluster of 55 atoms bound by Lennard-Jones forces, effectively Ar_{55} or by metallic binding forces. Besides its solid and liquid phases, this cluster (and others of similar size and constitution) can exhibit a *surface-melted phase* [15, 24, 25]. Strictly, as animations show, the term "surface melting" is not really accurate. In the phase that shows a high mobility of the atoms in the surface layer, the actual motion of almost all of those atoms is a large-amplitude, very anharmonic vibration, while at least one atom is promoted to move rather freely around the shell as a "floater"; the average is about one surface atom in 15 becomes a floater. The floater atom exchanges positions occasionally with an atom in the outer shell, so that, over time, all the surface atoms are, at some time, a floater. This process allows all the surface atoms to permute their positions and eventually to occupy all the surface sites – as one would expect of a liquid.

4 Observability of Coexistence in Apparent Violation of the Phase Rule

The next question is "How large can a cluster be and exhibit a band of coexisting solid and liquid phases?" What determines the size at which the phase rule begins to apply? The answer to this question lies in the property that most distinguishes solids and liquids, the difference in the entropies of the two forms [26, 27]. The approach requires an arbitrary decision as to what constitutes "observable" and the choice made in these references is that the minority phase should be present in an amount at least 10% as much as the majority phase. That means that one looks for conditions for which $0.1 < K_{\text{eq}} < 10$. This, in turn, means that $-2.3 < N\Delta\mu/k_{\text{B}}T < 2.3$. If we set the observable conditions at 1% instead of 10%, these values double. Of course $N\Delta\mu$ or ΔF is zero at the point of equal probability of the two phases, which we shall call, according to tradition, the melting point, where $\Delta E_m = T\Delta S_m$; here, the subscript m indicates the value at that melting point. We can assume that the energy and entropy changes, ΔE_m and ΔS_m in the vicinity of the melting point are very close to their values at the melting point. If we express the free energy change in units of $k_{\text{B}}T$, then $\Delta F = \Delta E/T - \Delta S$. From this, we can define the range of observability for the free energy as δF, the temperature derivative of ΔF evaluated at the melting point, or $\Delta E_m \delta T/T_m^2$. But since $\Delta E_m/T_m = \Delta S_m$, we can write the simple approximate expression $\delta T/T_m = \delta F/\Delta S$. If we set observability limits at 10% of the minority species, then δF is 4.6, or essentially 5, so we can make the estimate the observability as $\delta T \sim 5T_m//\Delta S$.

Computer-based and model-based estimates of the entropy changes for rare gas clusters allow us to approximate the entropy change per particle, and infer that for a 100-atom cluster of argon atoms, with a criterion of 10%, $\delta T \approx 0.1$ K, and with a criterion of 1%, this extends to about 0.4 K [26]. Metal clusters have much smaller entropy changes when they melt, because of their much higher densities of states in their solid phases, so their ranges of observability of coexistence extend to several hundred particles. Such coexistence ranges have been observed in experiments, e.g., with sodium clusters [28, 29]. The first to be observed exhibiting such coexistence was $\mathrm{Na}_{139}{}^{+}$.

5 Phase Diagrams for Small Systems

Because the solid and liquid phases of small systems can coexist over ranges of temperature and pressure and in varying ratios, a phase diagram for such a system requires one coordinate more than the traditional two-dimensional p–V plot. It is convenient to use the distribution D to define that third coordinate, so that when $D = -1$, the system is entirely solid and when $D = +1$, it is entirely liquid. Figure 2 shows two examples of such expanded phase diagrams: in (a), we have a macroscopic system, exhibiting a discontinuous jump of D between these two values at the melting point. Example (b) is a schematic representation of a small system, for which there are discontinuities at the freezing and melting limits of temperature, but a continuous variation of D between these two discontinuities. In the former, because there are no intermediate values of D, the third coordinate is superfluous,

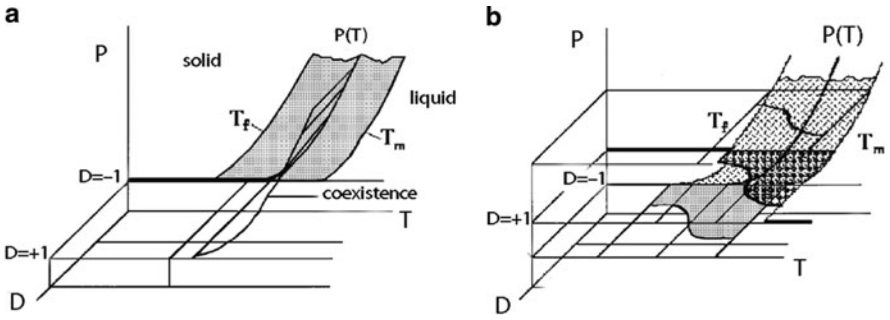

Fig. 2 Schematic phase diagrams for solid–liquid equilibria in three dimensions, pressure p, temperature T, and distribution D; (**a**) for a macroscopic system, in which the change from solid to liquid is discontinuous at the melting point $T_m(p)$ and D changes from -1 to +1; (**b**) for a small system, for which D changes discontinuously between -1 and an intermediate value, and again between a much higher intermediate value and +1, but varies continuously between those two intermediate values

but in the latter, we need the third variable D in order to show the composition of the system in the coexistence range.

6 Conclusions and Summary Remarks

This review has shown that the Gibbs phase rule, powerful as it is, is a consequence of the large numbers of atomic particles in all macroscopic systems. Small systems, of order hundreds of particles or fewer, violate that rule in that multiple phases can coexist in thermodynamic equilibrium over ranges of temperature and pressure, and still behave in a way consistent with the basic laws of thermodynamics. If we treat phase equilibria just as we treat equilibria of chemical isomers and reacting species, we find that for large systems, the free energy change in the vicinity of the traditional melting point is so sharp that the unflavored phase can be present only in unobservable small quantities at temperatures deviating only tiny amounts from that melting point. However, for small systems, the free energy difference between phases can be small enough that observable amounts of the unfavored minority phase can easily exist under attainable conditions away from the melting point or, more generally, the traditional coexistence curve. Moreover the same reasoning shows that multiple phases may coexist within such ranges. It is possible to estimate from the entropy change between phases what the maximum size is for such coexistence to be detectable. One can construct phase diagrams for the coexistence of two phases that show the relative amounts of each phase as a function of temperature and pressure.

While Carl Johan Ballhausen worked throughout his scientific career on properties of atomic and molecular systems, especially complex ions, he was always fully aware of the thermodynamic aspects of these systems. He also was always determined to “get things right,” whether they fit conventional notions or not. It is in that spirit that this work addresses one of those conventional, accepted concepts and, by examining its realm of validity, strives to “get things right.”

Acknowledgments R.S.B. wishes to acknowledge the hospitality of the Aspen Center for Physics, which enabled the writing of this chapter. He also wishes to recognize with deep appreciation and very dear memories the companionship and stimulation of Carl Johan Ballhausen, from the time they were first together in the research group of William Moffitt at Harvard, in the 1950s until his passing.

References

1. Gibbs JW (1876) Trans Conn Acad 3:108; (1878) Trans Conn Acad 3:343
2. Roozeboom HW (1887) Rec Trav Pays-Bas Belg 6:262
3. Servos JW (1990) Physical chemistry from Ostwald to Pauling, Chapter 3. Princeton University Press, Princeton, p 100

4. Daub EE (1976) J Chem Ed 53:747
5. Cotterill RMJ, Damgaard-Kristensen W, Martin JW, Peterson LB, Jensen EJ (1973) Comput Phys Comm 5:28
6. Cotterill RMJ (1975) Phil Mag 32:1283
7. Lee JK, Barker JA, Abraham FF (1973) J Chem Phys 58:3166
8. McGinty DJ (1973) J Chem Phys 58:4733
9. Damgaard-Kristensen W, Jensen EJ, Cotterill RMJ (1974) J Chem Phys 6:4161
10. Briant CL, Burton JJ (1975) J Chem Phys 63:2045
11. Etters RD, Kaelberer JB (1975) Phys Rev A 11:1068
12. Etters RD, Kaelberer JB (1977) J Chem Phys 66:5112
13. Kaelberer JB, Etters RD (1977) J Chem Phys 66:3233
14. Amini M, Fincham D, Hockney RW (1979) J Phys C 12:4707
15. Nauchitel VV, Pertsin AJ (1980) Mol Phys 40:1341
16. Garzon IL, Jellinek J (1991) Z Phys D 20:235
17. Jellinek J, Garzon IL (1991) Z Phys D 20:239
18. Farges J, de Feraudy MF, Raoult B, Torchet G (1983) J Chem Phys 84:3491
19. Bartell LS (1985) Chem Rev 86:492
20. Bartell LS, Harsanyi L, Valente EJ (1989) J Phys Chem 93:6201
21. Bartell LS, Dibble TS (1991) J Phys Chem 95:1159
22. Hill TL (1963) The thermodynamics of small systems, Part 1; (1964) Part II. Benjamin, New York
23. Berry RS, Jellinek J, Natanson G (1984) Phys Rev A 30:919
24. Cheng H-P, Berry RS (1992) Phys Rev A 45:7969
25. Kunz RE, Berry RS (1994) Phys Rev E 49:1895
26. Berry RS, Smirnov BM (2009) Int J Mass Spectrom 280:204
27. Berry RS (2010) In: Sattler K (ed) Handbook of nanophysics, V.1, Chapter 20. CRC Press, Taylor and Francis, Boca Raton, FL
28. Schmidt M, Kusche R, Kronmüller W, von Issendorf B, Haberland H (1997) Phys Rev Lett 79:99
29. Schmidt M, Donges J, Hippler T, Haberland H (2003) Phys Rev Lett 90:103401

Index